

**School of Electrical Engineering, Computing and
Mathematical Sciences**

**A Search for Molecules at Low Frequency with the
Murchison Widefield Array**

Chenoa Tremblay

**This thesis is presented for the Degree of
Doctor of Philosophy
of
Curtin University**

July 2018

To the best of my knowledge and belief this thesis contains no material previously published by any other person except where due acknowledgement has been made. This thesis contains no material which has been accepted for the award of any other degree or diploma in any university.

Chenoa Desir e Tremblay

“The more that you read, the more things you will know. The more that you learn, the more places you’ll go.”

- Dr. Seuss

“Chemistry begins in the stars. The stars are the source of the chemical elements, which are the building blocks of matter and the core of our subject.”

-Peter Atkins

Acknowledgements

Peter Carroll, an American football coach, once said “Each person holds so much power within themselves that needs to be let out. Sometimes they just need a little nudge, a little direction, a little support, a little coaching, and the greatest things can happen.” This journey has taken me 11 years, two countries, two universities, and a lot of help along the way.

This work would not have been possible without the continuous support and mentoring of all of my supervisors I have had the pleasure of working with. A special thanks to Greg Taylor at the University of New Mexico that taught me the foundations of radio astronomy and provided me guidance that lead me down the path of studying at Curtin University. I would also like to express my sincere gratitude to my advisors, past and present at Curtin, Prof. Steven Tingay, Prof. Igor Bray, Dr. Natasha Hurley-Walker, Dr. Andrew Walsh, Dr. Christopher Jordan and Dr. Maria Cunningham for their continuous support, patience, motivation, and immense knowledge. You have all played important roles and guidance which helped me during my research and writing of this thesis. I would also like to thank Paul A. Jones, who became a supervisor and mentor by default. Thank you for all the times you sat down to go over the science and data quality portions of my research.

I am grateful to my daughter and husband Helena and Steven, who have provided me thorough moral and emotional support in my life. Without your love, support, and guidance, I would never have started, let alone completed, this journey. I am also grateful to my other family members and friends who have supported me along the way.

I would also like to thank the management team and staff at MinAnalytical Laboratory Services, in particular Gary Wheeler, John McGrath and Dave Martin, that have allowed me to work flexible hours, change from full time to part time, and ability to travel during my studies. I really appreciate your support over the last 7 years and continued interest on my progress.

Abstract

Within the last 50 years, over 180 molecules have been discovered in interstellar space with the majority detected at the sub-millimetre radio wavelengths. Over the last decade, astrochemistry has been predominately conducted at GHz-frequencies and pushed up above 1 THz. However, in my work contained within this thesis, I took advantage of a new generation wide-field, low-frequency telescope to look for molecules whose lowest energy transitions reside around 100 MHz and atoms whose large size make for sensitive pressure probes of the interstellar medium. For example, simple molecules such as SH, are difficult to detect at higher frequencies, but have ground state transitions between 99–122 MHz. Utilising this same data, I helped set limits on the first low-frequency search for extraterrestrial signals towards known exoplanets. This thesis documents the creation of a pipeline to calibrate and analyse data from the Murchison Widefield Array and the results from surveys around the Galactic Centre and the Orion Nebula. The results of these surveys are highlighted within the science chapters contained within this thesis, and resulted in the world's first detection of molecules below 700 MHz and proof that high-mass stars may form in isolation.

Contents

Acknowledgements	vii
Abstract	ix
1 Introduction	1
1.1 Astrochemistry and its History	1
1.2 Thesis Overview	3
1.3 Detecting Molecules in Astrophysical Environments	6
1.3.1 Rotational Transitions	7
1.3.2 Vibrational Transitions	8
1.3.3 Fine Structure	9
1.3.4 Hyperfine Structure	10
1.3.5 Multiple Transitions	10
1.3.6 Abundances and Physical Conditions	11
1.4 Star Formation	13
1.4.1 Low-Mass Star Formation	15
1.4.2 High-Mass Star Formation	19
1.5 Astrochemical Observations	21
1.6 Spectral Line Surveys	22
1.6.1 Galactic Centre	23
1.6.2 Orion	24
1.7 Radio Recombination Lines	25
1.8 Low Frequency Observations and Instrumentation	26
1.9 Statement of Originality	28

2	Methods	31
2.1	Observational Design	31
2.2	The Murchison Widefield Array	33
2.3	Data Gathering Procedures	34
2.4	Data Analysis	35
2.4.1	Derive Phase and Amplitude Calibration Solution	37
2.4.2	Apply the Phase and Amplitude Calibration Solution to the Field Observation	38
2.4.3	Coarse Channel Imaging	39
2.4.4	Flux Density Scale, Primary Beam, and Ionospheric Cor- rections	43
2.4.5	Fine Channel Imaging	49
2.5	Create Final Spectral Cubes	53
2.5.1	Stacking Observation with Inverse Variance Weighting	53
2.5.2	Continuum Subtraction	54
2.6	Data Search and Visualisation	57
2.6.1	Search Strategies	57
2.6.2	Spectra Creation and Analysis	60
2.6.3	Data Visualisation	60
2.7	Confirmation of Sources	61
2.7.1	Gaussian Statistics	61
2.7.2	Splitting the Data Cubes	64
2.7.3	Stacking of Spectral Signals	64
2.8	Spectral Properties of the MWA	67
2.9	Python Code	68
3	The High Mass Star Forming Region G13.384+0.064: An Iso- lated Star?	73
3.1	Abstract	73
3.2	Introduction	74
3.3	Sample Selection	76
3.4	Results	76

3.4.1	Infrared & Radio Observation	76
3.4.2	Distance	81
3.4.3	Dust Derived Mass	82
3.4.4	Luminosity	83
3.4.5	Lyman Continuum Flux	85
3.4.6	Star Type	85
3.4.7	An unrelated evolved star	87
3.5	Discussion	87
3.5.1	Far Distance Consideration	87
3.5.2	Isolated vs. clustered star formation in G13.384+0.064 . .	88
3.6	Conclusions	90
3.7	Acknowledgements	90
4	A First Look for Molecules between 103 and 133 MHz using the Murchison Widefield Array	91
4.1	Abstract	91
4.2	Introduction	92
4.3	Observations and Data Reduction	93
4.3.1	Calibration and Imaging	95
4.4	Line Search and Identification	99
4.4.1	Survey Strategy	99
4.4.2	Line Search	99
4.5	Results	100
4.5.1	Targeted Search	100
4.5.2	Blind Search	107
4.6	Discussion	108
4.7	Summary and Conclusions	111
4.8	Acknowledgments	112
4.9	Appendix: Column Density	113
5	A Molecular Line Survey around Orion At Low Frequencies with the MWA	115

5.1	Abstract	115
5.2	Introduction	116
5.3	Observations and Data Reduction	117
5.3.1	RFI Flagging	120
5.4	Survey Strategy	121
5.5	Results and Discussion	123
5.5.1	Nitric Oxide Tentative Detections	124
5.5.2	Formic Acid Tentative Detection	127
5.5.3	Molecular Oxygen Tentative Detection	127
5.5.4	Unidentified Tentative Detections	129
5.5.5	Orion Chemical Environment	131
5.5.6	Connections to Laboratory Science	131
5.6	Conclusions	133
5.7	Acknowledgments	134

6 Low-Frequency Carbon Recombination Lines in the Orion Molecular Cloud Complex **137**

6.1	Abstract	137
6.2	Introduction	138
6.3	Observations & Data Reduction	139
6.3.1	Calibration & Imaging	140
6.3.2	Survey Details	141
6.4	Results	143
6.4.1	Radio Continuum, H α and Dust Emission	143
6.4.2	Carbon Recombination Lines	143
6.5	Discussion	145
6.5.1	Turn-over Frequency of CRRL Sources	145
6.5.2	Spectral Quality	149
6.5.3	Origin of CRRLs around Orion	149
6.6	Conclusions	151
6.7	Acknowledgements	151
6.8	Appendix: Full Spectra	152

7	Search for Extraterrestrial Signals with the MWA	159
7.1	Introduction	159
7.2	Narrowband or Wideband signal?	160
7.3	Frequency Selection	161
7.4	SETI with the MWA	162
7.5	Conclusion	163
8	Conclusion and Future Work	165
A	Co-Author Statements	169
B	Copy Right Information	173

List of Figures

1.1	Diagram showing the different energy levels of molecules experiencing ro-vibrational motions, also known as fine structure. The two black horizontal lines show two vibrational states as defined by equation 1.4. The J terms are discrete angular momentum levels described in equations 1.1 and 1.2. The red and blue arrows show two different rotational transitions of the molecules. (Image Credit: Michael Evans)	9
1.2	An example rotation diagram of Ammonia where the fit to the $\log \frac{N_u}{g_u}$ for each observed transition is proportional to the temperature of the environment. The y-axis is the column density divided by the rotational degeneracy (g_u) and spin degeneracy (S). The x-axis is the transition energy in Kelvin. The two linear lines show the best fit for the cold component (orange) and hot component (red). (Image Credit: Maxted et al. 2016)	14
1.3	A graphic demonstrating the life cycle of a sun-like star. (Image Credit: Greene 2001)	16
1.4	Image of dust grains and demonstration of the process of ice formation within the cold dense cloud before star formation begins. The molecules absorb on the surface in an “onion ring” like structure, creating a complex chemistry. (Image credit:Burke and Brown 2010)	18
1.5	Synthetic spectra of SO ₂ that shows the intensity of the molecular transitions at higher frequencies is greater than at lower frequencies (Image Credit: From Figure 2 of Herbst and van Dishoeck 2009).	28

2.1	The Galactic Centre and Orion region both represent significant areas for study of chemical tracers in the Interstellar Medium. The wide field-of-view from the MWA offers an increased testing ground for evaluation of stars and star formation regions. The image of the Galactic Centre at 103 MHz, on the left, is the continuum image from the pilot spectral line survey. The image on the right represents the Orion region at 99 MHz. For more detailed images of the survey fields see Chapter 4, 5, and 6 of this thesis.	32
2.2	An example of the sensitivity just off the phase centre of each observation within the Orion field, as observed during the Orion 114.6 MHz survey. The primary beam model is a set of normalised values which are one at zenith. These values are much lower than one as Orion was closer to the horizon during these observations. .	35
2.3	Flow Chart detailing the process of the developed pipeline used for spectral line analysis with the MWA. The left column in red summarises the stages the pipeline details where the blue rows represent the detail of that stage.	36
2.4	An image of a single coarse channel made by the WSCLEAN pseudo-Stokes I (an arithmetic mean of the XX and YY components of the dipoles), divided by a true Stokes I image. The image shows that the two match with a ratio of 1 except in some pixel locations, which are likely from errors in the deconvolution.	42
2.5	A primary beam model was created for each coarse channel within a single observation. The beam model from the first coarse channel was divided by the beam model for the remaining 23 coarse channels and the ratio of the sensitivities is shown.	44
2.6	Ratio of the flux density values between the Galactic Centre survey data from the MWA compared to the Molonglo Reference Catalogue (MRC). The plot shows ratio of the flux densities is one across the sky. Some sources that show differences greater than or less than one may be due to extended emission being broken up into multiple components in during the AEGEAN source finding. .	46

2.7	The difference in the source positions in the Galactic Centre survey (July 2014 data only) images in comparison to MRC prior to correction. The linear fit to the data, represented by the dashed line, demonstrates that the source shift caused by the ionosphere varies slightly as a function of wavelength squared. The error bars show the standard deviation from values of the sources within the field across the sky. The top plot is the position offsets in right ascension (RA) and the bottom plot is the position offsets in declination (Dec).	48
2.8	A plot of the mean positions shifts in RA, plotted for each observation from the 2014 and 2016 epochs of Galactic Centre data. The gap is caused by the observations being on different nights, two years apart.	49
2.9	Residual continuum in the three-dimensional data cube after continuum subtraction was done in CASA on the Galactic Centre data from 2014. (Image Credit: This image was created by Amr Hassan using spectral line cube visualisation software he created.)	55
2.10	Reduction of noise as a function of time. The top plot is from Figure 4.6 and shows that the noise continues to decrease as a function of square root of time, represented by the dashed line in both plots having a slope of -0.5. This plot also shows the approximate noise threshold we would need to achieve to obtain the column densities published at higher frequencies. The bottom plot is from the Orion survey at 114.6 MHz and also shows that the noise decreases as a function of square root of time once a correction for the primary beam sensitivity is applied.	58
2.11	Histogram of pixel values near one of the tentative detections from the Orion Survey region. This is an example but histograms were created near each potential detection to look for abnormalities caused by RFI. The y-axis is the pixel counts and the x-axis is the pixel values in Jy Beam ⁻¹ . The shape of the inverse parabola on the right hand plot suggests the noise is Gaussian.	62

2.12	An example signal-to-noise spectra near, but off, a potential detections on the left and the Gaussian plot from the survey's sky on the right. The central channel is flagged in the continuum-subtracted data cube due to instrumental effects, so the signal-to-noise is zero. (Image Credit: Paul A. Jones)	63
2.13	Example of one of the nitric oxide tentative detections at 107.36 from Chapter 4 (Galactic Plane survey) split across the two observation epochs of 2014 and 2016. The large central image is the published detections and the top right image is from observations taken in 2014 and the bottom right is from observations taken in 2016. All three images are created by setting the contours at the same values and imaging using the same noise threshold. A similar image was made for each of the tentative NO detections and the tentative SH detection from the Galactic Plane survey.	65
2.14	Average CRRLs C367–399 α lines in blue with the error bars of the local rms. The spectra in green represents a similarly stacked set of channels to show the background signal. The y-axis is the flux limits of a stacked region of 100 by 100 pixels over the Galactic Centre.	66
2.15	Average CRRLs C367–399 α lines in blue. The y-axis is the optical depth when compared to the Continuum reported in GLEAM.	67
2.16	Diagram from Figure 1 of Lonsdale et al. (2009) representing the MWA system design from Phase I of the MWA. This thesis did not use the Real Time data processing pipeline shown in this diagram as the data processing required for spectral line work needed additional considerations.	69
2.17	The full spectrum of one coarse channel with the MWA before continuum subtraction. The first 10 channels are a different flux density level and show the flagging completed at the correlator did not fully remove the fine channels affected by aliasing.	70

2.18	The images show the continuum image for a single channel (left), the continuum subtracted image for a single channel (middle), and the RMS map created from the continuum subtracted data cube. This shows that by leaving in the edge channels there is a lot of residual noise in the final subtracted cube that makes identification of new lines difficult.	70
2.19	The left image is an example spectrum from one coarse channel after the edge channels and continuum were removed. The mean RMS is $0.29 \text{ Jy beam}^{-1}$. The right image is a plot of the RMS in the centre of each image within one coarse channel. This shows that the noise towards the edges still is higher in some coarse channels even after the extra channels were removed.	71
3.1	Plot of clump mass versus Lyman photon flux for a series of ATLASGAL and CORNISH sources, similar to the upper panel of Figure 26 in Urquhart et al. (2013). When the clump mass is plotted against the bolometric luminosity, the source at G13.384+0.064 does not stand out as different compared to other star forming regions. This discrepancy is investigated in this paper. The error bars represent the best available data reported in this paper. . . .	77
3.2	GLIMPSE 3 colour image with blue as $3.6 \mu\text{m}$, green as $4.5 \mu\text{m}$ and and red as $8.0 \mu\text{m}$. Contour image on the left shows CORNISH 5 GHz radio continuum emission from 2 mJy/beam to 10 mJy/beam in steps of 2 mJy/beam. The white cross on the image on the left represents the centre of the ATLASGAL contours and the image on the right shows the GLIMPSE 3 colour image with ATLASGAL contours. The contour levels are from 0.25 Jy/beam and increase in steps of 0.25 Jy/beam up to 1.0 Jy/beam. We identify an evolved star, seen at G13.380+0.050 and discussed in section 3.8 that is unrelated to the source.	78

3.3	Colour-Colour diagram plotting sources 30 arc second around G13.384+0.064 (on source;blue) and 30 arc seconds around G13.36+0.075 (off source;red). The IMF curve is data representing a cluster $<10^5$ years old from Lejeune and Schaerer (2001). The vector represents the extinction vector plotted as per Nishiyama et al. (2009). There are no clear signs there are a cluster of main sequence stars. . . .	79
3.4	Three-colour image with red at K band, green at H band and blue at J band of UKIDSS data overlaid with contours from CORNISH 5 GHz radio continuum emission with contours at 0.19 and 0.32 Jy/beam.	80
3.5	The H _I continuum subtracted (left) and H _I continuum (right) profiles seen towards G13.384+0.064 and its associated H _{II} . In both of these panels, the source and tangent velocities are indicated by the red and blue vertical lines and the grey region shows a region 10 km s^{-1} either side of the source velocity. In the lower panel the green line indicates the maximum velocity found of the absorption features and the magenta line shows the 5σ rms noise for the H _I data (see Urquhart et al. 2012 for more details). The presence of an absorption feature at a similar velocity as the source in the upper panel and the lack of absorption features up to the tangent velocity in the lower panel both strongly support and near kinematic distance for this source.	82
3.6	Spectral energy distribution created by data of different surveys plotted on a log scale. To obtain the dust temperature and luminosity, a two-component model was fitted to the flux densities measured through aperture photometry from the MSX (Price et al., 2001), Hi-GAL (Molinari et al., 2010) and ATLASGAL (Schuller et al., 2009) maps (blue fit). Additionally, catalogued data of the extended emission from the radio as well as some select infrared and submillimetre data. Open Triangle-MSX(Egan et al., 2003), Diamond-BOLOCAM (Schlingman et al., 2011), Triangle-Nobeyama (Handa et al., 1987), Open Circle-VLA 5 GHz (Becker et al., 1994), and Triangle Right-VLA 1.5 GHz (Garwood et al., 1988).	86

4.1	Continuum image of the Galactic Centre observed by the MWA across the 30 MHz of bandwidth with a central frequency of 119.7 MHz. The left hand image represents the full region blindly searched for molecular signatures (see section Section4.2). The right-hand image is a zoomed in region around the Galactic Centre showing that the supernova remnants SNR 359.01 – 00.5 and SNR 359.0 – 00.9 are clearly resolved. The star-forming regions of Sagittarius B, Sagittarius C, Sagittarius D and Sagittarius A are unresolved in our observations.	94
4.2	Summary of the pipeline designed to create calibrated time-averaged spectral image cubes with the MWA.	94
4.3	Map of the RMS following the shape of the primary beam across the searched field-of-view. The cube of the fourth coarse channel, at 107 MHz, is shown in this figure, as a representation of the behaviour of the entire dataset. The stars on the image represent the positions of the nitric oxide tentative detections and the diamond represents the position of the mercapto radical tentative detection. See Section 4 for additional details. The contours are at the levels of 0.3 and 0.5 Jy beam ⁻¹	97
4.4	A tentative detection of the mercapto radical (SH) with a possible association to 2MASS J17360840 – 2533343. The image on the left is a contour plot of the detection with contours set at the 3, 4, 5, and 6 σ levels where 1 σ is 0.29 Jy beam ⁻¹ . The star in the image represents the optical position of the star labeled in the upper left-hand panel and size of the star represents the astrometric uncertainty after ionospheric correction. The right-hand panel shows the spectrum from 110.9 to 111.8 MHz at the position of 17 ^h 36 ^m 10 ^s -25°33' 51"(J2000).	103

4.5	Tentative detections of nitric oxide. The contours on each left-hand image are set to the 3, 4, 5, and 6 σ levels. The red star in each contour plot represents the optical position of the evolved star that is a plausible association with the detection, and the size of the star represents the astrometric uncertainty after ionospheric correction. The right-hand panel shows the full spectrum from 107 MHz to 108 MHz at the position of the tentative detection. (Top) NO tentative detection at the position of $17^h42^m55^s -24^\circ43' 9''$ (G003.27 +02.71) with a possible association to OGLE BLG-LPV 21112. The contour map uses a 1σ value of $0.38 \text{ Jy beam}^{-1}$. (Middle) NO tentative detection at the position of $17^h04^m12^s -36^\circ52' 31''$ (G348.58 +02.69) with a possible association to TYC 7372–165–1. The contour map uses a 1σ value of $0.50 \text{ Jy beam}^{-1}$. (Bottom) NO tentative detection at the position of $17^h50^m33^s -34^\circ07'46''$ (G356.11 –03.60) with a possible association to OGLE BLG-LPV 65700. The contour map uses a 1σ value of $0.40 \text{ Jy beam}^{-1}$	105
4.6	A plot of RMS noise against integration time, where red dots show the RMS versus time and the dashed line indicates the trend of square root of time. Therefore, more time integration on the same source should give improvement for possible detections. The blue and red shaded bars show the estimated sensitivity to start detecting thermal emission at a distance of 0.4 kpc and 8 kpc (approximate distance to the Galactic Plane) respectively.	110
5.1	Continuum image of the Orion survey region MWA across the 30.72 MHz of bandwidth with a central frequency of 114.6 MHz. The left hand image represents the full region blindly searched for molecular signatures (see Section 4). The right-hand image is a zoom of the region showing the Orion KL nebula in the center of the observed region. The white stars show the positions of the tentative detections reported here.	118
5.2	Summary of the pipeline designed to create calibrated time-averaged spectral image cubes with the MWA. In black are the additions to the pipeline that differ from the Galactic Center survey reported by Tremblay et al. (2017).	119

5.3	Tentative detections of nitric oxide in three stellar objects. The spectra on the right represent the full coarse channel data cube in which the tentative detections were made. The left panel shows the contours, set at 2, 3, 4, 5, and 6 σ of the continuum-subtracted image RMS, of the detection of the brightest signal. The ellipse in the lower right-hand corner of the contour plot shows the size and shape of the synthesized beam. The red star is the optical position for a plausible source associated with the signal. The size of the red star is the 1 σ astrometric error.	126
5.4	Tentative detections of Formic Acid with the right panel showing the spectra of the full coarse channel data cube containing the tentative detection. The left panel is the contours, set at 2, 3, 4, 5, and 6 σ of the image RMS, of the detected signal in the continuum-subtracted image. The ellipse in the lower right-hand corner of the contour plot shows the size and shape of the synthesized beam. . .	128
5.5	Tentative detections of Molecular Oxygen. The right panel shows the spectra of the full coarse channel data cube containing the tentative detection. The left panel is the contours, set at 2, 3, 4, 5, and 6 σ of the image RMS, of the detected signal in the continuum-subtracted image. The ellipse in the lower right-hand corner of the contour plot shows the size and shape of the synthesized beam. . .	130
5.6	Tentative detections of Unknown Molecules. The right panel shows the spectra of the full data cube containing the tentative detection. The left panel is the contours, set at 2, 3, 4, 5, and 6 σ of the image RMS, of the detected signal in the continuum-subtracted image. The ellipse in the lower right-hand corner of the contour plot shows the size and shape of the synthesized beam. The signal at G208.821-20.212 is located within the Nebula with the closest optical source at the peak pixel position, marked with a red star, is Parenago 811 an evolved star within the Nebula.	132

6.1	The upper left image is a continuum image of the Orion survey region across the 30.72 MHz of bandwidth with a central frequency of 114.6 MHz showing the full region blindly searched for molecular signatures and recombination lines. The upper right hand image is an RMS map showing the sensitivity of the MWA in a typical coarse channel data cube. The C393 α and C496 β transitions are represented by squares and stars respectively. The contours in cyan trace the image in the bottom left, which shows dust emission at 100 μ m surveyed by Schlegel et al. (1998). The blue contours and the image in the bottom right are the optical H α emission from the Southern H-Alpha Sky Survey Atlas (SHASSA) (Finkbeiner, 2003). We note that there is an image artifact in the 100 μ m survey data on the bottom, created by combining the data from different fields.	144
6.2	A tentative detection of the C393 α (107.98 MHz) and C496 β (107.19 MHz) at the Galactic coordinates listed on the top of each plot. The contours plot on the left represent the 3, 4, 5, and 6 σ levels of the associated detection. The spectrum on the right is representative of the spectrum of the coarse channel band in which the tentative detection was made with the flagged channels blanked. The spectra at G212.67 –25.56 also shows a possible detection of C496 β at 107.18 MHz and molecular oxygen (¹⁷ O ¹⁸ O) at 107.60 MHz.	146
6.3a	MWA spectra for a data cube used within this survey at the position of G212.67 –25.56. The alpha recombination rest frequency are marked in plum and the beta rest frequency positions are marked in green. Flagged channels are blanked out in the spectra.	153
6.3b	MWA spectra for a data cube used within this survey at the position of G212.67 –25.56. The alpha recombination rest frequency positions are marked in plum and the beta rest frequency positions are marked in green. Flagged channels are blanked out in the spectra.	154
6.4a	MWA spectra for a data cube used within this survey at the position of G194.67 –23.76. The alpha recombination rest frequency are marked in plum and the beta rest frequency positions are marked in green. Flagged channels are blanked out in the spectra.	155

6.4b	MWA spectra for a data cube used within this survey at the position of G210.67 -10.75 . The alpha recombination rest frequency positions are marked in plum and the beta rest frequency positions are marked in green. Flagged channels are blanked out in the spectra.	156
6.5a	MWA spectra for a data cube used within this survey at the position of G194.67 -23.76 . The alpha recombination rest frequency are marked in plum and the beta rest frequency positions are marked in green. Flagged channels are blanked out in the spectra.	157
6.5b	MWA spectra for a data cube used within this survey at the position of G194.67 -23.76 . The alpha recombination rest frequency positions are marked in plum and the beta rest frequency positions are marked in green. Flagged channels are blanked out in the spectra.	158
7.1	The fields searched for ETI signals with the MWA. The left is the fields centred on the Orion Nebula and the right in the field centred on Sagittarius Star A. The white circles in both represent the positions of known extrasolar planetary systems from the Kepler Catalogue.	163

Chapter 1

Introduction

1.1 Astrochemistry and its History

Approximately 400,000 years after the Big Bang, the expansion of the Universe sufficiently cooled matter such that electrons and protons could combine to form neutral atoms (Aver et al., 2013; Cyburt et al., 2016). The afterglow of the Big Bang is known today as the Cosmic Microwave Background and heralds the beginning of chemistry in our Universe. After hundreds of millions of years, mass accumulated to sufficient local overdensities that stars could form. Inside the stars, heavier atoms were formed and as these stars died, the explosion produced sufficient energy to create even heavier atoms.

Astrochemistry is defined by Dalgarno (2008) as “...the study of the formation, destruction, and excitation of molecules in astronomical environments and their influence on the structure, dynamics, and evolution of astronomical objects.” The stars within a galaxy have a major influence on the evolution of that galaxy (Clark et al., 2015). The study of molecules has played a major role in understanding how low- and medium-mass stars have formed (Herbst and van Dishoeck, 2009) and Codella et al. (2015) discusses the possibility that the study of molecules at frequencies $<1\text{GHz}$ can assist in understanding the formation mechanisms of high-mass stars ($>8 M_{\odot}$), which is currently unknown (Tan et al., 2014).

Spectral line studies have been used to explore our Galaxy since the 1800s when astronomers first classified stars. In the 1940s, the the first interstellar molecules were discovered in the ultraviolet region of the electromagnetic spectrum via narrow band absorption lines (Lequeux and Roueff, 1991). In the 1950s, Townes & Schklovski realised the potential for discovering molecules at radio wavelengths and from 1963 to 1968 water (H_2O), hydroxide (OH), ammonia

(NH₃), and formaldehyde (H₂CO) were discovered. The biggest discovery with millimetre wave radio telescopes was the detection of carbon monoxide (CO) in early 1970 (Lada, 1997; Wilson, 2015), as the abundance and ease of detecting the molecule with ground based telescopes allowed for the first large-scale structure maps within our Galaxy. It was in the early 1970s that the field of astrochemistry was really developed (Dalgarno, 2008). The launch of the UV (UltraViolet) satellite *Copernicus*, in 1974, advanced the study of molecular hydrogen (H₂) which improved the calculations of column density, provided the first estimates of the space-averaged densities, and allowed calculations of the temperature of the molecular gas within our Sun (Morton, 1975; Ferrière, 2001). In 1970 the National Radio Astronomy Observatory (NRAO) radio telescope on Kitt Peak was used to observe large amounts of CO, ¹³CO, and CS in the Orion Nebula at 115.3, 110.2 and 146.9 GHz respectively (Liszt et al., 1974) and by 1975, thirty-six molecular species had been discovered (Townes and Schawlow, 1975). Since that time, over 180 different molecules have been detected (van Dishoeck, 2014).

Although molecules are detected in a diversity of stellar atmospheres, most are found in cold dense interstellar gas contained in molecular clouds with masses up to 10⁵ M_⊙ (Herbst and van Dishoeck, 2009). The matter in these clouds is composed of both gas and solid phases, where the solids are typically carbon- or silicon-based ices and dust (Herbst and van Dishoeck, 2009; van Dishoeck, 2014). Wherever molecules are detected they are important tools in understanding the age, and physical and chemical conditions of the environment in which they are found.

Models of stellar and molecular cloud environments can help us understand the histories of these objects when used in conjunction with observations (Herbst and van Dishoeck, 2009). However, models are greatly limited by the reliability of rate coefficients of hundreds and thousands of reactions (van Dishoeck, 2014). Laboratory experiments have played an important role in understanding the chemistry of the Universe, but, even under the most extreme vacuum conditions on Earth, three-body interactions dominate the chemical interactions. Whereas, in space, due to the low densities, mainly two-body interactions of gas-phase molecules are thought to be important (van Dishoeck, 2014).

Observations of astronomical sources are greatly assisted by laboratory science and Hamiltonian simulations to identify emission and absorption signals. Laboratory experiments are done through instrumentation such as Fourier Transform Microwave (FTM) Spectroscopy. FTM spectroscopy is a laboratory technique that operates at 5–20 GHz at a rotational temperature of about 3 K allowing

molecules that have weak emission at room temperature to be easily detected (Travers et al., 1996).

A Hamiltonian model is a computational analysis that takes into account known information about molecular dynamics, using Newton’s equation of motion, and assumed boundary conditions. The positions of the molecular transitions are directly related to the eigenvalues of the Hamiltonian of an isolated molecule (Lequeux and Roueff, 1991) and can be solved theoretically from Schrödinger’s equation. By using the Born-Oppenheimer approximation the Hamiltonian can be split into the electronic motions and the nuclear motions by ignoring the coupling term between the electronic and nuclear motions. This approximation is valid because molecules have a large nuclear to electronic mass ratio. The Hamiltonian model is important for determining the frequency molecular transitions will occur, when experimentation is not practical or possible.

1.2 Thesis Overview

Within the last five years, a new generation of low-frequency radio telescopes are developed making observations of molecules and atoms below 700 MHz possible. The Murchison Widefield Array (MWA), located in the outback of Western Australia, is a telescope whose original focus was on continuum science and detection of the Epoch of Reionisation (Bowman et al., 2013), but the flexibility of its design allowed for other scientific endeavours as well. In particular, the MWA has the capabilities to detect spectral-line emission and absorption arising from molecular rotational transitions and recombination lines. A new pipeline for calibration, imaging, and searching MWA data for the use of spectral line science was required. The process designed and implemented, utilising Phase I of the MWA described in Tingay et al. (2013), is explained in Chapter 2.

Codella et al. (2015) discussed that observations around or below 1 GHz may provide new insights into the formation of high-mass stars, which is currently not well understood (Tan et al., 2014). There are currently two competing theories of high-mass star formation by accretion and a distinguishing characteristic between the two is whether or not stars can form in isolation. In the work within Chapter 3, Tremblay et al. (2015) compared the Lyman-Continuum flux from radio observations and the clump mass from observations in the infrared to locate regions of potential high-mass stars forming in isolation. We identified one source, G13.384+0.064, as a potential candidate but found it difficult to prove that it

was isolated, as the high-mass star dominated the Lyman flux; making it easy to hide a small cluster of low-mass stars. However, if high-mass stars can form in isolation, even rarely, it would have an impact on the initial mass function within the host galaxy.

Another approach for understanding high-mass star formation is through the chemical evolution of young stars. As described in Section 1.4, the observation, modelling, and analysis of molecules within low-mass and intermediate-mass stars has given us our most complete understanding of star formation. However, at high radio ($>20\text{GHz}$) and infrared frequencies, disentangling the molecular spectrum is difficult as it tends to be dominated by prominent¹ species, making identification of rare molecules challenging. At optical, infrared, and ultraviolet frequencies, the region around the high-mass star is optically thick, preventing direct observations of the stellar core through the ionised gas. However, at low radio frequencies, Hindson et al. (2016) found the HII regions around high-mass protostars to be optically thin at frequencies greater than 200 MHz. This suggests that observations between 1 GHz and 200 MHz could provide detailed information about the chemical evolution of high-mass stars in regions where ionised hydrogen is uniform. Observation at frequencies less than 200 MHz are important for identifying regions of increase generation of deuterated molecules, a known tracer for high-mass cold core collapse (Kong et al., 2015).

By utilising the MWA's wide field-of-view, blind molecular line surveys of the Orion Molecular Cloud Complex (Chapters 5 and 6) and the Galactic Plane (Chapter 4) have been completed to give new insight into known molecular rich environments or find new regions of interest to follow-up with high-resolution telescopes. Previous to the publication of the Galactic Centre survey, no one had ever reported the detections of molecules below 700 MHz (Lovas et al., 2003). Through the radiometer equation, it is predicted that molecular transitions detectable at low frequencies would likely be quasi-thermal² or maser emission. The results from the survey of the Galactic Plane and Orion support this. Also, the detection of molecules $<200\text{ MHz}$ are likely to be in cold gas environments dominated by collisional molecular interactions in the gas phase. This allows for the chance to detect unstable molecules rarely detected in hot or shocked gas.

Chapter 1 provides the motivation and the means by which we can detect

¹Prominent species are defined in this manuscript as molecules that have either intense line strength or a large quantity of transitions within a given frequency range.

²The emission that is boosted beyond the standard thermal limits to produce high brightness temperatures, but not necessarily a maser.

molecules. As we do not have the technology to visit a star or distant galaxy for up close analysis, we use the information encompassed within the electromagnetic signals to better understand the Universe around us. Molecules produce radiation through their motion and the interactions of the electrons and nucleus within the atom. As described in the Section 1.3, these interactions create a series of electromagnetic signals that provide a fingerprint in which we can identify not only the molecule itself, but at times the mechanism which caused the photon to be released. By evaluating the properties of the signal, such as intensity, width, and area under the curve, the conditions of the detected chemical environment can be assessed.

With some understanding of the mechanisms by which molecules emit and the types of environments (Sections 1.4 and 1.5) in which we would expect to detect them, we can fruitfully survey the Galaxy. As described in Section 1.6, spectral line surveys can provide detailed information regarding the distribution of chemicals, densities and temperatures. The two fields of particular focus within this thesis are the regions around the Orion Nebula and the Galactic Centre. Both regions represent known chemically-rich environments making them ideal locations for molecular studies with new telescopes.

Although most of the focus of this thesis is on molecules and their detection at low radio frequencies, the detection of carbon recombination lines (CRRLs) in high quantum states are important tracers of the cold neutral medium. As described in Section 1.7 and Chapter 6, large Rydberg atoms are particularly sensitive tracers of the densities of ionised gas within HII regions due to their macro dimensions. The study of CRRLs in the frequency range of the MWA are of particular interest because the transition between radiatively pumped emission and collisionally pumped emission occurs in the frequency range of 100–150 MHz. The analysis and search for molecular tracers is similar to the search for recombination lines, even though the interpretations of the results are very different.

Chapter 7 explains the serendipitous search for extraterrestrial signals using the same data cubes from the molecular and recombination line surveys. In work lead by Tingay et al. (2016, 2018), we focused on regions of known exoplanets to set limits for future surveys. Even though it is expected that a purposeful sent communication from another civilisation would likely be only a few Hertz wide, it is generally agreed that broad signals could come from passive communication. Therefore, a search in a different parameter space compared to traditional searches for extrasolar planetary communication is advantageous.

Overall, this research has advanced both the understanding of the require-

ments for the low-frequency component of the Square Kilometre Array (SKA) and proving that molecular transitions are detectable at low frequency as predicted by theory but never before discovered. Through the process of creating a calibration and data analysis pipeline, I have become intimately familiar with the spectral properties of the MWA, as outlined in Section 2.7. By working with the Pawsey SuperComputing Centre, I have provided feedback furthering the understanding of data-handling challenges this type of work poses. This work has allowed for a better understanding of the limitations and requirements for the “Cradle of Life” and Galactic Science SKA science goals, which includes the detection of complex organic molecules and recombination lines at frequencies less than 1 GHz. This thesis has also provided the world’s first detections of molecules below 700 MHz.

1.3 Detecting Molecules in Astrophysical Environments

Several molecules were discovered in space before they were synthesised or discovered on Earth, such as HCO^+ . Even helium was discovered in our Sun before it was detected on Earth. Herbst and van Dishoeck (2009) describes the process for confirming a detection of a molecule in an astronomical object as a series of up to three scenarios. The strongest of the three methods to prove unequivocally that the line is present is that “all predicted lines of the molecule based on LTE (Local Thermodynamic Equilibrium) spectrum at a well-defined rotational temperature and appropriately corrected for beam dilution³ are present at predicted relative intensities.” When this information is not known there are two other scenarios which are generally accepted but are not as strong as evidence of the molecule’s existence; detection at rest frequencies or correlation with other observations.

In some cases, laboratory experimental data and high-resolution Hamiltonian models can be used to determine a rest frequency for a molecular transition. In this case, there may only be a single detectable spectral line transition known within the observed frequency band. A tentative detection of a molecule can be obtained if a detected line is closely related to the rest frequency, but a second independent observation at other frequencies or the same frequencies are required

³When a source is significantly smaller than the synthesised beam, beam dilution occurs and a correction must be made. The signal intensity received by the telescope can be scaled to the assumed size of the source by a ratio of solid angles.

to confirm. Lastly, if a signal is detected at the known velocity of the source and has a single non-blended line, a detection is usually considered confirmed (Herbst and van Dishoeck, 2009).

The identification of different molecular species comes from the unique signatures due to the interaction of the various atoms and the interaction between an atom's nucleus and its electrons. Spectral lines in radio astronomy are usually detected from transitions of polar molecules. Molecules are polar when the charge distribution is uneven between the atoms as in CO or OH. The molecular transitions include rotational, vibrational, inversion, fine structure, and hyperfine structure. However, inversion is not covered within the context of this thesis as it is a rare phenomena.

1.3.1 Rotational Transitions

Rotational transitions are due to the quantisation of angular momentum. A diatomic molecule (consisting of two atoms) has rotational energy, E_r , is equal to:

$$E_r = \frac{L^2}{2I} = \frac{J(J+1)\hbar^2}{2I}, \quad J = 0, 1, 2, \dots, \quad (1.1)$$

where L is the angular momentum, I is the moment of inertia, J is the discrete quantum number related to the angular momentum, and \hbar is the reduced Planck's constant. As the molecule rotates, the energy (calculated in Equation 1.1) can be related to a photon release at a specific frequency (ν) by:

$$\nu = \frac{\Delta E_r}{h} = \frac{\hbar J}{2\pi I}, \quad J = 1, 2, 3, \dots, \quad (1.2)$$

The spectral lines in a radio spectrum for a molecule, from an interstellar cloud, represent emission at fundamental frequencies that are determined by the moments of inertia. The intensity of each peak depends on the temperature of the cloud as follows:

$$I_\nu = \frac{2\nu^2 kT}{c^2}, \quad (1.3)$$

where k is the Boltzmann's constant, T is the blackbody temperature, and c is the speed of light. If the upper level rotational energy (E_r) is much higher than kT , few molecules will be collisionally excited to that level and the line emission will be very weak. Most observed rotational transitions occur while the molecule is in the base vibrational energy state.

The transitions between rotational levels are detected with radio telescopes and millimetre spectra have been the main supplier for new identification of interstellar molecules (Lequeux and Roueff, 1991). When theoretical models are used to determine the frequency at which the transitions will emit or absorb energy, the transitions are represented by the electronic motions of the Hamiltonian. Rotational transitions are most easily detected in the cold interstellar medium in emission but are more likely detected in absorption when higher temperatures exist (Lequeux and Roueff, 1991).

Radiative transitions that change the discrete quantum number, J , by one, are electric dipoles. Non-polar diatomic molecules have no electric dipoles so the transitions represent changes in the quantum number by two, such as the H_2 quadrupole transition ($J=2 \rightarrow 0$), which is a weak-intensity transition. Therefore, except in rare cases, these transitions are not directly detected in the radio part of the electromagnetic spectrum.

Most of what we know about giant molecular clouds in galaxies outside of our own comes from the study of emission rotational lines of carbon monoxide. Molecules, in general, that have rotational state energies less than 5 K above the ground state will produce intense molecular lines that are detectable at high radio frequencies and in the infrared, even from low temperature environments.

1.3.2 Vibrational Transitions

Vibrational transitions from a molecule involve changes in the vibrational energy. Each bond between atoms can oscillate in a motion that mimics simple harmonics and can be simply modelled using Hooke's law for a spring. For a molecule with non-linear geometry the number of vibrational degrees of freedom is equal to $3n-6$ and for a molecule with linear geometry $3n-5$ where n is the number of atoms. The frequency of the energy release is:

$$\nu = \frac{1}{2\pi} \sqrt{\frac{k}{\mu}}, \quad (1.4)$$

when μ is the reduced mass ($\frac{m_1 \times m_2}{m_1 + m_2}$) and k is the bond force constant. When the two atoms on either side of the bond are not equal in mass, the motion becomes anharmonic with the potential well becoming a distorted parabola (Fletcher, 2002).

Rotational and vibrational transitions are both detected in the gas phase of astronomical environments. However, only vibrational transitions are detected in

the solid phase and the detected transitions and the intensity of the transitions tells us about the polar and non-polar ice mantles surrounding the interstellar dust grains with some contribution from the grains itself (Herbst and van Dishoeck, 2009). The vibrational transitions are detected in the infrared spectra, and some of the much sought-after vibrational transitions are a group of unidentified emission features, that modelling and laboratory experiments suggest are emission from anharmonic vibrational transitions of polycyclic hydrocarbons (e.g. Leger and Puget 1984; Barker et al. 1987)

1.3.3 Fine Structure

Fine structure comes from the combination of rotational and vibrational transitions (sometimes called ro-vibrational) since the energy from the rotational transition is less than that of the vibrational. As shown in Figure 1.1, the rotations are thought to move up and down in quantised amounts relative to the vibrational frequency.

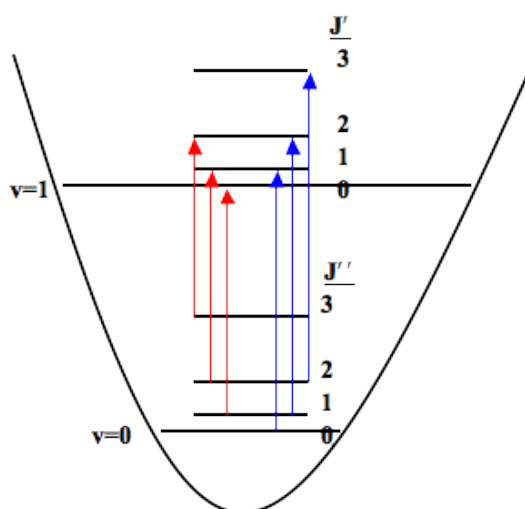


Figure 1.1: Diagram showing the different energy levels of molecules experiencing ro-vibrational motions, also known as fine structure. The two black horizontal lines show two vibrational states as defined by equation 1.4. The J terms are discrete angular momentum levels described in equations 1.1 and 1.2. The red and blue arrows show two different rotational transitions of the molecules. (Image Credit: Michael Evans)

As described in Section 1.1, the Hamiltonian model of molecular transitions can be separated into the electronic motions and nuclear motions by using the

Born-Oppenheimer approximation. This is because molecules have large nuclear to electronic mass ratio. When you split the Hamiltonian the nuclear motions are representative of ro-vibrational lines and are typically detected in the infrared. However, occasionally these lines, considered “forbidden transitions”, can arise from centrifugal distortions of polyatomic symmetrical molecules which do not have a permanent dipole moment (Lequeux and Roueff, 1991). This makes them detectable with radio telescopes.

1.3.4 Hyperfine Structure

Like the electron, the proton(s) within the atom also has spin and angular momentum with $s=\frac{1}{2}$ and associated with the angular momentum within the dipole moment. The changes in the electric and magnetic fields due to the charge distribution creates small shifts and splitting of the energy levels. This splitting is called hyperfine splitting. During the collision of one atom with another other atoms, the atom exchanges electrons. If the exchanged electron spin changes in relation to the spin of the protons, this causes the hyperfine energy splitting. This is most commonly detected in radicals, which have an open shell structure with residual angular momentum in the ground state, such as OH or HCN (Lequeux and Roueff, 1991).

These transitions are often detected in the radio part of the electromagnetic spectrum, and instead of a single detectable transition there are multiple. The relative ratio of these transitions can be determined theoretically, but the actual observable ratios can help us classify astrophysical objects. Qiao et al. (2016) found that the four hyperfine transitions of OH around 1.6 GHz were not always detected in every environment. The $^2\Pi_{3/2}$ ground state of OH is split by an interaction between the atomic nuclei and the unpaired electron motion around its orbit called Lamda splitting or Lambda doubling. This allows OH to be used to further characterise environments when this interaction occurs. Qiao et al. (2016) concluded that the detected transitions may be used to identify unknown objects.

1.3.5 Multiple Transitions

Each molecule can create multiple emission or absorption signals within a given frequency band. Also, for any one molecule there is the potential of several ions with charges (e.g. HCO^+ , C_4H^-), radicals with unpaired electrons (e.g. C_6H),

isomers with the same atoms but different orientation (e.g. HCN, HNC), isotopes with a different number of neutrons (e.g. ^{13}C , ^{15}N), and deuterated forms where the hydrogen, whose atomic structure contains a single proton and electron, also contains a neutron (e.g. DH). This makes identification of new molecules difficult, as sorting through all the known transitions can hinder the detection of new molecules (Herbst and van Dishoeck, 2009).

Accurate models can be used to subtract and peel back the layers of known prevalent emitters to find the rare molecules hidden inside the spectrum. Several laboratories have methods under development and there are software packages that can choose the most appropriate data model and create a synthetic spectra (Herbst and van Dishoeck, 2009). This can be coupled with a large number of molecular studies completed in microwave laboratory experiments such as those done by Townes and Schawlow (1975) in order to find new molecules or molecules of interest.

1.3.6 Abundances and Physical Conditions

Once molecules are identified by their transitions, information about the physical conditions of the region are extracted. The richness of molecular spectra yields detailed information on the gas, ice, and dust in a region. The rotational and vibrational spectra are observed in the far-infrared, sub-millimetre, and radio part of the electromagnetic spectrum. The detection of these molecules tells us about the temperature and density of the gas and the large scale motions such as collapse, outflows, and rotation. The vibration spectra, detected in the infrared and ultraviolet, yields information on the polar and non-polar nature of ice mantles surrounding the particles (Herbst and van Dishoeck, 2009).

The probability of the transition to occur is determined by the Einstein Coefficient for the allowed electronic dipole transitions. The Einstein Coefficient (A_{ul}) for any transition is calculated by:

$$A_{ul} = \frac{16\pi^3\nu^3}{3\epsilon_0hc^3}\mu^2, \quad (1.5)$$

where ν is the transition rest frequency, h is Planck's constant, ϵ_0 is the permittivity of free space, and μ is the electronic dipole moment.

The translation of observed intensities to physical properties, such as temperatures, densities, and chemical abundances requires the excitation of the molecule to be determined. An understanding of the mechanisms for photon release and how the photon makes its way to the telescope is also required for a complete

model to be determined (van Dishoeck, 2014). If we can assume that the lines are optically thin (light passes through the region) and that the populations can be characterised by a single rotation temperature (T_{rot}), then the main beam temperature $\int T_{\text{MB}}dV$ (km K s^{-1}) can be related to the column density by equation 1 in Herbst and van Dishoeck (2009):

$$\frac{N_u}{g_u} = \frac{N_{\text{tot}}}{Q_{\text{tot}}} = \frac{3k \int T_{\text{MB}}dV}{8\pi^3 \nu \mu^2 S}, \quad (1.6)$$

where g_u is the statistical weight of the upper energy level, N_{tot} is the total column density of the molecule, Q_{tot} is the rotational partition function, ν is the transition frequency, μ is the electronic dipole moment, and S is the Hol-London factor obtained from the angular integration of the transition moment and represents the intrinsic line strength of the molecule. In electronic transitions, the dipole moment is a function of the nuclear geometry and obtained as a matrix element of the electronic dipole between the initial and final wave functions expressed in the molecular structure (Lequeux and Roueff, 1991). Whenever a molecule has more than two atoms it will have multiple dipole moments. The value for μ in equation 1.6 is then a vector sum of each of the dipole moments.

For electronic transitions which are optically thin, the main beam temperature $\int T_{\text{MB}}dV$ (km K s^{-1}) is determined from the intrinsic line width. This can be calculated by:

$$W = \int \left(\frac{1 - I_\lambda}{I_o} \right) d\lambda, \quad (1.7)$$

where I_λ is the observed intensity and I_o is the background continuum intensity level (Lequeux and Roueff, 1991). The intrinsic line width (that depends on the decay time/Einstein coefficient only) can be compared to the observed line width, when high resolution telescopes are used, to determine the nature of the turbulence within the region being studied. Outflows and collapse within the region will change the width of the observed transition (Masunaga and Inutsuka, 2000). This line width is also related to the column density (N) by:

$$W_\lambda = 8.85 \times 10^{-13} \lambda^2 (\mu\text{m}) f N_{\text{tot}} (\text{cm}^{-2}), \quad (1.8)$$

where f is the oscillation strength of the transition. For detected transitions which are known to be unobstructed by transitions of other molecules and are not resolved enough to determine detailed information about the kinematics, the main beam temperature can be determined from the area under the spectral line

detected. However, when the region is known to be optically thick (meaning light does not easily pass through the area) at the observing frequencies, this assumption is no longer valid and the line profile must be known to calculate the column density.

In radio astronomy, the abundance of a molecule is determined by dividing the column density calculated by equation 1.6 for any molecule by the column density of any other known molecule in that region. As H_2 is the most abundant molecule in the Universe, it is commonly used as a basis for the “natural” abundance of the existence of that molecule. However, the value for the H_2 column density depends on the environment and surrounding structures. In evolved stars, in particular, the column density of H_2 is known to change in a striation effect depending on the distance from the star’s surface (Decin et al., 2010; Fonfría et al., 2011). It is important for this value to be determined, as molecules with low natural abundance are less likely to be detected.

When multiple transitions have been detected, the temperature of the environment can be determined from a rotation diagram. The rotation diagram is a plot of the $\log \frac{N_u}{g_u}$ versus the upper energy state of each detected transition. The slope of this line is inversely proportional to the temperature of the environment, as shown in Figure 1.2. The y-intercept represents the $\frac{N_{\text{tot}}}{Q_{\text{tot}}}$ from equation 1.6.

1.4 Star Formation

Observations from different wavelengths are correlated to create our most complete picture of star formation, as discussed in the review article by Kennicutt and Evans (2012). The detection of $\text{H}\alpha$ lines is an indicator of star forming regions in both local and distant galaxies. For high redshifts, Lyman alpha ($\text{Ly}\alpha$) lines are strong and can be used to identify distant star-forming regions (Shivaei et al., 2015). The problem with UV and Optical light, often used to study star formation in distant galaxies, is the sensitivity to interstellar dust attenuation. However, interstellar dust absorbs the star light and re-emits it into the infrared (IR). Small dust grains are heated by radiation in or near star forming regions and are easily detectable at wavelengths less than 3mm, but may be observed at other wavelengths as well. The combination of the UV, Optical and IR light can be used to measure the total absorbed and unabsorbed starlight directly and maps of UV, $\text{H}\alpha$, and IR emission can be used to study the population of star forming regions (Meurer et al., 1999; Shivaei et al., 2015).

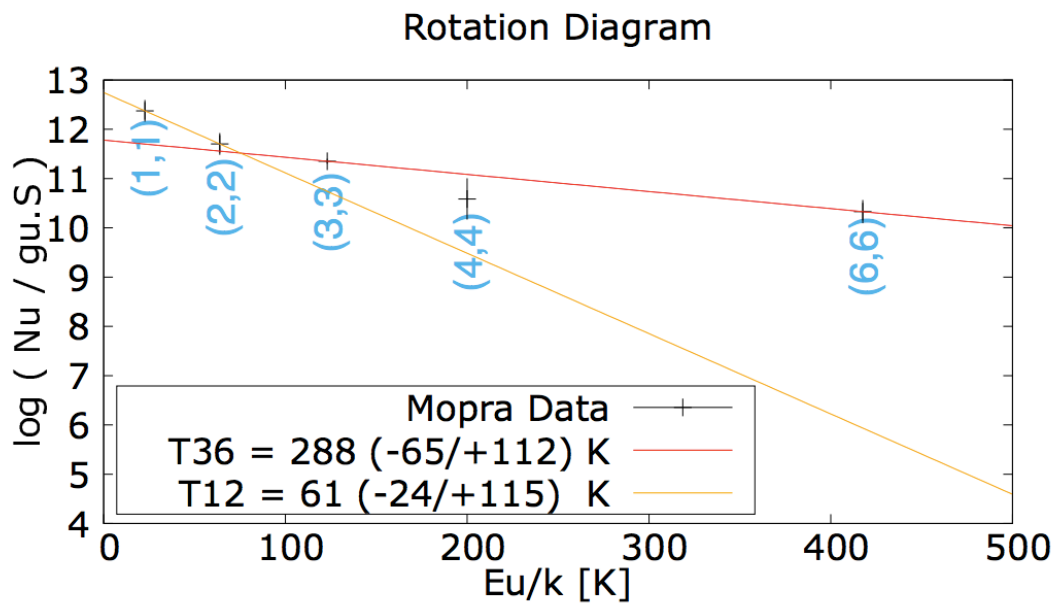


Figure 1.2: An example rotation diagram of Ammonia where the fit to the $\log \frac{N_u}{g_u S}$ for each observed transition is proportional to the temperature of the environment. The y-axis is the column density divided by the rotational degeneracy (g_u) and spin degeneracy (S). The x-axis is the transition energy in Kelvin. The two linear lines show the best fit for the cold component (orange) and hot component (red). (Image Credit: Maxted et al. 2016)

Radio observations, especially at low radio frequencies, do not suffer from dust attenuation as the large size of the waves are much larger than the size of the grains of interstellar dust (Kennicutt and Evans, 2012). This makes them ideally suited for studying astrophysical objects. Radio observations are sensitive to free-free thermal emission and synchrotron radiation. When non-thermal radiation decreases, the free-free thermal emission will increase proportionally. Many early discoveries of molecules were observed around 1 GHz in the star formation region of Sagittarius B2. Menten (2004) explains that this was because of population inversion continuum boosting, such that undetectable lines become observable. This may explain why some of the most complex molecules detected are only found in the Galactic Centre, specifically Sagittarius B2.

1.4.1 Low-Mass Star Formation

The understanding of the evolutionary phases of star formation has been assisted by the study of interstellar molecules (Herbst and van Dishoeck, 2009). Stars are formed from cold dense pre-stellar globulars or cores. The cores then begin to collapse in an isothermal manner and the molecules and atoms radiate as the collapse proceeds (Greene, 2001). Once a central condensation is formed, it starts to heat up further as collapse occurs, in an inside out manner, and emits infrared radiation (Kennicutt and Evans, 2012). Eventually, much of the remaining gas cloud is blown away and the star settles into life as a star with a protoplanetary disk. See Figure 1.3 for an illustration of this process.

Stars are formed from clouds of molecular gas with giant molecular clouds (GMC) accounting for the majority of the molecular mass of the Galaxy. Gravitationally bound, dense regions within the GMC start to form due to turbulence and these are known as clumps (Menten, 2004). For a perfect gas the kinetic energy (KE) is:

$$KE = \frac{3}{2}NkT = \frac{3}{2} \frac{MkT}{\mu m_{\text{H}}}, \quad (1.9)$$

where N is the total number of particles, k is Boltzman's constant, T is the thermal temperature, M is the total mass of the cloud, μ is the mean molecular mass (approx. 2.7), and m_{H} is the mass of molecular hydrogen. The product μm_{H} , is the mean mass of the gas particles in the cloud. A spherical homogenous cloud has a potential energy (PE) of:

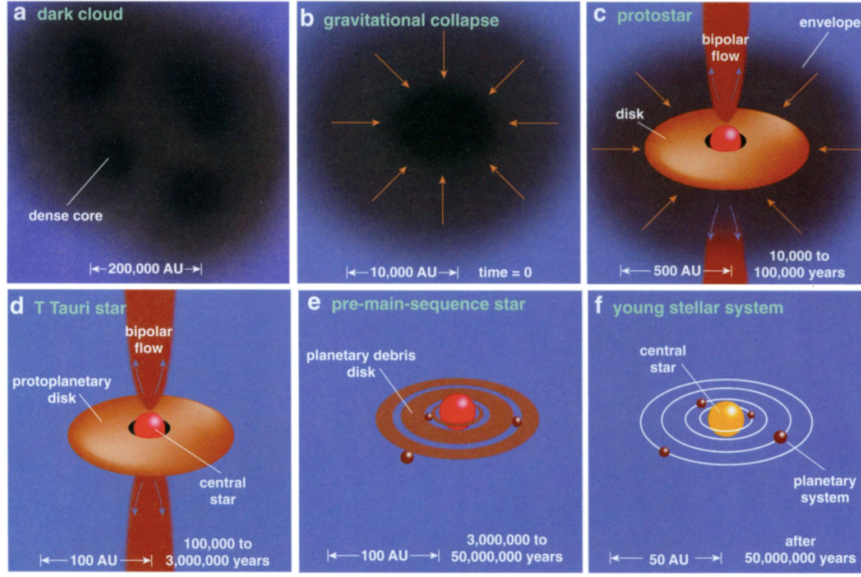


Figure 1.3: A graphic demonstrating the life cycle of a sun-like star. (Image Credit: Greene 2001)

$$PE = -\frac{3}{5} \frac{GM^2}{R}, \quad (1.10)$$

where R is the radius of the cloud and G is the gravitational constant. Using the equation for the total energy in a circular orbit as $KE = -1/2PE$, the total energy of the molecular cloud becomes:

$$\frac{3}{2} \frac{MkT}{\mu m_H} = \frac{3}{10} \frac{GM^2}{R} \quad (1.11)$$

If $M = \frac{4}{3}R^3\pi n$, the cloud radius can be calculated as

$$R = 3.57 \left(\frac{T}{K}\right)^{\frac{1}{2}} \left(\frac{n}{\text{cm}^{-3}}\right)^{-\frac{1}{2}} \text{pc}, \quad (1.12)$$

or

$$R_J = 0.08 \left(\frac{T}{K}\right)^{\frac{1}{2}} \left(\frac{n}{10^4 \text{cm}^{-3}}\right)^{-\frac{1}{2}} \text{pc}, \quad (1.13)$$

where R_J is the Jeans Length and n is the cloud density. When the radius of the molecular clump becomes less than the Jeans Length, the clump becomes unstable against gravitation and will collapse into a core. Within a single large molecular cloud, there can be several cores and regions where the core has less mass, but regions of dense gas are thought to be areas of star formation (Kennicutt

and Evans, 2012). To determine the difference between starless cores and pre-stellar cores, a good mass estimate and observations of spectral lines that trace kinematics is required.

Some authors have interpreted observational results to mean that dense clouds have a volume or density threshold before star formation can begin while others suggest that star formation increases as the density and volume of gas increase (Dobbs et al., 2014). Either way, star formation does not appear to occur in random regions or evenly throughout the region of a dense cloud, but in specific areas (Tan et al., 2014).

A core is thought to go through a series of three phases: cold core phase; a warm up phase; and a hot core phase (Herbst and van Dishoeck, 2009). During all three of these phases, the protostar continues to grow as the material funnels in and accretes around the protostar. This accretion disk is in Keplerian rotation around the protostar. Further accretion occurs in the innermost part of the disk in magneto-hydrodynamically mediated flows, at a rate that was found to match that of infall, and result in jets and winds (McKee and Ostriker, 2007). These outflows escape perpendicular to the accretion disk and interact with the surrounding molecular cloud. This in turn creates shocks that destroy grain material and liberate ices (Herbst and van Dishoeck, 2009; van Dishoeck, 2014).

As the cold core continues the process of isothermal collapse the icy mantles build up, in temperatures around 10 K. The atoms and molecules accrete onto dust particles called grains. As absorbrates accrete onto the cold surfaces a complex chemistry occurs with a combination of physical and chemical absorption to form layers (an “onion ring” model) of carbonaceous and siliceous ices. These icy layers are observed as producing molecules such as H_2O , CO , CO_2 , CH_4 , NH_3 , and CH_3OH (van Dishoeck, 2014). As shown in Figure 1.4, UV radiation can penetrate up to 50 layers of the ices, creating an accelerant for further complex chemistry to occur. The formation of molecules in the gas phase is only completed through exothermic reactions with no potential barriers, which causes the molecules to sublime off the surface of the ice into the gas phase (Herbst and van Dishoeck, 2009).

The warm-up phase occurs when the inner envelope of the protostar passively heats to temperatures of 100–300 K. This causes further sublimation of the molecules off the ice mantles into the gas phase. As the temperature rises, hydrogen atoms no longer reside on the grain surfaces long enough to dominate (Herbst and van Dishoeck, 2009).

In the final phase of core development, only gas phase chemistry can exist.

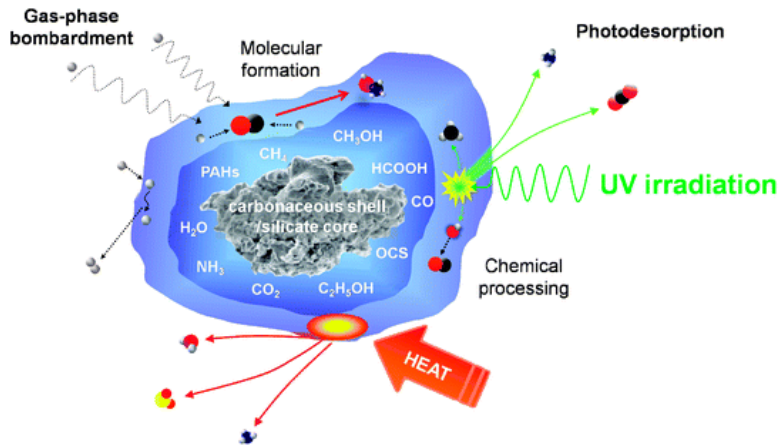


Figure 1.4: Image of dust grains and demonstration of the process of ice formation within the cold dense cloud before star formation begins. The molecules absorb on the surface in an “onion ring” like structure, creating a complex chemistry. (Image credit:Burke and Brown 2010)

This includes a combination of endothermic and exothermic reactions. When the gas starts to dissipate, a pre-main sequence protostar with a planetary disk remains. The term planetary disk comes from the increased collision rates that lead to the coagulation of dust grains to form pebbles and rocks.

Eventually, the young stellar object becomes hot enough for nuclear fusion of hydrogen to ignite, turning it into a stable main sequence star. The probability function mass of the final main sequence star is called the initial mass function (IMF) and as the evolution of the star is closely related to its mass, this is an important value in large studies.

Main sequence stars are classified based on their luminosity, effective temperatures, and their evolutionary status is tested on a Hertzsprung-Russell Diagram. Another model of stellar evolution have been created by Girardi et al. (1996). They suggest that stars follow three different evolutionary tracks based on low-mass, intermediate-mass, and high-mass stars. Low-mass stars are defined as stars that develop a degenerate helium core that go through a series of He burning episodes called He-Flashes, intermediate-mass stars avoid the He-Flash but contain electron degenerate oxygen and carbon cores with violent carbon reactions. High-mass stars avoid degeneracy until carbon-core ignition.

1.4.2 High-Mass Star Formation

High-mass stars are stars whose mass is at least eight times that of our own Sun and classified as spectral type of O or early-type B on the Hertzsprung-Russell Diagram. It is believed that the process by which they are formed is not just a scaled up version of low-mass star formation, although the process is thought to progress through many of the same events as pictured in Figure 1.3 and described in Section 1.4.1 (Zinnecker and Yorke, 2007). The main difference between the high-mass and low-mass star formation is the rate in which they burn through fuel. Although both start off by fusing Hydrogen into Helium, high-mass stars burn at a faster rate due to increased pressure and temperatures. Also, due to the increased temperature and pressure high-mass stars can form larger atoms such as Magnesium or Oxygen, where low-mass stars will fuse hydrogen to helium at a slow rate and may eventually fuse carbon atoms.

There are two main theories of high-mass star formation by accretion. Some recent observational analysis by Izumi et al. (2014) suggests that stellar collisions, a theory proposed by Bonnell et al. (1998), could also result in high-mass stars. However, due to the large stellar densities required it is thought that this is not a main mechanism of formation (Oh and Kroupa, 2018). The two main theories are core accretion (McKee and Tan, 2003) and competitive accretion (Bonnell et al., 2001; Bonnell and Bate, 2006). Both models agree that accretion disks are important to the stellar formation but in core accretion the accretion is ordered and compact from a self-gravitating clump, resulting in a single high-mass star. In competitive accretion, the accretion is more chaotic and the high-mass star forms from a “funnel” effect of gas from a cloud.

The observational difficulties in determining the formation mechanisms for high-mass stars are due to high dust extinction, the fact that they evolve quickly, and that the theoretical problem is complex, and that they are seldom, if ever, found in isolation⁴ (Zinnecker and Yorke, 2007). Tout et al. (1997); Weidner et al. (2009); Weidner and Kroupa (2005); Bressert et al. (2012), to name a few, have searched for forming high-mass stars in isolation primarily utilising infrared and optical survey data. However, these surveys require the star to be outside the natal HII cloud before they can be detected at these frequencies. Therefore, it can be difficult to determine how closely the surrounding environment mimics its

⁴Isolation of a high-mass star has different definitions within literature. The most commonly adopted definition is a single spectral type O or early-type B star within a cluster of low-mass stars. See Chapter 3 for further discussion.

natal environment. This is because a high mass star is known to drift away from the natal cluster, once it is evolved.

High-mass young stellar objects (YSOs) are often found in giant molecular clouds where they are associated with compact HII regions, masers, outflows, and warm gas, called hot cores (Herbst and van Dishoeck, 2009; Tan et al., 2014). Class II methanol (CH_3OH) masers observed at 6.7 GHz track exclusively with high-mass star formation (Zinnecker and Yorke, 2007). However, more complex organic molecules tend to be specific to each region, leaving astronomers questioning the differences between each hot core (van Dishoeck, 2014).

The formation of high-mass stars by accretion has also been studied through models (e.g. Krumholz et al. 2009; Kuiper et al. 2010; Bonnell and Bate 2006). Stars with masses greater than $20 M_\odot$ obtain their full luminosity while they are still accreting from their natal clouds and as the radiation diffuses outwards through the dusty gas it exerts a force countering gravity (Krumholz et al., 2009). This leads to a stellar light-to-mass ratio (L_\odot/M_\odot) that is determined by observation by relating the radio continuum flux density to the Lyman continuum photon flux as described in Kurtz et al. (1994). When the ratio is greater than 2500 the radiative to gravitation force exceeds unity and a star goes from the pre-stellar phase to the stellar phase.

The one-dimensional and two-dimensional models that include accretion and/or rotation find that radiation halts at $40 M_\odot$ and the star stops growing, which is lower than known stellar masses (Krumholz et al., 2009; Kuiper et al., 2010). However, three-dimensional models by Krumholz et al. (2009), where effects of radiative pressure are taken into account, were able to produce stars up to $100 M_\odot$. They found that the radiation pressure did not impact the star formation until $L_\odot/M_\odot=2500$ and the star was $17 M_\odot$. At this point, the radiation pressure force exceeded the gravitation and the star began to drive gas out in radiation filled bubbles. These bubbles are observed in the IR in areas around high-mass stars in formation and thought to be caused by strong stellar winds from the high-mass star (Weaver et al., 1977).

In order for a star to form, gravity must overcome pressure, magnetic fields, internal turbulence, and rotation (Zinnecker and Yorke, 2007). The high-mass YSOs are more luminous and hotter than lower mass stars (Tan et al., 2014). So with all things being equal it would be expected that thermal heating, dissociation and ionisation of hydrogen, and radiation pressure on dust will be important in forming a high-mass star instead of a low- or intermediate-mass star. All of these effects are forms of radiative feedback. In accretion models, such as core accretion

and competitive accretion, an important goal is understanding the impact that radiation feedback has on high-mass star formation (Tan et al., 2014).

1.5 Astrochemical Observations

When designing surveys with new telescopes or to look for new molecules, it is important to understand where they may be located or what you would expect to find. There are many different astrophysical environments in which new molecules have been discovered; circumstellar envelopes around stars, cold-cores, red giants, and Super giants, planetary nebulae, and the interstellar medium (ISM). The ISM contains about 90 per cent hydrogen, 8 per cent helium, and the rest is made up of all the other atoms such as carbon, nitrogen and sulfur. Inside the diffuse ISM the environment has very low densities (1 to 100 particles per cm^3), is cold (few 10s of Kelvin), and partially ionised from the UV radiation from stars. The dense ISM, also known as dark molecular clouds, has densities greater than 1000 particles per cm^3 and is partly or totally opaque to visible light and ultraviolet (UV) radiation (Kennicutt and Evans, 2012).

The standard gas phase molecules detected in the ISM range from 2-13 atoms, although C_{60} and C_{70} cyclic structures have also been detected. The dominant molecule in all dense clouds is molecular hydrogen (H_2) with carbon monoxide (CO) being the second most abundant, containing a fractional abundance $[\text{CO}/\text{H}_2]$ of 10^{-4} (Herbst and van Dishoeck, 2009). Telescopes that observe UV and infrared wavelength range can observe H_2 but the radiation is obscured by dust and, therefore, only surface analysis of molecular clouds can be completed. Additionally, Earth's atmosphere absorbs UV light, so astronomical observations must be completed from space, making study more restrictive. However, radio waves are not subject to interstellar extinction and can be used to detect molecules which have an uneven charge distribution, like CO.

A molecule is considered to be organic when it contains carbon. Most interstellar molecules are organic in nature and all of the species so far detected with greater than six atoms are organic (Herbst and van Dishoeck, 2009). A molecule is considered saturated when the organic molecule is rich in hydrogen with at least one double bond, such as CH_3OCH_3 , and unsaturated when there are few hydrogen atoms, such as bare carbon clusters (Herbst and van Dishoeck, 2009). Saturated molecules are typically found in hot cores of star formation. Unsaturated long chain carbon molecules are usually found in cold dark clouds prior to

star formation (van Dishoeck, 2014).

The circumstellar envelopes around evolved stars contain their own rich unique chemistry. The largest atoms, in molecules, such as MgCN, AlOH, and FeCN are only detected there (van Dishoeck, 2014). Most molecules detected in the circumstellar envelope around the carbon star IRC+10216 are long chain carbons with the largest being HC₉N (Woods et al., 2003). Oxygen-rich stars appear to have a more restricted chemistry and the mechanisms of dust formation are not well understood (Karovicova et al., 2013). Molecules typically found in carbon-rich stars have been observed in oxygen-rich star environments which may come about by large shock waves (Höfner and Andersen, 2007). Shock waves that propagate in both diffuse ISM and dense clouds make deep modifications to the physical properties and the chemistry within that region. The regions where shock waves are found tend to have high temperatures and high densities. This has the side effect of creating environments closely related to those simulated in laboratory conditions (Lequeux and Roueff, 1991).

1.6 Spectral Line Surveys

Molecular spectral line surveys are typically completed to either study a small subset of molecules across a wide range of sources or to study multiple molecules within a single source (Herbst and van Dishoeck, 2009). Many of the single or small subset molecular surveys have been completed to track motions and formation mechanisms within our Galactic Centre. Early large scale surveys of CO by Dame et al. (1987) and Dame et al. (2001), showed a correlation between CO and the 21 cm spin flip transitions of hydrogen (H_I) along the spiral arms within our Galaxy. From there they were able to create one of the most complete pictures of the motions of the inner Galaxy.

In addition to the work done by Dame et al. (1987) and Dame et al. (2001) other surveys such as MALT 90 (Jackson et al., 2013) and HOPS (Walsh et al., 2011) have great emphasis in using large area blind molecular surveys to study clouds, their molecular properties and how this information can be used to answer questions regarding the chemical association with astronomical objects. In HOPS (H₂O Southern Galactic Plane Survey), they studied one hundred square degrees of the Galactic plane using a combination of recombination lines, water masers, cyanoacetylene, and ammonia frequencies at 18.5 to 27.5 GHz. One of the goals was an untargeted survey to determine if water masers were indicative of star

formation or if other possible mechanisms existed.

Huettemeister (1998) suggests that large scale molecular studies at high resolution (suggested to be most useful < 2 arc sec) would be useful in understanding the structure of the central molecular zone (CMZ; Morris and Serabyn 1996; Kruijssen et al. 2015) and that has been the precise goal of instruments such as *Herschel Space Observatory* (Pilbratt et al., 2010) and Atacama Large Millimeter/submillimeter Array⁵. Large surveys like GLIMPSE (Benjamin et al., 2003; Churchwell et al., 2009), ATLASGAL (Schuller et al., 2009), MIPS GAL (Carey et al., 2009), and CORNISH (Purcell et al., 2013) have gone in search of molecular clouds of anticipated star formation, which have aided in identifying targets for further analysis. Although these surveys offer a mix of continuum and spectral lines, they provide detailed information about regions that may be of interests to future spectral lines surveys.

It has been a goal of many to use high-resolution surveys in an attempt to further understand what makes the Galactic Centre star formation regions unique compared to other large scale formations in the Galactic disk. A recent study by Neill et al. (2014) of Sagittarius B2 (Sgr B2) and Orion KL with the HIFI detector on *Herschel Space Observatory* identified 77 isotopologues⁶ from 44 different molecules at high spatial resolutions. They find that O and NO bearing species are more prevalent in Sgr B2 than Orion, with a few exceptions. However, CN species that were not detected in Sgr B2 are abundant in Orion.

1.6.1 Galactic Centre

Even though many molecules are detected in other galaxies, a focus on our Galaxy allows for better resolution mapping of objects, their motions, and their evolution (Herbst and van Dishoeck, 2009). The Galactic Centre offers a unique environment, compared to other regions within the Milky Way, with increased gas densities, temperatures (Menten, 2004), and possibly cosmic rays (Chambers et al., 2014). Some of the largest molecules detected in the Galactic Centre are associated with Srg B2, a hot core source. The close proximity also offers an observational advantage as the signals are easier to detect due to the relative proximity to Earth.

The Galactic Centre is the rotational centre of our Galaxy. Internal to the

⁵<http://www.almaobservatory.org/en/home/>

⁶Isotopologues are molecular isotopes, where at least one of the atoms has a different number of neutrons from its parent atom. See Section 1.3.5 for more detail.

circumnuclear disk (about a 3 pc area surrounding Sgr A*) is a compact area about 500 pc in size called the CMZ. The CMZ contains approximately $10^7 M_{\odot}$ of gas with properties different to that of the Galactic disk (Kruijssen et al., 2015). Many regions of high-mass star formation throughout our Galaxy are observed as having different molecular species and different relative abundances in comparison to each other (van Dishoeck, 2014). However, large scale analysis of the CMZ suggests that much of the active star formation may be coming from a single large gas mantle as the chemistry is remarkably similar in multiple areas (Herbst and van Dishoeck, 2009).

GRAVITY Collaboration et al. (2018) recently presented results about the Galactic Centre gathered through continuous observations of the star S2 through its 16 year orbit around Sagittarius A star (Sgr A*). The main goal of this project was to study General Relativity, but by combining the observations and models to analyse the data in three different ways they were able to derive a number of other results. In particular they derived list of parameters in Table 1a of the paper about the Galactic Centre, including the distance, in amazing precision. However, the authors do caution the reader on the significance of these early results which will be continually refined through further observations.

The study of star formation in the Galactic Centre is important as it allows a testing ground that can be applied to other galaxies, especially near their nuclei. Martín et al. (2008) studied the Galactic Centre of the Milky Way and NGC253 and found remarkable similarities between the two galaxies with the natural abundance in agreement for over 20 molecular species. Chambers et al. (2014) studied the differences in star formation from the CMZ to the Galactic disk using water (H_2O) and methanol (CH_3OH) masers along with infrared extended emission. They found that despite the temperature differences in the regions, there were no differences between the CH_3OH masers and the extended emission once star formation began. However, they did find a difference between H_2O and CH_3OH masers in the Galactic Centre versus the disk.

1.6.2 Orion

Orion represents a large region of active star formation whose population of stars, young and old, are a popular test subject for understanding star formation (O’Dell et al., 2015). The exact distance to Orion from Earth is not known, but the most recent value is determined to be 414 ± 7 pc (Menten et al., 2007). The proximity to Earth and the complex structure of Orion make it both a critical testing ground

for proofs of theoretical models and to be used for interpretations of more distant star forming regions (Muench et al., 2008).

The Orion region has several distinctive physical features that have been studied throughout the electromagnetic spectrum (Rice et al., 2015; Muench et al., 2008). From the north and south, there are a series of bright emission nebulae where there is a significant debate on the age of the stars due to the luminosity spread (Muench et al., 2008). The term “Trapezium” refers to four high-mass stars that are thought to be the core of the Orion Nebula Cluster (ONC; Hillenbrand and Hartmann 1998).

In the near foreground, there are layers of ionised gas that are known as the veil (O’Dell et al., 2015). The Orion A and Orion B giant molecular clouds (GMC), extend through the sword and belt region and are associated with diffuse H_I and H_{II} regions (van der Werf et al., 2013). In front of the ionising nebula is a, largely opaque, H_{II} region that is found to have three velocity components (Lockhart and Goss, 1978; van der Werf et al., 2013) and is modelled to be 1-3 pc in front of the Trapezium (Abel et al., 2004).

1.7 Radio Recombination Lines

A recombination line is the emission of a photon produced when a formerly free electrons recombines with ions and quickly cascades to the ground state. The Rydberg atoms⁷ detected at low frequencies often have macroscopic dimensions (Peters et al., 2010), making them particularly sensitive to the temperature, density, and pressure within the environment in which they are detected. Since the discovery of low-frequency (<300 MHz) carbon radio recombination lines (CRRLs) in the 1980s (Konovalenko and Sodin, 1980; Blake et al., 1980), CRRLs have been important probes of the cold neutral medium (CNM) of interstellar gas.

Stepkin et al. (2007) discovered the largest bound atoms ever detected with n-bound states (where n is the principal quantum number) up to 1009 and theoretical estimates have shown that atoms (particularly C, H, He, and S) can be stable up to n-bound states of ≈ 1500 . These are detectable at low frequencies due to the stimulated emission component by the domination of collisional excitation (Goldberg, 1966; Payne et al., 1989; Spitzer, 1998). The atoms that are in high quantum states are important tracers of ionised gas and photon dissociated

⁷Excited atom with one or more electrons

regions. It is widely believed that low-frequency RRLs arise in clouds associated with the HI (21-cm) component of the cold interstellar medium (ISM) with temperatures <100 K and gas densities $\approx 50 \text{ cm}^{-3}$.

The Low-Frequency ARay (LOFAR; van Haarlem et al. 2013) has been the current leader in the study and analysis of low-frequency carbon recombination lines with studies of Cassiopeia A (Asgekar et al., 2013; Salas et al., 2017), Cygnus A (Oonk et al., 2014) and the first extragalactic detection in M82 (Morabito et al., 2014). Recently Salgado et al. (2017a,b) published two in depth papers on the full theoretical analysis of carbon recombination lines at the quantum states of n -bound states >200 including the level population determination (influencing the strength of the detected lines) in order to develop CRRLs as tools to study the physical conditions of the local gas. Peters et al. (2010) details a historical view of CRRLs and their applicability to understanding the Galactic ISM.

1.8 Low Frequency Observations and Instrumentation

Most molecular astrochemistry is studied at frequencies from 20 GHz to over a 1 THz. Even though there are published studies in the frequency range of 1–20 GHz, work published for molecules below 1 GHz were in the 1970's. However, within the last five years, new low-frequency telescopes have come online for astronomical exploration in the 30–300 MHz frequency range, creating a resurgence of interest in low-frequency spectral lines. The discovery of recombination lines at 30-60 MHz (Oonk et al., 2014) with the Low Frequency ARray (LOFAR) (van Haarlem et al., 2013) has inspired the study of molecular gas environments at low radio frequencies. Previously, some of the lowest frequency detection of carbon recombination lines was made by Anantharamaiah and Kantharia (1999) at 68, 75, 80 and 325 MHz with the Greenbank Radio Telescope and Roshi et al. (2014) detected carbon recombination at 328.76 MHz and hydrogen at 329.59 MHz with the Ooty Radio Telescope. However, no observations of molecules below 700 MHz have been published (Lovas et al., 2003).

The Murchison Widefield Array (MWA) is a low frequency telescope operating between 70 to 300 MHz and the Phase I design used throughout this thesis work is described by Tingay et al. (2013). Even though the current setup does not have a high spectral resolution, it offers a unique opportunity to study the large-scale structure of astronomical objects, large molecules whose ground state

transitions are at low frequencies, and regions in which there are large amounts of line confusion at high frequencies. With many radio interferometers, the study of Asymptotic Giant Branch (AGB) stars and Planetary Nebulae (PN) are difficult due to the object size compared to the beam size⁸. As a low-mass or intermediate-mass star ages and nears the end of its life, it expands and becomes either an AGB or a Mira Variable Star (similar to an AGB but pulses at regular intervals) and then later progresses to a Planetary Nebula (Karovicova et al., 2013). A Planetary Nebula has an expanding glowing shell of ionised gas that is ejected from an AGB star or red giant star later in its life (Woods et al., 2003). The most famous of these is IRC+10216, which has been a testing ground for understanding the chemical environments around evolved stars, with over 50 molecules observed (Woods et al. 2003; Cernicharo et al. 2018 and references therein). Even so, little is known about these evolved star environments, as it is time consuming to get a full view with a high resolution instrument due to their large size.

By using observations in the frequency range of 99–300 MHz, a unique opportunity becomes available to initiate science in a new parameter space for the study of stars and star forming regions. This gives two major advantages; a decrease in molecular line confusion (Codella et al., 2015); and an opportunity to study long chain molecules whose low energy transitions exist in the band of the MWA. The study of molecular astrochemistry at higher radio frequencies (>20 GHz) is hindered by high energy molecules producing cluttered regions of spectral lines, making identification of lower energy molecules difficult. Figure 1.5 is a synthetic spectrum of SO₂. Starting at ≈ 5 GHz (in the cm wavelength range) the line confusion decreases. However, the observation frequency decreases, the more spread out the transitions become (Herbst and van Dishoeck, 2009).

Many long chain linear molecules have fundamental ($J=1 \rightarrow 0$) transitions at these low frequencies. The largest linear molecule discovered in the interstellar medium is the cyanopolyne HC₁₁N, discovered in IRC+10216 (Bell Burnell, 1979). From laboratory experiments, the rotation spectra are known up to HC₁₇N (Morales, 2012). It is conjectured that some of these long chain, wire-like molecules have led to the creation and, therefore, the discovery of fullerenes (Morales, 2012; Travers et al., 1996; Cami et al., 2010). Defrees and McLean (1986) estimate that the most likely frequency to detect HC₁₃N would be 107 MHz or 213 MHz, which is within the frequency band of the MWA. However, Codella et al. (2015) suggest that the detection of these molecules will take upwards of

⁸In some cases, this may be a source of 40-50 arc seconds and a beam size of <1 arc second

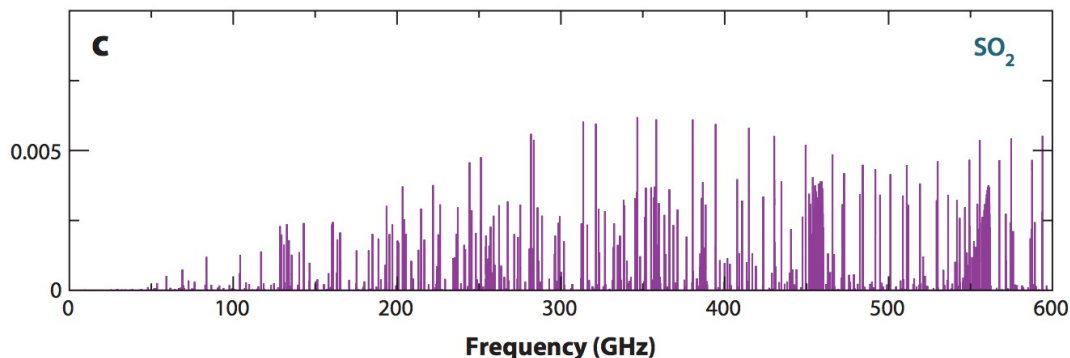


Figure 1.5: Synthetic spectra of SO_2 that shows the intensity of the molecular transitions at higher frequencies is greater than at lower frequencies (Image Credit: From Figure 2 of Herbst and van Dishoeck 2009).

100 hrs due to the decreased line intensity at low frequencies.

It is the goal of this project to use wide-field, low-frequency, observations from the MWA to both further understand the population of stars within the regions of Orion and the Galactic Centre and to understand the telescope design to provide feedback for future modifications enhancing future spectral line studies. There are many unanswered questions regarding high-mass star formation (Tan et al., 2014), the formation of sulfur bearing molecules (Millar and Herbst, 1990; Danilovich et al., 2016), and the formation of life (Codella et al., 2015) that we hope to answer by observing at low frequencies. This thesis represents a first look at using this new generation of telescopes to observe molecular lines at frequencies lower than previously reported to see if molecules can be detected, if their emission is boosted (non-thermal) as theoretically predicted (Spitzer, 1998), and what considerations need to be made to improve on this work with future telescopes like the SKA.

1.9 Statement of Originality

This section is to comply with the requirement for co-authors of published papers contained within this thesis. All authors have read the following statement and agreed with the description of participation. The communication of agreement to this statement is contained in Appendix A of this thesis. See Appendix B for the right to publish the papers within this thesis.

The idea of studying low-frequency molecular lines was proposed by Dr. Andrew Walsh, and the first data for the Galactic Centre in 2014 was obtained

through his request for Director's time. Both version 1 and version 2 of the data processing pipeline was completed by myself, under the direction of Dr. Natasha Hurley-Walker and with some programming assistance from Dr. Paul Hancock. The additional two hours of data requested in 2016 on the Galactic Centre was initiated by myself when no signals above 4 sigma were detected. The resultant paper published in Monthly Notices of the Royal Astronomical Society (Chapter 4) was written, almost in its entirety, by myself. Dr. Paul Hancock assisted in outlining the structure of the paper and Dr. Randall Wayth assisted in the structure of the Introduction after Reviewer comments suggested the aim of the work was unclear. The remaining authors, Dr. Andrew Walsh, and Prof. Igor Bray provided assistance with editing the paper and providing additional references with examples of previous or supporting work.

I was the principal investigator on the proposal for the Orion Survey submitted in October 2014. I chose the frequency ranges, times on source, and wrote the proposal with input from Slava Kitaeff, Steven Tremblay, and Natasha Hurley-Walker. The pipeline for the calibration, imaging, and the completion of the survey was completed and refined by myself, under the guidance of Dr. Natasha Hurley-Walker, Dr. Christopher Jordan, Dr. Maria Cunningham, Dr Paul Jones, Prof. Steven Tingay, and Prof. Igor Bray. From this work there are two papers accepted for publication; the Molecular Survey around Orion (Chapter 5) and Low Frequency Carbon Recombination Lines (Chapter 6). Both of these papers were written almost entirely by myself with editing assistance from the authors. Dr. Natasha Hurley-Walker provided additional guidance on the statistical analysis to prove the significance of the detections.

Both the Galactic Centre and Orion surveys allowed for an opportunistic analysis for the study of narrow band signals towards known exoplanets to search for extraterrestrial intelligence (SETI). Prof. Steven Tingay led the project, developed the science case, and wrote the two papers (summarised in Chapter 7). I searched the exoplanet catalogues to find the locations of known exoplanets, search the data cubes used in the spectral line surveys for SETI signals, wrote the observation section of the papers, and provided the data for both papers.

The search for High-mass stars in isolated formation (Chapter 3) was a project proposed by Dr. Steven Longmore and Dr. Andrew Walsh. I completed the search of survey data that included the region, contacted principal investigators of surveys to obtain and clarify results, completed data analysis of the survey data, and collected the analysis done by the other authors of the paper. The Introduction and Sample Selection was written by myself in collaboration with

Steven Longmore. In Section 3.4.2 (Distance) James Urquhart provided the data and analysis on the HI maps. Carsten König provided much of the analysis on the spectral energy distribution by adding Hi-GAL data to the other flux density values I had collected from other surveys. Dr Andrew Walsh completed the Monte Carlo simulation that went into the discussion portion of the paper and wrote most of the final version of the discussion. The rest of the paper was written by myself with editing done by the other authors.

Chapter 2

Methods

2.1 Observational Design

There are many unanswered questions including high mass star formation, the formation of sulfur bearing molecules, the disproportionate ratios of organic and inorganic molecules, and the formation of life that may be investigated by observing molecules at frequencies lower than previously searched (Codella et al., 2015; Danilovich et al., 2016). The detection of molecules at frequencies from 99–300 MHz requires the new generation of telescopes that have come online in the last five years, in particular the Murchison Widefield Array (MWA). Previous to starting this work, the focus of the MWA was on continuum science and detecting the Epoch of Reionization (Bowman et al., 2013), so a new pipeline for calibration and imaging is required for spectral line work.

Observations of the Galactic Plane in the frequency range 103–133 MHz for 120 minutes were obtained in July 2014, through Director’s time, to test a pipeline for calibration, imaging, continuum subtraction, and searching the wide-field images for potential spectral features associated with molecules. Following the creation of an initial pipeline, a full survey of spectral features was completed. In this frequency range there are 24 molecules known to have energy divided by the Boltzmann constant less than 300 K, a limit based on the Boltzmann distribution that suggests up to 83.2% of the molecules should be in that state. Any absorption and emission peaks over the 5σ observed noise limit were cross matched with known Galactic sources published in SIMBAD¹ and known molecular and atomic transitions in the databases: Cologne Database for Molecular Spectroscopy (CDMS; Müller et al. 2001); Spectral Line Atlas of Interstellar Molecules (SLAIM; Splat-

¹<http://simbad.u-strasbg.fr/simbad/sim-fcoo>

alogue²); Jet Propulsion Laboratory (JPL; Pickett et al. 1998); and Top Model (Carvajal et al., 2010).

Following this initial search, no potential sources with associated known molecular transitions were detected at or greater than the 5σ threshold, so an additional 120 minutes of observations were obtained in July 2016, that after calibration, were integrated with the initial 120 minutes from July 2014. The survey of the Galactic Centre yielded tentative detections of two molecules associated with four evolved stars (Chapter 4; Tremblay et al. 2017).

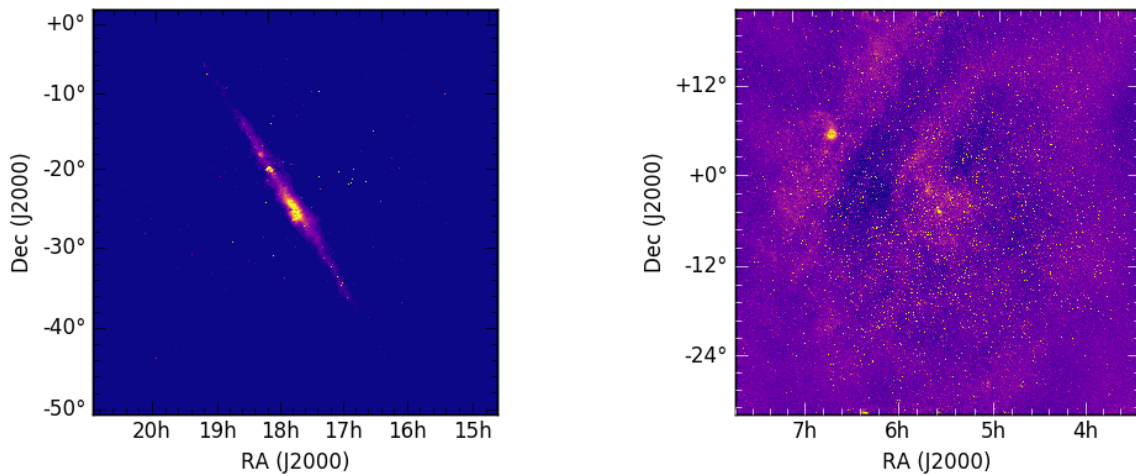


Figure 2.1: The Galactic Centre and Orion region both represent significant areas for study of chemical tracers in the Interstellar Medium. The wide field-of-view from the MWA offers an increased testing ground for evaluation of stars and star formation regions. The image of the Galactic Centre at 103 MHz, on the left, is the continuum image from the pilot spectral line survey. The image on the right represents the Orion region at 99 MHz. For more detailed images of the survey fields see Chapter 4, 5, and 6 of this thesis.

A second observing proposal was accepted to complete a full spectral line survey across the MWA observing frequencies of 99–300 MHz in the Orion region. These observations were completed in October and November 2015. The frequency range is broken up into a series of five observation segments, utilising frequency bandwidths avoiding known radio frequency interference (RFI), each being observed for a total of three hours. However, the top three frequency bands, between 179 and 300 MHz, are not included in this project as most of the snap-

²www.splatalogue.net

Table 2.1: MWA Observations used for this Ph.D. Thesis. The observations from July 2014 and July 2016 were integrated together for a single survey.

Parameter	Galactic Centre		Orion	
	25 July 2014	27 July 2016	21 November 2015	22 November 2015
Date Observed	25 July 2014	27 July 2016	21 November 2015	22 November 2015
Central frequency (MHz)	119.7	119.7	114.6	155.5
Total bandwidth(MHz)	30.72	30.72	30.72	30.72
Number of imaged channels	2400	2400	2400	2400
Channel separation	10 kHz (25 km s ⁻¹)	10 kHz (25 km s ⁻¹)	10 kHz (23 km s ⁻¹)	10 kHz (18 km s ⁻¹)
Synthesized beam FWHM	3.2'	3.2'	3.2'	2.1'
Survey Region (deg ²)	400	400	400	400
Phase center of image (J2000)	17h45m -29d00m	17h45m -29d00m	05h35m, -05d27m	05h35m, -05d27m
Time on source (hours)	2	2	3	3

shot observations had missing visibility data due to technical difficulties with the telescope. See Table 6.1 for a summary of the observations used for the surveys completed during this thesis and Figure 2.1 for the fields of interest.

It is the goal of these wide-field, low-frequency, observations to first determine if molecules are detectable by low-frequency dipole telescopes, and if so, further the understanding of the chemical evolution of stars and star forming regions around Orion and the Galactic plane. In addition to providing new information regarding stars and star formation, this work can be used to constrain the requirements that are needed for the development of the low-frequency component of the Square Kilometre Array (SKA) being built in Australia³ for the study of molecular and atomic gas within our Galaxy.

2.2 The Murchison Widefield Array

The MWA, for the duration of this thesis, consisted of 128 “tiles”, each containing 16 dual-polarisation dipole antennas located at the Murchison Radio-astronomy Observatory in Western Australia. Tingay et al. (2013) provides a detailed description of the MWA Phase I (with 3 km baselines) capabilities and design.

The output of the analogue polyphase filterbank consists of 24×1.28 MHz-wide “coarse” channels; each coarse channel was further subdivided into 128×10 kHz-wide “fine” channels, resulting 3072 (10 kHz-wide) spectral channels. The edges of each coarse channel suffer aliasing from the polyphase filterbank and were flagged out of each observation (See Section 2.8 for more detail). The central fine channel of each coarse channel contains the (non-zero) direct current component

³<http://www.ska.gov.au/>

from the polyphase filterbank and was flagged out as well (Thiagaraj et al., 2015). Additional flagging was performed in each observation using AOFLAGGER (Oftringa et al., 2010, 2012). This program is designed to find peaks in time and frequency that were likely the result of radio frequency interference (RFI). Due to the aliasing, only the central 100 of the 128 fine channels of each coarse channel were imaged, which equated to 78 per cent of the bandpass. See Section 2.8 for a discussion on this decision.

The MWA dipoles contain no moving parts that can track a source as it moves across the sky. Therefore, the observations are completed in two or five-minute snapshots to minimise the change in the primary beam over the duration of a single observation. Signals from the MWA dipoles are combined in an analog beamformer (Neben et al., 2016), with switchable delay lines to provide the ability to coarsely point the dipoles toward the source. Figure 2.2 shows an example of the sensitivity in the phase centre as a function of observation taken from the Orion observations at 114.6 MHz. As the source moves across the sky, the sensitivity in the phase centre changes. For observations of Orion, the observations started when Orion was close to the horizon so the values for the primary beam sensitivity are less than one, the value set at zenith. When the source tracks outside the field of the sensitive regions of the primary beam, the delays change. This process continues for each snapshot image until the observation sequence is finished.

2.3 Data Gathering Procedures

Surveys of molecular and recombination in emission and absorption covered ≈ 400 square degrees centred on $17^h45^m40^s -29^\circ00' 28''$ (J2000) for the Galactic Centre and $05^h35^m17.3^s -05^\circ23'28''$ for Orion. Data were collected in a 30.72 MHz contiguous band. For the Galactic Centre observations the central frequency was 119.7 MHz. The observations of Orion were broken up into five frequency bands with centre frequencies of 114.6, 155.5, 195.2, 225.9, and 284.8 MHz. However, the observations of Orion at 195.2, 225.9 and 284.8 had missing visibility data due to problems with the correlator.

The raw voltages for each of the polarisations are correlated and transferred from the Murchison Radio-astronomy Observatory to the Pawsey SuperComputing Centre in Perth, Western Australia (Wu et al., 2013). The data are obtained from archive using a PYTHON script in the MWA tool kit which downloads a set

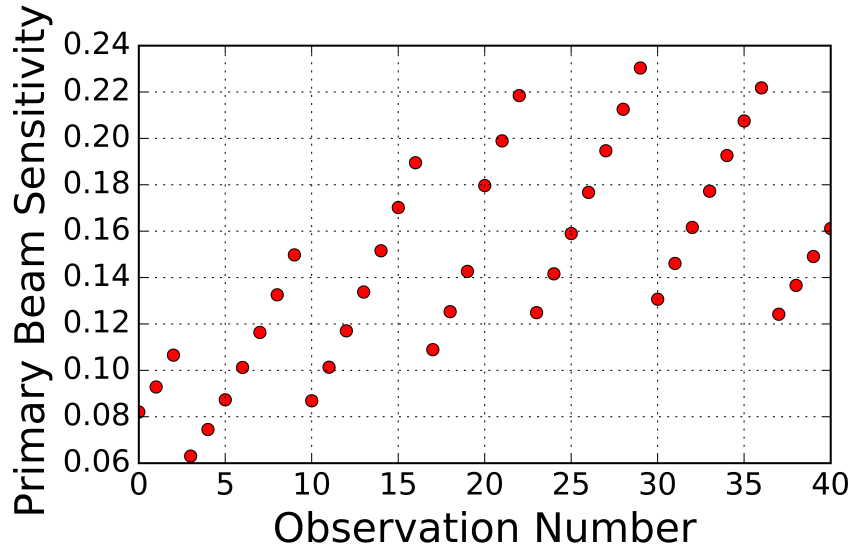


Figure 2.2: An example of the sensitivity just off the phase centre of each observation within the Orion field, as observed during the Orion 114.6 MHz survey. The primary beam model is a set of normalised values which are one at zenith. These values are much lower than one as Orion was closer to the horizon during these observations.

of GPUFITS, `metafits`, and flag files, containing all relevant information regarding the visibilities and the observations. The program COTTER (Offringa et al., 2015) is used to take the MWA GPUFITS and the `metafits` files to create a single set of the visibility data with a contiguous bandwidth. During this process, COTTER also rotates all the visibilities to a single phase centre and completes some corrections for cable lengths and bandpass.

In this process, COTTER is also used to apply the flagging information from the correlator (Ord et al., 2015), remove the baselines that are less than 60 meters apart (in the observation of the calibrator only) and average the data in 4 second time steps before creating a CASA (McMullin et al., 2007; Shaw et al., 2007) measurement set containing the corrected (u,v,w) data.

2.4 Data Analysis

To create searchable data cubes for spectral line work, a new pipeline was developed. Figure 2.3 shows the general process and the details of this pipeline are described in the sections below.

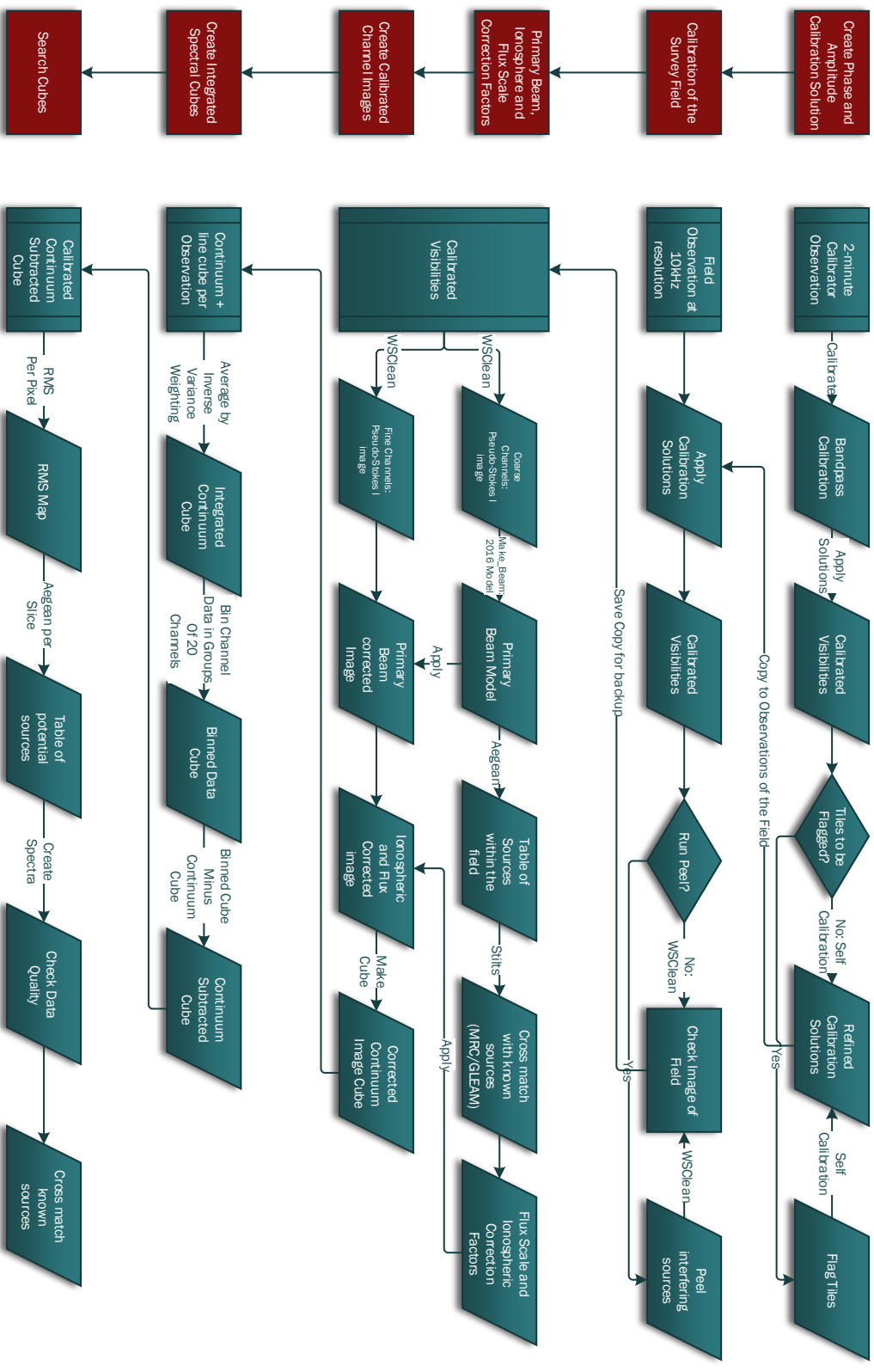


Figure 2.3: Flow Chart detailing the process of the developed pipeline used for spectral line analysis with the MWA. The left column in red summarises the stages the pipeline details where the blue rows represent the detail of that stage.

2.4.1 Derive Phase and Amplitude Calibration Solution

An interferometer measures the complex visibilities of the sources in the sky within the field of view of the telescope. Distortions can occur in the wavefront between the sources and the telescope which creates errors in the phases and amplitudes of the signal as a function of frequency (bandpass). Therefore, the visibilities need to be calibrated, as closely as possible, to the true visibilities by correcting the complex gains for the observation. The complex gains (amplitudes and phase) are corrected through a process called bandpass calibration and the steps are shown in the first line of the pipeline in Figure 2.3. As the MWA has no moving parts, the calibration observation is used to correct the changes in the frequency dependant amplitudes and phases of the instrument and not a correction of instrumental effects over time. However, observations of the calibrator were done at the beginning and end of the two hour observation run to assess any telescope and ionospheric instabilities, but only one of the calibration observations are applied to the field images.

Errors in the amplitude when the bandpass calibration is completed will limit the ability to detect emission in areas of strong continuum and can mimic changes in spectral line structure as a function of frequency. Errors in the phase may lead to spurious positional offsets of spectral features, mimicking proper motions. Also, errors in the phases can cause signals to decorrelate when the errors are not systematic.

The bandpass calibration for both the Galactic Centre and Orion were performed using the full-Jones MITHCAL algorithm; a tool developed for MWA calibration as described in Offringa et al. (2016). The bandpass solution was derived from a two minute observation of Hercules A for the Galactic Centre and Pictor A for Orion. As the MWA telescope observed around 900 square degrees in a single observation, there are bright sources in the sidelobes of the primary beam. Therefore, an amplitude and phase self calibration was performed to refine the complex gains solutions before they were applied to the observations of the Galactic Centre and Orion.

Self calibration is a technique where the calibrated sky model is used as a new sky model, allowing for better calibration of the antenna-based amplitudes and phases as a function of time. Self calibration technique can be used because the number of baselines for the MWA is larger than the number of tiles. With self calibration, calibration is completed that best match your data to your model. Then a model of the source is created by imaging the source. Using self cali-

bration for refining the calibration of MWA data was demonstrated in both the “The Murchison Widefield Array Commissioning Survey” (Hurley-Walker et al., 2014) and the “GaLactic and Extragalactic All-sky Murchison Widefield Array (GLEAM) survey” (Hurley-Walker et al., 2017) independently.

Data Processing in Miriad

In the initial phase of generating a pipeline for analysis of MWA data for spectral line work, the majority of the processing was constructed in MIRIAD. MIRIAD (Sault, 1994) is a radio interferometry data reduction software package particularly designed to handle calibration and imaging of continuum and spectral line data. This approach has been successfully utilised in some MWA projects where the interesting field-of-view is small and the target is within the centre of the primary beam. Even though a suitable calibration strategy was created, since this project aimed to survey 400 square degrees around the Galactic Centre (to utilise the full field-of-view of the MWA), the use of MIRIAD to fully image the continuum was not successful. This is partially due to the inability for the software to account for the w -terms.

In wide-field imaging with low frequency interferometers the relationship between the sky brightness and measured visibility function is no longer a simple Fourier Transform. Instead an extra phase term is used to relate the impact of the separation of antennas projected along the line of sight to the source. This effect, called the w -term, is present for all interferometers but is most notable at long baselines and long wavelengths. The errors when this is not accounted for, when working with the MWA, are displayed as distortions in the image (Cornwell et al., 2005). Further details is explained in Chapter 4 of this thesis.

2.4.2 Apply the Phase and Amplitude Calibration Solution to the Field Observation

To calibrate each observation of the Galactic Centre and Orion, as shown in row two of the pipeline in Figure 2.3, each observation is first downloaded as described in Section 2.3. The set of visibilities are calibrated with the solution derived in Section 2.4.1. During this step the phase centre is set in each observation to ensure, when the observations of the same source are averaged together, that the sources in the image are not blurred. For the Galactic Centre the phase centre is set at $17^h45^m40^s -29^\circ00' 28''$ (J2000) and $05^h35^m17.3^s -05^\circ23'28''$ for Orion

As the Crab Nebula, a radio source of $S \approx 1430$ Jy at 152 MHz (Parker, 1968), lies within the field-of-view of the observation centred on the Orion Nebula, we followed the method adopted by Hurley-Walker et al. (2017), which includes peeling the Crab Nebula out of the observations. The program PEEL, developed by André Offringa, subtracts off all the model components of a source based on a model file. The model file was created as part of the GLEAM survey (Hurley-Walker et al., 2017) and was used only for the observations of Orion in the 99–129 MHz frequency band.

2.4.3 Coarse Channel Imaging

Continuum images of each coarse channel are made to create a primary beam model, derive positional corrections for source shifts caused by the ionosphere, and to determine if direction-dependent flux density scaling is required. Each coarse channel image is created by using WSCLEAN (Offringa et al., 2014), which allows a variety of settings to ensure the image suits the science goals. A series of imaging experiments (Table 2.2) were conducted on the Galactic Centre data to identify the settings with which an image with the lowest noise and good source deconvolution could be made within the time-limit set by the Supercomputer control system (a 12 hour time limit in the queue system).

In the process of making a sky image from the visibility data, the visibilities are separated into cells and combined. The weighting of each cell was customised for each science goal (See Section 2.4.5 for more details). For the spectral line work, the weighting of Briggs with the robust parameter set to “-1” is used. This generates a compromise between natural weighting and uniform weighting, achieving better source resolution and low noise. Other parameters set and not varied in the imaging experiments include *smallinversion* turned on and *cleanborders* set to 1 per cent. By turning on *smallinversion*, the image inversion is performed at the Nyquist resolution and upsampled to the image size. This is used to speed up the process of converting the visibility data into an image. The *cleanborder* setting is the fraction of the height and width of the image that the CLEAN algorithm is not run.

CLEAN is the name of the deconvolution algorithm, introduced by Hogbom and Brouw (1974), and assumes the radio sky can be broken up into a series of point sources called “clean components”. The clean components are reconvolved or “restored” with Gaussians. By using Gaussians, the higher spatial frequencies are de-emphasised as they can be spuriously extrapolated.

The CLEAN algorithm operates by searching the dirty image (the inverse Fourier transform of the visibility data) for the position of the highest intensity pixel multiplied by the instrument response (dirty Point Spread Function or PSF), removing a fraction of it from the dirty image, and adding that component to the reconstructed image (known as the clean model). The algorithm will continue until a set threshold is reached or a set number of iterations is completed. What remains in the dirty image is the residuals. The accumulated CLEAN model is convolved with an idealised CLEAN beam, which is usually represented by an elliptical gaussian of the same size and shape as the inner part of the dirty beam. The convolved CLEAN model with the residuals added in creates the CLEAN image.

The WSCLEAN parameters varied for the coarse channels are the number of pixels imaged, the cleaning algorithm threshold, and the *mgain* value. The number of pixels, along with the *scale* (the number of pixels per synthesised beam imaged) setting in WSCLEAN determine the size of the final image. The bigger the image, the better the deconvolution of the sources within the sidelobes of the primary beam. The value for *mgain* is what the peak flux density is reduced by until a new major iteration is started.

In all the imaging experiments, the number of iterations (also known as major cycles or major iterations) is set at 400,000 such that this will not be the limiting factor in the deconvolution process. The threshold, however, is varied as shown in column three of Table 2.2. The values of 1 and 1.65 represent the levels of three and five times the noise in a test image produced from one of the observations. The value of “stopnegative” means that the CLEAN algorithm stops the first time a clean component has a negative value. The values “Stopped On (Jy)” in the table is the actual threshold value reached, as reported by WSCLEAN.

Choosing images produced in a 4000 by 4000 pixel field-of-view optimised the number of sources that could be used for the ionospheric corrections as well as deconvolve any bright sources in the sidelobes of the beam. By setting the *mgain* equal to 0.85, the CLEAN deconvolution algorithm is performed in two major iterations, lowering the sidelobe levels and thus the RMS that is caused by systematic errors. The conditions within experiment 14 from Table 2.2 is used for both the survey of the Galactic Centre and Orion.

Stokes Imaging

The Stokes parameters I, Q, U and V are a set of values used to describe the polarisation state of the incoming electromagnetic radiation. For most spec-

Table 2.2: Imaging experiments for the 1.28 MHz coarse channel images completed using the 2014 epoch of Galactic Centre data. The second column is the number of pixels imaged in a square grid. “Threshold” is the amount of sigma for WSCLEAN to clean down to, where “stopnegative” is the where the clean algorithm stops when it finds a negative clean component value. The “Stopped on” value is the actual threshold value it cleaned down to. The value “mgain” means that the peak flux density is reduced by 85% (for 0.85) until a new major iteration is started. The RMS is the resultant image determined by searching a clear patch of sky. The last three columns represent the outputs from the experiments.

	Imsize	Threshold	mgain	RMS	Iterations	Stopped on (Jy)	Real Time (Hours)
Experiment 1	2000	1	1	0.149	25000	0.999984	3.6
Experiment 2	2000	1	0.85	0.130	300	5.2014	
					24000	0.999993	5.7
Experiment 3	2000	1.65	1	0.151	8000	1.64998	3.5
Experiment 4	2000	1.65	0.85	0.135	300	5.20145	
					8000	1.64983	8.4
Experiment 5	2000	stopneg	1	0.154	500	4.3815	2.9
Experiment 6	2000	stopneg	0.85	0.143	300	5.2015	
					900	3.6057	8.4
Experiment 7	3000	1	1	0.138	33000	0.99973	4.4
Experiment 8	3000	1	0.85	0.123	300	5.21893	
					32000	0.999992	8.4
Experiment 9	3000	1.65	1	0.143	9000	1.64998	3.5
Experiment 10	3000	1.65	0.85	0.131	300	5.21893	
					9000	1.64949	5.6
Experiment 11	3000	stopneg	1	0.146	1000	3.356	3.5
Experiment 12	3000	stopneg	0.85	0.138	300	5.21893	
					1000	3.3329	8.4
Experiment 13	4000	1	1	0.133	24000	0.999971	5.2
Experiment 14	4000	1	0.85	0.119	300	5.2735	
					24000	0.999852	6.6
Experiment 15	4000	1.65	1				>12hrs
Experiment 16	4000	1.65	0.85	0.124	300	5.2735	
					8000	1.64998	5.3
Experiment 17	4000	stopneg	1	0.137	900	3.5676	3.6
Experiment 18	4000	stopneg	0.85	0.129	300	5.2735	
					1000	3.21092	5.0

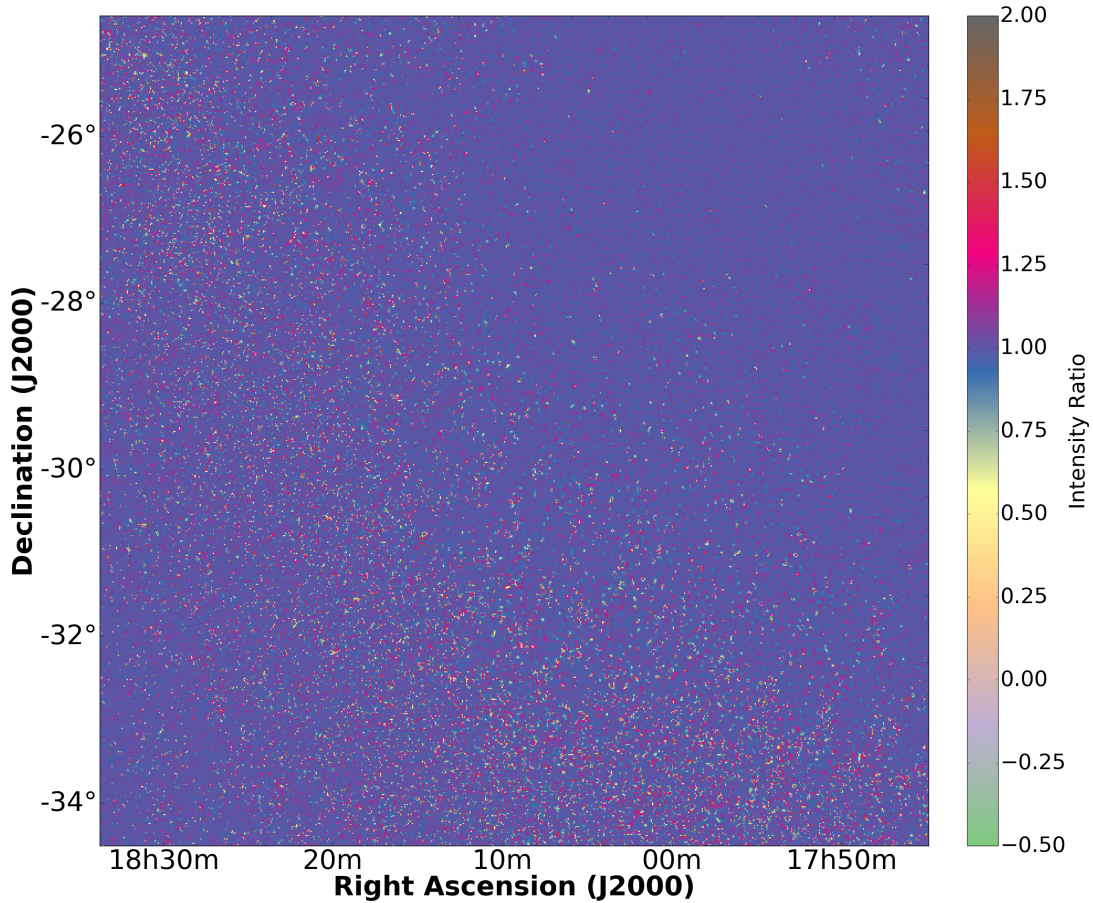


Figure 2.4: An image of a single coarse channel made by the WSCLEAN pseudo-Stokes I (an arithmetic mean of the XX and YY components of the dipoles), divided by a true Stokes I image. The image shows that the two match with a ratio of 1 except in some pixel locations, which are likely from errors in the deconvolution.

tral lines, the expectation is that the radiation is nonpolarised so the signal is quantified by Stokes I for the total intensity. Even though the full polarisation correlation products, XX, YY, XY, and YX, are stored by default (Lenc et al., 2017) WSCLEAN alone can not be used to create a true Stokes I image with MWA data, as the MWA does not have orthogonal feeds. A pseudo-Stokes I image can be created with WSCLEAN but the image represents the arithmetic mean of the signals from the XX and YY components of the dipoles and no cross terms are considered. To determine if this is sufficient for the spectral line work, a true Stokes I image is created by first imaging each polarisation and cross polarisation with WSCLEAN and then making a beam model for each. The PYTHON script in

the MWA Toolkit, `beam`, is used to create real Stokes I, Q, U and V images. The FITS image created by the WSCLEAN pseudo-Stokes I was divided by the true Stokes I image. As shown in Figure 2.4, the majority of the image has a ratio of one with some pixels having a difference up to twice the signal. These are likely differences in the deconvolution of bright sources which may be corrected by creating deeper images of the field of view, so that better deconvolution of bright sources is obtained.

2.4.4 Flux Density Scale, Primary Beam, and Ionospheric Corrections

Primary Beam

The primary beam is the sensitivity pattern the individual MWA tiles has on the sky as a function of direction and frequency. The dipoles are not uniformly sensitive to the incoming radiation from all directions, reducing the apparent flux density of sources located further away from the phase centre. Therefore, we have to correct for the changing brightness distribution on the sky by dividing the beam model by the final CLEAN image.

A model of the primary beam is created for each observation based on the the delays stored in the `metafits` file and using a PYTHON script in the MWA toolkit, `make_beam.py`. For all the observations of the Galactic Centre and Orion, the beam model generated for the XX, YY, YX and XY, polarisation's used the model developed by Sokolowski et al. (2017).

As explained in Perley et al. (2016), when only Stokes I images are created the sky images can be simply divided by the beam model to obtain a uniform flux scale across the image. The images from each coarse channel are then divided by the beam models of each coarse channel to correct for the sensitivity attenuation across the field of view. To create a pseudo-Stokes-I beam model, an arithmetic mean is created from the XX and YY beam model images, matching the calculation that WSCLEAN uses to create the pseudo-Stokes I images.

Although this process does correct for the attenuated source fluxes, after the primary correction is made, the image noise increases towards the edges of the image. This increased noise limits the amount of the sky in which we are sensitive to spectral line emission and absorption. The images created are larger than the survey region to ensure all the sources in the sidelobes of the primary beam are deconvolved.

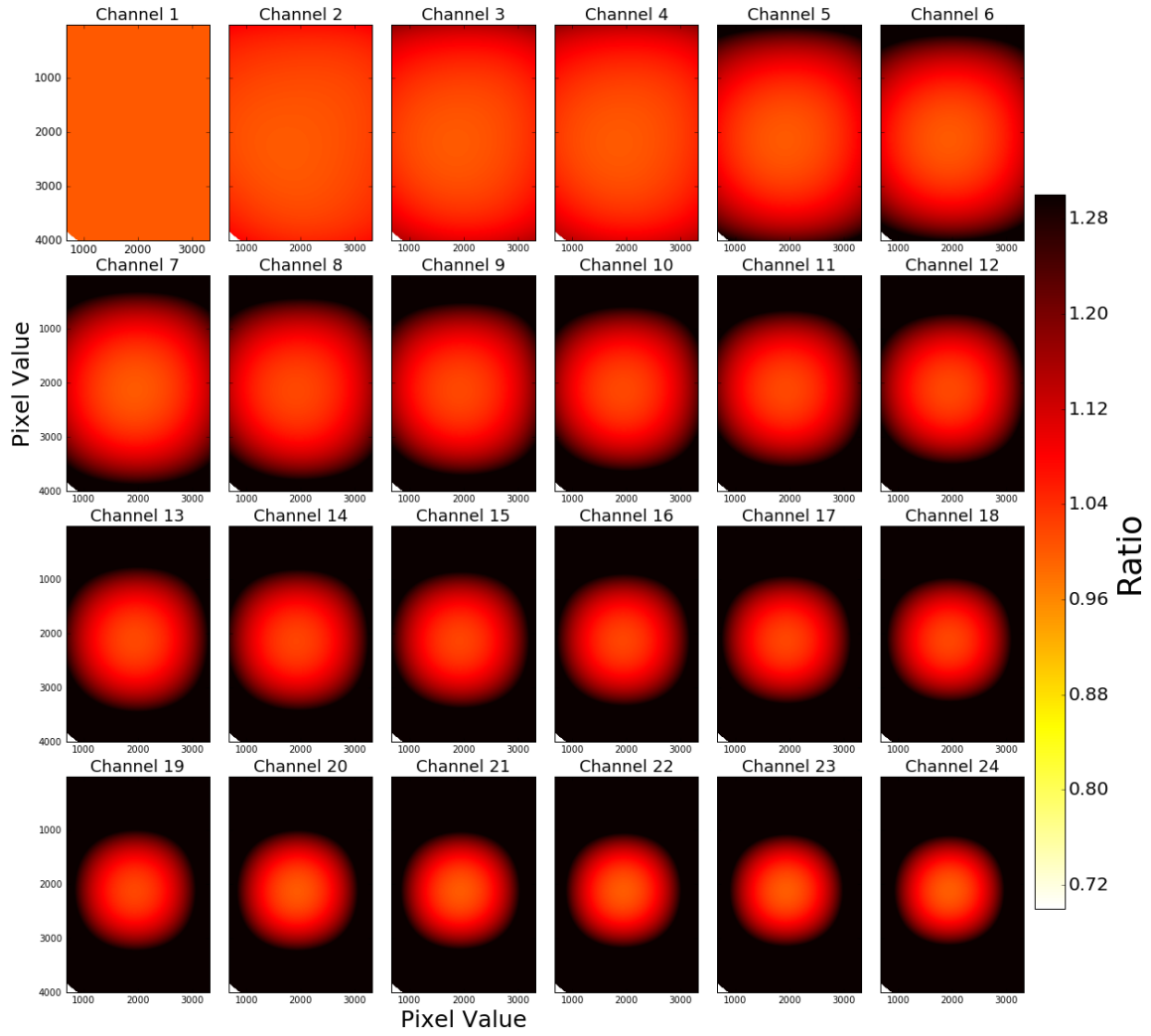


Figure 2.5: A primary beam model was created for each coarse channel within a single observation. The beam model from the first coarse channel was divided by the beam model for the remaining 23 coarse channels and the ratio of the sensitivities is shown.

For the creation of the coarse channel and fine channel images an evaluation is completed to determine how often the primary beam model needs to be created. To evaluate the rate of generation for the primary beam model, a pseudo-Stokes I image and beam model are made for each coarse channel. To test the extreme case of the instrument, the Galactic Centre observation (observation identification 1090335176) was used as it represented delays pointing close to the horizon. Each of the beam models were independently divided by the first coarse channel to qualitatively evaluate the change in the beam model as a function of frequency.

The results, as shown in Figure 2.5, demonstrated that the beam model changes rapidly for each coarse channel. If the beam model from the first coarse channels was applied to the last coarse channel, the flux scale would decrease by 70 per cent outside a few degrees from the phase centre. Therefore, beam models are created for each coarse channel for each observation independently.

Flux Density Calibration

Radio interferometers measure voltages which are then correlated across multiple receiving elements. The correlation coefficients representing the output signals need to relate to a known scale to exchange the information to a flux density. By comparing the known flux density of multiple observable objects to their measured intensities, a scaling factor can be obtained. The derived scaling factor is multiplied by each of the individual deconvolved (CLEAN) sky images to adjust the measured signals to an absolute flux density scale.

The main benefit for completing the flux density scaling is that, regardless what instrument observes a source, a similar science conclusion can be drawn. As described in Baars et al. (1977) and Scaife and Heald (2012), a flux density scale across the entire frequency range for calibrator sources allows for a universal correction to be made. Therefore, the need for flux density scaling is not limited to interferometers but a single dish will handle the flux density calibration differently than is utilised in these MWA observations.

For the spectral line observations, the flux density scaling is accomplished by first using the software package AEGEAN (Hancock et al., 2012, 2018) which searches for sources above a set sigma limit within the image, documents the source details such as position and flux density and accumulates the information into a source catalogue. A comparison of the flux densities for each radio source within the catalogue, with catalogues such as GLEAM or Molonglo Reference Catalogues (MRC; Large et al. 1981), is used to create a scaling factor. For the

MRC, a survey done at 408 MHz, a spectral index of -0.83 is used to scale the flux density down to the observed frequencies, as described in Chapter 4.

For the Galactic Centre survey the catalogue of sources generated by AEGEAN was compared with the MRC as it is a catalogue of sources close to our observing frequencies and is populated with sources within 3 degrees of the Galactic Centre. As shown in Figure 2.6, the mean difference between the flux density in our images to the MRC catalog is 0.01 ± 0.03 Jy, so no direction dependent corrections were required.

See the survey papers for the full details of the correction requirements for the Galactic Centre and Orion fields (Chapters 4, 5, and 6).

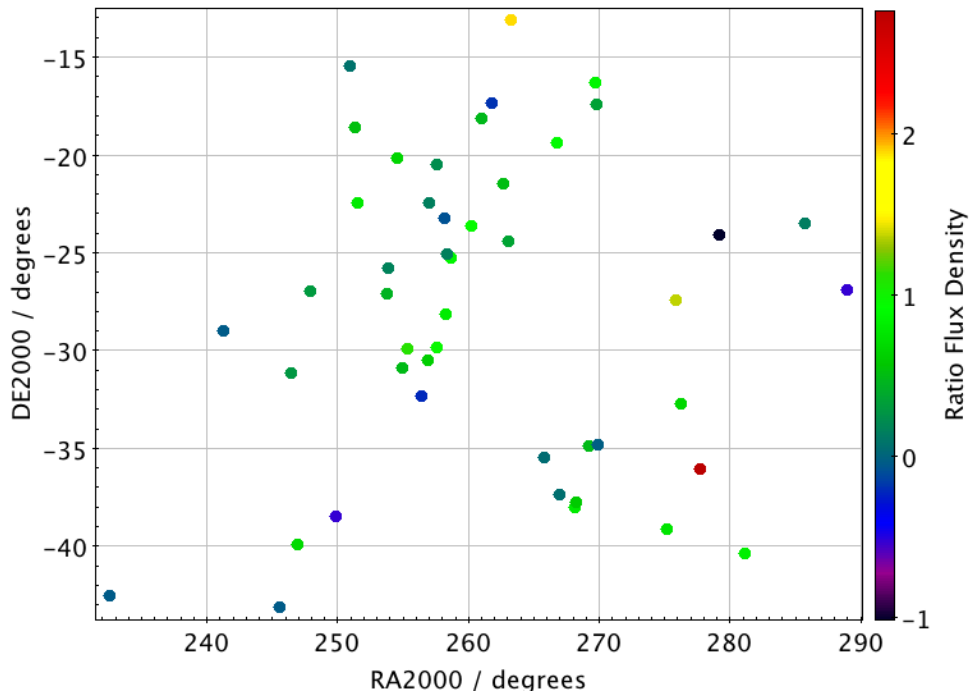


Figure 2.6: Ratio of the flux density values between the Galactic Centre survey data from the MWA compared to the Molonglo Reference Catalogue (MRC). The plot shows ratio of the flux densities is one across the sky. Some sources that show differences greater than or less than one may be due to extended emission being broken up into multiple components in during the AEGEAN source finding.

Ionospheric Corrections

The atmosphere surrounding the Earth is transparent to radio waves as long as none of its constituents can absorb or reflect the radiation, making the observable

range from ground-based telescopes 15 MHz to 1300 GHz⁴. At high frequencies, the water vapour and oxygen molecules within the troposphere make the atmosphere opaque to observations of interstellar water, oxygen, and other associated molecules. At low frequencies, the terrestrial atmosphere is no longer transparent because the free electrons in the ionosphere absorb or reflect the electromagnetic radiation.

Radio waves are then subjected to spatially variant refractions and propagation delays on their way to the instrument as a function of the square of the wavelength (Figure 2.7). At frequencies less than 300 MHz, these refractions impact the observations by shifting the apparent source positions on the sky. This affects the data in two ways. One is that we need to ensure the accuracy of the source position is maintained to have confidence relating line detections with sources within catalogues such as SIMBAD⁵ (Wenger et al., 2000). Additionally, if the source positions are changing per observation, when the observations are stacked together the point spread function will be smeared, creating an effective change in the shape of the final point spread function. An example of this is shown in Figure 2.8, where the mean position shift between the Galactic Centre observations and MRC are plotted for each observation.

The ionosphere is also found to create decorrelation but only with longer baselines, as discussed in Trott et al. (2018) and Mevius et al. (2016). This is partially due to the signal potentially passing through different phase plane screens of the ionosphere before reaching the telescope. For this, corrections for the ionosphere must be done in the visibilities prior to correlation. However, this work was done by utilising only 3km baselines in Phase I of the MWA, so a correction in the image plane for slight source shifts can be done to account for ionospheric effects (Hurley-Walker and Hancock, 2018).

For the spectral line observations, the ionospheric correction is accomplished by first using AEGEAN to create a catalogue of sources within the field, per each coarse channel image of each observation. A comparison of the positions for each radio source within the spectral line survey catalogue, with source catalogues such as GLEAM or MRC, is used to create a factor per coarse channel in which the sources are shifted. The mean positional offsets are applied to each fine channel that was imaged within the same coarse channel the offset was derived. The residual offset, along with the blurring of the point spread function are determined for each survey and documented in the associated survey paper. As an example of

⁴Although there are windows within this range that are unobservable due to other effects

⁵<http://simbad.u-strasbg.fr/simbad/>

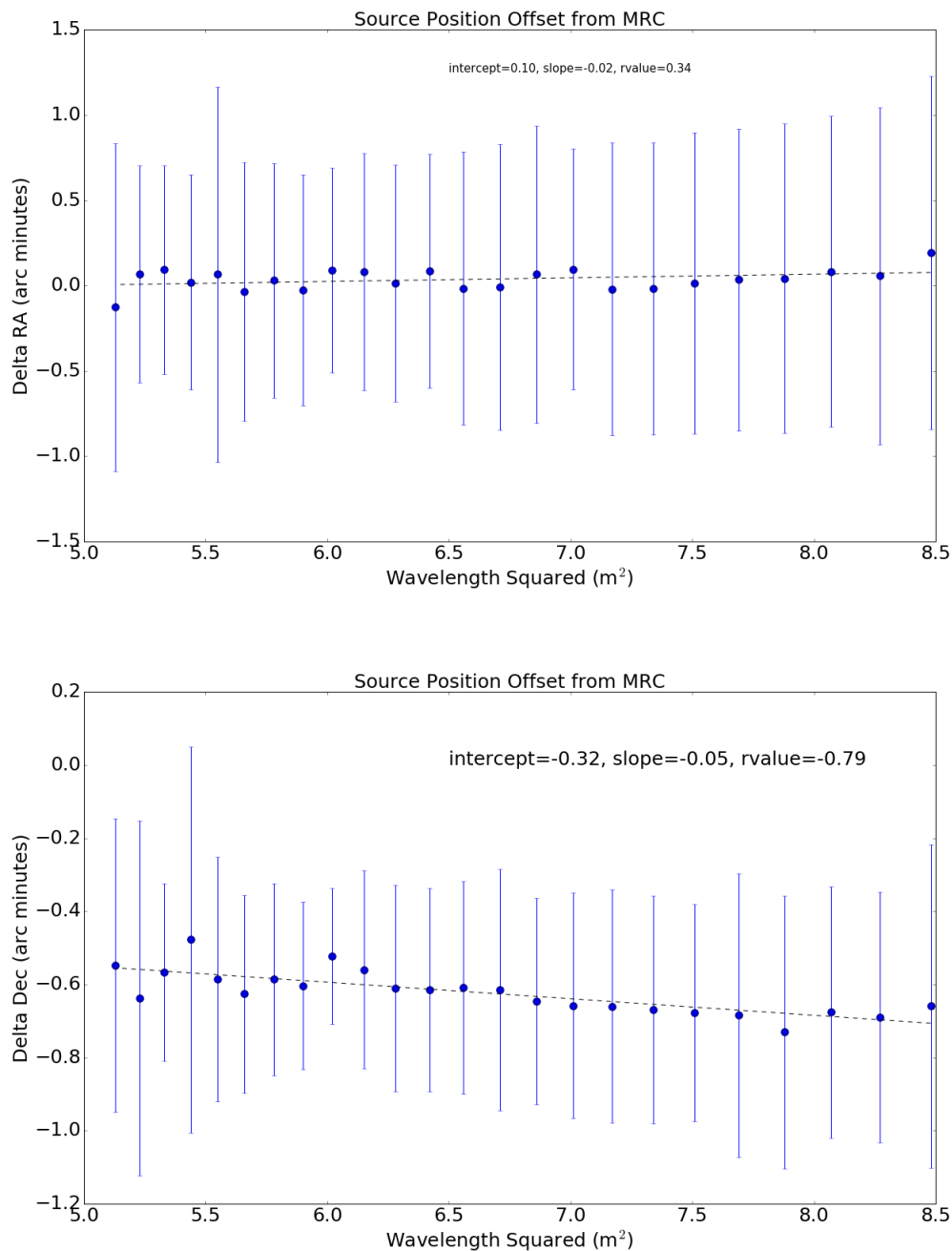


Figure 2.7: The difference in the source positions in the Galactic Centre survey (July 2014 data only) images in comparison to MRC prior to correction. The linear fit to the data, represented by the dashed line, demonstrates that the source shift caused by the ionosphere varies slightly as a function of wavelength squared. The error bars show the standard deviation from values of the sources within the field across the sky. The top plot is the position offsets in right ascension (RA) and the bottom plot is the position offsets in declination (Dec).

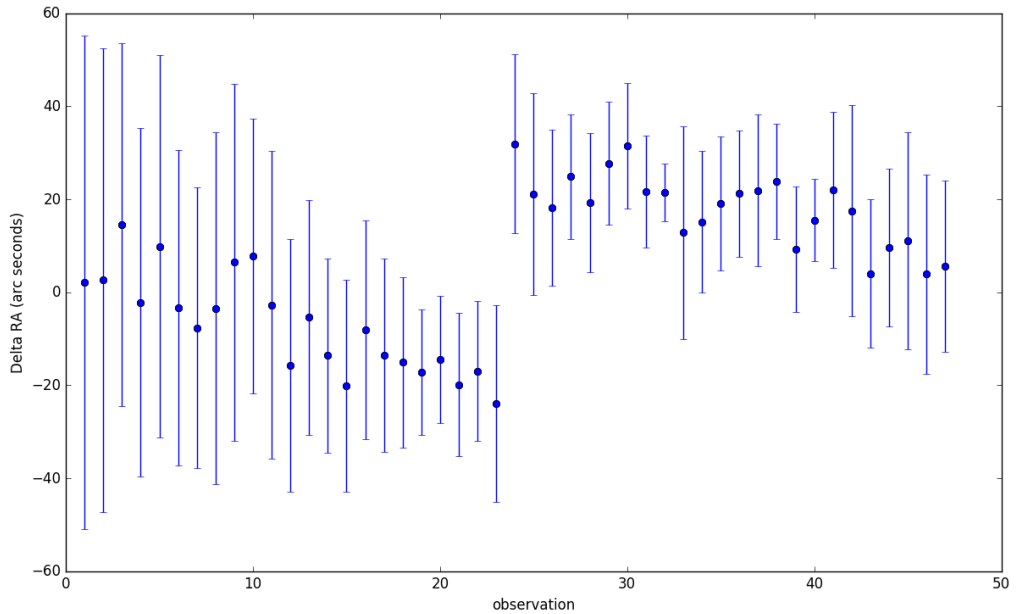


Figure 2.8: A plot of the mean positions shifts in RA, plotted for each observation from the 2014 and 2016 epochs of Galactic Centre data. The gap is caused by the observations being on different nights, two years apart.

the variation each observation experienced, see Figure 2.8. The Galactic Centre survey was a combination of two observing runs (2014 and 2016) and the positional offset in RA are shown for coarse channel 10 for every observation. The data from 2014 showed a greater variation in source position than those from 2016.

2.4.5 Fine Channel Imaging

The information about molecular and atomic transitions comes from imaging each of the 10 kHz fine channels from the MWA. Continuum images of each fine channel are created for 2400 of the 3072 available 10-kHz channels, representing the central 100 fine channels of each of the 24 coarse channels. This was done to remove channels subject to increased noise caused by the aliasing from the first stage poly-phase filterbank used to create the 1.28 MHz coarse channels.

The following sections describe the considerations that went into the fourth line of the pipeline in Figure 2.3.

Fine Channel Image Parameters

Similar to the considerations that went into the imaging of the coarse channels, a series of experiments were designed to find the best imaging parameters for each individual fine channel. The focus on this imaging process is on lowering the noise and increasing source deconvolution. However, the imaging had to be done within the wall time constraints (12 hours per job) of the supercomputer control software.

The experiments for the Galactic Centre data are shown in Table 2.3. Even though these imaging experiments are organised similarly to the set of parameters tested for the coarse channel images, different considerations had to be made. The thresholds of 2.5 and 4 represented 5 and 8 times the 1σ noise in a test image. In all the experiments, 100 fine channels from one coarse channel were imaged simultaneously. The WSCLEAN parameter *joinchannels* was used to create a multifrequency synthesis image from the coarse channel to find the CLEAN components and subtract them from each individual fine channel’s visibilities.

For the Galactic Centre data from 2014 and 2016, the imaging parameters from Experiment 4 were used. These parameters were used as they represented the lowest image RMS and the imaging consistently finished in under 12 hours real time. However, new capabilities were provided with WSCLEAN version 2.2 that were utilised in the Orion fine-channel imaging pipeline. In the new version “auto-threshold” was introduced which determines the RMS in the image and sets the threshold automatically based on an input sigma value. This was combined with “auto-mask”, which uses a multi-scale clean and puts in a scale dependant mask to produce an image with a lower noise. In both frequency ranges published in Chapters 5 and 6, an *auto – threshold* was set at “1” and *auto – mask* was set at “3”, to produce fine channel images with an RMS of 0.25 Jy, almost a factor of two better than using the Galactic Centre image parameters.

Weighting

In the process of creating an image of the sky, the visibility data are broken up into a regular grid and averaged together (Thompson et al., 2017). For all the points within each section of the grid, known as a cell, the weighted average is calculated based on the imaging settings to control the point spread function. Some of the most common weighting schemes used in radio astronomy are natural weighting and uniform weighting. There are also several customised weighting designs, such as robust (Briggs, 1995), that mix the concepts of natural and uniform weighting.

Table 2.3: Imaging experiments for the 10 kHz fine channel images using the 2014 epoch of Galactic Centre data. Pixel is the number of pixels imaged in a square grid. Threshold is the amount of sigma for WSCLEAN to clean down to, where “stopnegative” is the where the clean algorithm stops when it finds a negative clean component value. The value “mgain” means that the peak flux density is reduced by 70% (for 0.7) until a new major iteration is started. The RMS is the resultant image RMS in a clear patch of sky. The last three columns represent the outputs from the experiments.

	Imsize	Threshold	mgain	RMS (Jy)	Iteration	Stopped on	Real Time (Hours)
Experiment 1	2000	2.5 (5sigma)	1		133000	-3.54081	>12hrs
Experiment 2	2000	2.5 (5sigma)	0.7		136000	3.62627	>12hrs
Experiment 3	2000	4 (8sigma)	1	0.867	31000	3.99903	5.3
Experiment 4	2000	4 (8sigma)	0.7	0.493	600	18.0346	
					12000	5.58835	
					25000	3.99987	7.2
					600	16.617	
					11000	5.13222	
Experiment 5	2000	stopneg	1	0.900	4000	8.36154	2.6
					3000	8.66064	3.6
					2000	8.84886	10.8
					0.828		
Experiment 6	2000	stopneg	0.7				
Experiment 7	3000	2.5 (5sigma)	1		69000	4.4017	>12hrs
Experiment 8	3000	2.5 (5sigma)	0.7		65000	4.44874	>12hrs
Experiment 9	3000	4 (8sigma)	1		59000	4.59083	>12hrs
Experiment 10	3000	4 (8sigma)	0.7		26000	6.12824	>12hrs
Experiment 11	3000	stopneg	1	0.912	5000	10.9264	4.0
Experiment 12	3000	stopneg	0.7	0.898	1000	20.5026	
					5000	10.7838	5.6
Experiment 13	4000	2.5 (5sigma)	1		20000	6.28648	>12hrs
Experiment 14	4000	2.5 (5sigma)	0.7		1000	20.7011	
					18000	6.45428	>12hrs
Experiment 15	4000	4 (8sigma)	1		17000	6.74945	>12hrs
Experiment 16	4000	4 (8sigma)	0.7		1000	20.7011	
					18000	6.45428/	>12hrs
Experiment 17	4000	stopneg	1	1.284	7000	9.5203	6.5
Experiment 18	4000	stopneg	0.7	0.973	1000	20.7011	
					11000	8.08231	10.3

The weighting scheme used to image each observation, will be dictated based on the science goals.

Natural weighting is when the weight is equal to the number of points within the cell. Natural weighting gives the best signal to noise by placing equal emphasis on all cells, which means more total weight from receiving elements that are close together. However, this also results in a larger beam and therefore a reduced angular resolution. When a science goal requires imaging the extended and diffuse emission from faint sources, natural weighting provides the best results.

Uniform weighting sets all of the cells equal to each other, regardless of the number of visibilities in each cell, and places emphasis on the signal from receiving elements that are the furthest from each other. This results in the sky image having a reduced signal to noise in comparison to natural weighting, but uniform weighting offers an increase in the angular resolution. Images created using uniform weighting are sensitive to the small scale structure of bright sources within the observation.

Briggs weighting uses a parameterized filter to allow a continuous variation between the optimal resolution (uniform weighting) and an optimal signal to noise (natural weighting):

$$w_i = \frac{\omega_i}{1 + W_k f^2}, \quad (2.1)$$

where W_k is the uniform or super uniform weighting and

$$f^2 = \frac{(5 \times 10^{-R})^2}{\frac{\sum W_k^2}{\sum \omega_i}}. \quad (2.2)$$

The critical parameter in Briggs weighting is the robust parameter (R). The scaling of R is such that $R = 0$ gives a good trade-off between resolution and sensitivity. However, any value between -2.0 (close to uniform weighting) to 2.0 (close to natural) is utilised to obtain the required results.

Although almost all of these techniques have been demonstrated to successfully image MWA data, for the spectral line data we are using Briggs weighting with an R value set to “-1”. Natural weighting has been tested on these observation but the diffuse emission surrounding the Galactic Centre made it difficult to detect extragalactic sources used in the calibration of the flux density scale and ionosphere. By using Briggs “-1” there is a tradeoff between resolution and sensitivity while reducing some of the sidelobe confusion.

2.5 Create Final Spectral Cubes

After each of the 10 kHz fine channel images are created, they are corrected for the primary beam shape by dividing by the beam model created for the coarse channel in which the fine channels originated and corrected for the position offset caused by the ionosphere as determined for that coarse channel. Once these corrections are completed, the corrected fine channels are built into a three-dimensional data cube using the PYTHON script `CUBE_MAKE.PY` (See Section 2.9 for the github repository for the code). This is represented on line five of Figure 2.3 and is completed for each coarse channel of each observation.

Once a data cube is created for each coarse channel of each observation, the observations from each coarse channel are individually integrated together to form a full continuum plus line three-dimensional data cube. From there the continuum can be subtracted to reveal the spectral lines, as per the sections below.

2.5.1 Stacking Observation with Inverse Variance Weighting

The average, or arithmetic mean (AM), of a group of values is determined by calculating the sum of the values and dividing by the quantity of items within that group:

$$\text{Mean} = \frac{1}{n} \sum_{n=1}^n a_i = \frac{1}{n} (a_1 + a_2 + \dots + a_n). \quad (2.3)$$

A modification to the average, created by specifying a weight to each value before the data are averaged, is a process called weighted averaging. Inverse variance weighting is, therefore, averaging the results but dictating the level of importance of any individual value (a) based on one over the square of the standard deviation (ϕ) or root mean square (RMS) of the value:

$$\text{Weighted Mean} = \frac{\sum a_i / \phi_i^2}{\sum 1 / \phi_i^2}. \quad (2.4)$$

For the spectral line work, the MWA observations are taken in either five-minute or two-minute snapshots that, once calibrated, are combined to create a single integrated data cube for the region. By using inverse variance weighting, any observation with higher RMS will be down-weighted in importance when the observations are averaged together. If all the observations have similar variance, the weighted average will be similar to the arithmetic mean.

To obtain the RMS for each observation, an area average RMS from the associated coarse channel is determined using a PYTHON script and then writing it into a list in a text file. To integrate the data cube together, the FITS cubes are first converted into a MIRIAD file format. In MIRIAD all the snapshot images for each coarse channel are averaged together after the coordinates for each image are gridded to match the first input data cube.

2.5.2 Continuum Subtraction

To obtain an unobscured view of any possible spectral line detections, the continuum and the associated artefacts (i.e. sidelobes or deconvolution errors), within the image, must be removed (Cornwell et al., 1992). Traditionally, continuum subtraction by fitting a polynomial to the visibility data through an identified list of line-free channels is considered a robust method regardless of any systematic errors that may exist (Cornwell et al., 1992; Sault, 1994).

As an initial pass to subtract the continuum in the visibility plane, the CASA task *wvcontsub* was used to apply a first order polynomial across the spectral channels in each snap-shot observation. This CASA task subtracts the continuum on the real and imaginary separately. The continuum subtraction of the widefield image using CASA removed approximately 71% of the continuum. To remove the remaining bright sources in the field, a second method was used to subtract the continuum by using the MIRIAD task *moment* with “mom” set as “-1”, which created an average intensity map. This average intensity map was subtracted from each fine channel within the cube, removing approximately 99% of the total continuum.

Although this method produced a data cube that appeared to be clear of the continuum, the use of CASA to subtract the continuum produced an image in which some artefacts around bright continuum sources were visible in the image plane. These “streaking” artefacts, shown in Figure 2.9 may have been caused by *wvcontsub* not correcting for the *w*-terms when the continuum subtraction was done. However, it may have also been an effect of sources further from the phase centre will have a more sinusoidal response as a function of frequency.

When the continuum subtraction can not be performed on the visibilities, the common suggestions are subtracting a continuum image made from channels free of spectral lines or fitting a polynomial to the spectral data before deconvolution. This is because “..if the continuum is removed before deconvolution, no deconvolution errors are propagated to the line images” (Sault, 1994). Both

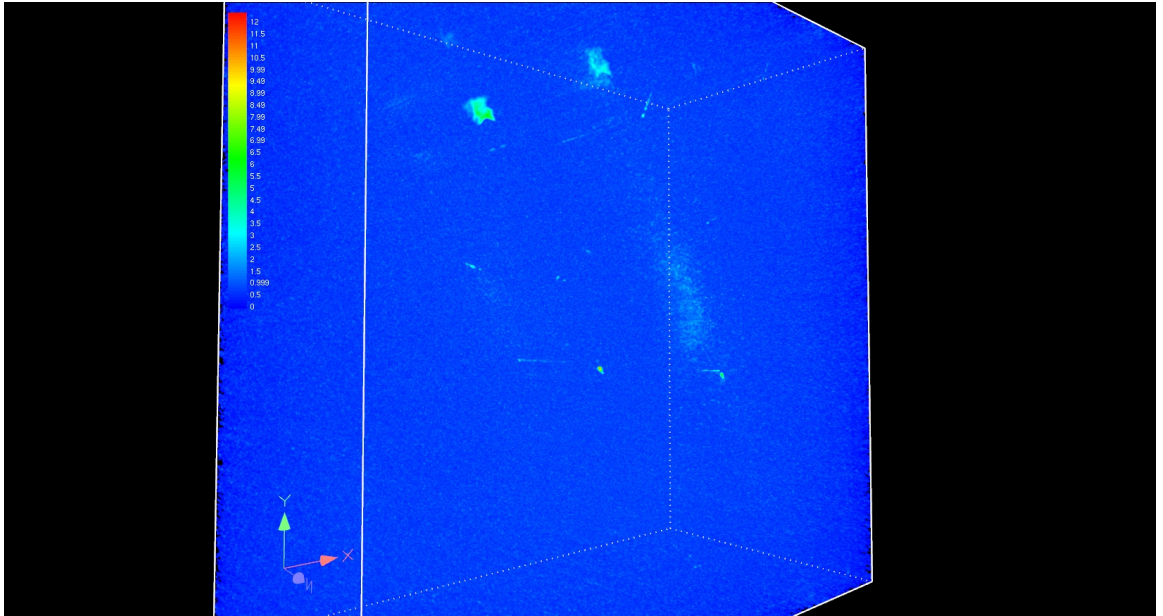


Figure 2.9: Residual continuum in the three-dimensional data cube after continuum subtraction was done in CASA on the Galactic Centre data from 2014. (Image Credit: This image was created by Amr Hassan using spectral line cube visualisation software he created.)

of these methods are robust against calibration artefacts that are independent in frequency. However, any residual continuum within the image will have large unsubtracted side lobes from the weak emission.

Continuum subtraction completed by subtracting an image free of spectral lines from the continuum image is only recommended if the fractional bandwidth is small. Otherwise, the bandwidth could be smeared, or the spectral index of bright sources may be altered (Sault, 1994). The MWA has a 30.72 MHz bandwidth with observing frequencies of 99-170 MHz for these surveys, so the fractional bandwidth is large and these methods are not recommended.

A requirement to stray from traditional methods is not unique to MWA data. We adopted a method created by the Southern Parkes Large-Area Survey in Hydroxyl (SPLASH) survey published by Dawson et al. (2014) where they binned the spectral data, creating a smooth curve that fits the spectral curvature at each pixel, and then subtract the binned spectra. This method creates a smooth subtraction across the field-of-view and frequency band, correcting for any residual bandpass shape. However, this can also result in some loss of intensity for each spectral transition.

To test the impact this technique for continuum subtraction may have on the

MWA survey regions, the data were binned in sizes of 5, 10, 15 and 20 channels and the impact on an injected 5σ detection was evaluated. For a region around a potential 5σ source, the difference in intensity between the binned data and the uncorrected data was approximately 1% with the 15 channel bin giving the closest intensity to the unsubtracted line intensity. The data in which 15 or 20 channels are binned, show the smoothest spectra and identifies the likely true spectral characteristics of the sky.

The continuum subtraction technique of binning 15 spectral fine channels together, regridding the data based on the original observation to extrapolate the missing information, and then subtracting the two data cubes was used for both surveys. All the steps involved were completed in MIRIAD on the final integrated data cube, as explained in Chapter 4.

Noise Reduction

Noise is normally defined as the unwanted signal and lowest threshold in which any signal may reside. However, noise can also mean unpredictable signals that carry no useful information. In signal processing noise can be considered uncorrelated to the signal of interest.

Signal averaging is a signal processing technique where signals, or potential areas of signal, are averaged over time to increase the strength of a signal of interest relative to the noise. If we can assume that the signal power (S) is constant in replicated measurements then:

$$S = \int_0^T E[s(t)^2] dt, \quad (2.5)$$

where $s(t)$ is the signal strength in respect to time and T is the total length of time. When the noise varies about a mean of zero with constant variance (σ) we can define the signal-to-noise ratio (SNR) as:

$$\text{SNR} = \frac{S}{\sigma^2} \quad (2.6)$$

and we would expect the noise to decrease as a function of square root of the averaged time or number of replicate measurements. To see if the MWA spectral line observations behaved in this manner, observations were randomly averaged together in sets and the image RMS in the coarse channel continuum image was determined. As shown in Figure 2.10, the noise continues to decrease as a function of square root of time as more observations are averaged together.

However, in the observations of Orion (bottom plot), this was not immediately evident until the sensitivity of the primary beam was applied. This is likely due to the observations being done close to the horizon, where effects of the changing primary beam are more evident.

This check is published in Chapter 5 and also had the added benefit of allowing us to predict how much time the MWA would need to start detecting thermal emission from molecules. The distance of 400 pc matches that of Orion and the distance of 8.6 kpc matches that of the Galactic Centre. This suggests that if the noise were continued to decrease in the same manner, we would require 30 hours of observations to be able to match the column densities calculated at higher frequencies for molecules which have transitions at the MWA frequencies.

2.6 Data Search and Visualisation

2.6.1 Search Strategies

The surveys of the Galactic Centre and Orion used different search strategies, but the challenge in both was to find emission and absorption signals in three-dimensional data cubes containing more than 2.3×10^8 voxels. The Galactic Centre survey was broken into two components: a targeted survey to search for nitric oxide and the mercapto radical; and a blind search to look for any signal over six times the background noise. However, the Orion survey was an untargeted survey looking for any signal in absorption or emission between 99–142 MHz that are at least five times the background noise.

The Galactic Centre targeted survey was completed manually to look within three spectral (10 kHz) channels from the rest velocity of nitric oxide (NO) transitions and the 111.55 MHz mercapto radical (SH) dominant hyperfine transition. As shown in Table 4.3, there are a number of NO transitions itself as well as the isotopologues. Observable in the MWA band is NO, ^{15}NO , N^{17}O , N^{18}O , and $^{15}\text{N}^{17}\text{O}$. It is expected that NO would be the most abundant and there is one low energy (7.25 K E_u/k_B) transition representing $J=\frac{3}{2}$, $\Omega = \frac{1}{2}$, $F=\frac{5}{2} - \frac{5}{2}$. Of the isotopologues for NO, ^{15}NO and N^{18}O also have low energy transitions at around 7 K.

The lowest energy (quartet) hyperfine transitions of SH emit at 100.30, 111.49, 111.55 and 122.73 MHz, all within the range of the MWA. The transition at 100.30 MHz is outside our observing band in the Galactic Centre. The lines at 111.49 and 111.55 MHz are the highest intensity transitions representing $^2\Pi_{3/2}J = \frac{3}{2}$,

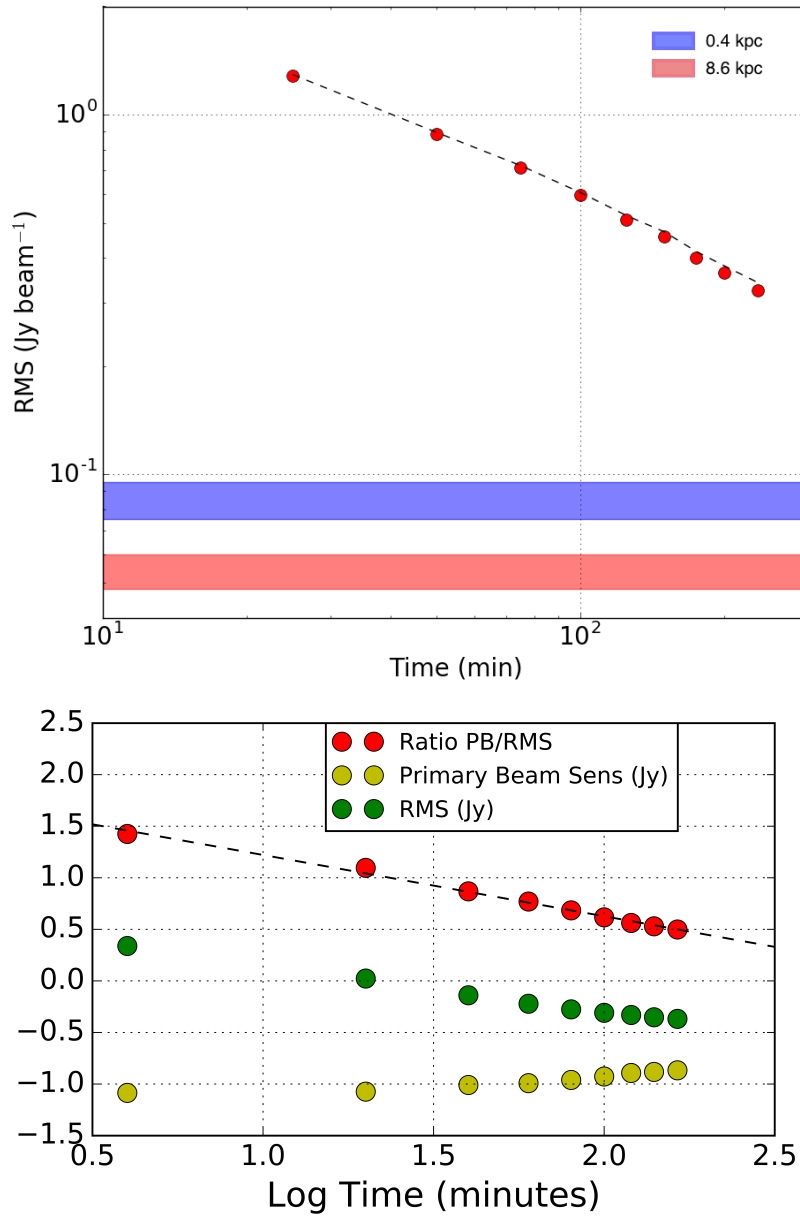


Figure 2.10: Reduction of noise as a function of time. The top plot is from Figure 4.6 and shows that the noise continues to decrease as a function of square root of time, represented by the dashed line in both plots having a slope of -0.5 . This plot also shows the approximate noise threshold we would need to achieve to obtain the column densities published at higher frequencies. The bottom plot is from the Orion survey at 114.6 MHz and also shows that the noise decreases as a function of square root of time once a correction for the primary beam sensitivity is applied.

$F = 1^+ - 1^-$ and ${}^2\Pi_{3/2} J = \frac{3}{2}$, $F = 2^+ - 2^-$ respectively, with energy at the upper excitation level of 5×10^{-4} K. See Chapter 4 Table 4.3 for more detail.

The manual approach involved first creating a root mean squared (RMS) image of the spectral RMS at each pixel position using PYTHON. Then each channel in the continuum subtracted cube was divided by the RMS image to create a signal-to-noise cube. The resultant channels were searched for pixels greater than 5. As a quality check, a contour plot and spectrum were created for each potential detection. This resulted in three tentative detections of nitric oxide and one of the mercapto radical published in Tremblay et al. (2017) (Chapter 4).

The untargeted (blind) survey over the observed frequency range of the Galactic Centre used a modified version of HOPSFIND developed by Walsh et al. (2012). Due to the low spectral and spatial resolution of the MWA, we would expect any spectral lines to be from unresolved sources and each transition within a single frequency channel, similar to the assumptions made in HOPS for water masers in the Galactic Centre. This process involved making a peak temperature map (PTM) in MIRIAD, which finds the peak value for each pixel within the continuum subtracted data cube and copies it into a map covering the full survey region. The PTM is divided by the RMS image created for the targeted survey for each coarse channel to create a signal-to-noise image. For any voxel over 6, a full spectrum and contour plot from the continuum subtracted cube was created to visually distinguish potential real signals from those likely associated imaging artefacts. A detected emission peak in the survey was found to meet these criteria and was associated with a star. However, there were no known associated molecules at or around the frequency of the signal.

The Orion survey, although covering a similar size on the sky, was designed to cover a much larger frequency range so a more automated approach was developed. A full description of the survey details and statistics are explained in Section 5.4. However, I will provide the motivation for the methodology here.

Koribalski (2012a,b) explain the increasing need for automated methods to search large data sets for potential molecular and atomic emission. They also describe the benefit of some of the source-finding software available and utilised in molecular surveys. Much of the current software takes large amounts of time to setup, such as DUCHAMP (Whiting, 2012), as it allows for a large number of parameters to be set (Walsh et al., 2012) and does not require all of the sources to be unresolved. Although software like DUCHAMP is successfully utilised in high resolution surveys, the surveys from the MWA are simplified because we would expect all signals to reside in a single frequency channel and the astro-

nomical sources to be unresolved, although they don't have to be in order for the source finding to work. Therefore, we utilised the source finding software AEGEAN version 2.0 (Hancock et al., 2018), to find signals in each continuum-subtracted channel image individually at a level of five times the noise or greater. AEGEAN offers the ability to utilise an input noise image, which was created in PYTHON, to represent the spectral RMS at each pixel position.

2.6.2 Spectra Creation and Analysis

Once signals of significance are located within the spectra, the frequency of the signal is compared to the frequencies of known rotational transitions from databases such as Cologne Database for Molecular Spectroscopy (CDMS; Müller et al. 2001), Spectral Line Atlas of Interstellar Molecules (SLAIM; Remijan et al. 2007), Jet Propulsion Laboratory (JPL; Pickett et al. 1998), and Top Model (Carvajal et al., 2010). These databases provide a mix of essential information regarding the quantum numbers, rotational states, line strengths; all of which are critical in spectral line identification (Herbst and van Dishoeck, 2009).

For observation taken at greater than 5 GHz, many of these catalogues are virtual-observatory compliant so software like CASSIS⁶ can be used to create artificial spectra and compare with observed spectra for molecular identification, especially in regions of overlapping transitions. However, when importing a FITS file into CASSIS from the MWA, the frequency units were incorrect, even when the FITS header information was correctly formatted. Also, a search on the Einstein coefficients and line strengths failed, as they are orders of magnitude different for those transitions at high observational frequencies. Therefore, all spectral analysis was completed with custom built software. See Section 2.8 for the gitub repositories where the PYTHON scripts used in spectra creation are stored.

2.6.3 Data Visualisation

Across many disciplines of science, it is important to be able to visualise the data. For the surveys completed with the MWA, most of the initial visualisation used KARMA-KVIS (Gooch, 1996). KVIS is a multi-wavelength imaging tool that works with spectral data cubes in multiple formats. By viewing the data in KVIS, an initial check of the image quality and spectral smoothness could be easily assessed to determine if the processing, in particular the continuum subtraction, worked

⁶CASSIS has been developed by IRAP-UPS/CNRS (<http://cassis.irap.omp.eu>)

as expected. After the AEGEAN catalog of sources was created, a selection of potential sources were also viewed in KVIS to assess if the input parameters in AEGEAN were stringent enough to find real sources.

To compare the continuum source catalog created by AEGEAN for the Orion and Galactic Centre surveys with GLEAM or MRC catalogs of source, TOPCAT (Taylor, 2005) was used to visualise the ionospheric effects and distribution of flux density differences. TOPCAT is an interactive graphical viewer, and although it has many functions, was used to compare two catalogues, used input calculations to determine the variance in source position and flux density values, and plot the results. However, the actual cross matching completed during the data processing used STILTS (Taylor, 2006), the command-line version of the same tool used for processing tabular data.

For the survey of Orion, where multiple detections were made, the catalog of potential molecular signals were overlaid onto an optical and infrared images using ALADIN (Boch and Fernique, 2014; Bonnarel et al., 2000). Overlaying the position of the potential detection over the image from the Two Micron All Sky Survey (2MASS; Skrutskie et al. 2006) allowed for easy identification of possible near-infrared counterparts for the detections. This also provided a view of the distribution of potential detections on the sky to determine if there were regions of stronger activity.

2.7 Confirmation of Sources

As the potential detections listed within Chapters 4–6 of this thesis are of low significance (5 to 6σ), a series of evaluations on the data and data quality were completed. The following sections describe the testing completed to provide the authors confidence that the signals are astronomically based and not RFI or image artefacts. To start, we imaged each potential detection and looked to see if the contour plot on the image plane is roughly beam shape. As we would expect all sources, given the size of the synthesised beam of 3.2 arc min, to be unresolved in these surveys this is a reasonable expectation.

2.7.1 Gaussian Statistics

In Chapter 4–6 contained within this thesis, we use Gaussian statistics to determine the significance of the detections. The data were scrutinised in a variety of ways including creating histograms in PYTHON and in MIRIAD to determine the

noise characteristics of the images. As shown in Figure 2.11 the noise properties around each source followed Gaussian behaviour as determined by the inverted parabola when plotting the log of the counts on the y-axis versus the pixel values on the x-axis.

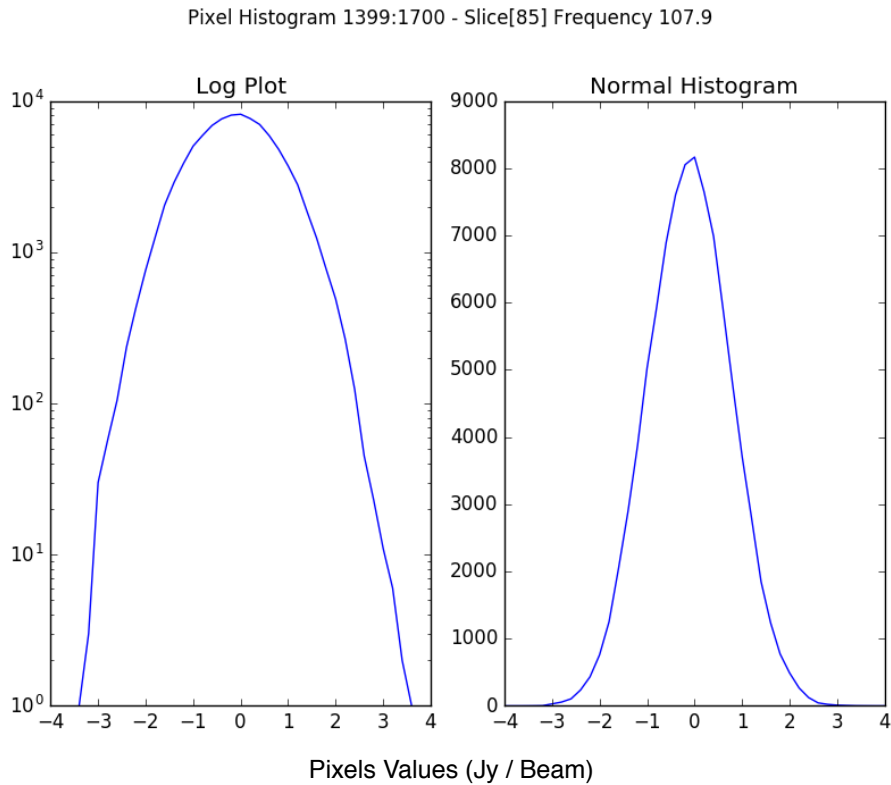


Figure 2.11: Histogram of pixel values near one of the tentative detections from the Orion Survey region. This is an example but histograms were created near each potential detection to look for abnormalities caused by RFI. The y-axis is the pixel counts and the x-axis is the pixel values in Jy Beam^{-1} . The shape of the inverse parabola on the right hand plot suggests the noise is Gaussian.

Another way to evaluate this was to create a signal-to-noise data cube by taking a “RMS” image representing the standard deviation across the frequency band at each pixel position and dividing by each channel in the continuum-subtracted spectral line cube. The signal-to-noise ratio cube had (as expected) a standard deviation of 1.00, as the spatial variation in RMS was divided out. However, the RMS does vary as a function of channel as shown in Figure 2.12, so when the histogram of the whole cube is plotted, the distribution is close to Gaussian, but with an excess of high and low points (above the drawn inverted parabola on Figure 2.12).

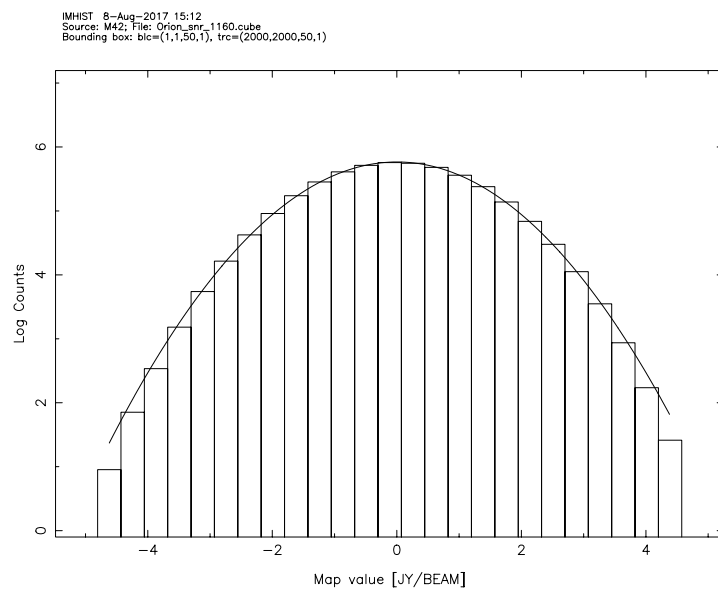
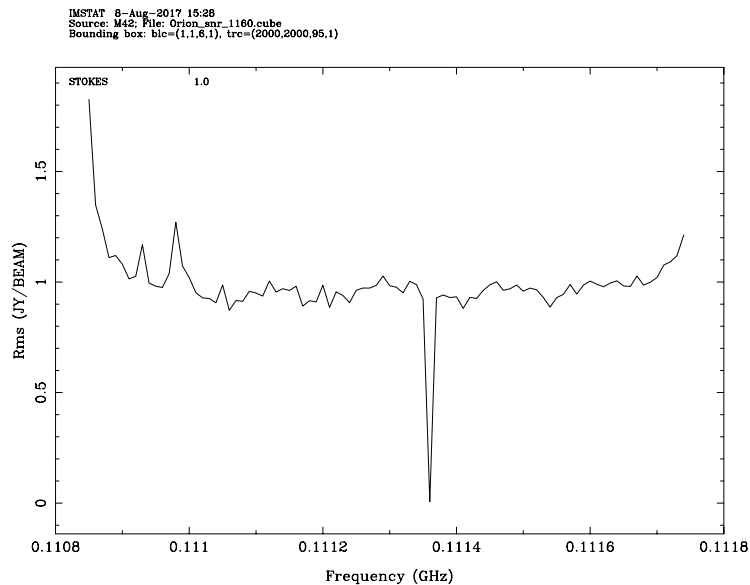


Figure 2.12: An example signal-to-noise spectra near, but off, a potential detections on the left and the Gaussian plot from the survey's sky on the right. The central channel is flagged in the continuum-subtracted data cube due to instrumental effects, so the signal-to-noise is zero. (Image Credit: Paul A. Jones)

So, in order to check whether the "5 sigma" peaks are real, or just the number expected for noise, the sigma from that channel is used. The images created are 2000 x 2000 pixels, so there is up to order $\approx 10^6$ independent points per plane (within a factor order unity, depending on how many pixels across a beam is) so this is getting close to expecting order one random noise peak per plane. As the number of random events at N sigma is a very steep function of N, even if there is Gaussian statistics, a small underestimate of sigma for that plane may give random peaks..

2.7.2 Splitting the Data Cubes

Splitting of data in different ways can help confirm that the detections are real as astronomical signals coming from photon release of molecules or atoms should be stable over the time frames of these observations. The Galactic Centre observations were completed in two epochs; for two hours in 2014 and two hours in 2016. To confirm the detections, the data were split between these two epochs and contour images were created for each epoch and the total combined data using the same contour values.

As show in Figure 2.13, the signals were found to be persistent in the two datasets. The data from 2016 had better sensitivity as more of the telescope tiles were functioning so a direct comparison of the signal strength could not be made. However, by comparing a ratio of the image RMS and signal strength, the detections were determined to be similar. The nitric oxide tentative detection at 107.36 from Chapter 4 is displayed in Figure 2.13, but this was completed for each detection for the Galactic Centre work. A similar test could have been done by splitting the polarisations, however, since the full polarisations were not imaged this could not be completed on this dataset.

The Orion data was taken in a continuous three hour block on a single night. Based on the sensitivity of the tentative detections, this type of analysis was not completed as it was deemed that the sensitivity in 1.5 hours would not produce significant signals.

2.7.3 Stacking of Spectral Signals

A way of increasing the sensitivity of weak astronomical signals is through stacking. Stacking can be done spatially over larger regions of the sky or spectrally across a number of frequency bins (channels). To see if there were detectable sig-

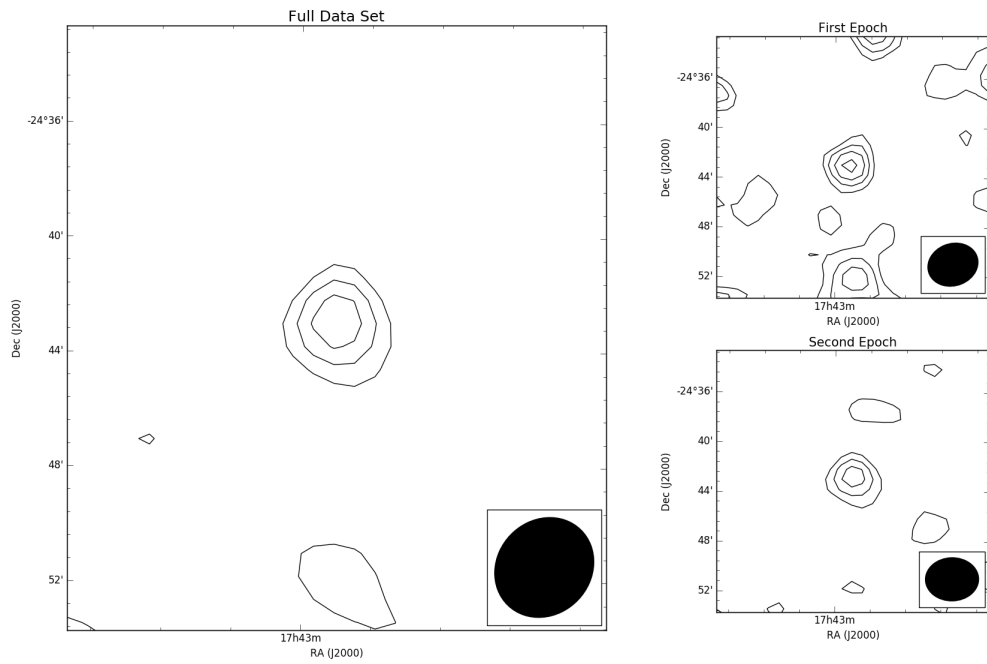


Figure 2.13: Example of one of the nitric oxide tentative detections at 107.36 from Chapter 4 (Galactic Plane survey) split across the two observation epochs of 2014 and 2016. The large central image is the published detections and the top right image is from observations taken in 2014 and the bottom right is from observations taken in 2016. All three images are created by setting the contours at the same values and imaging using the same noise threshold. A similar image was made for each of the tentative NO detections and the tentative SH detection from the Galactic Plane survey.

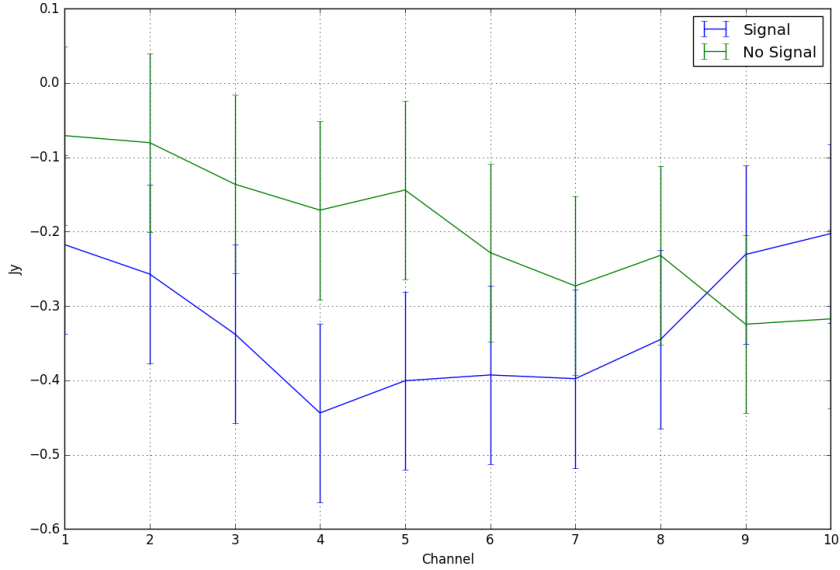


Figure 2.14: Average CRRLs C367–399 α lines in blue with the error bars of the local rms. The spectra in green represents a similarly stacked set of channels to show the background signal. The y-axis is the flux limits of a stacked region of 100 by 100 pixels over the Galactic Centre.

nals for carbon recombination lines (CRRLs) in the Galactic Plane, the data set from the published work of Tremblay et al. (2017) molecular line survey consisting of four hours of integrated time at 103 to 133 MHz is used.

Only 78% of the bandpass was imaged due to severe aliasing on the edges of each coarse channel resulting in 2400 ($\times 10$ kHz) fine frequency channels being imaged. Within the observed band there are 32 known carbon alpha lines (C_α) with eight of the lines flagged out of the observations; leaving 23 carbon recombination lines for this analysis.

The data used in this analysis has a spectral resolution of 10kHz which is equivalent to a velocity resolution of 26 km s^{-1} at 114 MHz. An average spectra was created of C367–399 α by stacking the channels around the rest frequency of each line.

The stacked data shown in Figure 2.14 did not yield a result significantly above the background. This was true even when a region of 100×100 pixel region around the Galactic Centre was stacked. As discussed in Chapter 6, this can be due to the nulling of the recombination lines around 100–150 MHz.

Similarly, stacking was done utilising the Orion survey data integrating across

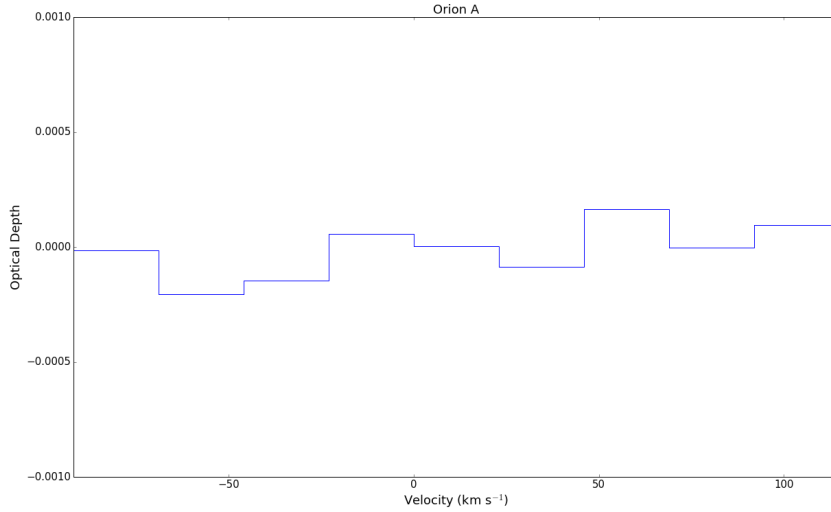


Figure 2.15: Average CRRLs C367–399 α lines in blue. The y-axis is the optical depth when compared to the Continuum reported in GLEAM.

the Orion Kleinmann–Low (Orion KL) Nebula. As shown in Figure 2.15, even at a low optical depth no lines were observed in the stacked spectra. To determine the optical depth, the continuum flux was used from GLEAM, as published in Tremblay et al. (2018) (Chapter 6). After private communications with the RRL team at LOFAR, it is expected that this is due to the nulling that happens between the frequency range of 100–150 MHz in the dense molecular cloud. As discussed in Chapter 6, the RRL emission mechanism changes between collisionally pumped to radiatively pumped between 100–150 MHz. The exact frequencies this happens at changes depending on the density of the environment and between the two the RRL transitions become non-detectable.

2.8 Spectral Properties of the MWA

The identification of spectral lines with the MWA requires a deep understanding of the spectral characteristics of the telescope. The system design is explained in Lonsdale et al. (2009) and Tingay et al. (2013) and a simplified system diagram is shown in Figure 2.16. The data are channelised through a two stage polyphase filter bank (PFB) where the first stage receives data from 16 receiver nodes carrying 24 by 1.28 MHz signals from the 128 MWA tiles. The second stage PFB boards execute a 128-channel operation on each of these streams, yielding

a spectral resolution of 10 kHz.

Through documents from the engineering team (i.e. Thiagaraj et al. 2015), the MWA is known to suffer from aliasing in the fine channels close to the edges of each of the 1.28 MHz coarse channels (Levine, A. internal communication). The centre 10 kHz fine channel from each coarse channel is also flagged out of each observation, as it represents a telescope introduced signal (Thiagaraj et al., 2015).

The simulation work on the two-stage polyphase filter bands used in the MWA, completed by Levine, A. (internal communication) suggested that up to 30% of the fine channels in each coarse channel would be affected by aliasing which would increase image noise and possibly mimic real sources. He also showed that the first 20 and last 20 fine channels have increased RMS when a sine wave signal is injected into the simulation. A spectrum of one full coarse channel from a Galactic Centre observation shown in Figure 2.17, shows that even after some channels were flagged in the telescope data pipeline (Wu et al., 2013) the fine channels are still affected.

As a test of the impact on the data analysis a full cube with continuum subtraction was made and is shown in Figure 2.18. The image on the left is a continuum image from a single fine channel and the centre image is the continuum subtracted image of the same fine channel. However, when continuum subtraction is completed, the cube containing all the fine channels of the coarse channels shows residual continuum, as shown in the RMS map on the left side of Figure 2.18.

Therefore, the first 14 channels and last 14 channels from each coarse channel were not imaged. By avoiding these channels in the spectral line analysis pipeline, after continuum subtraction a clean spectra could be created as shown in Figure 2.19.

2.9 Python Code

All code, written by me, for use in these surveys can be found in the following git repositories:

- https://github.com/Chenoachem/Spectra_Code.git
- https://github.com/Chenoachem/Cube_Code.git
- https://github.com/Chenoachem/Quality_Code.git
- https://github.com/Chenoachem/Recombination_Lines.git

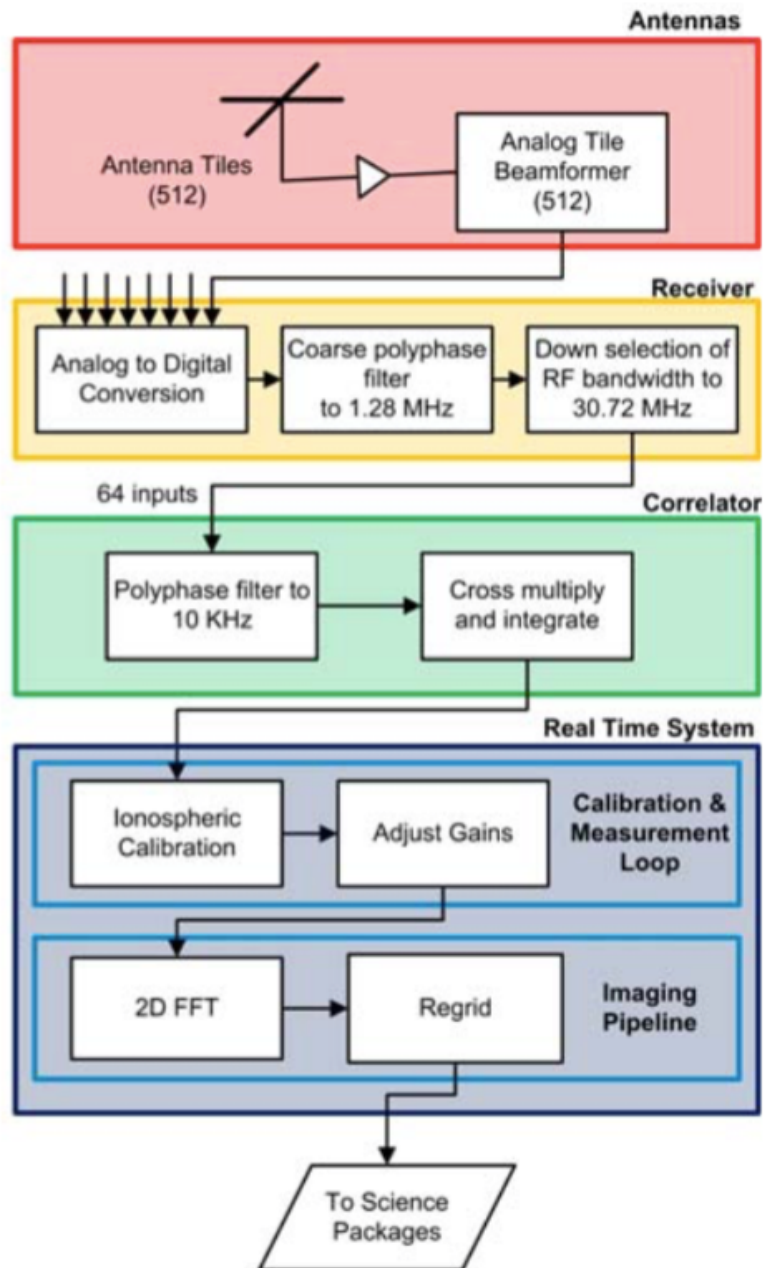


Figure 2.16: Diagram from Figure 1 of Lonsdale et al. (2009) representing the MWA system design from Phase I of the MWA. This thesis did not use the Real Time data processing pipeline shown in this diagram as the data processing required for spectral line work needed additional considerations.

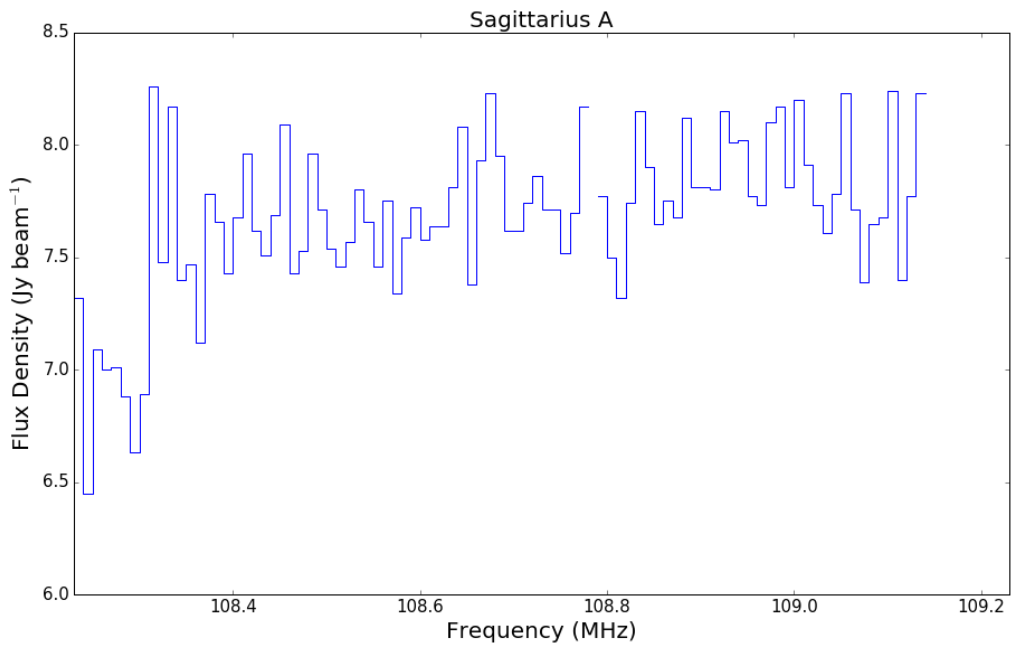


Figure 2.17: The full spectrum of one coarse channel with the MWA before continuum subtraction. The first 10 channels are a different flux density level and show the flagging completed at the correlator did not fully remove the fine channels affected by aliasing.

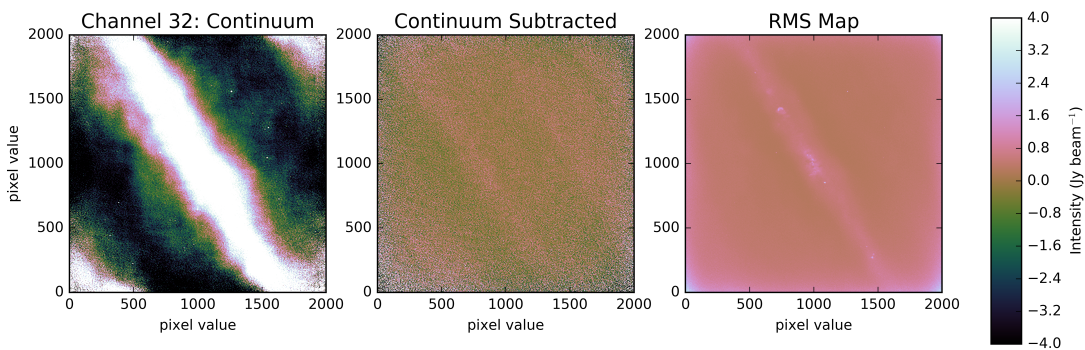


Figure 2.18: The images show the continuum image for a single channel (left), the continuum subtracted image for a single channel (middle), and the RMS map created from the continuum subtracted data cube. This shows that by leaving in the edge channels there is a lot of residual noise in the final subtracted cube that makes identification of new lines difficult.

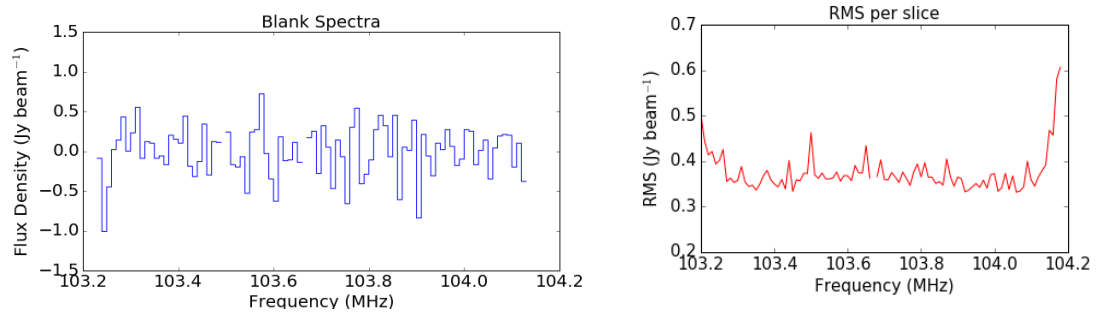


Figure 2.19: The left image is an example spectrum from one coarse channel after the edge channels and continuum were removed. The mean RMS is $0.29 \text{ Jy beam}^{-1}$. The right image is a plot of the RMS in the centre of each image within one coarse channel. This shows that the noise towards the edges still is higher in some coarse channels even after the extra channels were removed.

Chapter 3

The High Mass Star Forming Region G13.384+0.064: An Isolated Star?

This work, as written, was published by:

Tremblay, C. D, Walsh, A., Longmore, S., Urquhart, J., Konig C., “A search for High-Mass Stars Forming in Isolation using CORNISH & ATLASGAL” *Publications of the Astronomical Society of Australia*, Cambridge University Press, 2015, P 32, 47

Although this Chapter represents a published paper, edits have been made in response to the thesis examiners. Therefore, it is not an exact replica of the original publication. Every effort is made to maintain the integrity of this work as required by the copyright statements in the appendix of this thesis.

3.1 Abstract

Theoretical models of high-mass star formation lie between two extreme scenarios. At one extreme, all the mass comes from an initially gravitationally-bound core. At the other extreme, the majority of the mass comes from cluster scale gas, which lies far outside the initial core boundary. One way to unambiguously show high-mass stars can assemble their gas through the former route would be to find a high-mass star forming in isolation. Making use of recently available CORNISH and ATLASGAL Galactic plane survey data, we develop sample selection criteria to try and find such an object. From an initial list of approximately 200 sources, we identify the high-mass star forming region G13.384+0.064 as the

most promising candidate. The region contains a strong radio continuum source, that is powered by an early B-type star. The bolometric luminosity, derived from infrared measurements, is consistent with this. However, sub-millimetre continuum emission, measured in ATLASGAL, as well as dense gas tracers, such as $\text{HCO}^+(3-2)$ and $\text{N}_2\text{H}^+(3-2)$ indicate that there is less than $\sim 100 M_\odot$ of material surrounding this star. We conclude that this region is indeed a promising candidate for a high-mass star forming in isolation, but that deeper near-IR observations are required to put a stronger constraint on the upper mass limit of young, lower mass stars in the region. Finally, we discuss the challenges facing future studies in proving a given high-mass star is forming in isolation.

3.2 Introduction

High mass stars – O or early B type star of sufficient mass to produce a Type II supernova (Zinnecker and Yorke, 2007) or $>8 M_\odot$ (Miettinen, 2012) – dominate the energy cycles and chemical enrichment of galaxies. However, understanding the formation of high-mass stars remains a challenge, and several different theoretical formation scenarios have been proposed (Zinnecker and Yorke, 2007; Tan et al., 2014). The general observational phases (i.e. formation of cold dense cloud, gravitational collapse of a hot core, accretion, and formation of ultracompact HII regions) are typically agreed upon, but the dominant physical processes and their relevant time scales are still under debate. The problems associated with our understanding are that it is difficult to observe the early stages of formation due to high dust extinction, the theoretical problem is complex and high-mass stars are seldom, if ever, formed in isolation (Zinnecker and Yorke, 2007).

Over the last few decades, high-mass star formation theories have been discussed in the context of two extreme scenarios: that of the turbulent core (McKee and Tan, 2003) and the competitive accretion (Bonnell et al., 2001; Bonnell and Bate, 2006) scenarios. In the former, all the mass comes from an initially gravitationally-bound core. In the latter, the majority of the mass comes from cluster scale gas that is far outside the initial core boundary. Early debate suggested that stellar collisions (Bonnell et al., 1998) could be a potential creation mechanism, but this has largely been discounted due to the extremely high stellar densities required¹. More recent theoretical and simulation work, adding more

¹Although see (Izumi et al., 2014) who suggest a star system in the extreme outer galaxy (>18 kpc) may have been formed by large scale collision.

physics (e.g. radiation pressure, ionisation) and overcoming previous limitations in numerical methods, have found that increasing the feedback, initial density fluctuations and turbulence leads to an increase in the fraction of the final stellar mass which comes directly from an initial gravitationally-bound core (Krumholz et al., 2007; Krumholz and Thompson, 2012; Hennebelle et al., 2011; Commerçon et al., 2011; Myers et al., 2013; Bonnell et al., 2004; Peters et al., 2010). The apparent dichotomy between the competitive and core accretion models seems to be less extreme, or at least the reasons for the dichotomy are now better understood.

Nevertheless, understanding whether the two extreme formation scenarios are viable routes for high-mass stars to assemble their mass has important consequences for the host galaxy. If high-mass stars can only form in the presence of an attendant cluster, the stellar initial mass function (IMF) will be sampled very differently than if high-mass stars can (albeit rarely) form in isolation (Bastian et al., 2010). When averaged on galactic scales, this can make a dramatic difference in the number of (very) high-mass stars, and hence the level of feedback, chemical enrichment etc.

Given the wider importance of how the IMF is sampled, many observational studies have tried to find evidence of high-mass stars forming in isolation (Bressert et al., 2012; Tout et al., 1997; Weidner et al., 2009; Weidner and Kroupa, 2005; Parker and Goodwin, 2007; de Wit et al., 2005; Schilbach and Röser, 2008). These previous searches have primarily focused on optical and infrared data to find young high-mass stars with no lower mass young stars around them. However, as these high-mass stars must already have cleared their natal gas cloud in order to be optically visible, it is very difficult to determine if they *formed* at their present location, as opposed to having been ejected from their parent stellar nursery of lower mass stars.

In this paper, we try a different approach, aiming to find very young high-mass stars while they are still embedded in their natal gas cloud. While extinction makes it impossible to find these objects in the optical, near-IR and mid-IR, their prodigious luminosity and Lyman continuum flux means they should be conspicuous at far-IR wavelengths and have bright cm-continuum, free-free emission. Even in the most optimistic scenarios, high-mass stars forming in isolation are expected to be very rare, requiring large-area surveys to identify candidates. Thanks to an enormous effort from the Galactic observational community, Galactic plane surveys now exist across much of the electromagnetic spectrum at sufficient sensitivity and resolution to identify the majority of young high-mass star formation regions in the Galaxy. With the data now in hand, we aim to use a simple selec-

tion criterion to pick out the best candidates for young, high-mass stars forming in isolation.

3.3 Sample Selection

For this first attempt to try and find examples of high-mass stars forming in isolation, we used a series of data summarised by Urquhart et al. (2013) for ATLASGAL (Schuller et al., 2009) and CORNISH (Purcell et al., 2013; Urquhart et al., 2013) noted that targeted surveys of compact and ultra-compact (UC) HII regions identified by infrared colours can be contaminated with intermediate mass young stellar objects (YSOs) and planetary nebulae (PNe). However, by incorporating radio astronomy data mixed into the identification process, this is no longer a concern. Intermediate mass stars do not show radio continuum emission, so would be eliminated in the cross match. Planetary nebulae are not usually associated with dust that is bright enough to be detected by ATLASGAL².

We use their selection criteria to select approximately 200 bona fide YSOs, associated with compact and UC HII regions. Figure 3.1 compares the clump gas mass and Lyman continuum flux of these regions. The source G13.384+0.064 stands out in Figure 3.1 as having a very low gas mass for its Lyman continuum flux. This Figure is closely matched to the upper panel from Figure 26 in Urquhart et al. (2013). The aim of this paper is to better constrain the luminosity, mass and Lyman photon flux based on a thorough literature search of the region and using GLIMPSE (Churchwell et al., 2009; Benjamin et al., 2003) and MIPS GAL (Carey et al., 2009) data to test for evidence of a surrounding cluster. We selected this as the most promising candidate in our initial sample for a high-mass star forming in isolation. Below we describe our efforts to use data in the literature to determine whether or not we can confirm or rule out this status.

3.4 Results

3.4.1 Infrared & Radio Observation

The GLIMPSE (Churchwell et al., 2009; Benjamin et al., 2003) and MIPS GAL (Carey et al., 2009) images of the star forming region G13.384+0.064 show a

²There were some instances noted where PNe were identified in ATLASGAL by their mid-infrared emission. However, they were removed from the source list and monte-carlo simulations agreed with their identified numbers.

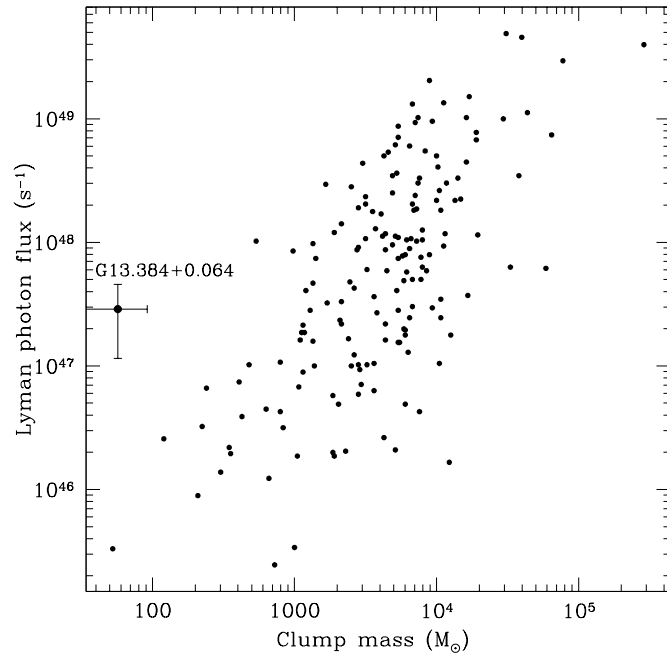


Figure 3.1: Plot of clump mass versus Lyman photon flux for a series of ATLAS-GAL and CORNISH sources, similar to the upper panel of Figure 26 in Urquhart et al. (2013). When the clump mass is plotted against the bolometric luminosity, the source at G13.384+0.064 does not stand out as different compared to other star forming regions. This discrepancy is investigated in this paper. The error bars represent the best available data reported in this paper.

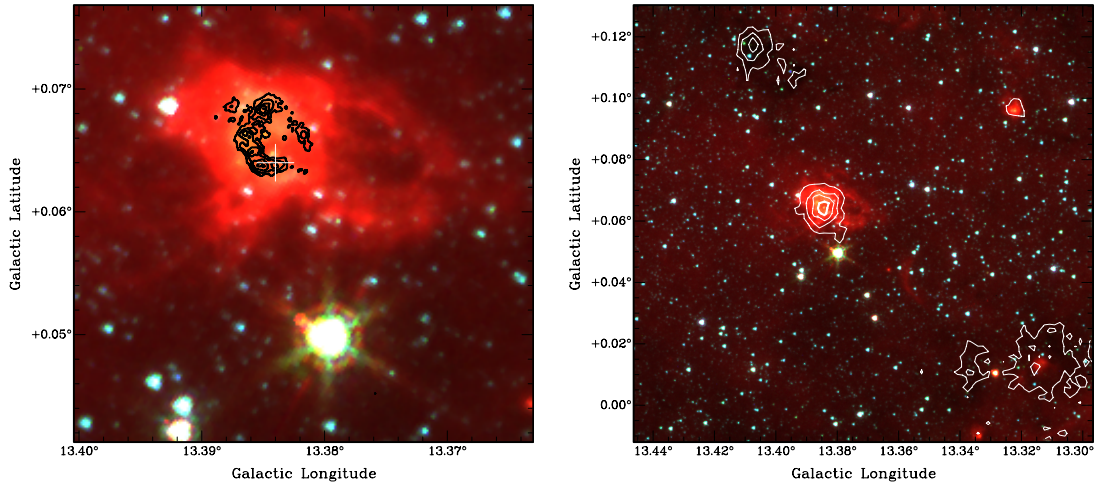


Figure 3.2: GLIMPSE 3 colour image with blue as $3.6 \mu m$, green as $4.5 \mu m$ and red as $8.0 \mu m$. Contour image on the left shows CORNISH 5 GHz radio continuum emission from 2 mJy/beam to 10 mJy/beam in steps of 2 mJy/beam. The white cross on the image on the left represents the centre of the ATLASGAL contours and the image on the right shows the GLIMPSE 3 colour image with ATLASGAL contours. The contour levels are from 0.25 Jy/beam and increase in steps of 0.25 Jy/beam up to 1.0 Jy/beam. We identify an evolved star, seen at G13.380+0.050 and discussed in section 3.8 that is unrelated to the source.

bright core surrounded by gas with an empty area or bubble between the two (Figure 3.2). The bubbles are similar to those seen in other high-mass star forming regions and they are likely to be created by stellar feedback (e.g. Weaver et al. 1977). The CORNISH radio continuum image has sufficient resolution to show an extended shell like source in the centre of the region (Figure 3.2). The region inside the radio emission also contains low levels of diffuse emission in the UKIRT Infrared Deep Sky Survey (UKIDSS) K band images, as shown in Figure 3.4. It is likely this emission corresponds to Brackett Gamma ($Br\gamma$) emission associated with the HII region, as the morphology of the diffuse K band emission resembles the radio continuum contours Beck et al. (2010).

We used data from UKIDSS (Lawrence et al., 2007), 2MASS (Skrutskie et al., 2006) and GLIMPSE (Churchwell et al., 2009; Benjamin et al., 2003) to investigate the near and mid-IR source populations surrounding G13.384+0.064 and search for an embedded young stellar population. First, we downloaded all the sources in the UKIDSS point source catalogue within a 10 arc minute radius of G13.384+0.064 and looked for an increase in the surface density of infrared ob-

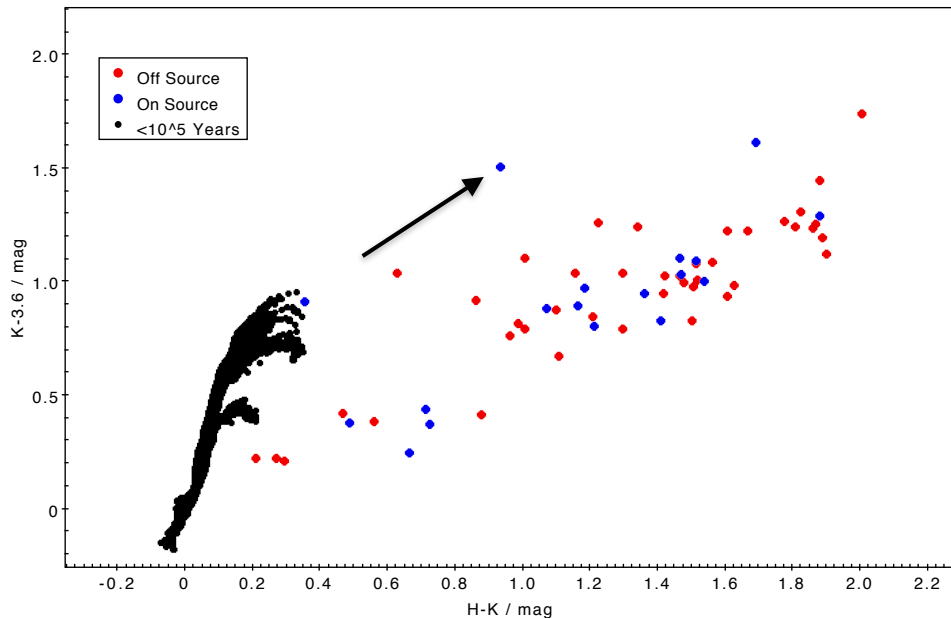


Figure 3.3: Colour-Colour diagram plotting sources 30 arc second around G13.384+0.064 (on source;blue) and 30 arc seconds around G13.36+0.075 (off source;red). The IMF curve is data representing a cluster $<10^5$ years old from Lejeune and Schaerer (2001). The vector represents the extinction vector plotted as per Nishiyama et al. (2009). There are no clear signs there are a cluster of main sequence stars.

jects towards the source. There is no statistical difference in the surface density of infrared sources at the location of G13.384+0.064 compared to similar regions close to, but offset from the ATLASGAL contours. We conclude there is no evidence of a cluster based on source density.

The 3-colour diagram of UKIDSS data, Figure 3.4, shows some red stars within the contours from CORNISH. To determine if these are field stars behind the dust cloud or if they are within the cloud, we use the UKIDSS, 2MASS (for saturated UKIDSS sources) and GLIMPSE photometry data to plot a colour-colour diagram (CCD) and colour-magnitude diagrams (CMDs) of the infrared sources on and off G13.384+0.064. Figure 3.3 shows a representative colour-colour diagram using H and K-band data from UKIDSS (Lawrence et al., 2007) and 2MASS (Skrutskie et al., 2006) and L ($3.6\ \mu\text{m}$) band data from GLIMPSE (Churchwell et al., 2009; Benjamin et al., 2003) for a 30 arc second radius around the source at G13.384+0.064 (matching with the contours from ATLASGAL shown in Figure 2) and off the source at G13.36+0.075, as shown in Figure 3.3. The reddening

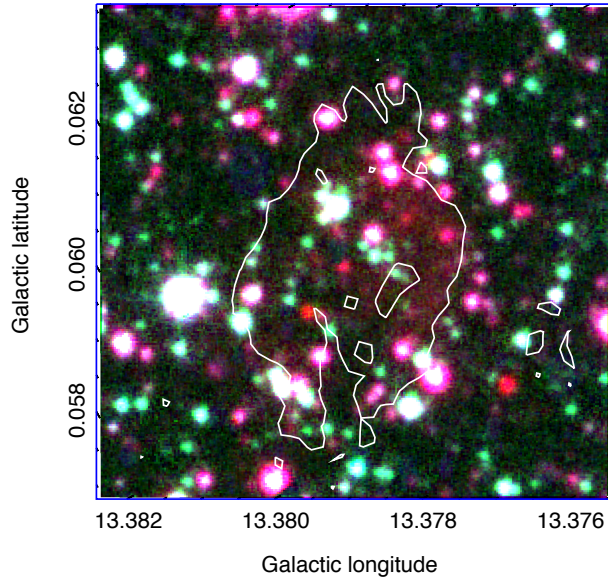


Figure 3.4: Three-colour image with red at K band, green at H band and blue at J band of UKIDSS data overlaid with contours from CORNISH 5 GHz radio continuum emission with contours at 0.19 and 0.32 Jy/beam.

vector was determined from Nishiyama et al. (2009) and the IMF data was plotted from Lejeune and Schaerer (2001) for a cluster less than 10^5 years old. While there are clearly reddened sources in the field, the CCD does not show an obvious excess of intrinsically red stars towards G13.384+0.064. The reddening value for each star was measured and a KS test was completed to see if the two populations of data (on and off source) were similar. The results suggest that two populations could not be differentiated, making the red stars (from K band UKIDSS data) in Figure 3.4 likely to be field stars and not representative of a cluster. The only possible exceptions are the two blue dots at $[K] - [3.6] \sim 1.5$, which are potential candidates for YSOs of interest. However, without higher resolution data it is not possible to determine if these are simply highly extinguished background stars or intrinsically red YSOs. Regardless of the nature of these two sources, the IR information from these 3 surveys data show no evidence of a sizeable distributed population of YSOs in the region.

We also note that these data may not be sensitive enough to detect stars deeply embedded into the natal cloud. As described in Feldt et al. (1998), it might be possible to hide a cluster of smaller stars. For further discussion see §4.2.

3.4.2 Distance

The near kinematic distance of 1.9 kpc and far distance of 14.1 kpc was estimated by Schlingman et al. (2011) using $\text{HCO}^+(3-2)$ and $\text{N}_2\text{H}^+(3-2)$ observed by the Heinrich Hertz Submillimeter Telescope at 1.1 mm. The velocity observed for these two molecules are 15.1 km s^{-1} for HCO^+ and 14.1 km s^{-1} for N_2H^+ . Lockman (1989) reported 3 cm radio recombination line observations completed using the Greenbank telescope with an observed V_{LSR} of $18.3 \pm 1.8 \text{ km s}^{-1}$. However, Lockman (1989) commented that the FWHM line for this source was so broad that the results could not be easily interpreted.

H_2CO was observed at 4.83 GHz, using the Nanshan station (Du et al., 2011). The results for the source G13.384 +0.064 show two molecular clouds. The first cloud has a velocity of $10.71 \pm 0.40 \text{ km s}^{-1}$ and the second has a velocity of $51.34 \pm 0.28 \text{ km s}^{-1}$. The velocity of the first cloud agrees well with the HCO^+ , N_2H^+ and radio recombination observations. Data from the James Clark Maxwell Telescope (JCMT) reported three velocity components for $^{12}\text{CO}(J=3-2)$ at 10, 15 and 50 km s^{-1} (Dempsey et al., 2013). It is likely, then, that the star formation is associated with the gas at 15 km s^{-1} , rather than the 50 km s^{-1} , since the gas at 50 km s^{-1} only appears in the relatively low density gas tracers of H_2CO and ^{12}CO and the star formation is most likely associated with the denser gas.

The distance to this region has been determined by Schlingman et al. (2011) from the radial velocity and the Brand and Blitz (1993) Galactic rotation curve. An issue that affects all sources located inside the solar circle is that there are two kinematic solutions spaced at equal distances from the tangent position. These distance ambiguities can be resolved using H I data by comparing the velocity of absorption dips seen in the spectra with the source velocity as measured from thermally excited molecular lines. The two most commonly used methods are H I self-absorption (HISA; e.g., Jackson et al. (2002)) and H I emission-absorption (HIEA; e.g., Kolpak et al. 2003; Urquhart et al. 2012).

In Figure 3.5 we present the HISA profile (continuum subtracted) and HIEA (continuum included) H I profiles seen towards G13.384+0.064 and its associated H II region. The source velocity is approximately coincident with the velocity of a broad absorption feature seen in the H I profile; this is consistent with the source being located at the near distance due to the fact that there is too much intervening warm H I gas at the same velocity as the source for any absorption to be present for sources located at the far distance.

The HIEA method is based on the principle that for any strong emission

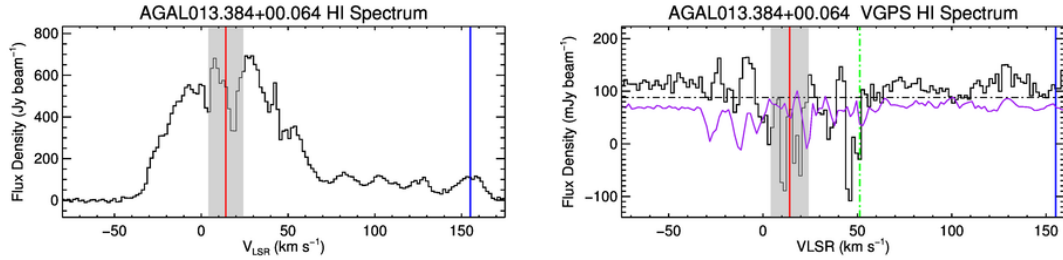


Figure 3.5: The HI continuum subtracted (left) and HI continuum (right) profiles seen towards G13.384+0.064 and its associated HII. In both of these panels, the source and tangent velocities are indicated by the red and blue vertical lines and the grey region shows a region 10 km s^{-1} either side of the source velocity. In the lower panel the green line indicates the maximum velocity found of the absorption features and the magenta line shows the 5σ rms noise for the HI data (see Urquhart et al. 2012 for more details). The presence of an absorption feature at a similar velocity as the source in the upper panel and the lack of absorption features up to the tangent velocity in the lower panel both strongly support and near kinematic distance for this source.

source located at the far distance we would expect to observe absorption features at all velocities up to and including the tangent velocity. This is due to the high density of cold HI clouds along any line of sight through the inner Galaxy. The lack of any absorption features between 50 and 150 km s^{-1} would suggest that the source is again located at the near distance. The absorption seen at 50 km s^{-1} may suggest that the source velocity may be incorrectly assigned to this source and may in fact be associated with another object within the line of sight. However, the lack of any emission from high-density molecular tracers (HCO^+ and N_2H^+) would rule out this possibility. Both methods therefore suggest a near distance is more likely. For further discussion see §3.5.1.

The uncertainties in the near kinematic distance, allowing for $\pm 10 \text{ km s}^{-1}$ when the streaming motions and peculiar velocities are considered, is $\pm 0.8 \text{ kpc}$.

3.4.3 Dust Derived Mass

The near distance of $1.9 \pm 0.8 \text{ kpc}$ was used by Miettinen (2012) and Urquhart et al. (2013) to calculate the mass of the cloud surrounding the star as being 65 ± 47 and $105 \pm 73 M_{\odot}$, respectively. Urquhart et al. (2013) used the integrated flux measured in ATLASGAL (Contreras et al., 2013) at $870 \mu\text{m}$ and a temperature of 20 K . Miettinen (2012) used $870 \mu\text{m}$ observations from LABOCA and assumed

a temperature of 35 K. Since both reported masses are from the same instrument the differences are from the different temperatures and calibration errors. By using the Hildebrand (1983) equation and making the same assumption as stated in equation 1 of Urquhart et al. (2013), we determine the cloud mass to a greater accuracy from the derived values specific to this source.

$$\frac{M_{clump}}{M_{\odot}} = \left(\frac{D}{kpc}\right)^2 \left(\frac{S_{\nu}}{mJy}\right) \frac{R}{B_{\nu}(T_{dust})\kappa_{\nu}} \quad (3.1)$$

where S_{ν} is the integrated flux at $870 \mu\text{m}$ of 603.94 mJy (Schuller et al., 2009), D is the heliocentric distance to the source ($1.9 \pm 0.8 \text{ kpc}$; §3.2), R is the dust-to-gas mass ratio (assumed to be 100), B_{ν} is the Planck function for a dust temperature T_{dust} (calculated in §3.4 to be $33.7 \pm 1.5 \text{ K}$) and κ_{ν} is the dust absorption coefficient taken as $1.85 \text{ cm}^2 \text{ g}^{-1}$ (as used by Urquhart et al. 2013). This yields a value for the clump mass around the star as $57 \pm 35 M_{\odot}$.

3.4.4 Luminosity

An estimation of the luminosity was determined from the IRAS fluxes (Neugebauer et al., 1984) using the equation initially published by Casoli et al. (1986) but using the same assumptions as equation 3 of Walsh et al. (1997).

$$F_{tot} = (f_{12}\delta\nu_{12} + f_{25}\delta\nu_{25} + f_{60}\delta\nu_{60} + f_{100}\delta\nu_{100})/0.61 \quad (3.2)$$

This yielded a value of $7.2 \times 10^3 L_{\odot}$. This value is similar to that reported by Miettinen (2012) of $7.4 \times 10^3 L_{\odot}$, which also uses the IRAS flux, but using the same assumptions as Casoli et al. (1986). The bolometric luminosity reported by Urquhart et al. (2013), calculated by scaling the MSX $21 \mu\text{m}$ flux, was $3.4 \times 10^3 L_{\odot}$ which is almost half the value calculated from the IRAS fluxes. We note that the luminosity values reported by Miettinen (2012), Urquhart et al. (2013) and contained in this work, all assume a distance of 1.9 kpc .

The IRAS measurements can be considered as a strong upper limit on the bolometric luminosity. The large IRAS beam encapsulates all emission and there is no loss of flux due to extended emission that is masked out with other observations employing nodding or jittering method, such as BOLOCAM or ATLASGAL.

A more accurate value of the bolometric luminosity is measured using two component fitting of the spectral energy distribution (SED). The integrated flux data was compiled from a combination of reported catalogues values ranging from $4 \mu\text{m}$ to 21 cm as well as measured values through aperture photometry from

the MSX (Price et al., 2001), Hi-GAL (Molinari et al., 2010) and ATLASGAL (Schuller et al., 2009) maps. A plot of the integrated fluxes versus wavelength shows a curve that peaks in the IR and is flat at radio wavelengths as shown in Figure 3.6. This curve is typical of the spectral energy distribution of an embedded forming high-mass star. The peak in the infrared emission is characteristic of the short wavelength stellar light being reprocessed to longer wavelengths by dust in the surrounding gas cloud, and the flat region is from free-free radio emission characteristic of an HII region.

The flux density from the MSX, Hi-GAL and ATLASGAL maps, F_{app} , was measured within an aperture radius of 35.7 arcseconds, corresponding to 3σ of a Gaussian fitted to the source and centred on the peak flux pixel position of the 250 μm image. The background flux density, F_{bg} , was obtained as the median pixel value from an annulus with $r_{inner}=47.6$ arcsec to $r_{outer}=59.5$ arcsec around the aperture. Subtracting the background flux density from the aperture flux density yields the background corrected source flux $F = F_{app} - F_{bg}$, reconstructing the SED in 10 bands from 8 μm to 870 μm . The errors of the flux densities are calculated by adding the absolute calibration uncertainty to the intrinsic measurement error in quadrature. We assume a measurement uncertainty of 20 per cent for all bands except for the 500 μm band, where we take into account the large pixel size of 15 arcseconds, hence assuming a measurement uncertainty of 50 per cent.

The SED was then fitted with a two-component model consisting of a greybody and blackbody. The greybody (i.e. a modified blackbody) models the cold dust envelope's emission, taking into account the wavelength dependence of the dust in the far-infrared to submm wavelength regime, whereas the blackbody models a hot, optically thick, deeply embedded component:

$$F_{\lambda}(T_d, \beta, \tau_{870}, T_h, \Omega_h) = F_{\lambda,hot}(T_h, \Omega_h) + F_{\lambda,dust}(T_d, \tau_{870}) \quad (3.3)$$

where $F_{\lambda,hot}$ is the hot component given by a blackbody scaled with the effective solid angle of the hot component and $F_{\lambda,dust}$ is the greybody emission from the dust envelope given by:

$$F_{\lambda,dust}(T_d, \tau_{870}) = \Omega_d \cdot B_{\lambda}(T_d) \cdot \left(1 - e^{-\tau_{870} \left(\frac{870\mu\text{m}}{\lambda}\right)^{\beta}}\right) \quad (3.4)$$

where Ω_d is the solid angle subtended by the source, $B_{\lambda}(T_d)$ the blackbody intensity at the dust temperature T_d , τ_{870} the dust optical depth at the reference wavelength of 870 μm and β the dust spectral index. We leave the dust spectral index β fixed to a value of 1.75, as computed as the mean value from the dust

opacities of Ossenkopf and Henning (1994) for the submm regime. As a result the dust temperature was determined to be 33.7 ± 1.5 K, which is consistent with the result used by Miettinen (2012) and a luminosity of $4.1(\pm 1.7) \times 10^3 L_{\odot}$ which is comparable to that reported by Urquhart et al. (2013) and is consistent with the upper limit from the IRAS measurements .

3.4.5 Lyman Continuum Flux

A number of observations of the region were completed in the radio using the National Radio Astronomy Observatory Very Large Array (VLA; Zoonematkermani et al. 1990; Becker et al. 1994; Garwood et al. 1988; Purcell et al. 2013), Nanshan Radio Telescope (Du et al., 2011), NRAO Green Bank (GBT; Lockman 1989), and the Effelsberg 100'm Telescope (Altenhoff et al., 1979). The integrated flux from two 6 cm observations, CORNISH (Purcell et al., 2013) and VLA 5 GHz Survey (Becker et al., 1994), were used to calculate the Lyman-continuum flux based on equation 1 and 3 in Kurtz et al. (1994), which represent modified equations presented by Mezger and Henderson (1967). Both of these surveys were completed using the NRAO VLA but CORNISH used B configuration, with a restoring beam of $1.5''$, which is not as sensitive to the extended emission as the survey done by Becker et al. (1994) which was conducted in C configuration and has a restoring beam of $4''$. Therefore, we expect the C-array data to recover more emission. The logarithm of the number of Lyman continuum photons per second ($\text{Log } N_c$) using the CORNISH integrated flux of 603 mJy and an assumed gas to dust ratio of 100, was determined to be $47.3 \text{ photon s}^{-1}$, as reported by Urquhart et al. (2013). Using the integrated flux from Becker et al. (1994) of 891.8 ± 20.9 mJy, $\text{Log } (N_c) = 47.3^{+0.2}_{-0.4} \text{ Log } (\text{photon s}^{-1})$.

The flux derived by Altenhoff et al. (1979) for the 100 m Effelsberg telescope at 4.9 GHz is 0.9 Jy, which is similar to the value reported by Becker et al. (1994) of 0.891 Jy. This suggests that all the extended emission was accounted for in the C configuration observations.

3.4.6 Star Type

The Lyman-continuum flux and bolometric luminosity are compared to Table 1 in Davies et al. (2011) to determine a mass of the star powering the HII region. The bolometric luminosity as determined by the SED fit is $\text{Log}(L_{\star}/L_{\odot}) = 3.61 \pm 0.14$. This relates to a star between $9-12 M_{\odot}$. The Log of the Lyman photon flux is

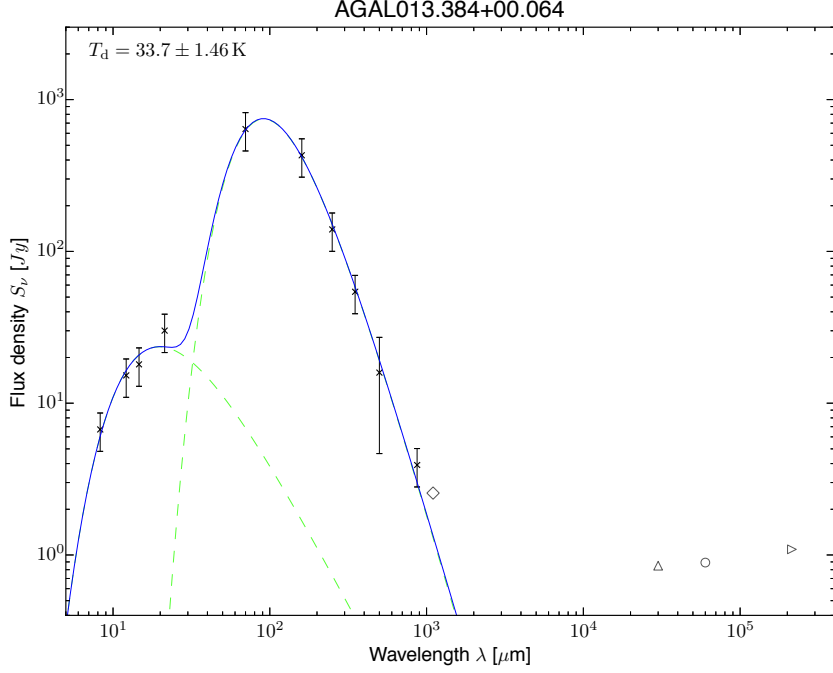


Figure 3.6: Spectral energy distribution created by data of different surveys plotted on a log scale. To obtain the dust temperature and luminosity, a two-component model was fitted to the flux densities measured through aperture photometry from the MSX (Price et al., 2001), Hi-GAL (Molinari et al., 2010) and ATLASGAL (Schuller et al., 2009) maps (blue fit). Additionally, catalogued data of the extended emission from the radio as well as some select infrared and sub-millimetre data. Open Triangle-MSX(Egan et al., 2003), Diamond-BOLOCAM (Schlingman et al., 2011), Triangle-Nobeyama (Handa et al., 1987), Open Circle-VLA 5 GHz (Becker et al., 1994), and Triangle Right-VLA 1.5 GHz (Garwood et al., 1988).

$47.3_{-0.4}^{+0.2}$ photons s^{-1} . This relates to a star between $15\text{-}20 M_{\odot}$.

The mass measured using the SED fit is $13 \pm 6 M_{\odot}$. A main sequence star type B, is a star with a mass of $2.1\text{-}16 M_{\odot}$ which is consistent with the values measured for this source. As B stars are known to have an excess of Lyman flux (see § 4.1), the star is likely to be between $9\text{-}12 M_{\odot}$ as suggested by the bolometric luminosity measurement (as suggested by Table 1 in Davies et al. (2011) and SED curve in Figure 6).

3.4.7 An unrelated evolved star

Figure 3.2 shows a bright infrared star at G13.380+0.050, approximately one arcminute to the south. This star coincides with a 1612 MHz OH maser, detected by Sevenster et al. (2001), indicating that the star is evolved and unlikely to be part of the same star formation process. Given the offset between this star and G13.384+0.064, the projected distance is 0.5 pc. The image in Figure 3.2 shows the structure of the cloud in the infrared extends toward the star at G13.380+0.050 but does not overlap with this star. Furthermore, there is no edge brightening in the extended infrared emission observed. This suggests that the bright star is unlikely to have a direct physical influence on the star forming region and is most likely an unrelated star projected along the line of sight, but not necessarily physically close to the star forming region.

3.5 Discussion

3.5.1 Far Distance Consideration

The radio continuum-derived luminosity of $3.6(\pm 0.14) \times 10^4 L_{\odot}$ derived in §3.5 is a factor of ten greater than the dust-derived luminosity $4.1(\pm 1.7) \times 10^3 L_{\odot}$. We must reconcile this difference.

If we assume that G13.384+0.064 is at the far kinematic distance of 14.1 kpc, then the radio-derived and dust-derived luminosities are $3.2 \times 10^5 L_{\odot}$ and $2.2 \times 10^5 L_{\odot}$, respectively. These two luminosities are more consistent than those when the near distance is assumed. However, even though this luminosity argument favours the far kinematic distance, we still favour the near kinematic distance for the following reasons.

Firstly, as discussed in §3.2, the HI observations strongly favour the near distance. The HI observations analysed by Urquhart et al. (2013) and shown in Figure 3.5 shows little evidence of high velocity HI self-absorption, which would be expected from intervening gas, if it was at the far kinematic distance. The only high velocity absorption is seen around 50 km s^{-1} . This corresponds to the velocity of the cloud seen in the H₂CO and ¹²CO observations reported previously and so the absorption is most likely not related to G13.384+0.064.

Secondly, there are uncertainties in the expected Lyman continuum flux from young high-mass stars. Smith (2014) concludes that the Lyman continuum flux of early B type stars may be in excess of previous models, caused by the accretion

of cold gas from the circumstellar disk onto hot-spots on the surface of the young star. Comparing the measurements for G13.384+0.064, we find that it sits on the upper edge of their model such that the excess radio continuum flux is consistent with the bolometric luminosity. If the radio continuum flux were much larger, this source would show an unaccounted for excess of radio continuum, compared to the dust-derived luminosity.

A final consideration is the expected number of lower mass stars surrounding the high-mass star if it were at the near vs far kinematic distance. If G13.384+0.064 was at the far distance of 14.1 kpc, then the mass of the star would be approximately $38 M_{\odot}$, based on the mass to luminosity relationship. The mass of the surrounding gas cloud would increase to $5800 M_{\odot}$, making it very likely that a cluster is present. However, as discussed in § 3.4.1, no evidence for a cluster is seen in the infrared images.

3.5.2 Isolated vs. clustered star formation in G13.384+0.064

We now seek to use the properties derived above to determine whether G13.384+0.064 is indeed a high-mass star forming in isolation.

Parker et al. (2007) defines an isolated B type star as a star $10 M_{\odot} < M_{*} < 17.5 M_{\odot}$ in which the cluster mass is $< 100 M_{\odot}$ and there are no O-stars present. The estimated mass of the star based on the SED curve is $13 \pm 6 M_{\odot}$ and the estimated remaining clump mass is $57 \pm 35 M_{\odot}$. Both of these are consistent with the definition described by Parker et al. (2007) for isolated high-mass star formation.

Based solely on the detection of a strong radio continuum source, we can conclude that there must be at least one embedded high-mass star. Incorporating a model by Smith (2014), we find that such a star must account for nearly all (if not, all) of the infrared flux, leaving little room for a cluster. This is because lower mass stars will not contribute significantly to the radio-derived luminosity, but will significantly contribute to the infrared or dust-derived luminosity.

We can model what a cluster might look like, by constraining the quantities of dust-derived luminosity and Lyman continuum flux. In order to do this, we use a Monte-Carlo simulation of the initial mass function (IMF) to generate a cluster. Based on previous work by Walsh et al. (2001), we found that commonly-used functions of the IMF do not greatly affect the make-up of simulated clusters, so we choose the IMF model of Kroupa et al. (1993). In our simulation, we randomly generate stars between masses of 0.1 and $100 M_{\odot}$, according to this IMF and then calculate the cluster physical parameters, such as total mass, luminosity

and Lyman continuum flux. In order to measure the relationship between Lyman continuum flux and luminosity, we use the values given in Table 1 of Thompson (1984) but we note that previous studies have found an excess of Lyman continuum photons from early B-type stars (eg. Urquhart et al. 2013). Therefore, in order to take into account the work of Smith (2014) we apply their most extreme case for ratio of Lyman flux, compared to previous models, where the Lyman flux may be reduced by up to an order of magnitude for the same star with the same bolometric luminosity (ie. reduction of $10^{47.3}$ to $10^{46.3}$ photon s^{-1}). It is important to note that in taking such an extreme reduction in Lyman flux, our simulation will favour the formation of a cluster, rather than an isolated star. This allows us to use the data of Thompson (1984) and correct it for more recent modelling by Smith (2014).

In our Monte-Carlo simulation, we continue to add members to the cluster until the total cluster luminosity is greater than $4.1 \times 10^3 L_{\odot}$. We generated 68,877 clusters with sufficient luminosity to meet this criterion. However, we note that the majority of generated clusters have total luminosities far in excess of this value. This is because the last star added to the cluster is typically a high-mass star with very high luminosity. Thus, we exclude those generated clusters that have luminosities in excess of the IRAS-derived luminosity ($7.2 \times 10^3 L_{\odot}$), leaving 30,601 clusters. We choose the IRAS-derived luminosity here because it is a strong upper limit on the bolometric luminosity, given that IRAS will likely overestimate the total infrared flux, but not underestimate it.

Of our remaining clusters, we find that the median luminosity for the highest mass star in each cluster is $2.8 \times 10^3 L_{\odot}$ which means that for most clusters, the luminosity is dominated by one star. We also find that the highest mass star generated in any cluster has a luminosity of $7.1 \times 10^3 L_{\odot}$, which we calculate has a corresponding Lyman continuum flux of $10^{45.7}$ photons s^{-1} . This Lyman flux is lower than we expect ($10^{46.3}$ photons s^{-1}) by about an order of magnitude. In summary, our simulations indicate that it is very difficult to randomly generate a cluster with the properties that we observe for G13.384+0.064. The only way to generate a good match is for the first star selected from the IMF to be a high-mass star with the right luminosity and Lyman flux properties. However, classifying such a single star as a cluster is questionable.

3.6 Conclusions

In this paper we compared the Lyman-continuum photon flux and clump mass of approximately 200 star forming regions to search for high-mass stars forming in isolation. We identified one source, G13.384+0.064, as a very promising candidate. Analysis completed in both the infrared and the radio, combined with Monte Carlo modelling, shows this source is consistent with a single high-mass star in formation, and there is no strong evidence of a cluster. This verifies the choice of using Lyman flux and bolometric luminosity to identify such candidates. While the observations in the literature allowed us to rule out a large population of embedded young stars, further high-resolution, deep, infrared and sub-mm observations are required to quantify just how small this population is, and thereby unambiguously determine if G13.384+0.064 is a high-mass star forming in isolation.

3.7 Acknowledgements

The authors would like to thank the referee for the comments and advice. SNL would like to thank Andy Longmore for very helpful discussions about the analysis of the infrared data. This research has made use of the SIMBAD database, operated at CDS, Strasbourg, France. This research has also made use of the VizieR catalogue access tool, CDS, Strasbourg, France. The original description of the VizieR service was published in A&AS 143, 23.

Chapter 4

A First Look for Molecules between 103 and 133 MHz using the Murchison Widefield Array

This work, as written, was published by:

Tremblay, C. D., Hurley-Walker, N., Cunningham, M., Jones, P.A., Hancock, P., Wayth, R., Jordan, C.H., “A First Look for Molecules between 103 and 133 MHz using the Murchison Widefield Array”, 2017, *Monthly Notices of the Royal Australian Society*, Oxford Press, 471,4,p.4144-4154

Although this Chapter represents a published paper, edits have been made in response to the thesis examiners. Therefore, it is not an exact replica of the original publication. Every effort is made to maintain the integrity of this work as required by the copyright statements in the appendix of this thesis.

4.1 Abstract

We detail and present results from a pilot study to assess the feasibility of detecting molecular lines at low radio frequencies. We observed a 400 square degree region centred on the Galactic Centre with the Murchison Widefield Array (MWA) between 103 and 133 MHz targeting 28 known molecular species that have significant transitions. The results of this survey yield tentative detections of nitric oxide (NO) and the mercapto radical (SH). Both of these molecules appear to be associated with evolved stars.

4.2 Introduction

In the last five years, new radio telescopes have been commissioned for use in the frequency range of 30 to 300 MHz, including the Long Wavelength Array (LWA; Taylor et al. 2012), the Low-Frequency Array (LOFAR; van Haarlem et al. 2013) and the Murchison Widefield Array (MWA; Tingay et al. 2013; Lonsdale et al. 2009). The capabilities of this new generation of radio telescopes, as well as upgraded facilities such as the Karl G. Jansky Very Large Array (JVLA; Perley et al. 2011) and Giant Metrewave Radio Telescope (uGMRT; Gupta 2014), allow us to revisit low radio frequencies to study spectral lines.

Radio spectral line emission from within our Galaxy is a widely-used probe of astrophysics (Herbst and van Dishoeck, 2009). Comparison of different spectral lines, and therefore different molecules, can be used as a probe of many interstellar processes including the chemical and physical evolution of stars (van Dishoeck, 2014) and planets (Cosmovici, 1979). Many of the recent large molecular line surveys in the radio, infrared, and submillimetre, such as MALT 45 (Jordan et al., 2015), MALT 90 (Jackson et al., 2013), Herschel/Hi-GAL follow-up (e.g. Olmi et al. 2014, 2015) and HOPS (Walsh et al., 2011) were motivated by studying and characterising molecular clouds, high mass stars, and their environments.

One of the challenges faced by sensitive spectral line surveys at high frequencies is line confusion of multiple transitions, making identification of new molecules difficult. For example, the IRAM 30 m survey of the Orion region between 80 and 281 GHz, is significantly hindered by known prominent spectral lines when searching for rarer molecules such as methyl formate (CH_3OCHO ; Tercero et al. 2015). As we observe in frequencies down towards 100 MHz, these transition spread out, making them less confused.

The formation pathways for many molecules, especially for complex organics, are still unknown. Recent articles suggest that observations at the lower frequencies may provide key information by observing long chain molecules and low energy transitions of simple diatomics that are not easily identified with observations at higher frequency (e.g. Codella et al. 2015; Danilovich et al. 2016). This was demonstrated recently in the search for propylene oxide ($\text{c-CH}_3\text{C}_2\text{H}_3\text{O}$) where previous attempts to find the molecule at 99 GHz (Cunningham et al., 2007) failed but more recent results at 12.1 GHz yielded detections of three transitions (McGuire et al., 2016).

Low-frequency observations may also be beneficial to study the formation mechanisms of high-mass stars through the detections of molecules typically hin-

dered by line confusion in higher frequencies (Codella et al., 2015). Isella et al. (2015) suggest that the ionised hydrogen (HII) regions around high mass stars may be optically thick, hiding the central molecular emission of high mass protostars, at frequencies less than 10 GHz. Hindson et al. (2016) found that the HII regions are optically thin until around 200 MHz, suggesting that observations between 1 GHz and 200 MHz could provide contributions to understanding the chemical evolution of high-mass stars and thus their formation in regions where the ionised hydrogen is uniform. Lower frequencies could still contribute in early stages of formation before the star ignites and when the gas is clumpy.

Sulfur is one of the most abundant elements in the universe. However, there is an apparent lack in molecular form in the interstellar medium. Gorai et al. (2017) review the current issues regarding the missing interstellar sulfur-containing molecules during their research of the formation mechanisms of thiols¹. Currently, observations have only accounted for one-quarter of the total interstellar sulfur thought to be associated with molecules, which may be due to molecular instability at higher temperatures (Millar and Herbst, 1990).

Motivated by the possibility of detecting molecular spectral lines at radio frequencies that are not normally accessible (instrumentation limitations or radio-frequency interference), we have used the MWA to perform a pilot survey around the Galactic centre region. Within this region we would expect to detect molecular lines within evolved stars and molecular clouds. However, with the dominance of synchrotron radiation at these frequencies and the lack of good prediction models, it is difficult to know what to expect. A primary science goal of the MWA is the search for redshifted HI 21 cm emission from the Epoch of Reionisation (EoR) (Bowman et al., 2013). The design requirements for the EoR experiment make the MWA well suited for large-area blind spectral line surveys.

The primary goal of this work was to assess the feasibility of using a new, multi-purpose, wide-field, low-frequency radio telescope, such as the MWA, to study molecular spectral lines and to demonstrate a pipeline for processing MWA data for such an analysis.

4.3 Observations and Data Reduction

The region under study, shown in Figure 4.1, is 400 square degrees centred on $17^h45^m40^s -29^{\circ}00' 28''$ (J2000).

¹The sulfur analogue of alcohols

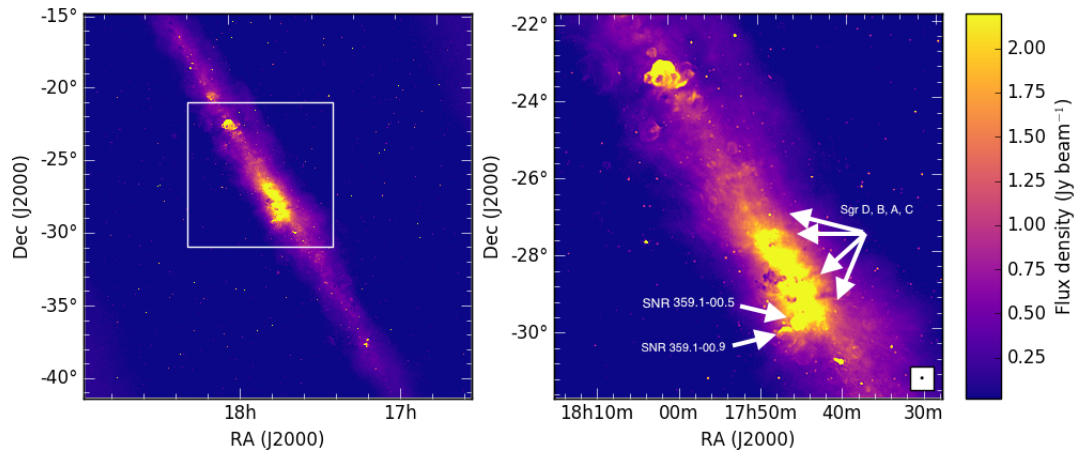


Figure 4.1: Continuum image of the Galactic Centre observed by the MWA across the 30 MHz of bandwidth with a central frequency of 119.7 MHz. The left hand image represents the full region blindly searched for molecular signatures (see section Section4.2). The right-hand image is a zoomed in region around the Galactic Centre showing that the supernova remnants SNR 359.01 – 00.5 and SNR 359.0 – 00.9 are clearly resolved. The star-forming regions of Sagittarius B, Sagittarius C, Sagittarius D and Sagittarius A are unresolved in our observations.

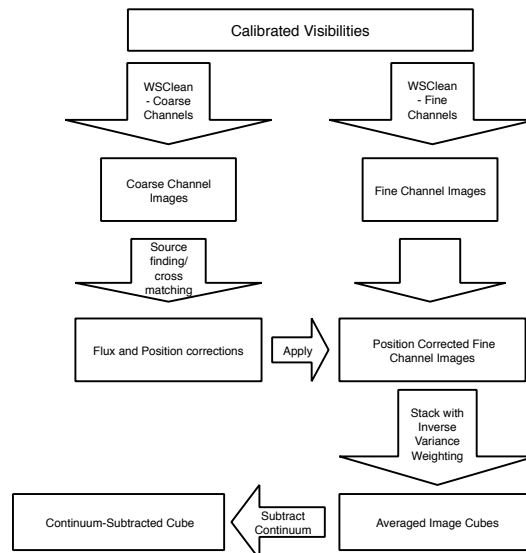


Figure 4.2: Summary of the pipeline designed to create calibrated time-averaged spectral image cubes with the MWA.

The observations were performed using the MWA, which is located at the Murchison Radio-astronomy Observatory in Western Australia, on 25 July 2014 and 27 July 2016 for 120 minutes each night. A detailed description of the MWA, including its capabilities and specifications, are found in Tingay et al. (2013). However, we provide a short outline and details pertinent to this work. The MWA consists of 128 antenna “tiles”, each containing 16 dual-polarisation dipole antennas, with a maximum baseline length of 3 km. At 120 MHz, the FWHM of the primary beam (field-of-view) and synthesised beam (resolution) are 30 degrees and 3.2 arc minutes, respectively.

For each of the two nights, the observations were completed in 24 five-minute snapshots using a standard MWA observing procedure. At the beginning of each five-minute snapshot, the antenna tiles are re-pointed to track the field over the night.

Data were collected in a 30.72 MHz contiguous band, centred at 119.7 MHz. The MWA uses a two-stage filterbank to channelise the signal. The output of the first filterbank consists of 24×1.28 MHz “coarse” channels; each coarse channel is further subdivided into 128×10 kHz “fine” channels, resulting in 3072 (10 kHz-wide) spectral channels. The 10 kHz channel width corresponds to a velocity resolution of 26 km s^{-1} .

The edges of each coarse channel suffer from aliasing in the first stage filterbank, hence the 14 fine channels on both edges of each coarse channel were flagged. The central fine channel of each coarse channel contains the (non-zero) DC component of the polyphase filterbank (Thiagaraj et al., 2015) and was also flagged. Additional flagging for radio-frequency interference was performed in each observation using standard MWA tools that are based on AOFLAGGER (Offringa et al., 2010, 2012). This program is designed to find peaks in time and frequency that are likely to be the result of radio frequency interference (RFI).

In summary, the central 100 fine channels of each coarse channel were imaged. This resulted in 78 per cent of the bandpass being imaged.

4.3.1 Calibration and Imaging

The MWA tool COTTER (Offringa et al., 2015) was used to apply the flags and set the phase centre for every observation to $17^{\text{h}}45^{\text{m}}40^{\text{s}} -29^{\circ}00' 28''$ (J2000).

The bright radio source Hercules A was observed for two minutes each night and was used for initial bandpass calibration, using the MITHCAL calibration tool described in Offringa et al. (2016). Radio source 3C353 also lies within the

field-of-view of the observation centred on Hercules A, hence we followed the approach adopted by Hurley-Walker et al. (2014) to incorporate 3C353 using self calibration. The revised bandpass solution was then applied to each of the five-minute observations of the Galactic Centre.

As this was the first attempt to analyse MWA observations for spectral lines, we designed a novel method to create searchable image cubes; the pipeline is summarised in Figure 5.2.

In widefield interferometric imaging with a non-coplanar array, the visibility (u, v, w) data can no longer be related to the sky (l, m) by a simple 2-D Fourier Transform, because the values of w are no longer negligible (Cornwell et al., 2005). WSClean (Offringa et al., 2014), uses w -stacking to perform a computationally-efficient transformation of visibility data into sky images. This software was used to simultaneously clean and image the fine channels associated with each coarse channel by searching for the clean components in a multi-frequency synthesis image and then subtracting the components from each individual fine channel of the visibilities. We used a Briggs weighting (Briggs, 1995) of “-1” for the gridded visibility data to compromise between image resolution and sensitivity.

For each of the 24 coarse channels, 100 of the 10kHz fine channels were imaged to ensure that channels that may be affected by aliasing have been removed. The 10 kHz channel images, made using 4.2 pixels per synthesised beam FWHM, were combined to produce a single image cube which was then converted into a MIRIAD (Sault et al., 1995) file format. In MIRIAD, all of the five-minute snapshot images were time-averaged together using inverse variance weighting, after flux density calibration (Section 2.1.1) and ionospheric correction (Section 2.1.2), to form a single image cube for each coarse channel, representing 235 minutes of integration time.

As shown in Figure 5.2, a continuum image of each coarse channel is used to derive the primary beam model, check the flux density calibration and determine the ionospheric correction values that are applied to each of the fine channel continuum images.

Observations at these low frequencies are sky-noise-dominated. The measured noise within the continuum subtracted image, after primary beam correction, is approximately $150 \text{ mJy beam}^{-1}$ for most image cubes at the pointing centre and lower than the $300 \text{ mJy beam}^{-1}$ theoretical RMS derived from the background sky temperature and the system temperature reported in Tingay et al. (2013). However, the RMS noise increases to approximately $300 \text{ mJy beam}^{-1}$ six degrees from the Galactic Centre, following the shape of the primary beam as shown in

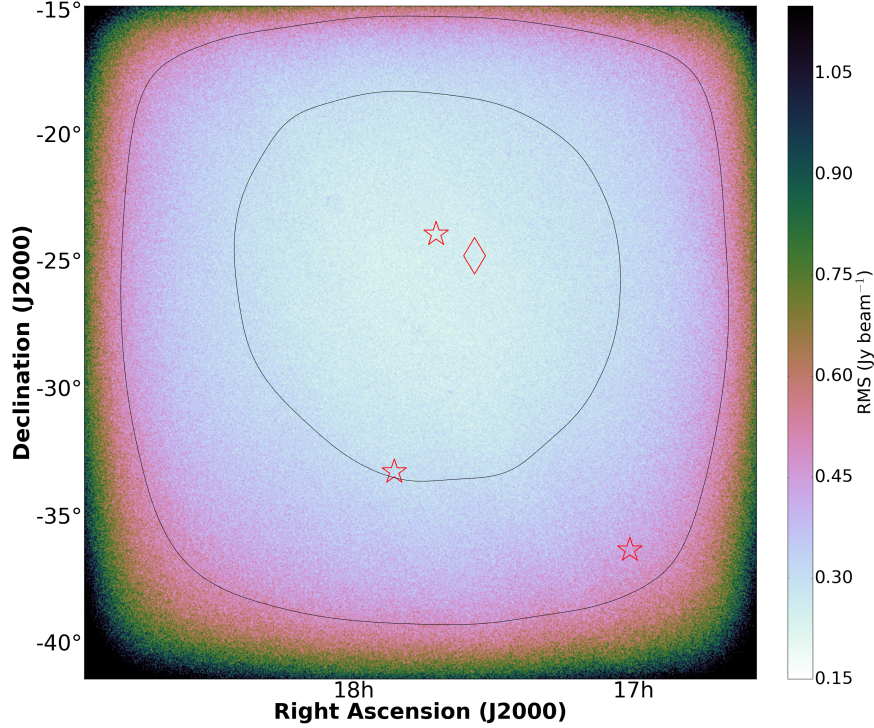


Figure 4.3: Map of the RMS following the shape of the primary beam across the searched field-of-view. The cube of the fourth coarse channel, at 107 MHz, is shown in this figure, as a representation of the behaviour of the entire dataset. The stars on the image represent the positions of the nitric oxide tentative detections and the diamond represents the position of the mercapto radical tentative detection. See Section 4 for additional details. The contours are at the levels of 0.3 and 0.5 Jy beam^{-1}

Figure 4.3. The estimated sky temperature, through a scaling of the Haslam model (Remazeilles et al., 2015), for the Galactic Centre was $T_{\text{sky}} = 3582 \text{ K}$, which was a factor of ten greater than the nominal T_{sky} , due to the bright diffuse synchrotron emission from this part of the Galaxy.

Flux Density Calibration

The primary beam is the sensitivity pattern of the individual receiving elements (tiles for the MWA) and is direction and frequency dependent. The dipoles are not uniformly sensitive to the incoming radiation from all directions, reducing the apparent flux density of sources located further away from the pointing centre. Therefore, we must correct for the changing brightness distribution on the sky by dividing the fine channel continuum image by the beam model derived from each

coarse channel for each observation. The flux densities of observed sources are then compared to those published in the Molonglo Reference Catalogue (MRC; Large et al. 1981), as the 408 MHz catalogue is close to our observing frequencies and it has sources within $|b| > 3$. The values for each cross-matched point source in the MRC were scaled down to our frequency using a spectral index of -0.83 (Hurley-Walker et al., 2017). The flux densities were found to have a flux density scale difference of 3 per cent over 25 sources, so no direction-dependent calibration was required.

Ionospheric Correction

Each five-minute observation over the two epochs experienced slightly different phase distortions due to changing ionospheric conditions. This manifested as small (≈ 20 – 40 arc seconds) direction-dependent shift to the positions of sources in every observation. Using the software AEGEAN (Hancock et al., 2012), the source positions within each coarse channel continuum image was determined. These positions were compared to those reported in the MRC and the mean shift was applied to each image cube, before the observations were averaged together (Section 2.1).

After corrections were made and the image cubes were averaged together, the residual shift in source position, compared to MRC, is 1 arc second in right ascension (RA) and -2 arc seconds in declination (Dec). The ratio of the peak flux density and the integrated flux density was calculated to determine the amount of blurring from residual uncorrected ionospheric shifts and found to be 1.10 ± 0.11 . Based on the standard deviation of the position offsets of the sources from MRC, the astrometric precision for a typical source position is 18 arc seconds with the dominant error being uncorrected residual shifts within each observation.

Continuum Subtraction

The MWA is made up of dipole antennas that observe a wide field of view, so traditional methods of continuum subtraction in (u, v, w) space could not be used. Early attempts to use the CASA command UVCONTSUB to subtract the continuum using a first order polynomial, resulted in only removing 71 per cent of the continuum and created severe smearing of sources away from the phase centre. These were likely due to the inability of UVCONTSUB to correct for the w -terms. Therefore, the continuum was subtracted in the image domain.

We followed a method similar to that which was developed for and used in

the Southern Parkes Large-Area Survey in Hydroxyl (SPLASH; Dawson et al. 2014) to subtract the continuum and residual bandpass. A smoothed image cube was created by binning together the spectral signal in sets of 15 fine channels, for each pixel position, and subtracting the new smoothed image cube from the continuum image cube.

4.4 Line Search and Identification

4.4.1 Survey Strategy

In this survey, we performed two different search strategies to find spectral lines within these image cubes. First, we completed a targeted search by looking for lines we thought were most likely to be detected based on the line strengths, quantum numbers, and energies listed within the databases Cologne Database for Molecular Spectroscopy (CDMS; Müller et al. 2001), Spectral Line Atlas of Interstellar Molecules (SLAIM; Splatalogue²), Jet Propulsion Laboratory (JPL Pickett et al. 1998) and Top Model (Section 4.1). Second, we completed a blind search over 1920 of the 2400 imaged spectral channels and looked for lines brighter than the 6σ limit of the local RMS within the image cube in both emission and absorption (Section 4.2). The Galactic Centre is of particular interest in the blind search as the Galactic centre offers a stimulated environment with increased gas densities, temperatures (Menten, 2004) and possibly cosmic rays (Chambers et al., 2014). These additional factors may be responsible for the fact that transitions from the largest molecules have only been detected toward the Galactic centre (Jones et al., 2012).

4.4.2 Line Search

As this is the first survey of molecular lines at 100 MHz and many of the channels are affected by aliasing (Section 2.1), a conservative search approach was used. A limit of 6σ of the local RMS in the final image cube for the blind search and 5σ for the targeted search, was set for the molecular line search in both emission and absorption. To perform the search, an RMS map of each averaged image cube, each representing one of the 24 coarse channels, was created. The RMS map was divided by the continuum-subtracted image cube to create a signal-to-noise (SNR) data cube. The SNR cube was converted into a MIRIAD (Sault et al., 1995)

²www.splatalogue.net

file format and a map of the peak intensity of each pixel was created by fitting a three-point quadratic to every three adjacent fine channels in each pixel position (see MIRIAD documentation on moment map “-2” for additional details).³ The software AEGEAN (Hancock et al., 2012) was used to look for peaks over 6 in each of the 24 coarse channel maps for the blind search and for peaks over 5 in two of the coarse channel maps for the targeted search.

Each potential spectral line found by AEGEAN was further investigated by observing the location in the continuum subtracted image cube. For any peak associated with a known molecular line, the data were then cross-matched with objects in SIMBAD⁴ lying within three arc minutes of the centre pixel, the size of the FWHM of the synthesised beam.

4.5 Results

4.5.1 Targeted Search

Based on line strengths and energies, given in Tables 4.1, 5.3 and 4.3, we expect the most likely detections to be the mercapto radical (SH) and nitric oxide (NO). Nitric oxide has a significant number of known low energy transitions at the frequencies of 103–133 MHz and was determined by Gerin et al. (1992) to have abundances similar to C¹⁸O. The ground-state hyperfine-splitting transitions of SH lie in the range 100-123 MHz.

These two molecules have been detected in other transitions towards astrophysical objects. However, we expect some of the excitation mechanisms for these low frequency detections to be different. Many of the molecular transitions detected at higher frequencies are of shocked or hot gas. The expectation is that at low frequencies the transitions would primarily be emitted from cold gas.

Based on a confirmed Gaussian noise distribution, at a 5σ level, we would expect 1 false detection per image cube. However, using the source density described in Section 4.2, we would expect 0.003 channels to have a signal that correlates with a known molecular line and a known object.

We have tentatively detected the Mercapto radical (Section 4.1.1) and nitric oxide (Section 4.1.2). Both of these detections appear to be associated with evolved stars which are plausible chemical environments for these molecules. The

³https://www.cfa.harvard.edu/sma/miriad/manuals/ATNFuserguide_US.pdf

⁴<http://simbad.u-strasbg.fr/simbad/sim-fcoo>

chances of these peaks being the result of noise, instead of molecular detections is 0.03, using similar source densities and statistics as described in Section 4.2.

Tentative Detection of Mercapto radical (SH)

Diatomic hydrides are the simplest interstellar molecules and may provide key information about the interstellar medium (ISM); the reactions that lead to their production in interstellar environments are characterised by low activation energies and high critical densities (Bruderer et al., 2010; Godard et al., 2012). The lowest energy hyperfine transitions (in a quartet) of SH emit at 100.30, 111.49, 111.55 and 122.73 MHz, all within the range of the MWA (Table 4.1). The transition at 100.30 MHz is outside our observing band. The lines at 111.49 and 111.55 MHz are the highest intensity transitions representing ${}^2\Pi_{3/2} J = \frac{3}{2}$, $F = 1^+ - 1^-$ and ${}^2\Pi_{3/2} J = \frac{3}{2}$, $F = 2^+ - 2^-$ respectively, with energy at the upper excitation level of 5×10^{-4} K (See Table 4.1 for more information).

We have tentatively detected the ${}^2\Pi_{3/2} J = \frac{3}{2}$, $F = 2^+ - 2^-$ SH transition at 111.56 MHz around the evolved star 2MASS J17360840 – 2533343 (Figure 4.1). This transition represents the most intense line and so the most likely to be detected.

The SH hyperfine transitions are analogues to those of the hydroxyl radical (OH) at 1.6 GHz (Dawson et al., 2014). The OH transitions are well-known strong masers that originate from star-forming regions and evolved stars. Therefore, it might be expected that the SH analogue transitions might also exhibit maser activity. This would significantly increase their detectability, although predicting the maser gain for such transitions is difficult. It may also be possible that SH may experience Lambda Splitting, and therefore only a single detectable line is representative of the particular environment.

If we assume similar thermal emission properties, we can use the known abundance information about OH to predict the flux of SH in these observations. The sensitivity calculation uses a standard ratio of the relative abundance of sulfur compared to oxygen, which is 1/21 (Wilson and Rood, 1994) and the detected concentration of OH in the Galactic Centre with SPLASH (Dawson et al., 2014). With this, we estimate SH should show absorption of about 0.3 and 0.5 Jy for the 111.49 and 111.55 MHz transitions respectively. This intensity is around the 3σ noise threshold of our observations in the Galactic centre, suggesting that the tentative detection shows signs of maser activity. We note that our estimate is simplistic in that it does not consider the chemistry of SH and so should be

treated with some caution.

There are two reported infrared detections of SH, representing warm shocked gas in absorption. Yamamura et al. (2000) detected the molecule in the S-type star R Andromedae with a calculated column density of $4.0 \times 10^{20} \text{ cm}^{-2}$ using the Kitt Peak 4 m telescope. Neufeld et al. (2012) detected SH using SOFIA in the diffuse cloud, W49N, and calculated the column density to be $4.6 \times 10^{12} \text{ cm}^{-2}$. Neufeld et al. (2012) noted that the abundance is higher than expected, but SH is expected to have a boosted abundance in areas of warm bow shocks (Neufeld et al., 2012; Yamamura et al., 2000).

In the radio, we expect to detect these low energy transitions within areas of cold gas, instead of the shocked gas in which the infrared detections were made. Assuming standard thermal absorption mechanisms, we calculate a total column density of $2.2 \times 10^{20} \text{ cm}^{-2}$, using the partition function and upper level degeneracy, for low temperatures, as quoted in the CDMS catalogue. This is the same order of magnitude as reported by Yamamura et al. (2000) in the infrared, and the beam sizes are likely to be similar.

The star 2MASS J17360840 – 2533343, has not been part of any study and no information is known regarding its distance or velocity. However, the velocity of $26 \pm 13 \text{ km s}^{-1}$ is realistic based the Galactic rotation curve in CO generated by Dame et al. (2001). There are no other known molecular transitions within 200 km s^{-1} of this transitions, so no other molecule can be assigned to this absorption peak.

Tentative Detection of Nitric Oxide (NO)

In the frequency band of these observations, there are several hyper-fine transitions of nitric oxide with an upper energy level for the transitions greater than 300 K; so therefore we did not search at these frequencies as they are unlikely to be detected. However, one nitric oxide transition listed in Table 5.3 and transitions for four nitric oxide isotopologues listed in Table 4.3 have low enough energies to be likely detectable. The transition at 107.37 MHz represents $J = \frac{3}{2}$, $\Omega = \frac{1}{2}$, $F = \frac{5}{2} - \frac{5}{2}$ with an upper energy level of 7.195 K, so is the most likely to be detected. At this frequency we have tentatively detected NO in three objects at the level of 5σ , as shown in Figure 4.5.

At the frequency of 107.36 MHz, we tentatively detect emission which appears to be associated with a semi-regular pulsating star OGLE BLG-LPV 21112. This star was identified by Soszyński et al. (2013) in a survey of variable stars around

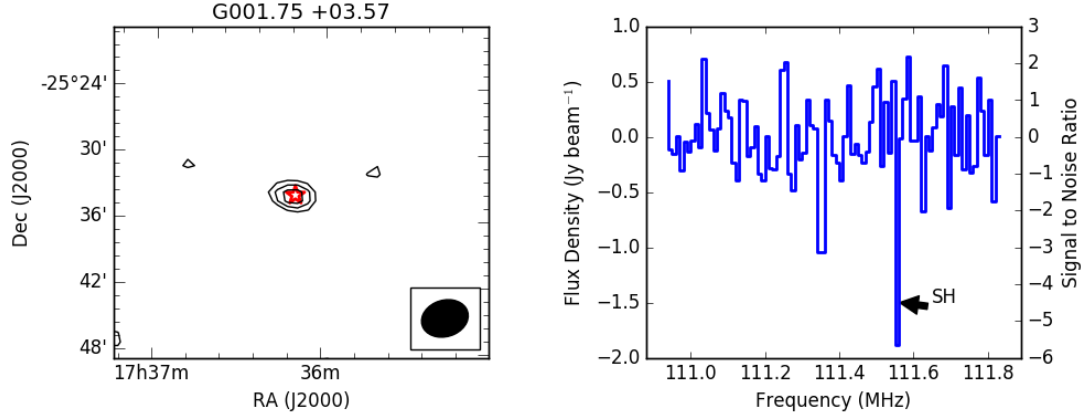


Figure 4.4: A tentative detection of the mercapto radical (SH) with a possible association to 2MASS J17360840 – 2533343. The image on the left is a contour plot of the detection with contours set at the 3, 4, 5, and 6 σ levels where 1 σ is 0.29 Jy beam⁻¹. The star in the image represents the optical position of the star labeled in the upper left-hand panel and size of the star represents the astrometric uncertainty after ionospheric correction. The right-hand panel shows the spectrum from 110.9 to 111.8 MHz at the position of 17^h36^m10^s -25°33' 51''(J2000).

Table 4.1: Results for the search for the mercapto radical (SH). The rest frequency is listed in the second row and the third row lists the upper energy level divided by the Boltzmann constant for the transition. The line strengths in terms of $S\mu^2$, with units of Debye² in the fourth row and the Einstein Coefficient (A_{ij}) in the fifth row. The last row lists the column density without taking into account beam dilution and assuming standard thermal emission or absorption properties (Section 3.1.2). However, the column densities may be non-physical quantities if these represent boosted emission, such as maser activity.

Molecule	SH*	SH*	SH*	SH*
Rest Frequency (MHz)	100.29	111.49	111.55	122.74
E_U / k_B (K)	0.00	0.01	0.01	0.01
$S\mu^2$ (D ²)	0.17	0.86	1.55	0.17
$\text{Log}_{10}(A_{ij})$	-15.17	-14.34	-14.30	-15.13
Velocity (km s ⁻¹)	Not Observed	Not Detected	-26±13	Not Detected
Quantum Numbers	$^2\Pi_{3/2} J = \frac{3}{2}, F = 1^+ - 2^-$	$^2\Pi_{3/2} J = \frac{3}{2}, F = 1^+ - 1^-$	$^2\Pi_{3/2} J = \frac{3}{2}, F = 2^+ - 2^-$	$^2\Pi_{3/2} J = \frac{3}{2}, F = 2^+ - 1^-$
Source	2MASS J17360840 – 2533343			
Position (J2000)	17 ^h 36 ^m 10 ^s -25°33' 51''			
Position (Galactic)	001.75 +03.57			
N_{tot} (cm ⁻²)	2.2(±0.6)×10 ²⁰			

Catalogue – JPL – Jet Propulsion Laboratory Spectral Line Catalogue, (Pickett et al., 1998)

* Molecule detected in evolved stars as per the NIST Spectral Database (Lovas et al., 2003)

the Galactic bulge. At the frequency of 107.37 and 107.40 MHz, we tentatively detect NO in absorption at the position of G348.58 +02.69 and G356.11 -03.60.

Both Quintana-Lacaci et al. (2013) and Chen et al. (2014) suggest NO is observed in the same regions as hydroxyl (OH) in shocked gas and interacts by the reaction $\text{OH} + \text{N} \rightarrow \text{NO} + \text{H}$. Hydroxyl masers are found in regions of high-mass star formation, main sequence evolved stars and around the expanding circumstellar envelopes of variable red giant stars (Benson et al., 1990; Rudnitskij, 2002). In these variable stars, Rudnitskij (2002) explains that a quasi-stationary layer of gas and dust, about 10 solar radii from the centre of the star, hosts a variety molecules. Occasionally, a small shock wave of approximately $6\text{--}10 \text{ km s}^{-1}$ crosses this layer, creating a pumping mechanism for masers to occur.

The emission and absorption peaks tentatively detected are at 107.36 MHz, 107.37 and 107.40 MHz (Table 5.3), could represent one of two nitric oxide transitions. The nitric oxide transition $J=\frac{17}{2}$, $\Omega = \frac{3}{2}$, $F=\frac{19^+}{2} - \frac{19^-}{2}$ at 107.400 MHz is a hyperfine transition with an upper energy level of 370 K. The other transition represents $J=\frac{3}{2}$, $\Omega = \frac{1}{2}$, $F=\frac{5}{2} - \frac{5}{2}$ at 107.368 MHz with an upper energy level of 7.195 K. Since we did not detect any of the other hyperfine transitions on the individual sources and the energy of the transition at a rest frequency of 107.400 MHz is high, we expect the emission to be associated with $J=\frac{3}{2}$, $\Omega = \frac{1}{2}$, $F=\frac{5}{2} - \frac{5}{2}$ at 107.36 MHz.

When the source position for OGLE BLG-LPV 65700 is compared to the Galactic rotation curve in CO generated by Dame et al. (2001), the velocity of $78\pm 13 \text{ km s}^{-1}$ is determined to be realistic. An alternative transition around 107.37 MHz is N^{18}O at 107.311 MHz, which has an upper energy of 6.86 K and represents the $J = \frac{3}{2} - \frac{3}{2}$, $\Omega = \frac{1}{2}$, $F = \frac{5^-}{2} - \frac{3^+}{2}$ transition. However, this would mean the velocity is approximately -221 km s^{-1} for each source, which is higher than standard velocities, so is an unlikely association.

The column density for the emission and absorption lines were calculated as per Appendix 1 using the partition function and upper level degeneracy, for low temperatures, as quoted in the CDMS catalogue. For the absorption lines, the optical depth (τ) was close to unity for both objects when the continuum brightness temperature for detection location was scaled from the Haslam 408 MHz map. The brightness temperature for the emission line, using the Rayleigh-Jeans approximation, is 4370 K. This suggests the emission is non-thermal and that the column density calculation may be non-representative of the environment.

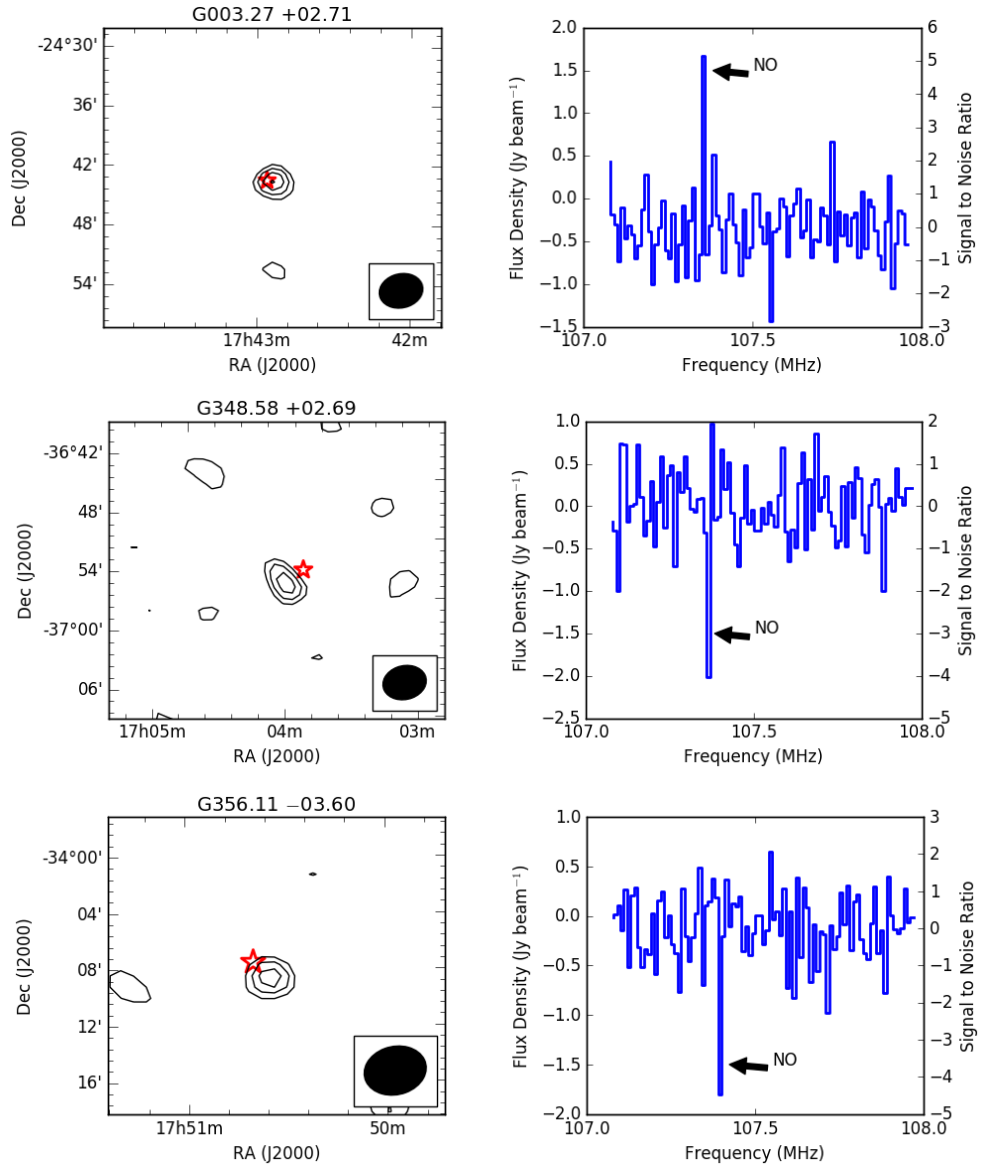


Figure 4.5: Tentative detections of nitric oxide. The contours on each left-hand image are set to the 3, 4, 5, and 6 σ levels. The red star in each contour plot represents the optical position of the evolved star that is a plausible association with the detection, and the size of the star represents the astrometric uncertainty after ionospheric correction. The right-hand panel shows the full spectrum from 107 MHz to 108 MHz at the position of the tentative detection. (Top) NO tentative detection at the position of $17^{\text{h}}42^{\text{m}}55^{\text{s}} -24^{\circ}43'9''$ (G003.27 +02.71) with a possible association to OGLE BLG-LPV 21112. The contour map uses a 1σ value of $0.38 \text{ Jy beam}^{-1}$. (Middle) NO tentative detection at the position of $17^{\text{h}}04^{\text{m}}12^{\text{s}} -36^{\circ}52'31''$ (G348.58 +02.69) with a possible association to TYC 7372 – 165 – 1. The contour map uses a 1σ value of $0.50 \text{ Jy beam}^{-1}$. (Bottom) NO tentative detection at the position of $17^{\text{h}}50^{\text{m}}33^{\text{s}} -34^{\circ}07'46''$ (G356.11 –03.60) with a possible association to OGLE BLG-LPV 65700.¹⁰⁵ The contour map uses a 1σ value of $0.40 \text{ Jy beam}^{-1}$.

Table 4.2: Results for the search for nitric oxide. The rest frequency is listed in the second row and the third row lists the upper energy level divided by the Boltzmann constant for the transition. We quote the line strength in terms of $S\mu^2$ in Einstein Coefficient (A_{ij}) in the third and fourth row. The fifth and sixth row lists the source position in J2000 and Galactic coordinates. The last row lists the column density without taking into account beam dilution and assuming standard thermal emission or absorption properties (Section 3.1.2). However, the column densities may be non-physical quantities if these represent boosted emission, such as maser activity.

Molecule	NO [†] *	NO [†] *	NO [†] *
Rest Frequency (MHz)	107.37	107.37	107.37
E_U/k_B (K)	7.25	7.25	7.25
$S\mu^2$ (D ²)	0.00	0.00	0.00
$\text{Log}_{10}(A_{ij})$	-18.49	-18.49	-18.49
Velocity (km s ⁻¹)	-26±13	0±13	78±13
Quantum Numbers	$J=\frac{17}{2}, \Omega = \frac{3}{2}, F=\frac{19^+}{2} - \frac{19^-}{2}$	$J=\frac{17}{2}, \Omega = \frac{3}{2}, F=\frac{19^+}{2} - \frac{19^-}{2}$	$J=\frac{17}{2}, \Omega = \frac{3}{2}, F=\frac{19^+}{2} - \frac{19^-}{2}$
Source	OGLE BLG-LPV 21112	TYC 7372 - 165 - 1	OGLE BLG-LPV 65700
Position (J2000)	17 ^h 42 ^m 55 ^s -24°43' 9''	17 ^h 04 ^m 12 ^s -36°52' 31''	17 ^h 50 ^m 33 ^s -34°07'46''
Position (Galactic)	003.27 +02.71	348.58 +02.69	356.11 -03.60
N_u (cm ⁻²)	1.2(±0.8)×10 ¹⁵		
N_{tot} (cm ⁻²)	1.3(±0.8)×10 ¹⁴	8.5(±0.8)×10 ²⁰	1.0(±0.9)×10 ²¹

Catalogue – CDMS – Cologne Database for Molecular Spectroscopy (Müller et al., 2001)

† Molecule detected in star-forming regions as per the NIST Spectral Database (Lovas et al., 2003)

* Molecule detected in evolved stars as per the NIST Spectral Database (Lovas et al., 2003)

4.5.2 Blind Search

A blind search in both absorption and emission was completed at a threshold of 6σ of the local RMS measured in each final image cube. This corresponds to a flux density limit of $0.75 \text{ Jy beam}^{-1}$ in the Galactic Centre and 1.8 Jy beam^{-1} approximately six degrees from the Galactic Centre region. Of the 2400 channels imaged, only 1920 channels were used in the search for spectral lines due to the aliasing effects near the edge channels (see Section 2.1 for details). Since the spectral noise across the image is confirmed to be Gaussian, at 6σ we can expect one false detection in the 1920 channels and 4×10^6 pixels that were imaged.

Any peak over the 6σ limit was then compared with known molecular lines from the databases CDMS, SLAIM, JPL and Top Model. In the frequency band of 103 to 133 MHz, there are 28 known species that have published transitions with energy in the upper excitation state less than 300 K. A selection of 22 of the molecules most likely to be detected based on their line strengths, energy levels and quantum mechanics are listed in Table 4.3. The rest frequencies for each transition were determined from a mix of laboratory experiments and theoretical modelling. The details are found in the associated database listed in Table 4.3. For any known molecular lines, the data were then correlated with objects in SIMBAD for any sources within three arc minutes of the centre pixel.

We discovered one peak above the 6σ threshold at 124.91 MHz that was associated with the known star OGLE BLG RRLYR 1344 ($17^h 40^m 27^s -21^\circ 22' 53''$), but was not associated with any known molecular transition. Further laboratory experiments for molecular transitions, at these low frequencies, would be helpful to determine useful targets and integration times for more sensitive searches.

To calculate the chance of a false detection corresponding to a known molecular line and known source position, we used an OH survey to approximate a source density within our field-of-view. This is a reasonable proxy because OH masers are known to occur within different astrophysical objects in which spectral lines are prominent, such as evolved stars and star-forming regions. In the OH survey by Sevenster et al. (2001), a 105 square degree search of the Galactic Centre yielded 286 objects hosting OH masers. If we extrapolate this to our field of 400 square degrees, we could expect around 1144 sources. Molecular lines can have a velocity of up to 150 km s^{-1} around the Galactic Centre (Olofsson et al., 1982). This velocity means that a molecular transition can shift up to 5 channels in either direction from the rest frequency. Therefore, we would expect molecular lines to be within only 111 channels of the 1920 searched. Taking these num-

bers into account we would expect 0.00002 channels (or 0.0022 chance) to have a peak flux density greater than 6σ and coincidentally correspond with a known molecular line and a known source.

This survey yielded no results in emission or absorption above the 6σ limit that were associated with known objects and known molecular lines. The results in Table 4.3 represent the upper limit on the column densities for 22 molecules potentially detectable within these observations. The limit on the column densities are calculated assuming standard thermal excitation mechanisms. However, this may not be the case for low frequency transitions.

4.6 Discussion

This survey is the first reported molecular search at low frequency and the goal was to assess the feasibility of using the MWA for this style of work. Within the 400 square degree field-of-view, we would expect up to 1,100 sources (as discussed in Section 4.2) to contain molecular rich environments in which molecular transitions could be detected. The telescope’s wide field-of-view, along with the extreme radio quiet of the Murchison Radio-astronomy Observatory (Offringa et al., 2015), makes it a great survey instrument to find new and interesting molecular regions. The search yielded tentative detections of nitric oxide in three objects at 107.37 MHz and the mercapto radical at 111.55 MHz in one evolved star. Here we attempt to explain the difference between the number of objects with tentative detections and the total potential sources within the field of view.

At radio frequencies, the ratio of photon energy to kinetic energy ($h\nu/kT$) at a temperature T is very small ($\ll 1$). This makes almost every object a thermal radio source, as the brightness of the blackbody emitter is proportional to the square of the frequency (ν^2). For radio spectral lines, $h\nu/kT \ll 1$ lowers the opacity limits and makes the emission strength independent of temperature of the emitting gas. The emission is then proportional to the number of atoms in the proper stage of ionisation (Condon and Ransom, 2016) and allows for maser emission with only a small population inversion (Spitzer, 1998). Therefore, at frequencies less than 1 GHz, we are more sensitive to stimulated emission and maser transitions.

The set-up of the MWA used during this survey offers a few challenges. Only 78 per cent of the bandpass was imaged due to aliasing from the polyphase filter bank. This reduced the number of potentially detectable known transitions by

Table 4.3: Molecules in the ground vibrational state that have known transitions in the 103 to 133 MHz range with upper level energies less than 300 K. The rest frequency is listed in the second column and the third column lists the upper energy level divided by the Boltzmann constant for the transition. We quote the line strengths in terms of $S\mu^2$, with units of Debye² in the fourth column and the Einstein Coefficient (A_{ij}) in the fifth column. The sixth column lists the catalogue used to source the data and the last column lists the upper limit on the column density (Section 3.1.2) for the most probable line of each molecule. Note that the detectability of any spectral line will depend on the $S\mu^2$ and A_{ij} value and the relative abundance of the molecule. However, relative abundances for most of the molecules listed are not known.

Molecule	Rest Frequency (MHz)	E_U / k_B (K) (K)	$S\mu^2$ (D ²)	$\text{Log}_{10}(A_{ij})$	Catalogue [◇]	N_u (cm ⁻²)	N_{tot} (cm ⁻²)
CH ₂ OO [†]	104.52	152.20	58.96	-13.54	SLAIM	Flagged	Flagged
CH ₃ O ¹³ CHO [†]	113.86	4.38	0.10	-15.45	Top Model	$<4.24 \times 10^{12}$	$<1.64 \times 10^{13}$
l-C ₃ H ^{†*}	107.98	32.93	9.20	-13.91	JPL	Flagged	Flagged
l-C ₄ H ₂	107.33	144.09	7.76	-14.57	SLAIM	$<8.59 \times 10^{12}$	$<1.05 \times 10^{17}$
	129.91	153.09	7.39	-14.36	SLAIM	Flagged	Flagged
t-DCOOH [†]	124.80	42.40	5.41	-14.03	JPL	$<6.10 \times 10^{12}$	$<3.48 \times 10^{13}$
cis-H ¹³ COOH [†]	105.78	20.38	16.37	-13.49	JPL	Flagged	Flagged
	110.82	182.72	14.42	-14.13	JPL	Flagged	Flagged
cis-HCOOD [†]	106.53	190.60	13.55	-14.24	JPL		
	118.78	76.16	13.31	-13.86	JPL	$<9.39 \times 10^{11}$	$<6.64 \times 10^{13}$
H ₂ ¹³ CO [†]	116.90	201.85	39.28	-12.90	CDMS	$<2.44 \times 10^{12}$	$<1.72 \times 10^{19}$
l-H ₂ CCCO	111.69	56.58	14.56	-14.62	JPL	$<2.28 \times 10^{10}$	$<1.86 \times 10^{11}$
	128.93	7.57	20.92	-13.24	JPL	Flagged	Flagged
H ₂ CS ^{†*}	104.46	77.39	3.99	-13.87	CDMS	$<5.52 \times 10^{12}$	$<5.39 \times 10^{14}$
H ₂ C ₂ S	114.96	14.03	4.59	-14.04	CDMS	$<1.32 \times 10^{13}$	$<5.32 \times 10^{13}$
HCCCH ₂ OH	118.06	195.95	1.67	-15.23	JPL		
	125.00	71.74	1.72	-14.77	JPL	$<7.47 \times 10^{12}$	$<1.31 \times 10^{14}$
	125.91	134.32	1.87	-14.95	JPL	Flagged	Flagged
	129.90	239.05	2.18	-15.01	JPL	Flagged	Flagged
HCCCHO	107.54	256.84	5.80	-14.86	SLAIM		
	117.22	95.85	5.71	-14.51	SLAIM	$<1.71 \times 10^{12}$	$<1.71 \times 10^{15}$
t-HONO	105.03	22.35	4.43	-14.07	JPL	Flagged	Flagged
t-HCOOD [†]	106.19	123.92	4.95	-14.56	JPL	$<6.16 \times 10^{12}$	$<1.12 \times 10^{14}$
HD ¹³ CO [†]	129.09	41.13	18.23	-13.04	JPL	$<2.21 \times 10^{12}$	$<4.00 \times 10^{12}$
NH ₂ CH ₂ CH ₂ OH	103.09	124.82	31.85	-14.00	JPL	Flagged	Flagged
	106.87	82.74	29.42	-13.90	JPL	Flagged	Flagged
	107.84	100.59	5.33	-14.72	JPL		
	114.75	41.80	4.12	-14.57	JPL	$<1.69 \times 10^{12}$	$<1.37 \times 10^{13}$
	123.20	171.85	6.17	-14.60	JPL		
¹⁵ NO	105.74	18.61	<0.01	-18.31	CDMS	Flagged	Flagged
	120.27	6.99	<0.01	-18.93	CDMS	$<5.11 \times 10^{12}$	$<7.12 \times 10^{13}$
N ¹⁷ O	105.34	0.01	0.01	-16.48	CDMS	$<5.84 \times 10^{14}$	$<2.07 \times 10^{14}$
	108.52	191.69	0.01	-16.53	CDMS		
	109.20	0.01	0.04	-16.23	CDMS		
	114.46	191.69	0.01	-16.39	CDMS	Flagged	Flagged
N ¹⁸ O	107.31	6.87	<0.01	-18.49	CDMS	$<5.73 \times 10^{12}$	$<5.99 \times 10^{13}$
¹⁵ N ¹⁷ O	109.17	54.93	<0.01	-17.13	CDMS		
	109.34	54.21	<0.01	-17.14	CDMS	$<5.63 \times 10^{14}$	$<2.78 \times 10^{16}$
	109.48	142.24	0.01	-17.12	CDMS	Flagged	Flagged
	129.78	79.04	0.01	-16.97	CDMS		
c-SiC ₃ [*]	112.70	35.16	48.77	-13.32	SLAIM	$<7.79 \times 10^{11}$	$<7.54 \times 10^{12}$
	114.62	86.28	50.42	-13.52	SLAIM	Flagged	Flagged
	124.02	292.73	56.67	-13.66	SLAIM	Flagged	Flagged

◇SLAIM-Spectral Line Atlas of Interstellar Molecules (NRAO Splatologue), JPL-Jet Propulsion Laboratory Spectral Line Catalogue, (Pickett et al., 1998), CDMS-Cologne Database for Molecular Spectroscopy (Müller et al., 2001), TopModel-(Carvajal et al., 2010)

† Molecule detected in star-forming regions as per the NIST Spectral Database (Lovas et al., 2003)

* Molecule detected in evolved stars as per the NIST Spectral Database (Lovas et al., 2003)

36 per cent. Also, with the 3 km baselines, the FWHM of the synthesised beam is 3 arc min, resulting in a large beam dilution factor for objects in or near the Galactic centre, as determined by a ratio of solid angles.

The beam dilution could be mitigated by increased integration time. For this survey, the addition of the data observed in 2016 and integrated with the observations from 2014, demonstrated the continuation of the sensitivity increase as a function of square root of time, as expected from the radiometer equation. In order to obtain the sensitivity to match the column densities set by higher frequency observations, we would need to observe for 65 to 100 hours for a five sigma detection (see Figure 4.6). This is the same order of magnitude determined by Codella et al. (2015) for integration time required to observe complex organic molecules with SKA1-Mid at around 1 GHz. However, any stimulated emission would boost the detectability and therefore, reduce the required amount of integration time. In the context of this survey, with four hours of total integration time, we are only sensitive to unique stimulated environments.

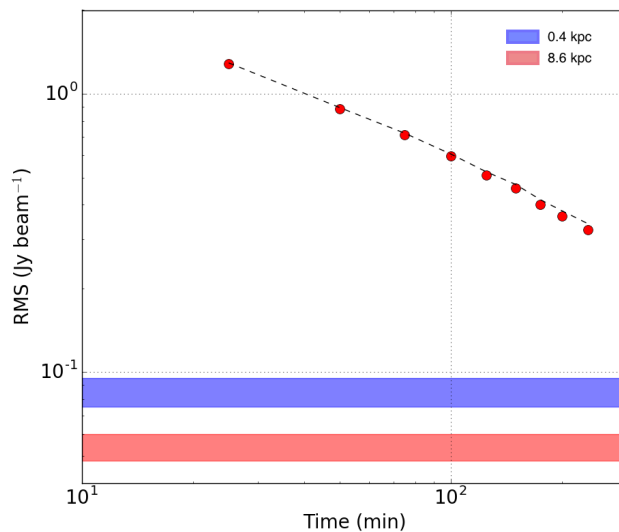


Figure 4.6: A plot of RMS noise against integration time, where red dots show the RMS versus time and the dashed line indicates the trend of square root of time. Therefore, more time integration on the same source should give improvement for possible detections. The blue and red shaded bars show the estimated sensitivity to start detecting thermal emission at a distance of 0.4 kpc and 8 kpc (approximate distance to the Galactic Plane) respectively.

The MWA is undergoing an upgrade to add baselines of lengths up to 6 km, which reduces the beam size and therefore the beam dilution. This would increase

the angular resolution to 1.6 arc minutes, could increase the sensitivity to less abundant molecules and increase our ability to resolve the regions in which the molecules are detected.

Telescopes observing around 100 MHz are strongly influenced by the ionosphere, causing changes in the apparent position of the sources. As discussed in Section 2.1.2, this was corrected with a single correction factor for each snapshot observation. However, with longer baselines, not all of the dipoles will be observing the same isoplanatic patch of the ionosphere and different tools will need to be utilised.

The biggest challenge in this style of work with the MWA and possibly with the future SKA-Low is the spectral sensitivity. The aliasing from the polyphase filterbank reduced the number of transitions we could detect and the spectral shape of each fine channel reduced our sensitivity to transitions near the edges of the fine channels. This is especially apparent with the channel resolution of 26 km s^{-1} , where most spectral line transitions have a velocity of only a few kilometres per second.

Overall, the setup of the MWA during this survey, combined with the amount of integration time and beam dilution, made us sensitive only to bright stimulated transitions with broad velocity components. Although we have estimated there are likely upwards of 1100 potential sources with potential molecular transitions, these restrictions reduce our chance of detection, but it is difficult to predict by how much, as the expected intensity of the transitions and abundance of the molecules is unknown.

4.7 Summary and Conclusions

The goal of this pilot survey was to assess the feasibility of using low frequency telescopes to observe spectral lines, develop a method for observing molecular lines with the MWA and search for molecular lines in and around the Galactic Centre. From the setup of the MWA described in Section 2, we are only sensitive to bright molecular transitions with broad excitation. Therefore, there is likely a selection effect to only detect molecules in extraordinary environments. The excitation in these environments is likely non-thermal in emission, as the brightness temperatures are determined to be $>1000 \text{ K}$, suggesting either quasi-thermal or maser type emission and absorption.

In this survey, any peak of over 6σ local RMS in the blind search and 5σ

in the targeted search for NO and SH, was cross-matched with known molecular lines and known sources. We have tentatively detected SH and NO in evolved stars at a level of 5σ . However, since both molecules only have a single transition observed in a single channel, they are considered tentative. The column densities calculated are similar to those reported in other surveys, when a correction for beam size is applied.

The RMS decreases with respect to the square root of time. To match the column densities reported in other radio surveys for NO, and to take into account our beam dilution, we would need approximately 30 hours of observations with the MWA to obtain a five sigma detection, assuming standard thermal emission or absorption processes at distances of around 400 pc and 65–100 hours for detections at distances closer to the Galactic Centre. Therefore, the next stage of assessing the low-frequency sky is to complete a full survey of the Orion region from 99–270 MHz. Orion is known as a unique environment with a mix of star-forming and evolved stars, at a distance of approximately 400pc.

At low radio frequencies we are more likely to detect maser activity than is possible at the higher frequency as the emission strengths are independent of temperature of the emitting gas and maser activity is possible with only a small population inversion (Spitzer, 1998). This significantly increases the detectability of molecular transitions. However, it is unknown if all detectable transitions would be stimulated or not.

Overall, the analysis and tentative detections show that it is feasible to detect molecules with the new generation of low-frequency instruments.

4.8 Acknowledgments

CDT would like to thank Steven Tremblay for very helpful discussions about low frequency radio astronomy. Parts of this research were conducted by the Australian Research Council Centre of Excellence for All-sky Astrophysics (CAASTRO), through project number CE110001020. This work was supported by resources provided by the Pawsey Supercomputing Centre with funding from the Australian Government and the Government of Western Australia.

This scientific work makes use of the Murchison Radio-astronomy Observatory, operated by CSIRO. We acknowledge the Wajarri Yamatji people as the traditional owners of the Observatory site. Support for the operation of the MWA is provided by the Australian Government (NCRIS), under a contract to

4.9 Appendix: Column Density

Column density is a quantity used in understanding the physical and chemical nature of an object, as well as a starting point for analysis of isomer ratios, isotopomer ratios, and chemical composition (Mangum and Shirley, 2015). The calculation of the column density in the energy at the upper excitation level level (N_u), when the optical depth is assumed to be small and the lines are in emission, is given by:

$$N_u = \frac{8k\pi\nu^2}{A_{ul}hc^3} \int T_b dv \quad (4.1)$$

where ν is the rest frequency, k is Boltzmann's Constant, h is Planck's constant, c is the speed of light, and $\int T_b dv$ represents the integrated intensity of the spectral line along the velocity axis (v). The Einstein coefficient for the transition, A_{ul} , is calculated using the formula:

$$A_{ul} = \frac{16\pi\nu^3}{3\varepsilon_0hc^3}\mu^2 \quad (4.2)$$

where ε_0 is the permittivity of free space and μ is the electric dipole moment for a pair of opposite charges. For molecules that have multiple dimensional components, the vector sum is calculated by taking the square root of the summation of the squares of each dimensional value.

The total column density (N_{tot}) can then be calculated by:

$$N_{tot} = \frac{N_u}{g_u} e^{\frac{E_u}{kT}} Q_{rot}(T_{ex}) \quad (4.3)$$

where E_u is the energy in the upper excitation state and g_u is the total degeneracy term for the energy of a particular transition. We also make the assumption that the observed molecule has a single excitation temperature, $T_{ex}=T_{rot}$ (Hildebrand, 1983). The Q_{rot} is the rotational partition function at an assumed temperature, for which we use 9.375 K based on the analysis done by Jones et al. (2013) that showed that T_{ex} of 10 K is reasonable for the central molecular zone. However, assuming a excitation temperature of 18 K would increase the total column density by approximately 12. The Q_{rot} , E_u and g_u values are taken from the CDMS.

When the transitions are in absorption, a correction to the total column density must be made to account for the strong continuum. As described by Comito et al. (2003), the total column density (N_{tot}) then becomes:

$$N_{\text{tot}} = \frac{8\pi\nu^3}{A_{\text{ul}}c^3} \frac{g_l}{g_u} \tau \Delta v \quad (4.4)$$

where Δv is the change in velocity across the transition and τ is the optical depth defined as:

$$\tau = -\ln\left[1 - \frac{T_L}{T_C}\right] \quad (4.5)$$

The value of T_C is the brightness temperature of the continuum which is derived from scaling the Haslam 408 MHz (Remazeilles et al., 2015) map to the frequency of the molecular line, using a spectral index of -2.5 (Zheng et al., 2017). T_L is the brightness temperature of the spectral line, using the Rayleigh-Jeans approximation. All values and constants use standard (SI) units.

A standard assumption in the calculation of column density is that the source fills the telescope synthesised beam (Herbst and van Dishoeck, 2009). When this assumption is not valid, beam dilution occurs, and a correction must be made. The FWHM of the synthesised beam for the MWA at 120 MHz is three arc minutes and the objects of interest may be much smaller. The column densities can be scaled to the assumed size of the source by a ratio of solid angles.

With a channel resolution of 26 km s^{-1} , it is expected that most lines will emit in a single channel. However, the area under the curve used in determining the integrated intensity will be preserved when compared to higher spectral resolution instruments in which emission will span multiple channels. Therefore, no correction is required for channel smearing.

Chapter 5

A Molecular Line Survey around Orion At Low Frequencies with the MWA

This work, as written, was published by:

Tremblay C. D., Jones P.A., Cunningham M., Jordan C. H., Hurley-Walker N. “A Molecular Line Survey around Orion at Low Frequencies with the MWA” *The Astrophysical Journal*, 2018 June 20, Volume 860, 145 (9pp)

Although this Chapter represents a published paper, edits have been made in response to the thesis examiners. Therefore, it is not an exact replica of the original publication. Every effort is made to maintain the integrity of this work as required by the copyright statements in the appendix of this thesis.

5.1 Abstract

The low-frequency sky may reveal some of the secrets yet to be discovered. Until recently, molecules had never been detected within interstellar clouds at frequencies below 700 MHz. Following the pilot survey toward the Galactic center at 103–133 MHz with the Murchison Widefield Array, we surveyed 400 deg² centered on the Orion KL nebula from 99 to 170 MHz. Orion is a nearby region of active star formation and known to be a chemically rich environment. In this paper, we present tentative detections of nitric oxide and its isotopologues, singularly deuterated formic acid, molecular oxygen, and several unidentified transitions. The three identified molecules are particularly interesting, as laboratory experiments have suggested that these molecules are precursors to the formation of

amines.

5.2 Introduction

New low-frequency aperture arrays in radio-quiet environments, like the Murchison Widefield Array (MWA), allow for simultaneous observations of thousands of stars and starforming regions in a single field of view (FOV). In Tremblay et al. (2017), we completed a pilot survey of the Galactic center to determine the practicality of using the MWA to observe spectral lines. In a blind survey of 400 deg², we tentatively detected transitions of nitric oxide and the mercapto radical in evolved stars. However, based on the detection limits for the column densities of other potential transitions within the band, it was concluded that observing a region at a distance of 400 pc (in comparison to the Galactic center that is 8600 pc away) would reduce the beam dilution by an order of magnitude. The increased sensitivity would potentially allow for detections of even more molecules.

The Orion molecular cloud represents a nearby (414 ± 7 pc Menten et al. 2007) active star formation region whose population of stars, young and old, are used for studying star formation and high-mass stars (O’Dell et al., 2015). The proximity and complex structure of Orion make it both a critical testing ground for theoretical models and for the interpretation of results from more distant star forming regions (Muench et al., 2008).

In a single survey of the Orion Kleinmann–LowNebula (Orion KL) from 80 to 280 GHz using the IRAM 30 m telescope, approximately 15,400 spectral features were detected with 11,000 identified from 50 different molecular species (Tercero et al., 2015). Although these observations were completed at much higher frequencies, they demonstrate the chemically rich nature of the region. As most of the interstellar molecules so far detected can be found in the Orion molecular cloud complex (Baudry et al., 2016), it is an ideal location for a spectral line survey with a new telescope.

Currently, our understanding of the formation of high-mass stars is limited (Tan et al., 2014) due to the dust opacity of the HII region surrounding the star and the significant overlap of spectral features observed at high-radio frequencies. Codella et al. (2015) suggested that the observation of these regions at low frequencies may be key to disentangling the complex molecular structure as the spacing between transitions increases. Also, the low-energy transitions of long chain molecules reside at low radio frequencies.

High-frequency observations made with telescopes such as IRAM 30 m mainly detect thermal transitions. However, at low frequencies the detected transitions are mainly from emission that is directly related to the number of atoms in a given state, making the detection of boosted emission a more likely scenario (Spitzer, 1998; Salgado et al., 2017a). This has the potential of yielding new understanding of this complex environment.

This paper details the molecular line survey centered on the Orion KL, the brightest object within the Orion molecular cloud (Neill et al., 2013), and the results of these candidate detections made with the MWA.

5.3 Observations and Data Reduction

The observations were carried out using the Murchison Widefield Array (MWA, Tingay et al. 2013) located at the Murchison Radio-astronomy Observatory, on 2015 November 21 and 22. The observations of the Orion region, centered on $05^h35^m17.3^s -05^\circ23'28''$ (Figure 6.1), were broken up into two continuous frequency bands with central frequencies of 114.6 and 155.5 MHz. At the time of these observations, the telescope had 128 dipole tiles, spread across 3 km with a primary beam of 30 degrees full width at half maximum (FWHM) and a synthesized beam of 2.1 arc minutes FWHM at 150 MHz.

The MWA uses a two-stage polyphase filter bank to channelize the data. The first stage separates the 30.72 MHz bandwidth into 24×1.28 MHz coarse channels while the second stage breaks up each coarse channel to 128×10 kHz fine channels. For this survey, the velocity resolution of each 10 kHz spectral channel within the 99–129 MHz frequency band ranged from 23 to 30 km s^{-1} and 17 to 20 km s^{-1} at 140–170 MHz. Doppler correction terms are currently not incorporated into the MWA imaging pipeline; however, the velocity uncertainty is 3.4 km s^{-1} , which is significantly less than the channel width of the MWA.

Data processing is completed using the pipeline published and explained by Tremblay et al. (2017) (Figure 5.2). However, we will highlight here some different data reduction considerations made for the Orion field.

The MWA tiles are electronically steered so two-minute snapshot imaging was used to keep the Orion KL Nebula within the most sensitive regions of the primary beam. Due to the large FOV of the MWA, other bright sources in the grating sidelobes of the primary beam can make a significant contribution to the image noise. The primary difference in data processing from the Galactic cen-

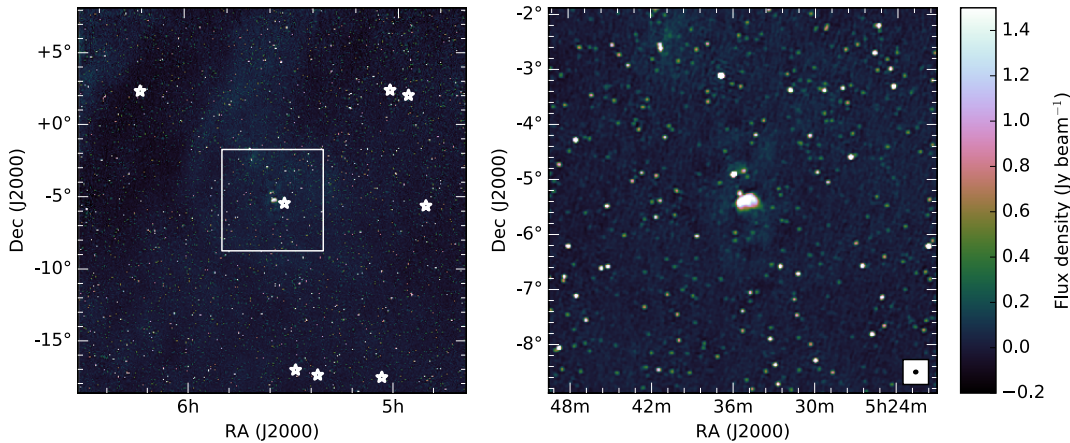


Figure 5.1: Continuum image of the Orion survey region MWA across the 30.72 MHz of bandwidth with a central frequency of 114.6 MHz. The left hand image represents the full region blindly searched for molecular signatures (see Section 4). The right-hand image is a zoom of the region showing the Orion KL nebula in the center of the observed region. The white stars show the positions of the tentative detections reported here.

ter, shown in black in Figure 5.2, is that the Crab Nebula (R.A.= $05^h34^m34.94^s$ decl.= $+22^\circ00'37.6''$, J2000; 1256 Jy at 160 MHz) was in the sidelobes of the primary beam. Therefore, we adopted the procedure developed during the GaLactic and Extragalactic All-sky Murchison Widefield Array (GLEAM) survey (Hurley-Walker et al., 2017), to “peel” the Crab nebula from the visibilities.

The compact core of the MWA increases our sensitivity to diffuse emission within our Galaxy that is intensified at low radio frequencies due to the increased brightness temperature produced by synchrotron radiation. So even though natural weighting can be used to reduce the background noise in an image, the extended emission posed a challenge for continuum subtraction. Therefore, natural weighting was not used to produce sky images. Uniform weighting would provide a smaller synthesized beam, thus reducing the beam dilution of signals from compact sources. However, by using uniform weighting, centre we may be less sensitive to carbon recombination lines known to trace the diffuse cold interstellar medium. Due to the large volume of data contained within this survey, the data were not processed multiple times using different weighting schemes. Instead the images of each coarse (1.28 MHz) and fine (10 kHz) channel were created using WSCLEAN (Offringa et al., 2014) with Briggs grid weighting with a robust value of “-1” (Briggs, 1995), a compromise between image resolution and sensitivity.

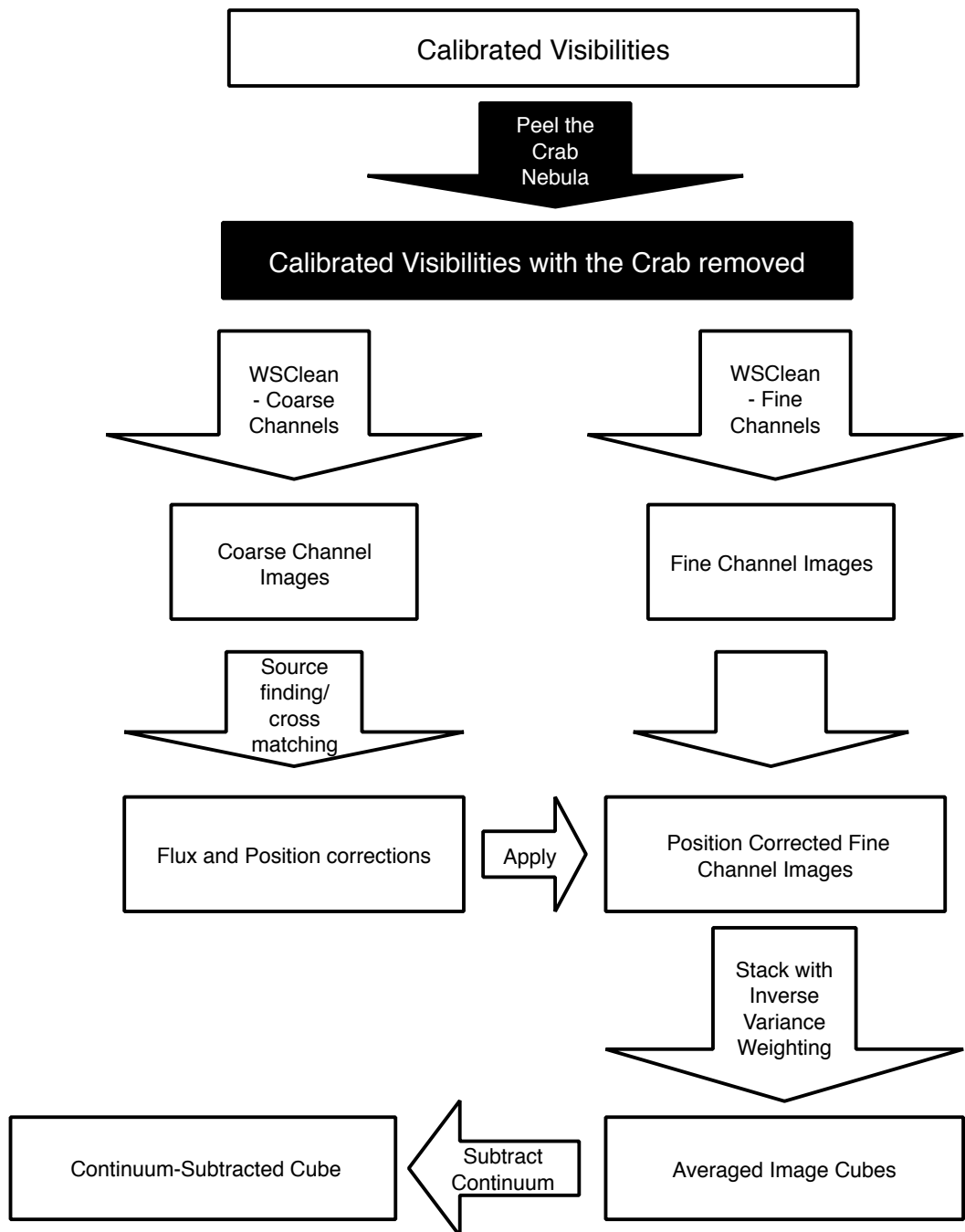


Figure 5.2: Summary of the pipeline designed to create calibrated time-averaged spectral image cubes with the MWA. In black are the additions to the pipeline that differ from the Galactic Center survey reported by Tremblay et al. (2017).

The images from each coarse channel were used to check the flux density scale of observed sources in the integrated continuum image, compared to those published in the GLEAM catalog, and was found to have a mean difference of 0.1%.

The refractive effect of the ionosphere on incident electromagnetic waves is proportional to the wavelength squared. This causes an apparent shift in radio source positions which increases in magnitude at the lower end of our band. Therefore, a correction is built into the data processing pipeline to correct for these distortions. Single positional R.A. and decl. offsets were applied to each fine channel of each observation based on a comparison of the source positions within the GLEAM catalog at 200 MHz (see Figure 5.2). After correction, the observations of 2015 November 22nd had mean residual positional offsets of -1 ± 17 arcsec in right ascension and 5 ± 17 arcsec in declination. Although the distribution is large, without the correction, the smearing of the point spread function would be larger than 10%, impacting the source structure. The observations on the 2015 of November 21st had less than one arc second source offsets when compared to GLEAM, so no corrections were performed. After time-averaging all observations, the ratio of integrated flux density to peak flux density is calculated from extragalactic continuum sources within the image to be 1.01 ± 0.07 , suggesting the ionosphere is adequately corrected.

The individual fine channels, as shown in Figure 5.2, are corrected for the ionospheric effects that are derived in each coarse channel for each observation. Due to aliasing of the polyphase filter bank, only 2400 of the 3072 fine (22%) channels are imaged within the analysis pipeline. The channel images are built into a data cube and each observation was phase centered to the Orion KL Nebula prior to stacking. This created a final integrated image of 180 minutes for each frequency band.

5.3.1 RFI Flagging

The observation at 140–170 MHz, on 2015 November 21st, was significantly impacted by radio frequency interference (RFI). Standard conditions at the observatory are radio quiet between 100–200 MHz (Offringa et al., 2015; Sokolowski et al., 2017) with the exception of ORBCOMM¹ at 135 MHz, but transient RFI on November 21st affected 98% of the data. Therefore, only the first 2 MHz in this frequency band is surveyed for spectral transitions. The observations from

¹A family of American low Earth orbit satellites responsible for machine to machine communication.

99–129 MHz on 22nd November did not suffer from the same RFI problems.

RFI flagging is completed in a two-stage approach to ensure any signal that is likely due to terrestrial communication is removed. The first stage flagged the visibility data using AOFLAGGER (Offringa et al., 2016) to remove RFI by a statistical method in each 2-minute snap-shot observation. As we would expect any astronomical sources to produce a weak signal in a 2-minute observation over 10kHz, the assumption is that any bright signals are likely associated with terrestrial communications. AOFLAGGER removed <1% of the fine channels from the individual observations at 99–129 MHz and approximately 8% of the channels in the observations at 140–170 MHz.

The RMS in the center of most continuum-subtracted images is 0.4 Jy beam^{-1} . To manually flag channels with spurious RFI, the image RMS is calculated for each continuum-subtracted spectral fine channel within a 300×300 pixel box in the middle of the fine channel continuum-subtracted image and any channel containing an $\text{RMS} > 0.6 \text{ Jy beam}^{-1}$ is flagged². After the two-stage RFI removal in the final cubes, the 2400 imaged channels in each frequency band are reduced to 1240 surveyed in the 99–130 MHz data and to 200 surveyed channels in the observations at 140–172 MHz ($\approx 55\%$ of the imaged bandpass).

5.4 Survey Strategy

As this survey covers a wide FOV and a large frequency range, an automated pipeline was developed to detect spectral signals in emission or absorption in the data, filter the data based on quality, and then determine if the detections are associated with known molecular transitions. We note that the search strategy explained here is different from the pilot survey and represented the next logical progression on completing large molecular line surveys with the MWA.

The primary beam is the sensitivity pattern of the interferometer on the sky. The 625 square degrees (Figure 6.1) imaged region around Orion is reduced using MIMAS (Hancock et al., 2012) to ensure only the most sensitive region of the primary beam (the central $\approx 65\%$ or down to ≈ 400 square degrees) is surveyed.

Each of the 1440 continuum-subtracted fine-channel (10 kHz) images are independently searched using the source-finding software AEGEAN (Hancock et al., 2012, 2018) using the function “slice” to set which channel in the cube is searched

²We note that by removing channels based on image RMS we may remove channels with increased spectral signals. However, since these observations are in the same band as commercial radio, we have taken this conservative approach.

and a “seed clip” value of 5, which searches the image for pixels with a peak flux density value greater than 5σ in comparison to an input RMS image. For the search in absorption, the option “negative” was used to search for sources with negative flux densities. The input RMS image is a map of the spectral RMS value at each pixel position within the continuum-subtracted data cube created for the coarse channel (100 fine channels) searched.

Within the 95000 (3-arc minute FWHM) independent synthesized beams over the 400 square degree FOV and 1440 channels searched using AEGEAN we found 174 potential detections in emission and absorption. To publish only the most reliable detections, the catalogs of potential detections were further evaluated (or filtered) on two additional criteria; the spectral RMS and the difference between the image and spectral RMS, at the location of the spectral line detection.

The mean spectral RMS across the frequency band is 0.3 Jy beam^{-1} and a filter of a spectral RMS of $<0.5 \text{ Jy beam}^{-1}$ threshold is applied to the catalog of potential detections to remove the chance of false detection due to poor continuum subtraction or image artefacts. To assess the impact of filtering the cataloged results based on the spectral RMS, we search the RMS map used in the AEGEAN search to find the percentage of the data impacted by this threshold. This reduced the effective search volume by 85–90%, depending on the coarse channel.

In order to simplify the statistics to regions that demonstrate Gaussian behavior, the catalog of potential detections was further filtered to signals where the spectral signal-to-noise ratio (S/R) and image S/R both show a signal that is at least 5 and the ratio of the two RMS values (spectral and image) are within 20% of each other. On average, this reduced the effective search volume by 74%.

By using two-sided Gaussian statistics at a threshold of 5σ , and filtering the catalog as described above, we would expect no more than one signal to be a potential false positive. However, we found 11 positions on the sky, with 13 signals, that passed these criteria.

We note here that AEGEAN uses a Gaussian fit to the pixel data and a correction of the background to calculate the flux density for these potential detections. However, to make the spectrum reported here, the peak flux density represents the flux density at the pixel position of potential detection as reported by AEGEAN. Therefore, it is possible that the flux densities shown in each spectrum are underestimated, and their significance is greater than as listed. Our false positive rate may also be a slight overestimate as a result.

All 13 signals meeting our selection criteria were compared to known molecular and atomic transitions within the databases: Cologne Database for Molecular

Spectroscopy (CDMS; Müller et al. 2001); Spectral Line Atlas of Interstellar Molecules (SLAIM; Splatalogue³); Jet Propulsion Laboratory (JPL; Pickett et al. 1998); and Top Model (Carvajal et al., 2010), for known transitions within three spectral channels ($\approx 75 \text{ km s}^{-1}$ at 114 MHz) of the detected signal. Additionally, the source positions were searched in SIMBAD (Wenger et al., 2000) for plausible source emission environments, like evolved stars or nebula, within the synthesized beam.

There are 273 known recombination and molecular transitions with upper level energy divided by the Boltzmann constant less than 300 K (See section §4) within the 99–129 MHz band and 25 known transitions from 140–142 MHz, with 58% of the known transition contained in flagged channels. Therefore, we would expect no more than one signal greater than 5σ within the 33 MHz observed or a 0.06% chance any 5σ signal, within ± 3 channels of a known transition, is random noise. When multiple transitions of a particular molecule are cospatially located and at the same relative velocity, the chance of the signals being noise is decreased to less than 0.01%.

If the detected signals are also associated with a known optical or infrared source that could feasibly create molecular emission, the chance that the signal is from noise is further decreased. However, we make no assumption here regarding what the line-generating source density of the region is, as no large regional molecular surveys have been performed. This is further complicated as there is a non-negligible chance that a molecular transition could be associated with a source not visible in optical or infrared surveys.

Of the 13 signals passing our selection criteria, we found 8 that are associated with known molecular transitions, 3 are unidentified, and 5 are associated with known recombination lines. In this paper, we report on the molecular and unknown signals. For information regarding the recombination lines see Tremblay et al. (2018).

5.5 Results and Discussion

A blind search, in emission and absorption, was completed as discussed in Section 3. This corresponds to a mean flux density limit of $\approx 1.2 \text{ Jy beam}^{-1}$ within the center of the primary beam. The search yielded detections of 13 signals in 11 locations. In this paper, we discuss the eight signals associated with known

³www.splatalogue.net

molecular transitions and three unidentified signals.

Within the frequency bands of 99–129 and 140–141 MHz there are 203 known molecular transitions from 18 molecules with upper state energies divided by the Boltzmann constant of 300 K. Although, the excitation mechanisms are not well understood at these frequencies, we consider this to be a reasonable limit and it reduces our chances of erroneous associations. Of the 3072 fine channels within each band, only 1440 fine channels were used across the two bands due to instrumental effects and RFI. This reduced the number of transitions detectable in this survey by 58%.

Here we report tentative detections of Nitric Oxide (NO), a deuterated form of Formic Acid (*t*-DCOOH), Molecular Oxygen (^{17}OO), and other unidentified molecular transitions. As this is a new frequency range for this style of work, additional modeling and laboratory experiments are required to broaden the knowledge of detectable isotopologues.

The column densities for the signals in absorption and emission are calculated using the equations in the Appendix of Tremblay et al. (2017). For each transition, we use the partition function and upper level degeneracy, for low temperatures (<10 K), as quoted in the CDMS catalog. We do note that since these tentative detections have brightness temperatures of over 4000 K, so the column densities may not be physical quantities. Instead, maser or other boosted emission mechanisms may be involved. However, the values are provided to compare these tentative detections with detections of similar molecules in other frequency ranges.

5.5.1 Nitric Oxide Tentative Detections

Both nitrogen and oxygen are among the most common elements in the Galaxy. Despite their relative abundance, the detection of nitric oxide (NO) is rare. This gas-phase molecule is detected toward star-forming regions (Liszt and Turner, 1978; Gerin et al., 1992) and the circumstellar envelope (CSE) of evolved stars (Quintana-Lacaci et al., 2013; Velilla Prieto et al., 2015; Tremblay et al., 2017) with an expected formation chemistry from nitrogen atoms colliding with hydroxyl (OH) molecules (Hily-Blant et al., 2010).

The spectra in Figure 5.3 and the data in Table 5.1 show multiple detections of NO and its isotopologues in three stellar environments that are plausible sources of the molecule. We have tentatively detected N^{17}O at 107.82 MHz and 107.17 MHz and $^{15}\text{N}^{17}\text{O}$ at 102.04 MHz. We also potentially detected a weak (3σ)

Table 5.1: Information on the nitric oxide transitions tentatively and possibly detected in this survey. The source name and type, as displayed in SIMBAD, is listed in the first column. The first section of rows provides information regarding the transitions including the rest frequency, the energy in the upper level state, the Einstein coefficient (A_{ij}), and the quantum numbers. The following rows are information regarding the the peak pixel position in J2000 and Galactic coordinates and the column densities, assuming thermal emission and absorption (see §4 for more details).

Source		$^{15}\text{N}^{17}\text{O}$	N^{17}O	N^{17}O	NO
Line Parameters	Rest Frequency (MHz)	102.04	107.17	107.82	107.36
	E_U/k_B (K)	191.15	191.68	187.32	7.24
	$\text{Log}_{10}(A_{ij})$	-16.62	-16.48	-17.30	-17.3
	Quantum Numbers	$J=\frac{5}{2}-\frac{5}{2}$	$J=\frac{3}{2}-\frac{3}{2}$,	$J=\frac{15}{2}-\frac{15}{2}$,	$J=\frac{3}{2}-\frac{3}{2}$,
		$p=-1-1$	$\Omega=\frac{3}{2}$	$\Omega=\frac{3}{2}$	$\Omega=\frac{1}{2}$
	$F_1=3-4, F_2=3-4$	$F_1=\frac{5}{2}^+-\frac{7}{2}^-$, $F_2=\frac{3}{2}^+-\frac{5}{2}^-$	$F_1=\frac{13}{2}^+-\frac{15}{2}^-$, $F_2=\frac{15}{2}^+-\frac{17}{2}^-$	$F=\frac{5}{2}^+-\frac{3}{2}^-$	
CRTS J0457275 +015840	Position (J2000)	4h57m32s +01°56'53''			
W UMA Eclipsing Binary	Position (Galactic)	197.196 -24.117			
	Velocity (km s^{-1})	-56±28			
	N_u (cm^{-2})	1.2×10^{21}			
	N_{tot} (cm^{-2})	1.1×10^{23}			
UCAC2 25008117	Position (J2000)	5h22m12s -17°33'02''			
Evolved Star	Position (Galactic)	219.614 -27.363			
	Velocity (km s^{-1})	-56±28		-56±28	
	N_u (cm^{-2})	6.9×10^{20}		9.5×10^{20}	
	N_{tot} (cm^{-2})	3.3×10^{23}		8.5×10^{22}	
BD-17 1144	Position (J2000)	5h28m37s -17°12'21''			
Evolved Star	Position (Galactic)	219.903 -25.815			
	Velocity (km s^{-1})	-94±32			
	N_u (cm^{-2})	1.6×10^{21}			
	N_{tot} (cm^{-2})	4.1×10^{23}			

All transition values are from the CDMS – Cologne Database for Molecular Spectroscopy Database (Müller et al., 2001)

peak of NO at 107.36 MHz in both emission and absorption. The three signals at G219.61 –27.36 are all around 3–4 σ but they are still of interest as they are all known transitions of NO at the same peak pixel position, reducing the chance that these signals are purely the result of noise.

The column density for the NO absorption peak at 107.36 MHz is similar to the column densities of the detection of the same transition in evolved stars in the Galactic Center survey by Tremblay et al. (2017) and are within the same order of magnitude of the NO column density in an evolved star detected by Quintana-Lacaci et al. (2013).

In the three stellar objects listed in Table 5.1, no other molecular studies or detections within these objects have been published.

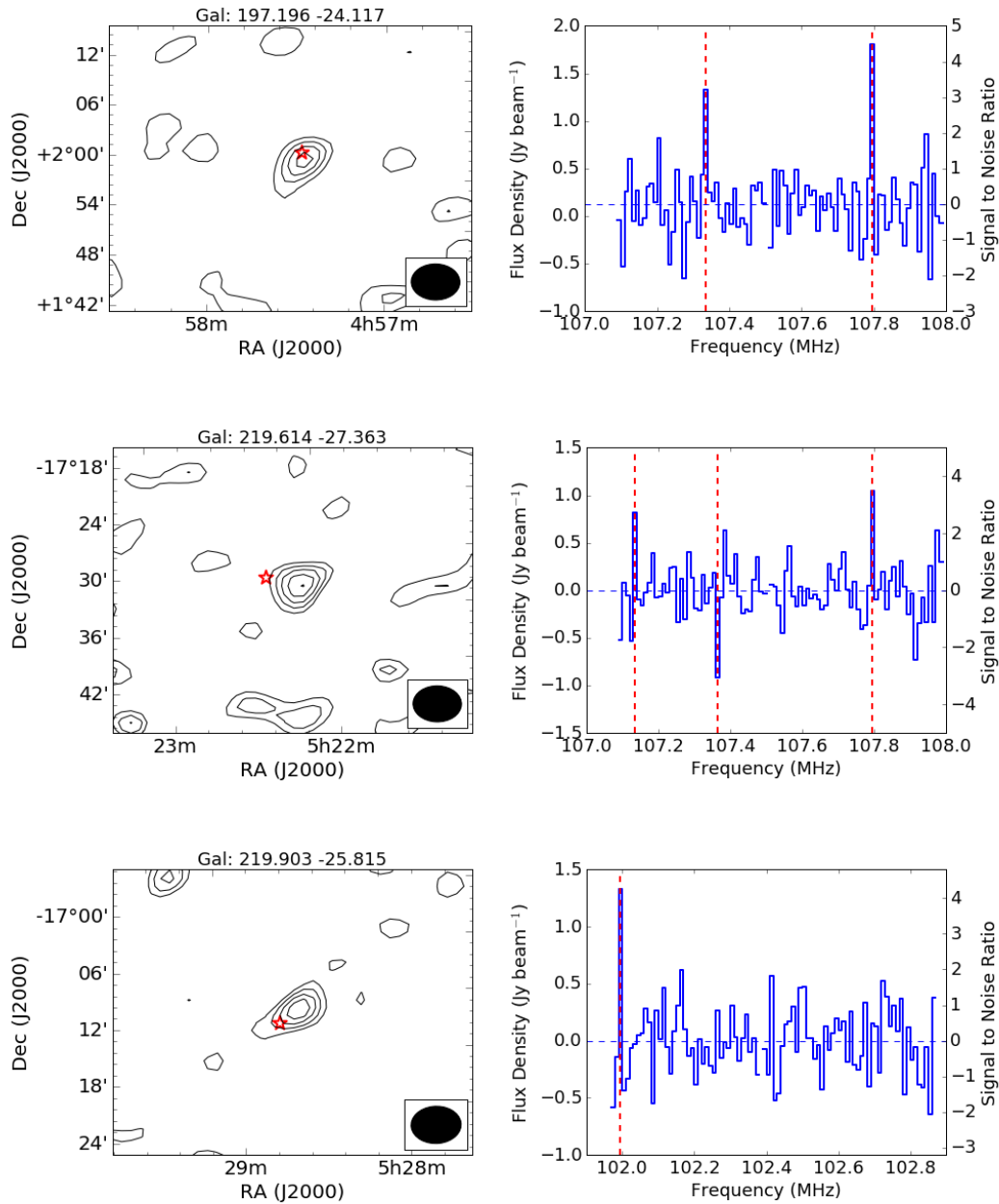


Figure 5.3: Tentative detections of nitric oxide in three stellar objects. The spectra on the right represent the full coarse channel data cube in which the tentative detections were made. The left panel shows the contours, set at 2, 3, 4, 5, and 6 σ of the continuum-subtracted image RMS, of the detection of the brightest signal. The ellipse in the lower right-hand corner of the contour plot shows the size and shape of the synthesized beam. The red star is the optical position for a plausible source associated with the signal. The size of the red star is the 1 σ astrometric error.

5.5.2 Formic Acid Tentative Detection

The smallest of the organic acids, formic acid, is an abundant gas-phase molecule (Bisschop et al., 2007) observed in regions of star formation and quiescent clouds (Bennett et al., 2011; Linnartz et al., 2015). While the formation routes are debated, laboratory experiments have shown that formic acid can form through hydrogenation of the H–O C–O complex at low temperatures in oxygen rich environments (Ioppolo et al., 2011).

We have tentatively detected a singly deuterated form of formic acid (t -DCOOH), where one of the hydrogens is replaced with deuterium (also known as heavy hydrogen or ^2H), a stable isotope of hydrogen formed during Big Bang Nucleosynthesis. The spectra of the tentative detection at 140.5 MHz (Figure 5.4) is not associated with any known source contained in SIMBAD but is located within the Orion molecular cloud. Deuterated species are expected to be enhanced in cold regions of early star formation (Neill et al., 2013), so this may not be surprising.

Theory suggests that the ratio of D/H is $\approx 10^{-5}$ (Lacour et al., 2005) but Neill et al. (2013) found regions of the enhanced D/H ratio in the Orion molecular ridge to be $\approx 5 \times 10^{-3}$. These enhanced regions D/H are correlated with the first cold prestellar phase of star formation (Skouteris et al., 2017) because of the CO depletion onto the surface of dust grains, which makes deuterated molecules important for studying the dynamics of molecular clouds (Das et al., 2015).

The column density, in Table 5.2 of 3.6×10^{20} is higher than other deuterated species calculated by Neill et al. (2013) with the difference possibly due to the boosted emission likely detected at low frequencies (Spitzer, 1998). One other known transition of this molecule within our frequency band is at 124.80 MHz and is a channel flagged in these observations.

5.5.3 Molecular Oxygen Tentative Detection

Oxygen is the most abundant heavy element in our Galaxy and is expected to be primarily tied up in CO, O₂ and H₂O, with O₂ following closely with the abundance of CO (Goldsmith et al., 2011). Due to the water in the troposphere around Earth and oxygen in our atmosphere, the detection of O₂ and H₂O within the Milky Way at high frequencies is difficult with millimeter-wave ground-based telescopes. However, at low radio frequencies the Earth’s atmosphere is optically thin and so detections of oxygen transitions become viable. Goldsmith et al. (2011) provides a review of detections of molecular oxygen in the interstellar

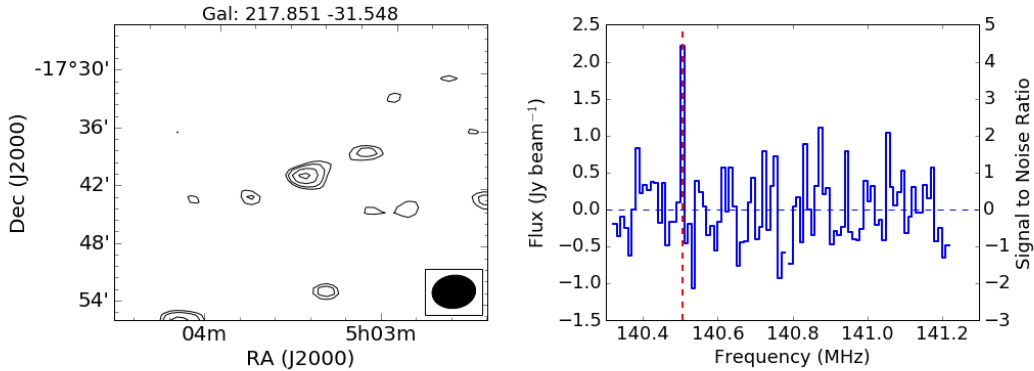


Figure 5.4: Tentative detections of Formic Acid with the right panel showing the spectra of the full coarse channel data cube containing the tentative detection. The left panel is the contours, set at 2, 3, 4, 5, and 6 σ of the image RMS, of the detected signal in the continuum-subtracted image. The ellipse in the lower right-hand corner of the contour plot shows the size and shape of the synthesized beam.

Table 5.2: Information on the deuterated formic acid transition tentatively and possibly detected within this survey. The first row provides information regarding the transition including the rest frequency, the energy in the upper level state, the Einstein coefficient (A_{ij}), and the quantum numbers. The proceeding rows are information regarding the the peak pixel position in J2000 and Galactic coordinates, the velocity of the transition, and the column densities, assuming thermal emission and absorption (See §4 for more details).

Source	Unknown
Molecule	<i>t</i> -DCOOH
Rest Frequency (MHz)	140.50
$E_U/k_B(K)$	200.16
$\text{Log}_{10}(A_{ij})$	-14.24
Quantum Numbers	16(5,11)–16(5,12)
Position (J2000)	5h03m30s -17°40′28″
Position (Galactic)	219.903 -25.815
Velocity (km s^{-1})	0±17
$N_u (\text{cm}^{-2})$	1.1×10^{19}
$N_{tot} (\text{cm}^{-2})$	3.6×10^{20}

All transition values are from the JPL – Jet Propulsion Laboratory Spectral Line Catalog (Pickett et al., 1998)

medium and laboratory experimentation as well as reporting detections in the Orion molecular cloud with the *Herschel Space Observatory*. Their detections of molecular oxygen at 487, 774 and 1121 GHz had velocities of 11 to 12 km s⁻¹ with line widths of 3 km s⁻¹ and column densities averaging around 5 × 10¹⁶ cm⁻².

The formation pathway of O₂ and its isotopologues is thought to be initiated by the reaction of atomic oxygen and H₃⁺, which is produced through the ionisation of H₂ from cosmic rays (Goldsmith et al., 2011). The recent calculation of reaction rates suggest that large O₂ production in the gas phase is possible (Lique et al., 2009) and Goldsmith et al. (2011) calculated that the three transitions they detected came from a source of 5 arc seconds in angular size, 10–11 M_⊙, and not associated with any sources of previous molecular detections.

We have tentatively detected molecular oxygen (¹⁷O¹⁶O) at a level of 5 σ in comparison to the spectral RMS. The asymmetric nature of the (¹⁷O¹⁶O) molecule gives it a dipole moment, allowing it to be detected at radio frequencies. Pagani et al. (1993) made the first tentative radio detection of molecular oxygen (¹⁶O¹⁸O) in the stacked spectra of interstellar cloud NGC7538 and L134N with a calculated integrated intensity of 13 and 5 mK km s⁻¹, respectively. However, these detections were never replicated (Goldsmith et al., 2011).

Within our observations there are 34 transitions of ¹⁷OO but 18 of them are flagged out of our observations. The detected signal at 107.60 MHz is one of the lowest energy transitions. At 111.03 MHz the transition with the quantum numbers N=3–3, J=2–2, F=7/2–5/2 has an E_u/k_b of 23.7 K, but was not detected within this survey. Although, ¹⁸OO may be more abundant, no known transitions exist in the observed frequency range.

The detection, shown in Figure 5.5, is not at a location of any known source listed in SIMBAD. The column density in Table 5.3 of 1.3 × 10²⁵ cm³ is higher than the *Herschel* detections, but that could be due to the non-thermal emission or our incorrect assumption on the rotational temperature (assumed 9 K for this work).

5.5.4 Unidentified Tentative Detections

We have tentatively detected three signals at around 5 σ in comparison to the spectral RMS that are not associated with any known molecular or recombination line transitions at 104.09, 140.36, and 140.84 MHz (Figure 5.6). Neither of the first two transitions are co-located with a known object listed in SIMBAD within the area of our synthesized beam. However, the signal at 140.84 MHz is located

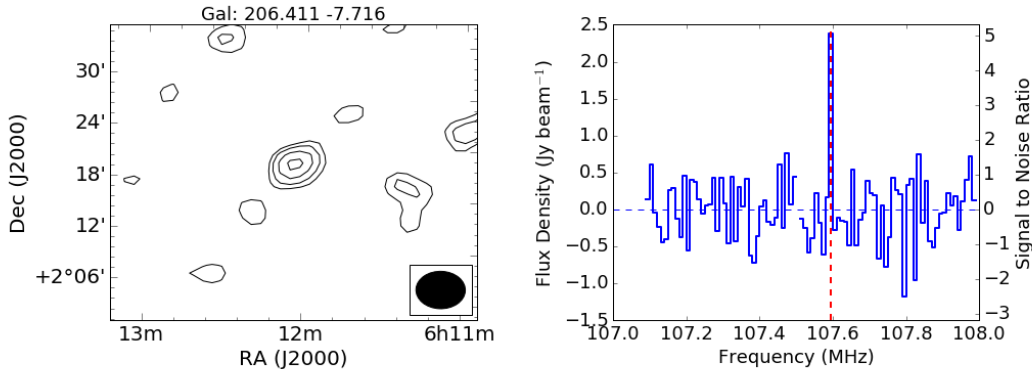


Figure 5.5: Tentative detections of Molecular Oxygen. The right panel shows the spectra of the full coarse channel data cube containing the tentative detection. The left panel is the contours, set at 2, 3, 4, 5, and 6 σ of the image RMS, of the detected signal in the continuum-subtracted image. The ellipse in the lower right-hand corner of the contour plot shows the size and shape of the synthesized beam.

Table 5.3: Information on the molecular oxygen transition tentatively and possibly detected within this survey. The first row provides information regarding the transition including the rest frequency, the energy in the upper level state, the Einstein coefficient (A_{ij}), and the quantum numbers. The proceeding rows are information regarding the the peak pixel position in J2000 and Galactic coordinates, the velocity of the transition, and the column densities, assuming thermal emission and absorption (See §4 for more details).

Source	Unknown
Molecule	$^{17}\text{O}^{16}\text{O}$
Rest Frequency (MHz)	107.60
E_U/k_B (K)	39.81
$\text{Log}_{10}(A_{ij})$	-18.01
Quantum Numbers	$N=4-4, J=3-3, F=\frac{7}{2}-\frac{5}{2}$
Position (J2000)	6h12m04s +02°13'54''
Position (Galactic)	206.411 +7.716
Velocity (km s^{-1})	0 ± 17
N_u (cm^{-2})	1.2×10^{24}
N_{tot} (cm^{-2})	1.3×10^{25}

All transition values are from the JPL – Jet Propulsion Laboratory Spectral Line Catalog (Pickett et al., 1998)

within the Orion KL region and is most closely associated with the evolved star Parengo 811.

5.5.5 Orion Chemical Environment

Baudry et al. (2016) provides a summary of the complex chemical environment of the Orion molecular cloud with a particular focus on high resolution information provided by the Atacama Large Millimeter/submillimeter Array (ALMA) and IRAM 30 m telescopes. They state that although most of the interstellar molecules detected can be found in Orion, there is a dominance of nitrogen and oxygen complex molecules. The *Herschel Space Observatory* with the HIFI detector has also provided a wealth of detailed information regarding the chemical complexity of Orion over recent years (e.g. Goldsmith et al. 2011; Neill et al. 2013; Crockett et al. 2014), in particular with detection of molecules like molecular oxygen which can be difficult with ground based telescopes.

Most of the molecules detected around Orion KL Nebula or the molecular cloud have velocities $<15 \text{ km s}^{-1}$ and line widths around 3 km s^{-1} . The resolution of the MWA of $17\text{--}30 \text{ km s}^{-1}$ suggests that all the detections would be within one channel and close to the rest frequency, which is what is observed for molecular oxygen and formic acid. However, the nitric oxide and nitric oxide isotopologue detections have a higher velocity and are possibly associated with evolved stars, which are known to have velocities up to 150 km s^{-1} (Olofsson et al., 1982). Velilla Prieto et al. (2015) observed several transitions of NO at 150 to 350 GHz in the CSE of OH231.8+4.2, with velocities of $35\text{--}40 \text{ km s}^{-1}$ and line widths up to 50 km^{-1} , which is consistent with the expectation of detecting broad velocity components with the MWA due to our spectral resolution.

5.5.6 Connections to Laboratory Science

Fedoseev et al. (2012) confirmed that NO plays an important role in the formation of hydroxylamine (H_3NO), which is an important molecule in the pathway of the formation of amino acids. Laboratory experiments have created enamines (precursors to amines) with deuterated Formic Acids in a neutral medium (Himmele et al., 1979), suggesting that the tentative detections of deuterated formic acid and nitric oxide may point to the production of amines within the Orion molecular cloud. NO is also of particular interest as it is thought to be critically important in primitive life on Earth (Feelisch and Martin, 1995; Santana et al.,

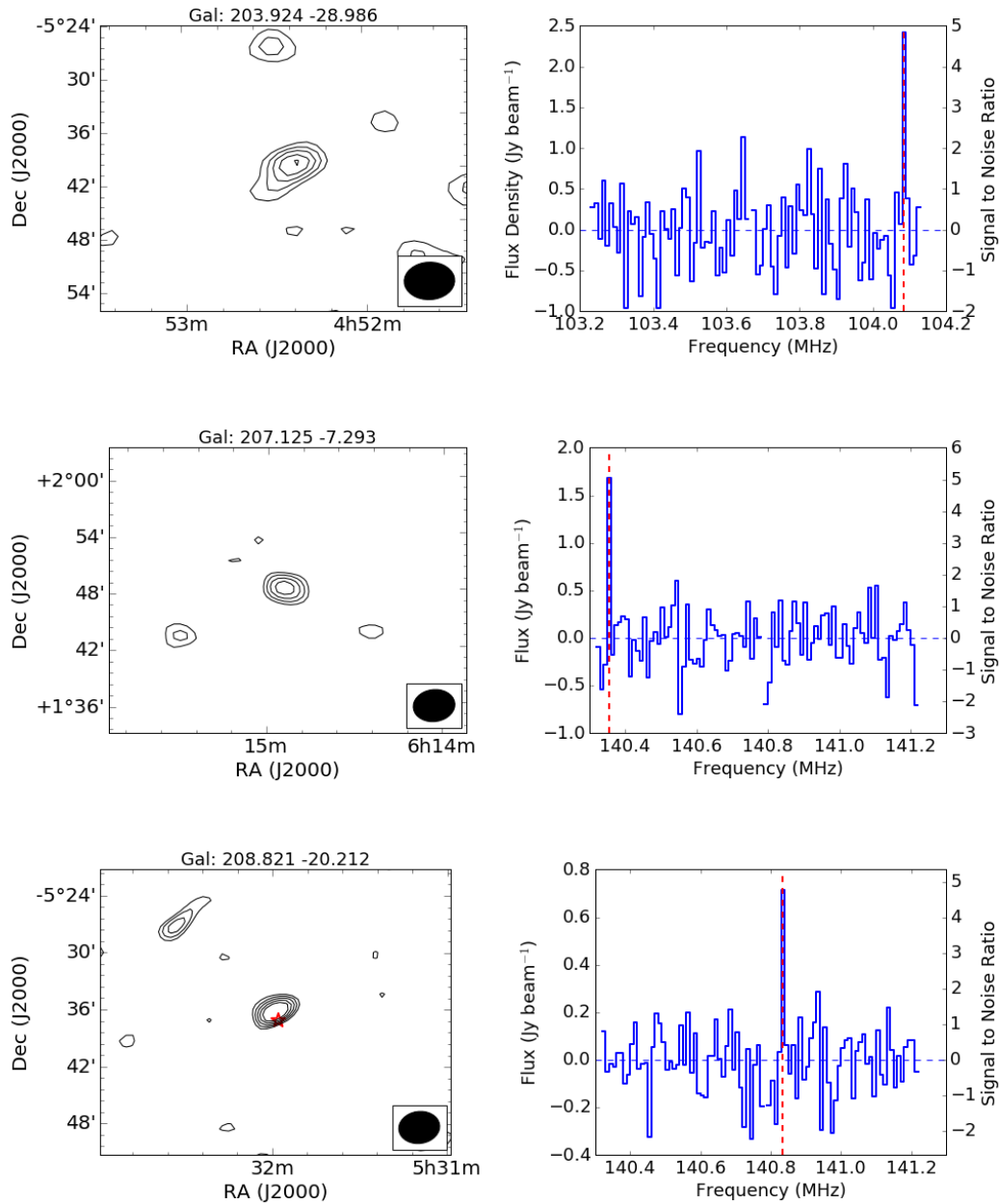


Figure 5.6: Tentative detections of Unknown Molecules. The right panel shows the spectra of the full data cube containing the tentative detection. The left panel is the contours, set at 2, 3, 4, 5, and 6 σ of the image RMS, of the detected signal in the continuum-subtracted image. The ellipse in the lower right-hand corner of the contour plot shows the size and shape of the synthesized beam. The signal at G208.821 -20.212 is located within the Nebula with the closest optical source at the peak pixel position, marked with a red star, is Parenago 811 an evolved star within the Nebula.

2017).

The detection of signals not associated with known molecules or known position of sources is not unexpected. As the study of molecules within the frequency range of 100–170 MHz is new, not a lot of emphasis has been put into publishing transitions at these frequencies. Additionally, the wide FOV of the MWA is unique, giving us the opportunity to study much larger regions than previously available in the radio part of the electromagnetic spectrum. Many molecular studies are completed in regions where interesting sources are already known to exist instead of blind surveys. Additional laboratory experiments at these frequency ranges would allow us to better identify potential molecules and start to understand the abundances of the molecules we are detecting.

5.6 Conclusions

We completed a survey from 99–170 MHz centered on the Orion KL nebula to search for molecules. Due to unusual RFI and instrumental effects only 23% of the channelized data were available to search for absorption and emission signals likely associated with molecular transitions. Despite this we have tentatively detected multiple transitions of nitric oxide, deuterated formic acid, and molecular oxygen. We also have three tentative detections of signals that have no known molecular or recombination line associations. We call these tentative as they are all around 5σ and are contained within one channel.

With an integration time of three hours and the wide velocity width of the MWA, we are likely only sensitive to boosted emission with broad velocity components. However, our results are consistent with our Galactic plane survey (Tremblay et al., 2017) and theoretical assumptions of the nature of the transitions we would expect at low frequencies (Spitzer, 1998; Condon and Ransom, 2016). Although the individual tentative detections represent low significance, the fact that we see multiple transitions of nitric oxide within the same object is promising.

Molecules are often used as classification tools for identifying and studying environments in greater detail than continuum observations can provide. Although the spectral resolution of the MWA does not allow us to study the kinematics of the regions, the MWA’s wide FOV is well suited to finding new and interesting molecular environments that can be followed up with high-resolution telescopes. In this survey, we detected deuterated formic acid; deuterated molecules are

known to be enhanced during the early stages of star formation. Therefore, future observations with the MWA, using a longer integration time to reduce the thermal noise, will be useful for identifying regions for further study to understand the early stages of star formation.

The detections of both molecular oxygen and deuterated formic acid point to the possible formation of amines within the Orion complex. As the fundamental transitions of larger molecules like amines reside at low radio frequencies, they are ideal frequencies for searching for these missing building blocks in molecular evolution.

The MWA has recently undergone an upgrade to longer baselines and new software is being designed to improve the spectral quality and channel resolution. These together with increased integration time will allow for improved blind surveys in the future. Additionally, all of these are in preparation for understanding requirements for the low-frequency Square Kilometre Array (SKA) planned to be built on the same site as the MWA.

Future work with the MWA is planned to use the new long baselines and increased integration times. As found by Tremblay et al. (2017), it will take approximately 30 hours of observation to get to the sensitivity limits to find new or rare molecules. Therefore, future observations are in progress to observe the Vela Molecular Ridge and Gum Nebula for over 30 hours.

The work reported here further validates the feasibility of using low-frequency radio telescopes to complement the work at high frequencies. Both ranges have their own strengths and low frequencies can provide insights into environments as they probe different conditions (eg. nonthermal excitation).

5.7 Acknowledgments

We would like to thank the referee for their insightful comments and time dedicated to improving our manuscript. The authors would like to acknowledge the contribution of an Australian Government Research Training Program Scholarship in supporting this research. This work was supported by resources provided by the Pawsey Supercomputing center with funding from the Australian Government and the Government of Western Australia. This scientific work makes use of the Murchison Radio-astronomy Observatory, operated by CSIRO. We acknowledge the Wajarri Yamatji people as the traditional owners of the Observatory site. Support for the operation of the MWA is provided by the Australian

Government (NCRIS), under a contract to Curtin University administered by Astronomy Australia Limited.

Chapter 6

Low-Frequency Carbon Recombination Lines in the Orion Molecular Cloud Complex

This paper, as written, was published by:

Tremblay C. D., Jordan C. H., Cunningham M., Jones P.A., Hurley-Walker, N.
“Low Frequency Carbon Recombination Lines in the Orion Molecular Cloud
Complex” *Publications of the Astronomical Society of Australia*, Cambridge Uni-
versity Press, 2018, 35, e018

Although this Chapter represents a published paper, edits have been made in response to the thesis examiners. Therefore, it is not an exact replica of the original publication. Every effort is made to maintain the integrity of this work as required by the copyright statements in the appendix of this thesis.

6.1 Abstract

We detail tentative detections of low-frequency carbon radio recombination lines from within the Orion molecular cloud complex observed at 99–129 MHz. These tentative detections include one alpha transition and one beta transition over three locations and are located within the diffuse regions of dust observed in the infrared at $100\ \mu\text{m}$, the $\text{H}\alpha$ emission detected in the optical, and the synchrotron radiation observed in the radio. With these observations, we are able to study the radiation mechanism transition from collisionally pumped to radiatively pumped within the HII regions within the Orion molecular cloud complex.

6.2 Introduction

Radio recombination lines (RRLs) are produced in regions of diffuse partially ionised gas, typically associated with interstellar radiation fields from stars (Sorochenko and Tsivilev, 2010). Atoms in high quantum states are important tracers of ionised gas within photon-dominated regions (PDRs), where the far-ultraviolet (FUV) radiation from stars that are embedded within the molecular clouds interact with the neutral hydrogen gas surrounding the HII regions (Andree-Labsch et al., 2017). In particular, FUV photons originating from high-mass stars embedded within their natal molecular clouds with energies greater than 11.3 eV are able to penetrate their surroundings by greater than parsec scales (Howe et al., 1993) to ionise atomic carbon in regions where hydrogen is mostly neutral (Salgado et al., 2017b).

Seon et al. (2011) found a strong correlation of FUV radiation field with H α emission outside the bright HII regions due to escaping ionised photons from OB stars through low-density pathways in the warm ionising medium. Cooling of the gas in the PDR is dominated by CII infrared line emission at 158 μm , molecular rotational lines of CO (J=1 \rightarrow 0), and generates a mechanism to create carbon radio recombination lines (CRRLs) detectable in the radio part of the electromagnetic spectrum (Sorochenko and Tsivilev, 2010; Andree-Labsch et al., 2017)

The Orion molecular cloud complex is one of the closest regions of active high-mass star formation, making it ideal for the study of PDRs (Gordon and Sorochenko, 2009; O’Dell et al., 2015). The Orion molecular cloud was first modeled to have multiple layers of ionised gas by Ahmad (1976) and Boughton (1978) further elaborated on the ideas. Boughton (1978) concluded that within the HI foreground region, carbon must be a significant source of the free electrons. Both studies suggest that the low-frequency RRLs ($n > 190$) arise in clouds associated with the HI (21 cm) component of the cold interstellar medium with temperatures < 100 K and gas densities $\approx 50 \text{ cm}^3$.

Since then, a complex filamentary structure around Orion, on both large and small scales, has been widely observed and discussed (Pon et al., 2014, 2016; Andree-Labsch et al., 2017). Even early optical studies with high angular resolution (Osterbrock and Flather, 1959) suggest that the filamentary structure of the HII regions is on scales that would not be resolved with most telescopes and Gordon and Sorochenko (2009) suggest that many of the models have not incorporated these inhomogeneities, making interpretation of observational results

difficult.

Recent three-dimensional modeling, mixed with observational data by Andree-Labsch et al. (2017), of the PDRs around Orion show fractal structures that contain layers and explains why a large fraction of molecular material is located near the surface of the cloud. Pon et al. (2014) identified linear HI features extended radially away from the Orion Kleinmann–Low Nebula (Orion KL) with significant increases in regions where the H α decreases. Pon et al. (2016) attributed this behavior to ionizing photons breaking out of the Orion-Eridanus superbubble surrounding the Orion region, extending about 180 pc from our Sun.

Observations of H α (Finkbeiner, 2003), C I, C II, CO (6 \rightarrow 5) (Stutzki et al., 1991; Howe et al., 1993), CO(1 \rightarrow 0) (Dame et al., 2001), and CO(7 \rightarrow 6) (Schmid-Burgk et al., 1989; Howe et al., 1993) completed in and around Orion trace the complex regions of PDRs. Howe et al. (1993) constrained the gas temperature of the Orion KL to greater than 40 K and found the H $_2$ gas to have column densities exceeding 10^{22} cm $^{-2}$.

By using the Murchison Widefield Array (MWA) we are able to image and study a large fraction of the Orion molecular cloud complex, including both Orion A and Orion B, within a single field-of-view. In this paper we present the lowest frequency detections (around 100 MHz) of alpha and beta carbon radio recombination lines in the Orion region. This work is done in conjunction with a molecular line survey published by Tremblay et al. (2018), using a field-of-view of 400 square degrees centred on the Orion KL Nebula.

6.3 Observations & Data Reduction

Using the Murchison Widefield Array (MWA; Tingay et al. 2013) at a centre frequency of 114.56 MHz, we observed the Orion Nebula (RA(2000) = 05^h35^m, Dec.(2000) = -05°27') for three hours on November 22, 2015 (see Table 6.1 for more details). The observations used snapshot imaging, which involve recording data in two minute intervals before adjusting the pointing. Pictor A (RA(2000) = 05^h19^m49.7^s, Dec.(2000) = -45°46'44", 452 Jy at 160 MHz) was observed for use as a primary calibrator at the start and end of the observation run. Each observation of Pictor A includes two minutes of data, and these data were used to calibrate tile bandpasses and phases.

The MWA has a contiguous bandwidth of 30.72 MHz and using a two stage polyphase filterbank the data are channelised into 24 \times 1.28 MHz ‘coarse’ chan-

Table 6.1: MWA Observing Parameters

Parameter	Value
Central frequency	114.56 MHz
Total bandwidth	30.72 MHz
Number of imaged channels	2400
Channel separation	10 kHz (23 km s ⁻¹)
Synthesized beam FWHM	3.2'
Primary beam FWHM	30 degrees
Phase center of image (J2000)	05h35m, -05d27m
Time on source	3 hours

nels and each coarse channel is divided into 128×10 kHz ‘fine’ spectral channels. This allows for simultaneous observations of multiple carbon RRL transitions, including 34 α -lines and 35 β -lines, as identified from the Splatalogue database (Remijan et al., 2007). Even though the MWA offers 3072×10 kHz frequency spectral channels, only 2400 (100 fine channels of the 24 coarse channels) were imaged, in an effort to avoid imaging artifacts caused by the aliasing of the polyphase filter bank. Thus, only 78 per cent of the bandpass was imaged, which could potentially detect 12 of the carbon α -lines and 12 β -lines.

6.3.1 Calibration & Imaging

The data calibration and imaging was completed as described in Tremblay et al. (2017) for the molecular line survey of the Galactic Centre. At the observing frequencies used for these data, the MWA has a 900 deg^2 full-width at half-maximum (FWHM) field-of-view (FOV) in the primary beam, but also has considerably large sidelobes. Bright sources in these sidelobes can corrupt observations by adding additional noise, and therefore need to be handled to correctly represent the desired radio data. To this end, we followed the approach used in the GaLactic and Extragalactic All-sky Murchison Widefield Array (GLEAM) survey (Hurley-Walker et al., 2017) to “peel” bright sources from the visibilities; in particular for these data, the Crab Nebula (RA(2000) = $05^{\text{h}}34^{\text{m}}34.94^{\text{s}}$, Dec(2000) = $22^{\circ}00'37.6''$; 1256 Jy at 160 MHz).

Each two-minute observation experienced slightly different phase distortions due to the changing ionospheric conditions. This manifested as small (≈ 20 arcsec) direction-dependent shift to the positions of sources in every observation. A continuum image for each coarse channel of each observation is used to derive

a single correction in R.A. and Dec. that is applied to each image cube. After correction, the residual position offset is -1 ± 17 arcsec in R.A. and 5 ± 17 arcsec in Dec within the integrated image. To calculate the amount of image blurring of the point spread function, likely dominated by the ionosphere, the ratio of integrated flux density to peak flux density was computed and found to have an average value of 1.01 ± 0.07 , suggesting that we are robust against ionospheric activity for these observations. The average flux density error, when compared to the GLEAM catalog, was 0.1%.

The velocity resolution within the 99–129 MHz frequency band ranged from 23 to 30 km s^{-1} . Doppler correction terms are currently not incorporated into the MWA imaging pipeline so the uncertainty of the velocity is 3.4 km s^{-1} , significantly less than the channel width of the MWA.

6.3.2 Survey Details

A full description of the survey strategy and statistical analysis is presented in the Orion molecular line survey by Tremblay et al. (2018). In this paper, we provide a brief description.

The continuum-subtracted 10 kHz spectral fine channels had a mean RMS of 0.4 Jy beam^{-1} at the phase centre. Any channel having a RMS of $>0.6 \text{ Jy beam}^{-1}$ was flagged to remove channels effected by spurious RFI. This reduced the search volume from the 2400 imaged channels to 1240 channels.

The primary beam is the sensitivity pattern the telescope has on the sky. Although 625 square degrees is imaged (see Figure 6.1) the search is limited to the most sensitive region of the primary beam using MIMAS (Hancock et al., 2012) to reduce the search volume to ≈ 400 square degrees (35% reduction).

Each continuum-subtracted fine channel is independently searched using AEGEAN (Hancock et al. 2012, 2018) to find pixels, in absorption and emission, with peak flux densities greater than 5σ in comparison to an input RMS image. The RMS image (as shown in in the upper right hand panel of Figure 6.1) is the spectral RMS at each pixel position for each coarse channel (100 fine channels). The resultant catalog of potential sources was further reduced by removing signals that had a spectral RMS $> 0.5 \text{ Jy beam}^{-1}$ to reduce the chance of a false detection due to uncorrected continuum subtraction or image artifacts.

The remaining sources in the catalog were further filtered. Any source where the spectral RMS and image RMS were not within 20% of each other, were removed from the catalog. After this last stage of filtering on the catalog of

sources from AEGEAN we found 8 positions on the sky, with 12 signals, that passed these criteria; of which 5 potential detections are presented within this work.

Using two-sided Gaussian statistics, we would expect no more than 78 signals with the 95000 independent synthesised beams and 1240 channels searched at a 5σ threshold. However, by filtering the data on quality to ensure the spectral RMS is $<0.5 \text{ Jy beam}^{-1}$ (85–90% reduction in search volume) and to ensure that the spectral and image RMS were within 20% of each other (74% further reduction in search volume), the expected number of false positives due to thermal noise (in this reduced search volume) is less than one.

We note here that AEGEAN fits Gaussians to the pixel data and applies a correction of the background to calculate the flux density for these potential detections. The background is calculated as the 50th percentile of flux distribution in a zone 30 times the size of the synthesised beam. However, to make the spectrum contained within this paper, the peak flux density in the spectrum is the flux density at the pixel position of potential detection as reported by AEGEAN but not the flux density reported by AEGEAN. Therefore, it is possible that the flux densities shown in our spectra are underestimated, and consequently their significance is also underestimated. Our false positive rate may also be a slight overestimate as a result.

In the frequency range of 99–129 MHz there are 273 known molecular and recombination line transitions within the 30.72 MHz bandwidth. Therefore, we would expect most of the 2400 imaged fine channels to be free of lines, as we observed. The separation, in frequency, between the known atomic and molecular transitions is significant enough that incorrect identification of a detected signal is unlikely. However, it may be possible that a recombination line overlaps with an unknown molecular transition and the identification we have made is incorrect.

The chance that a noise signal being identified as an atomic or molecular line, that is within three fine spectral channels ($< 90 \text{ km s}^{-1}$) of the rest frequency, is 0.4%. The chance of a significant noise peak being confused for a real detection, when multiple transitions are detected in a single location, is $<0.1\%$.

6.4 Results

6.4.1 Radio Continuum, H α and Dust Emission

A continuum image from these observations centered on the Orion Nebula at 114.56 MHz is shown in the top left image in Figure 6.1. The angular resolution of the 114 MHz image obtained from the MWA is $73'' \times 67''$ and the total flux density in the Orion Nebula is 45 ± 4 Jy.

The top right hand image of Figure 6.1 shows the H α emission at 653 nm (Finkbeiner, 2003) in blue contours overlaid on a RMS map for the coarse channel data cube at 103 MHz, which is representative of the typical RMS map. The RMS map shows the sensitivity pattern on the sky across the 625 square degrees FOV imaged in this survey.

The H α emission, shown in the bottom right hand side of Figure 6.1 was observed by the Southern H-Alpha Sky Survey Atlas (SHASSA; Finkbeiner 2003) survey and traces the Bernard's loop, the Lambda Ori bubble (supernova remnant), and the Orion-Eridanus filaments. Bernard's loop is a photoionised region that is particularly interesting as theoretical models and observations only agree if the region is enhanced with heavy metals (Odell et al., 2011). It is suggested that the crescent shape is caused by an old supernova remnant that, as the bubble expanded, has swept up dust and gas as it moved through the high density and pressure gradients associated with the Galactic gas layer (Wilson et al., 2005; Pon et al., 2016).

Within the continuum image of our survey, on the top left, the faint synchrotron radiation is correlated with the H α emission surrounding the nebula. The cyan contours on the RMS map and the image in the bottom left, trace the dust emission at $100 \mu\text{m}$ (Schlegel et al., 1998) and the tentative detections are mostly contained in the region of the cloud complex where the dust and H α emission is decreased and where the HI density is expected to increase (Pon et al., 2014).

6.4.2 Carbon Recombination Lines

Carbon recombination lines C393 α and C496 β are tentatively detected within the Orion molecular cloud complex, as shown in the spectra in Figure 6.2. These detected transitions appear to be co-located with H α filamentary structure and in regions where the $100 \mu\text{m}$ dust density is decreased.

The derived parameters for each source are found in Table 6.2 and 6.3. The

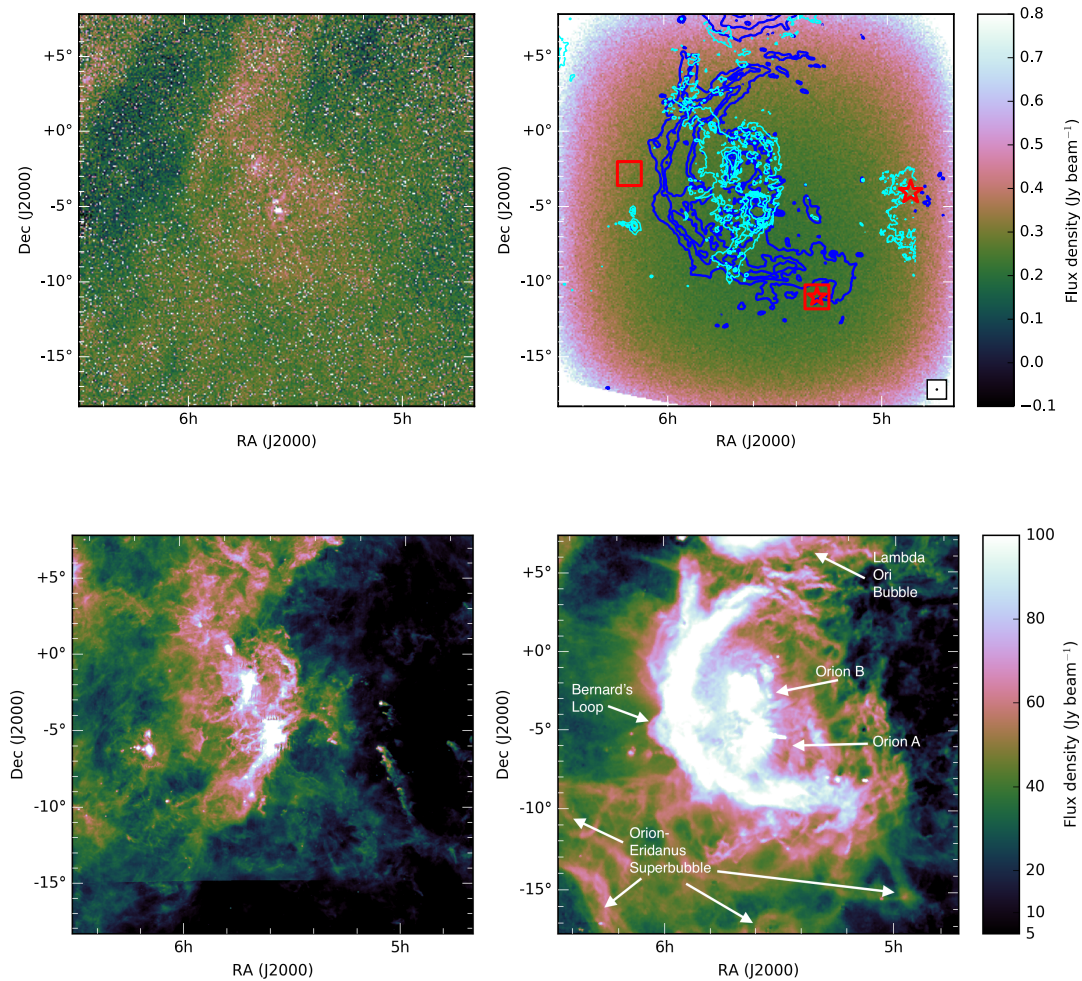


Figure 6.1: The upper left image is a continuum image of the Orion survey region across the 30.72 MHz of bandwidth with a central frequency of 114.6 MHz showing the full region blindly searched for molecular signatures and recombination lines. The upper right hand image is an RMS map showing the sensitivity of the MWA in a typical coarse channel data cube. The $C393\alpha$ and $C496\beta$ transitions are represented by squares and stars respectively. The contours in cyan trace the image in the bottom left, which shows dust emission at $100\ \mu\text{m}$ surveyed by Schlegel et al. (1998). The blue contours and the image in the bottom right are the optical $H\alpha$ emission from the Southern H-Alpha Sky Survey Atlas (SHASSA) (Finkbeiner, 2003). We note that there is an image artifact in the $100\ \mu\text{m}$ survey data on the bottom, created by combining the data from different fields.

Rayleigh-Jeans approximation is used to determine the brightness temperature (T_B):

$$T_B = \frac{\lambda^2}{2k\Omega} S, \quad (6.1)$$

where λ is the wavelength of the recombination line, k is the Boltzmann constant, Ω is the beam solid angle, and S is the flux density in Jy beam^{-1} . Since the signal is not resolved spectrally, the integrated intensity is the brightness temperature integrated over the velocity resolution of the single channel.

$$\int \text{Intensity} = S \times v \quad (6.2)$$

where v is the velocity resolution of the channel of the detected recombination line. The calculated brightness temperature of ≈ 4000 K for the sources is not unexpected, as low-frequency transitions have a stimulated emission component by the domination of collisional excitation (Salgado et al., 2017b). The temperature of the background continuum (T_c) is largely uniform over the FOV and is calculated as 1100 K scaled from the Haslam model (Remazeilles et al., 2015) at 408 MHz using a spectral index of -2.6 .

The full spectrum from the position of each of the potential detections is shown in the Appendix. This shows that no other transitions of carbon alpha or beta lines were detected. However, at the position of G212.67 -25.56 the data cube contains a signal around 5σ associated with the rest frequency of C393 α and also contains two emission peaks around 3σ that are associated with the rest frequency of the C496 β line at 107.18 MHz and the rest frequency of molecular oxygen ($^{17}\text{O}^{18}\text{O}$) at 107.60 MHz. The upper energy level divided by the Boltzmann constant for the transition of molecular oxygen at 107.60 MHz is 39.81 K and represents the $N=4-4$, $J=3-3$, $F=7/2-5/2$ transition. The same transition of molecular oxygen is possibly detected at the position of G194.471 -23.755 in absorption (Figure 6.2) and other locations reported in the molecular survey paper (Tremblay et al., submitted).

6.5 Discussion

6.5.1 Turn-over Frequency of CRRL Sources

Observations of CRRLs have spanned frequencies of 10 to over 5000 MHz (Payne et al., 1994; Roshi et al., 2014; Salas et al., 2017). Peters et al. (2010) summarised

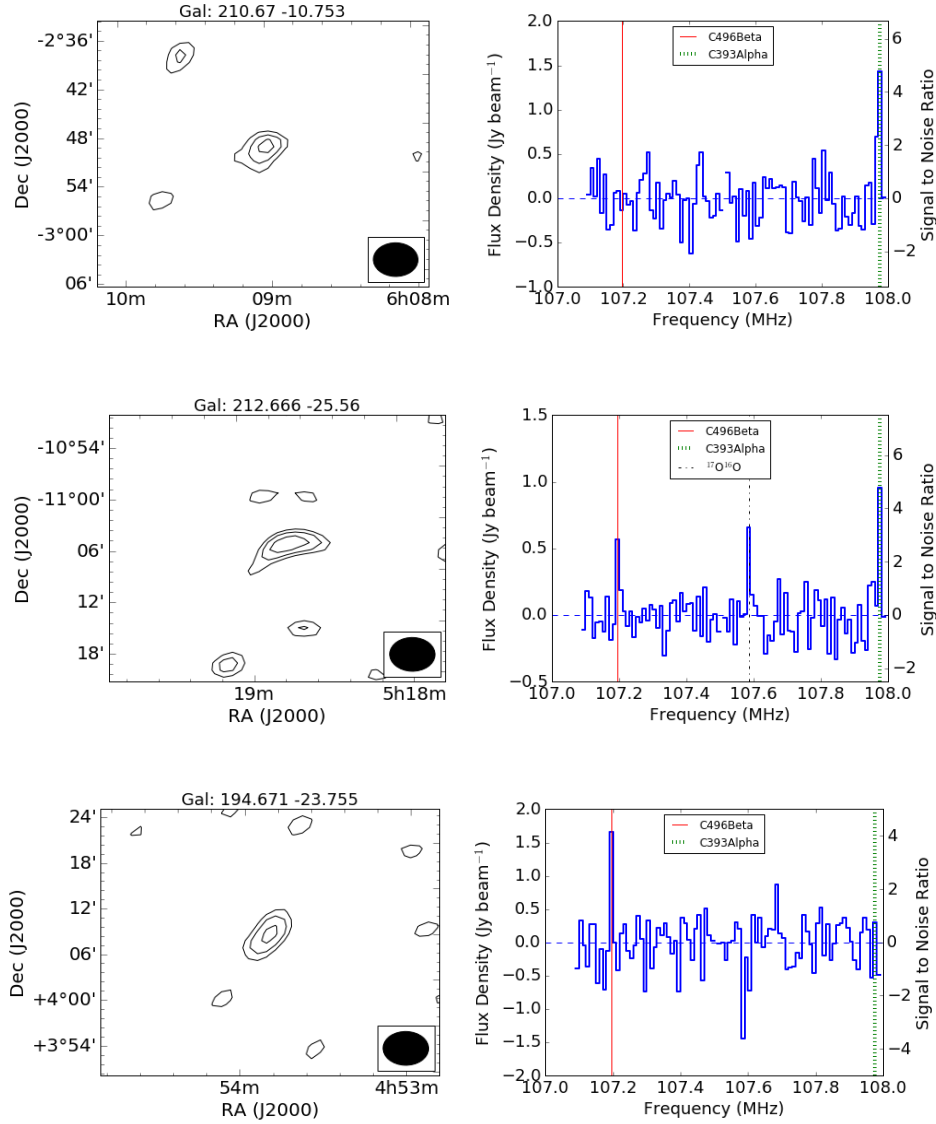


Figure 6.2: A tentative detection of the $C393\alpha$ (107.98 MHz) and $C496\beta$ (107.19 MHz) at the Galactic coordinates listed on the top of each plot. The contours plot on the left represent the 3, 4, 5, and 6 σ levels of the associated detection. The spectrum on the right is representative of the spectrum of the coarse channel band in which the tentative detection was made with the flagged channels blanked. The spectra at G212.67 – 25.56 also shows a possible detection of $C496\beta$ at 107.18 MHz and molecular oxygen ($^{17}\text{O}^{18}\text{O}$) at 107.60 MHz.

Table 6.2: Information about the tentative detections of C393 α . The peak-pixel positions of each tentative detection is listed in Galactic coordinates (source), as well as Right Ascension (R.A.) and Declination (Dec.). The flux density, velocity, integrated intensity and brightness temperature are provided for each location the transition was detection.

		C393 α	
Source		G210.67 -10.75	G212.67 -25.56
R.A.	(J2000)	6:09:02	5:18:48
Dec.	(J2000)	-2:53:56	-11:07:41
Flux			
Density	(Jy beam ⁻¹)	1.43 \pm 0.14	0.97 \pm 0.10
V _{lsr}	(km s ⁻¹)	0 \pm 24	0 \pm 24
\int Intensity	(K km s ⁻¹)	9.9(\pm 0.9) \times 10 ⁴	9.5(\pm 1.0) \times 10 ⁴
T _B	(K)	4136 \pm 414	4107 \pm 411

Table 6.3: Information about the tentative detections of C496 β . The peak-pixel positions of each tentative detection is listed in Galactic coordinates (source), as well as Right Ascension (R.A.) and Declination (Dec.). The velocity, integrated intensity and brightness temperature are provided for each location the transition was detected.

		C496 β	
Source		G212.67 -25.56	G194.67 -23.76
R.A.	(J2000)	5:18:48	4:53:56
Dec.	(J2000)	-11:07:41	+04:06:13.42
Flux			
Density	(Jy beam ⁻¹)	0.97 \pm 0.10	1.72 \pm 0.17
V _{lsr}	(km s ⁻¹)	24 \pm 24	24 \pm 24
\int Intensity	(K km s ⁻¹)	6.7(\pm 0.7) \times 10 ⁴	12(\pm 1.2) \times 10 ⁴
T _B	(K)	2805 \pm 281	4974 \pm 497

the information about known Galactic low-frequency CRRLs and, using a modified version of the radiometer equation, calculated the approximate amount of observing time required in order for the new generation of low-frequency telescopes to detect them. The MWA was not on the list, but using the same equation we could expect to detect them in the averaged spectra in ≈ 2 hours if all the observed lines are in either absorption or emission. However, due to the population effects, the exchange from absorption to emission will likely occur between 100 and 150 MHz, making this a difficult experiment.

At large n -bound states, observed at frequencies less than 100 MHz, the relative populations of atomic levels are controlled primarily by collisional processes. This makes the population levels close to the kinetic temperatures of less than 100K and so the lines are detected in absorption along the line of sight toward strong continuum sources. At lower n -bound states, observed at frequencies greater than 200 MHz, the relative populations are dominated by radiative processes; moving the excitation temperature away from the kinetic temperature towards negative values. The level populations then become inverted and the recombination lines are detected in emission. This happens even if the brightness temperature is higher than the kinetic temperature (Payne et al., 1989; Salgado et al., 2017a).

The transition between emission and absorption, often defined as the position where the optical depth is between 1 and 1.5 (Gordon and Sorochenko, 2009), was first modeled by Shaver (1975) and later observed by Payne et al. (1989) in Cassiopeia A. The transition between absorption and emission must occur regardless of the details of the population mechanism but the actual turnover frequency and the strength of the emission lines will depend on the density and temperature of the clouds being observed.

Gordon and Sorochenko (2009) explain this in terms of the Bohr atom. At low radio frequencies, the size of the atoms is large, making them more likely to interact with the charged particles in the diffuse HII gas. The wavelength of these turnover frequencies is directly related to the probabilities of these collisions happening, such that, as the gas densities increase the rate of the collision decreases. So, in dense gas the turn-over frequency is likely to be at higher observational frequencies than in diffuse gas.

Therefore, the observation of CRRLs in the frequency range of 100–200 MHz is an important probe toward understanding the cold neutral medium around PDRs and HII regions. The observed emission of the alpha and beta lines reported here at 107–108 MHz, suggest the turnover is at frequencies less than 107 MHz

for the ionisation layer and, as expected, the transitions are observed in emission within the regions of diffuse gas.

Payne et al. (1989) observations of the turn-over between emission and absorption within Cassiopeia A demonstrated that in between these two states, the spectra are flat and recombination lines are undetectable. That may explain why we are not detecting signals associated with CRRLs below 107 MHz but above 108 MHz we would expect to detect the other known transitions in emission. Historically, due to various instrumental and population effects, not all expected transitions are observed (e.g. Bell et al. 1997) or the observations were focused on a single transition (e.g. Wyrowski et al. 1997), both of which is not unexpected within the spectral line community (Herbst and van Dishoeck, 2009). However, we will explain possible reasons for the discrepancy within our data.

6.5.2 Spectral Quality

Each fine (10 kHz) spectral channel is individually imaged for each of the two-minute snap-shot observations and then built into an image cube for a single coarse channel. For a single coarse channel, all the observations are integrated together using inverse variance weighting. Therefore each integrated image cube has unique sensitivities in comparison to any other coarse channel cubes within the observation set. Also, due to the polyphase filterbank that channelizes the MWA data, each fine spectral channel has a steep bandpass shape, such that any detected signal that may not be centered within the 30 km s^{-1} resolution, may be lost.

These tentative detections are of low significance ($\approx 5\sigma$). The low significance, combined with the knowledge of the data processing and characteristics of the MWA described above, each spectral cube for each coarse channel has different noise properties. This suggests that it is not improbable that all the transitions for the same atom are not detected. Therefore, we call these detections tentative as they are unresolved and the subsequent, unflagged, transitions within our band were not detected.

6.5.3 Origin of CRRLs around Orion

Modeling and observations from Ahmad (1976) and Boughton (1978) introduced the idea that the Orion complex contains multiple layers of ionised gas. Boughton (1978), and later confirmed by Wyrowski et al. (1997), determined that the carbon

around Orion is ionised in a layer that is between the observer and the nebula and not within the nebula itself. This is consistent with other observations within the region where most emission is identified from a region of ionised gas on the observer’s side of the Orion Molecular cloud and in a PDR beyond the primary ionisation front (O’Dell et al., 2015).

Theoretical modeling by Pon et al. (2016) suggests that the Orion-Eridanus super-bubble is a layer of expanding ionised gas with the outer regions about 180 pc from the Sun. They also determined that the total ionizing luminosity of the Orion star-forming region is sufficient to produce the $H\alpha$ emission observed within this super-bubble.

Reported here are the lowest frequency spectral line observations of the Orion region published to date, as far as we are aware. With the resolution of the MWA it is likely these recombination line detections are within the diffuse filamentary structure of the near-field ionisation layer. However, the frequency resolution of the MWA does not allow for analysis of the collisional and radiation broadening effects on the spectral line. Therefore, no attempt to place upper limits on the electron temperature are made here.

Ahmad (1976) discussed the discrepancy of velocities at frequencies greater than 5 GHz versus observations of CRRLs at frequencies less than 5 GHz. He suggested that the low-frequency observations are in cold gas in front of the HII region while carbon recombination lines at higher frequencies are detecting warm regions behind the HII region.

Typical velocities for carbon recombination lines detected in the Orion KL, Orion A, and Orion B portions of the giant molecular cloud complex range from $\approx -9 \text{ km s}^{-1}$ (Ahmad, 1976; Wyrowski et al., 1997; Roshi et al., 2014) at frequencies greater than 5 GHz and $\approx -6 \text{ km s}^{-1}$ at frequencies down to 600 MHz (Chaisson and Lada, 1974). However, Anantharamaiah et al. (1990) detected carbon and hydrogen recombinations lines in the southern edge of Orion B with velocities of $\approx 48 \text{ km s}^{-1}$.

Observations of the carbon monoxide $J=1\rightarrow 0$ transition around the Orion molecular cloud trace the complex structure of carbon within the ionised frontal layer. Wilson et al. (2005) observed velocities ranging from -1 to 18.5 km s^{-1} with knots of compressed gas in regions of active star-formation, suggesting that there is a large gradient of possible velocities for carbon atoms within the Orion ionisation front.

The tentative detections of $C393\alpha$ and $C496\beta$ lines have velocities of $0\pm 24 \text{ km s}^{-1}$ and $24\pm 24 \text{ km s}^{-1}$ respectively which are consistent with previous CRRL obser-

vations within the region. However, due to the velocity resolution of the MWA we can not discriminate between the previously observed velocities within the different ionisation layers.

6.6 Conclusions

We have tentatively detected one carbon alpha transition and one beta transition across three positions within the Orion molecular cloud complex ionisation layer in front of the HII region, at a level greater than 5σ . The transition between emission and absorption, at frequencies between 100–200 MHz are important to identify and study the cloud dynamics. However, due to the spectral resolution of the MWA we can not provide analysis of the collisional and radiative broadening effects. We can conclude that the transition within these regions is less than 107 MHz as the signals detected in emission are at frequencies greater than this and the detected regions correspond to hot-spots of the diffuse hydrogen alpha emission observed with optical telescopes.

6.7 Acknowledgements

The authors would like to thank the referee for their useful comments and feedback. CDT would like to thank Paul Hancock with help with the coding used in data reduction. The authors would like to acknowledge the contribution of an Australian Government Research Training Program Scholarship in supporting this research. This work was supported by resources provided by the Pawsey Supercomputing Centre with funding from the Australian Government and the Government of Western Australia. This scientific work makes use of the Murchison Radio-astronomy Observatory, operated by CSIRO. We acknowledge the Wajarri Yamatji people as the traditional owners of the Observatory site. Support for the operation of the MWA is provided by the Australian Government (NCRIS), under a contract to Curtin University administered by Astronomy Australia Limited. We gratefully acknowledge the support of NASA and contributors of SkyView surveys.

6.8 Appendix: Full Spectra

We present the full spectra from the MWA in the band of 99–122 MHz to show the quality of the data. The spectra represents the data in the positions of all three tentative detections.

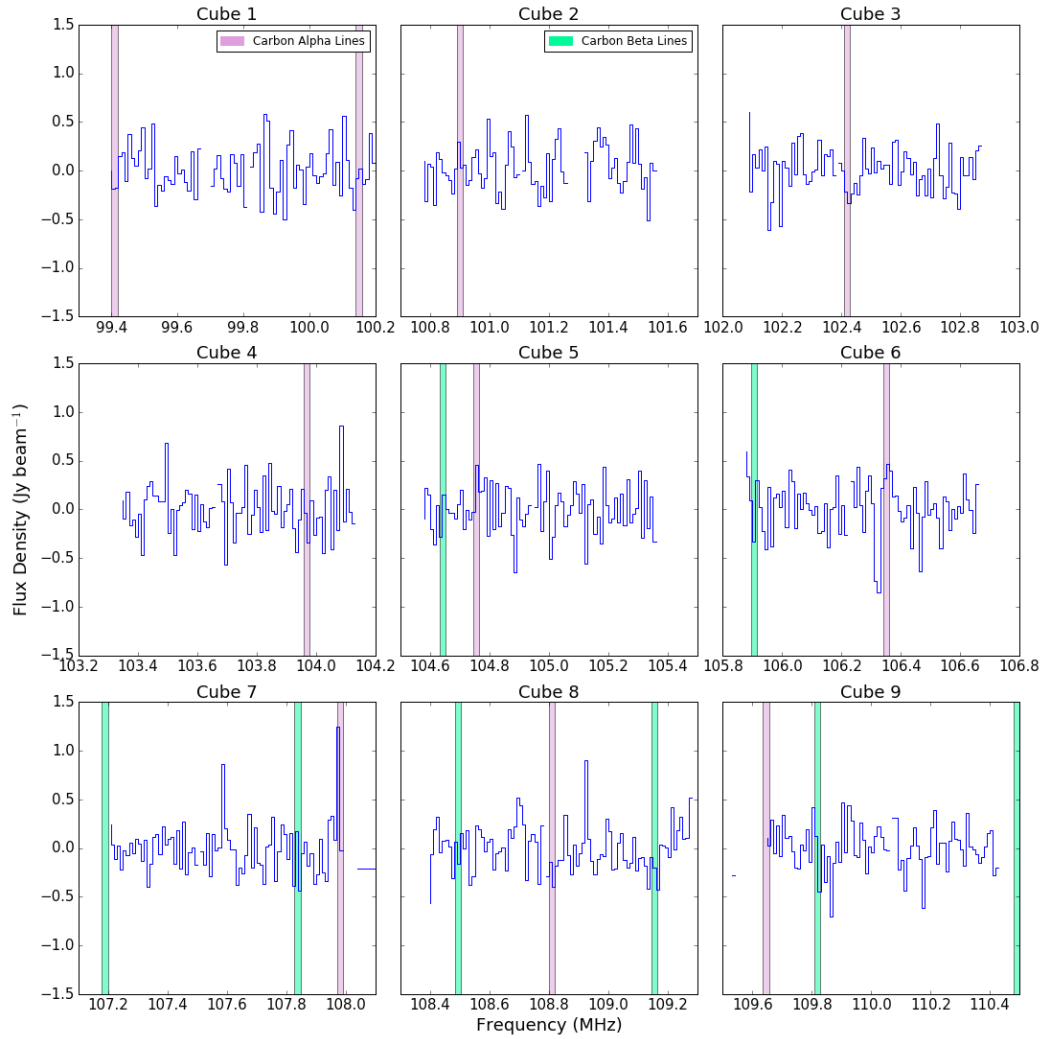


Figure 6.3a: MWA spectra for a data cube used within this survey at the position of G212.67 -25.56 . The alpha recombination rest frequency are marked in plum and the beta rest frequency positions are marked in green. Flashed channels are blanked out in the spectra.

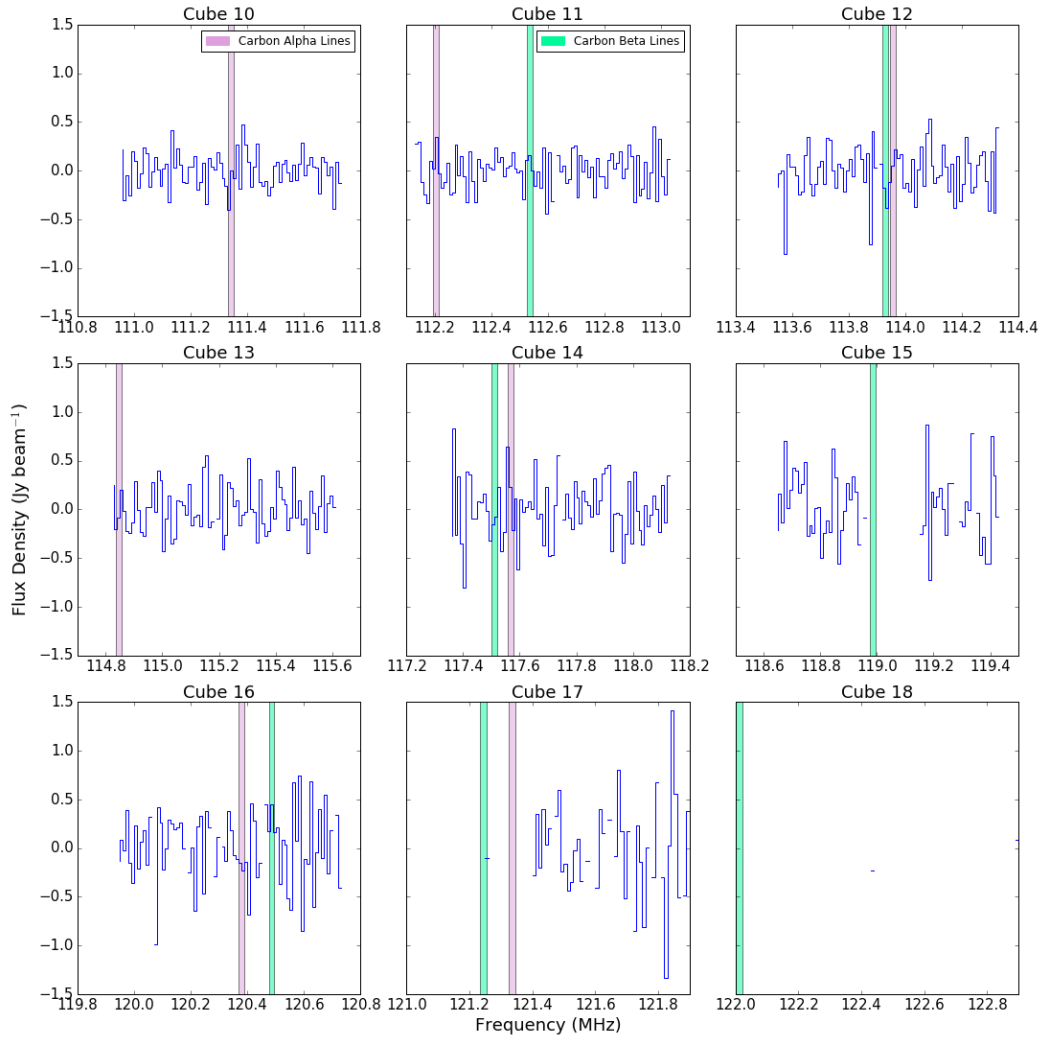


Figure 6.3b: MWA spectra for a data cube used within this survey at the position of G212.67 –25.56. The alpha recombination rest frequency positions are marked in plum and the beta rest frequency positions are marked in green. Flagged channels are blanked out in the spectra.

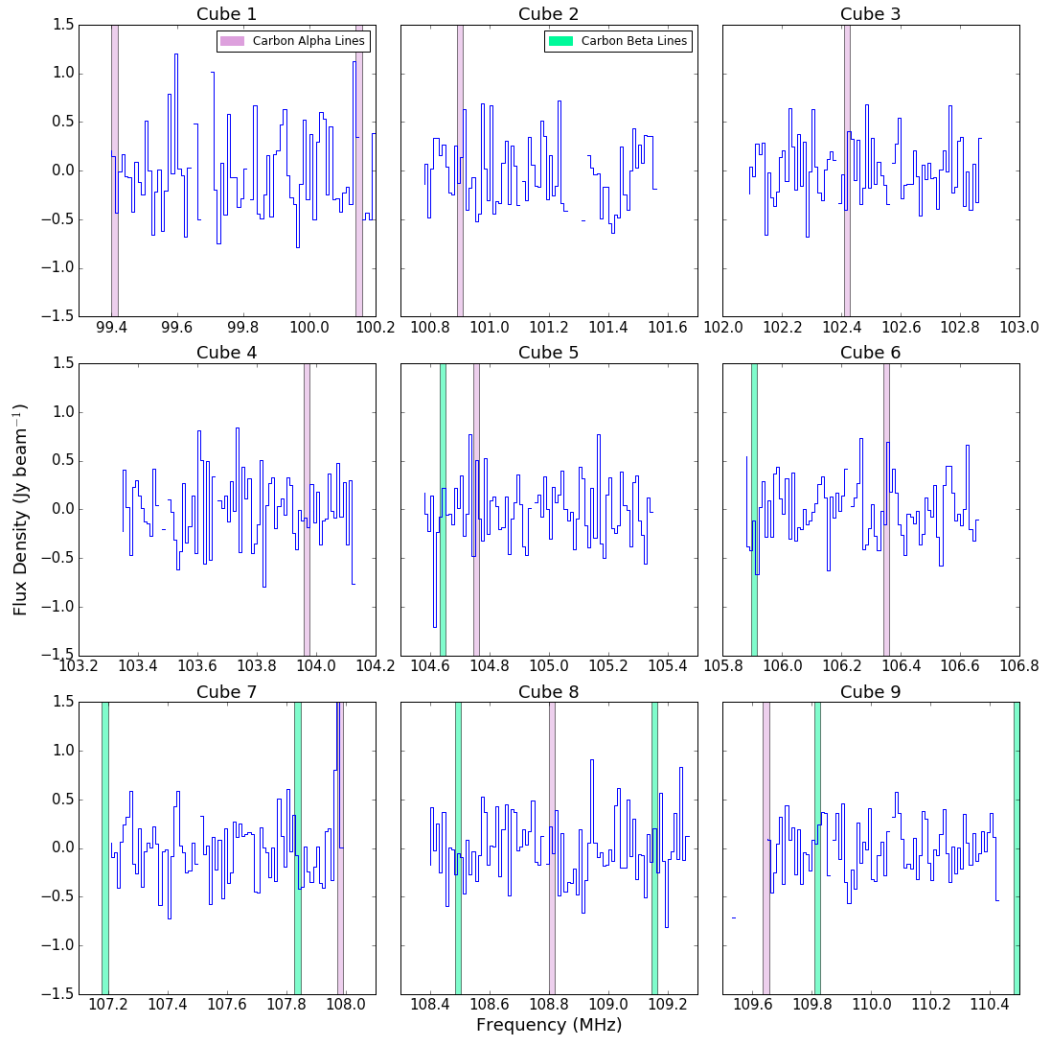


Figure 6.4a: MWA spectra for a data cube used within this survey at the position of G194.67 -23.76 . The alpha recombination rest frequency are marked in plum and the beta rest frequency positions are marked in green. Flashed channels are blanked out in the spectra.

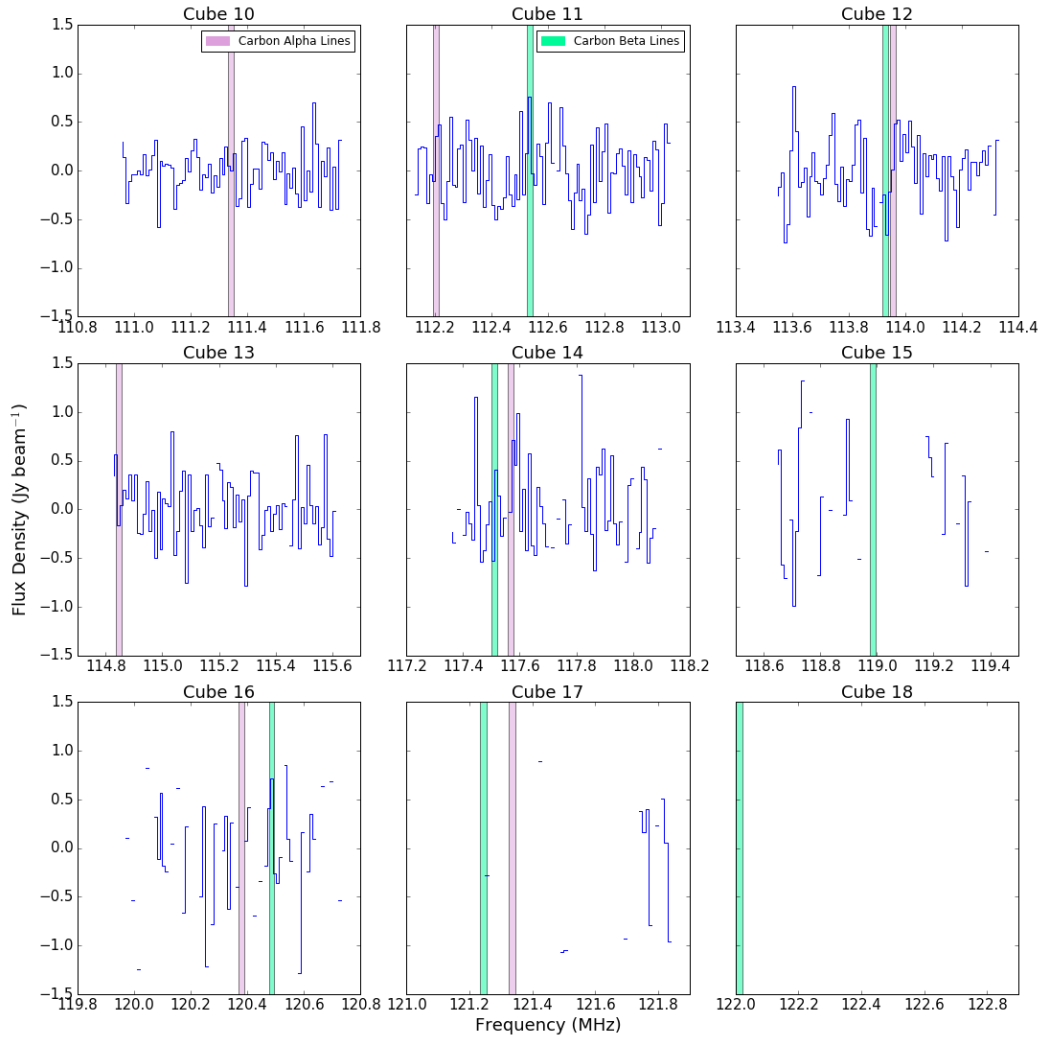


Figure 6.4b: MWA spectra for a data cube used within this survey at the position of G210.67 – 10.75. The alpha recombination rest frequency positions are marked in plum and the beta rest frequency positions are marked in green. Flagged channels are blanked out in the spectra.

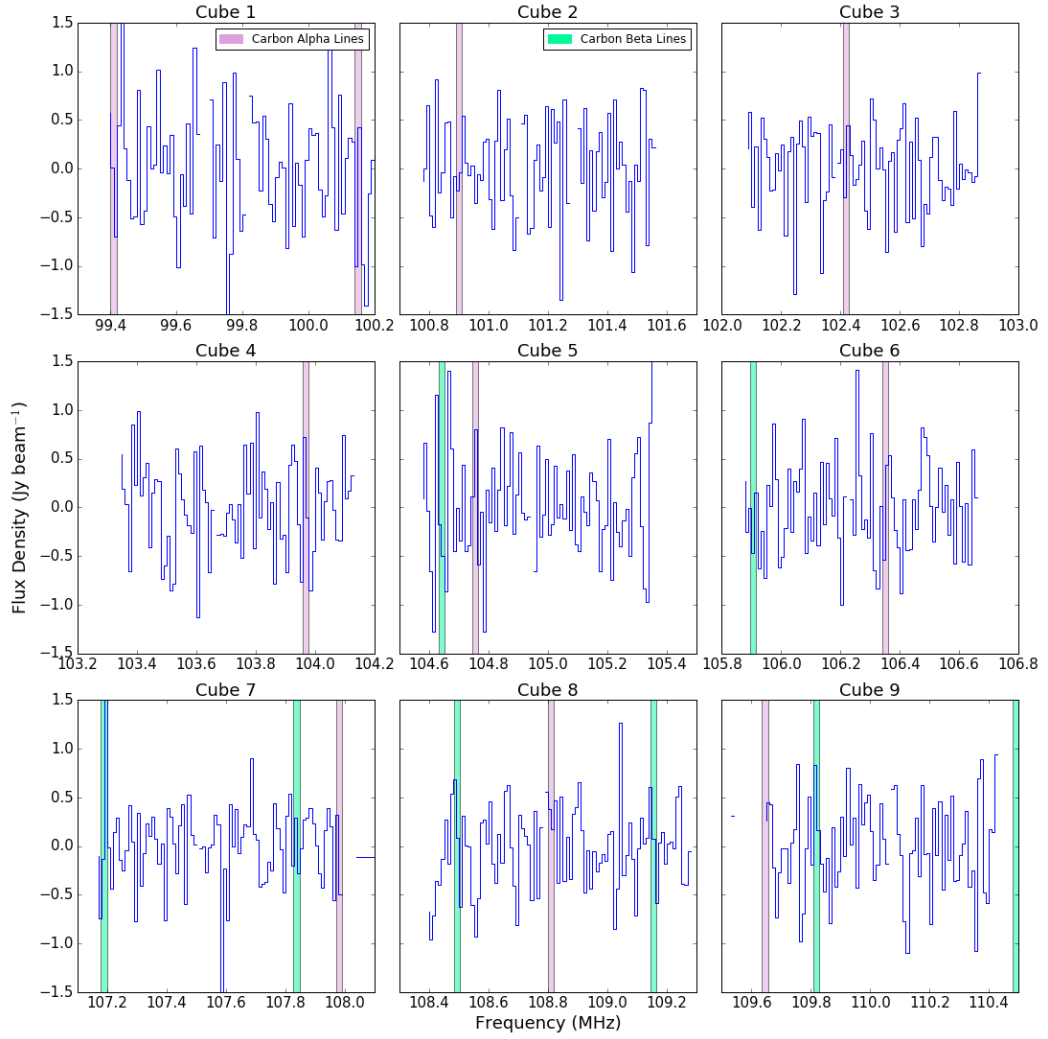


Figure 6.5a: MWA spectra for a data cube used within this survey at the position of G194.67 -23.76 . The alpha recombination rest frequency are marked in plum and the beta rest frequency positions are marked in green. Flagged channels are blanked out in the spectra.

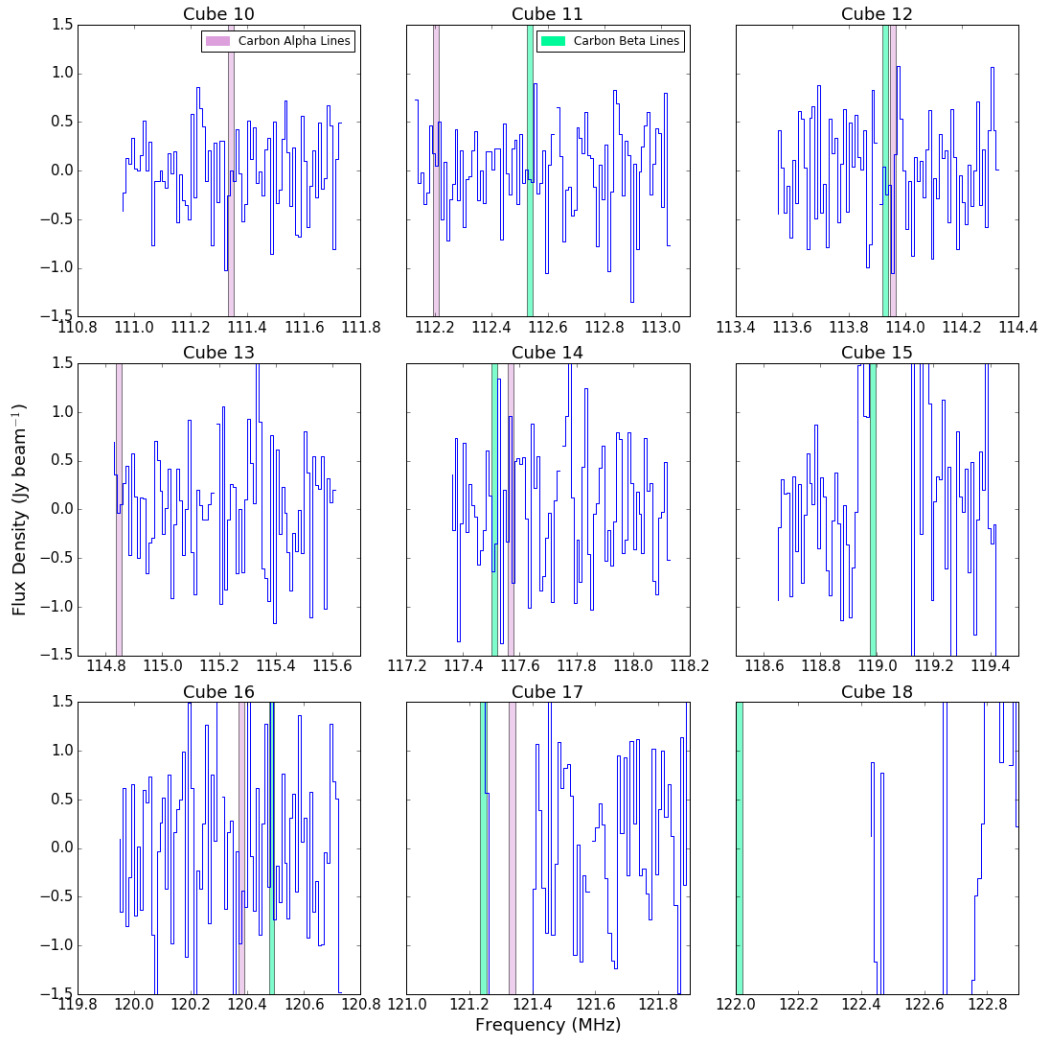


Figure 6.5b: MWA spectra for a data cube used within this survey at the position of G194.67 $-$ 23.76. The alpha recombination rest frequency positions are marked in plum and the beta rest frequency positions are marked in green. Flagged channels are blanked out in the spectra.

Chapter 7

Search for Extraterrestrial Signals with the MWA

This chapter is a summary of work published in:

Tingay S.J., Tremblay C.D., and Croft S. “A search for ExtraTerrestrial Intelligence (SETI) toward the Galactic Anticenter with the Murchison Widefield Array” 2018, *ApJ*, 856, 1, 31, 5

Tingay S.J., Tremblay C.D., Walsh A., and Urquhart R., “An Opportunistic Search for ExtraTerrestrial Intelligence (SETI) with the Murchison Widefield Array” 2016, *ApJ Letters*, 827, 2, L22, 5

7.1 Introduction

The search for extraterrestrial intelligence (SETI) is a relatively new field, thought to be started with a published *Nature* article by Cocconi and Morrison (1959). Since then SETI has represented a study involving astrophysics, biology, technological advancements, and sociological implications. However, over the last 50 years the main focus has been in detecting signals generated by other intelligent life forms. As Paul Shuch points out “The photon is, after all, the fastest spaceship known to man”. So if we are to find proof of another civilisation it will likely be in the form of electronic communication (Shuch, 2011). Although, Wright (2018) suggests that the astrobiology and the search for biomolecules, not just electronic communication, is an aspect that should not be ignored.

Disentangling the astrophysical signals from potential SETI signals is a difficult challenge. For one, it is unknown at what frequency a signal may be emitted

or where it may come from. Directed searches by the SETI community have covered over a thousand star systems known or thought to contain planetary bodies (e.g. Isaacson et al. 2017; Enriquez and Breakthrough Listen Team 2018). But a null result is not proof that there are no other habitable planets, only that we may not have looked in the right place, at the right time, or in the right way.

Many signals that have been detected from outside our planet, that met the current ideas of what a SETI signal may look like, turned out to be an astrophysical object we did not understand. Even pulsars were first labeled “LGM” for little green men (Bell Burnell, 1979), until we understood the physics of rapidly rotating neutron stars. Therefore, the SETI community has developed a set of criteria that would signify the signal originated from intelligent civilisations (Shuch, 2011). These include signals that follow the Doppler motion of planets or frequency selection which exhibits a knowledge of one or more universal constants.

7.2 Narrowband or Wideband signal?

Light traveling through space can suffer from attenuation and dispersion. Attenuation comes from a loss of amplitude as a signal propagates over time, especially those generated by modern electronics. As the signal travels through the intergalactic medium, the flux density decreases as the square of the distance traveled, so we would expect the signal to be weak. The signals also can become dispersed from passing through the diffuse gas and dust, forcing the light to travel at different speeds depending on frequency, effectively broadening the signal.

It is considered that the most purposeful signal would be narrowband, as most astrophysical sources are broadband emitters, making an ETI signal differentiable from the background (Shuch, 2011). The narrowest possible signal is a pure continuous wave carrier but this is considered a one-bit message suggesting the presence of intelligence but with no information. Therefore, much of the present day SETI is completed looking for signals at resolutions up to 1 kHz. Searches like those completed by Margot et al. (2018) do not assume a particular bandwidth, but still limit to a few kHz for their expected signal.

However, a way to know with certainty we are detecting proof of other life, would be to find rich messages full of information about the civilisation. For these styles of communication, broadband signals would be required (Clancy, 1980). One consideration to ensure detection, would be employing a modulation

mode that contains individual narrow-band components, strewn across a broader stretch of the electromagnetic spectrum. This would assume the other civilisations were purposefully trying to signal and draw attention to themselves. More passive escaping signals from a civilisations day-to-day life would be broadband generated, potentially as they communicate amongst themselves (Shuch, 2011; Margot et al., 2018).

7.3 Frequency Selection

No one knows at what frequencies another civilisation may broadcast at to get attention across the Galaxy. Also, due to signal attenuation and Doppler motions caused by the movement of planets and the Galaxy, the signal may be shifted in frequency away from the frequency it was originally emitted at. Early discussion regarding SETI suggested looking at gamma-rays because the high-energy photons could travel large distances (Hippke and Forgan, 2017). However, Cocconi and Morrison (1959) realised that radio was a more practical route as there were more photons and the technology was cheaper.

Project Cyclops (Oliver and Billingham, 1971), designed by a group of scientists specifically put together to study the SETI problem, suggested that the cleanest astrophysical window for observing signals from ETI would be between 1.4 and 1.7 GHz, the bridge between H_I and OH emission. This is due to the dip in astrophysical signals between thermal and non-thermal emission mechanism of sources. So much of SETI is completed in these frequencies (Shuch, 2011). The space between 1.4 and 1.7 GHz is termed the “water hole” and had the added significance of a place where sentient beings would come together to communicate.

However, a lot of the setup for SETI observations was based on what is easiest observationally and not necessarily about what form of communication was most efficient. Hippke and Forgan (2017) discuss this precise problem. They suggest that the main concern presented by groups such as Project Cyclops was that the signal would be indistinguishable from blackbody radiation. However, very few astrophysical objects are perfect blackbody emitters, suggesting if the SETI is completed at high resolution, an astrophysical object should have characteristic absorption lines from elements and molecules, where ETI signals would not. Overall, they conclude that the best chances for ETI detections would be from highly collimated X-rays with energies between 0.5 and 2 keV.

Since the 1990’s optical SETI studies were promoted (Shuch, 2011), and with

recent developments with LASER technology, studies as those completed by Stewart and Lubin (2017) are considered a reasonable pursuit. Although, it is considered that simultaneous narrow-band signals across multiple wavelengths would be one of the best proofs of ETI.

Garrett et al. (2017) suggest another approach. They suggest that by using aperture arrays, like the MWA, with its all-sky coverage offers an interesting possibility completing broad ETI searches. However, they suggest that an aperture array operating in the water-hole would be most interesting.

7.4 SETI with the MWA

The MWA has the ability to cover two aspects of SETI simultaneously with the look for biomolecule tracers and the search for passive or active technological signals. In work published by Tingay et al. (2016) and Tingay et al. (2018), we generated spectra towards known exo-planetary systems from the Kepler catalogue (Akeson et al., 2013). The searches utilised the same fields and data generated from the Orion region (Tremblay et al., 2018) and Galactic plane (Tremblay et al., 2017) surveys of molecular and recombination lines with the MWA.

The MWA offers a couple of unique properties over previous SETI research, in particular its wide field-of-view and low observing frequencies. As discussed by Garrett et al. (2017), the MWA being an aperture array allows it to cover a field-of-view of 625 square degrees in a single pointing, for simultaneous observation of 39 known exo-planetary system towards the Galactic Centre and 17 towards Orion (Figure 7.1). However, the synthesised beam resolution of 3.2 arc minutes does not allow for distinction of individual planets.

The low observing frequencies with the MWA allowed us to search the region of 99–130 MHz, the typical band of radio communication and digital TV on Earth. The radio quiet zone of the MWA (Offringa et al., 2015; Sokolowski et al., 2017), plus careful RFI removal and data quality checks (Chapter 6), allow for the search of passive signals from exo-planetary systems that may have technology comparable to ourselves.

The Equivalent Isotropic Radiated Power (EIRP), calculated in both fields are comparable to other studies, as show in Figure 9 of Gray and Mooley (2017). Most of the planets within the Galactic Centre field were discovered through microlensing techniques, so represent average distances of kpc away. However, those from the Orion field, represent a much closer population of stars, with an

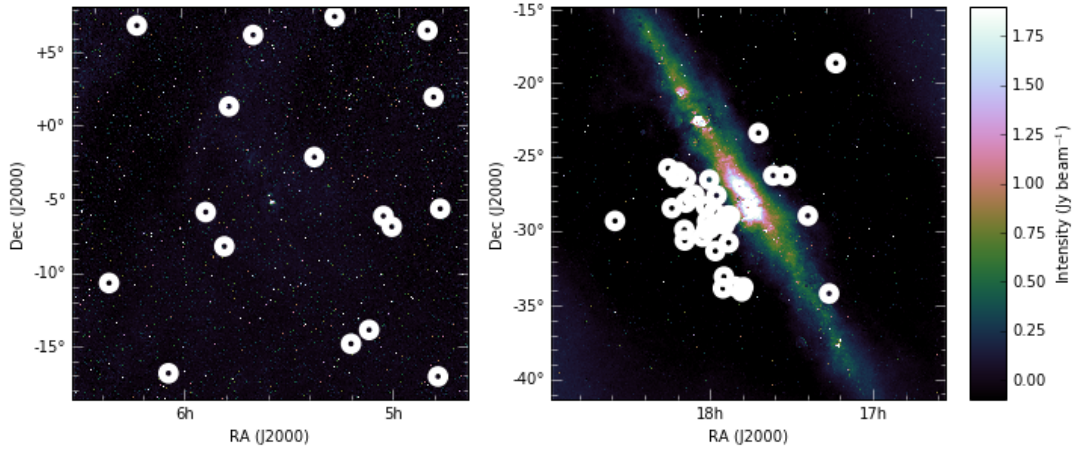


Figure 7.1: The fields searched for ETI signals with the MWA. The left is the fields centred on the Orion Nebula and the right in the field centred on Sagittarius Star A. The white circles in both represent the positions of known extrasolar planetary systems from the Kepler Catalogue.

average distance of 50 pc (Tingay et al., 2018), reducing the power to the range of practical values for detecting ETI.

The current imaging mode on the MWA has a limitation of 10 kHz spectral resolution but the telescope also has the versatility of using the voltage capture system (Tremblay et al., 2015) to capture the raw voltages and exchange the time resolution for further frequency resolution. Through collaboration with Breakthrough Listen (Isaacson and Siemion, 2017; Enriquez and Breakthrough Listen Team, 2018), new methodologies are being investigated to reduce the frequency resolutions that will be comparable to searches for narrow-band signals and has the added benefit to study the kinematics of environments where molecules or atoms are detected.

7.5 Conclusion

The wide field-of-view of the MWA allowed us to study 58 planetary systems with two pointings of the telescope. The two studies by Tingay et al. (2016, 2018) represent the first published low-frequency limits and the values for the EIRP are comparable to those published at higher radio frequencies. Although most searches for ETI are completed in the so-called “water-hole”, we do not really know what frequency we may expect a signal from another civilisation. Therefore, utilising the new generation of high-powered low-frequency arrays extends the

range of searchable frequencies.

The frequency resolution of the MWA is greater than an anticipated ETI signal but the increased channel width constrains the signal within a single channel. Instead of searching many channels in anticipation of Doppler motions, a wider-total bandwidth can be searched.

Chapter 8

Conclusion and Future Work

This thesis project aimed to develop the capabilities to use the Murchison Wide-field array (MWA) to find molecules in the low-frequency radio sky. To develop and test a pipeline to accomplish this goal, a pilot survey (detailed in Chapter 4) of 400 square degrees around the Galactic Centre was completed and resulted in tentative detections of two molecules in four stellar environments at a level of 5σ and one detection of an unknown molecular transition at a level of 6σ . The region was also searched for carbon recombination lines, but none were detected, even in stacked spectra.

As discussed in Section 4.6, at low radio frequencies the strength of the emission from molecules is no longer dependant on the temperature of the gas. Therefore, molecular transitions at low radio frequencies are more sensitive to maser or maser-like boosted emission. As predicted, all transitions detected in the survey had brightness temperatures greater than 4000 K. It may still be possible to detect thermal emission at low radio frequencies but more integration time may be required.

After the pilot survey, a second survey (detailed in Chapters 5 & 6) of 400 square degrees, centred on the Orion Kleinmann–Low (Orion KL) Nebula, was completed. This survey was originally designed to cover five (30.72 MHz) frequency bands between 99–300 MHz. However, due to problems with the correlator, only the first two bands between 99–170 MHz were used. Even though only 23% of the observed data were available for the search of spectral features, due to radio frequency interference and instrumental effects, we detected 13 signals associated with 11 positions on the sky. Only four of these signals were associated with known optical or infrared sources. This is not unexpected. The detection of the singly deuterated formic acid is typically associated with cold core col-

lapse during early star formation, so no optical or infrared counterpart would be detectable. The detection of recombination lines and molecular oxygen are likely associated with diffuse filamentary structure, and are found to correspond to regions where the emission of hydrogen alpha at 608 nm is decreased.

All of the detections found in the survey were considered tentative, even when multiple transitions were observed. This is because the channel width and beam size of the MWA imply all potential detections are point sources with spectral features contained within a single fine (10 kHz) channel. The velocities of all the lines matched expectations derived from previous observations of associated molecules, the Galactic rotation determined by CO, or expectations of stellar velocities.

Between the two surveys of the Galactic Centre and Orion, improvements to the data processing and molecular searches were made. However, further improvements are required to not only process the data more efficiently, but also to monitor the progress of an observation and improve the data quality checks. During these surveys, after the supercomputer jobs were completed, the plots of RMS and image quality were manually assessed. Also, if a job did not fully complete due to supercomputer error, the script was manually resubmitted to the supercomputer. The Orion and Galactic Centre surveys provided a lot of insight which can be utilised to improve the data processing efficiency of the pipeline.

Additional testing can also be completed to test the functionality and completeness of the survey search methods. By taking an image from the MWA and inserting Gaussians as fake sources, the pipeline could be tested for recovery and finding of these sources. This will also allow for a handle on false positive rates. Much of what was found around Orion was not published as the authors collectively decided to only report those detections that are most likely. Testing such as this could help determine how much of the data may have been culled that could be real.

To increase the sensitivity to detect molecular and atomic transitions, we stacked a series of observations to increase the effective integration time. The different CRRL transitions were also stacked, in both surveys, to determine if a discernible signal could be found. However, in future work, we may look at stacking selected regions of the sky where known sources of similar types exist. This may not be a feasible process until the size of the synthesised beam is reduced, as most sources are not resolved.

The MWA has recently undergone an upgrade to Phase II (Wayth et al., 2018), extending the baselines to around 6 km. This will reduce the beam size,

in matched surveys, from 3.2 arc min to 1.6 arc min, significantly reducing the beam dilution. The increased baseline length also reduces the confusion limit, so deeper surveys are more practical. To this end, an additional accepted proposal was recently accepted and observations have commenced to extend the survey of Orion from three hours to six hours to confirm weaker signals. Although this upgrade does not alter the spectral quality of the MWA, we may be able to detect extended emission and more transitions of the same molecules.

From the ratio of column densities we calculated during the Galactic Plane Survey to the column densities observed at higher frequencies, we derived that to detect thermal transitions we would need upwards of 30 hours of observation on a source around 400 pc away (See Figure 4.6). Therefore, an additional proposal was submitted and accepted to observe the Vela Molecular Ridge and the Gum Nebula (within the same field-of-view) for 30 hours with the MWA, utilising the Phase II extended array. This deeper survey will allow for further assessment of the noise properties of the MWA, investigation into molecular emission mechanisms at low radio frequencies, and investigation into distribution of carbon recombination lines at high n -bound states.

In order to account for supercomputer limits of input/output rates and wall time for submitted jobs, the fine channels within each coarse channel for each observation was imaged individually. Being able to image a larger frequency range within the multi-frequency synthesis image would allow for better image deconvolution. Therefore, an increase in supercomputing availability would allow for a reduction in image noise and increase deconvolution of sources within the field. This is especially important when creating the individual fine channel images used in creation of the final data cubes.

When the snap-shot observations are stacked, they are averaged together on a per coarse channel basis utilising inverse-variance weighting. The weighting comes from the RMS in a multi-frequency synthesis image of that coarse channel, so noisier observations are down-weighted when the observations are stacked. If the RMS weighting for each coarse channel, for a given observation, was consistent then the stacked observations would be comparable for each coarse channel. Instead the coarse channel RMS was not consistent relative to the other observations, so this assumption can not be made. Therefore, each coarse channel had a unique sensitivity making it difficult to search for transitions from the same molecule or atom, that spanned across multiple coarse channels.

To make it possible to look not only for the presence of multiple transitions from the same molecule or atom, but to compare the relative intensities, changes

to the pipeline are required. One way this may be accomplished is to remove the weighting and include more data flagging prior to the observations being stacked. However, this creates relative differences when one group of fine channels may include every observation while another may suffer in sensitivity due to missing channel data. Salas et al. (2017) handled this by maintaining a RMS sensitivity curve, but was greatly benefited by LOFARs 0.3 kHz frequency resolution. It is expected that RFI would exhibit narrow band behaviour differentiable from the broader band astrophysical signals. However, with the channel width of the MWA, this is not true and all RFI and astronomical signals are likely within a single fine channel.

Overall, the work completed within this thesis has proven that the search for molecules and atoms at low radio frequencies (<300 MHz) is feasible and provides the first insights into the study of chemical evolution as viewed at low radio frequencies.

Appendix A

Co-Author Statements

A written statement, placed into the Introduction (Chapter 1), explains the contributions of co-authors and myself as the candidate. Below are the acceptance statements from each co-author for the Statement of Originality.

From: Natasha Hurley-Walker nhurleywalker@cantab.net

Subject: Re: Thesis Statement of Contribution

Date: 27 March 2018 at 2:28 PM

To: Chenoa Tremblay chenoa.tremblay@postgrad.curtin.edu.au

I agree with the statement and believe it clearly represents my contribution to the work. Natasha

From: Steven Tingay s.tingay@curtin.edu.au

Re: Thesis Statement of Contribution

27 March 2018 at 2:45 PM

The statement of originality is fine for me. Steven

From: Maria.Cunningham@unsw.edu.au

Re: Thesis Statement of Contribution

6 Apr 2018, at 4:56 PM

I agree with your statement of originality, and am happy for you to include it in your thesis as is. Best wishes, Maria

From: Christopher.Jordan@curtin.edu.au

Re: Thesis Statement of Contribution

10 Apr 2018, at 3:36 PM

I agree with the statement of contribution. Regards, Chris

From: Andrew Walsh (awalsh@clubtelco.com)

Re: Thesis Statement of Contribution

24 Apr 2018, at 7:26AM

I have read through your statement of contributions and I agree with it. Regards,
Andrew

From: S.N.Longmore@ljmu.ac.uk

Re: Thesis Statement of Contribution

11 Apr 2018, at 12:42 AM

I agree with the statement of contribution. Regards, Chris

As requested, I agree with your representation of my contribution to the work.

Kind regards, Steve

From: Paul.Hancock@curtin.edu.au

Re: Thesis Statement of Contribution

11 Apr 2018, at 12:28 PM

I have read your statement of contributions and am happy with the representation of work as outlined. Paul

From: paulcojones@gmail.com

Re: Thesis Statement of Contribution

12 Apr 2018, at 9:11 AM

I agree with the statement. Paul

From: koenig@mpifr-bonn.mpg.de

Re: Thesis Statement of Contribution

12 Apr 2018, at 4:09 PM

Of course I agree with the statement you wrote and confirm that my contribution is to the work is represented! Cheers, Carsten

From: R.Wayth@curtin.edu.au

Re: Thesis Statement of Contribution

12 Apr 2018, at 4:36 PM

I have read the statement and agree with it. A/Prof Randall Wayth

From: j.s.urquhart@gmail.com

Re: Thesis Statement of Contribution

15 Apr 2018, at 6:03 AM

I have read the statement of originality you have prepared and I am happy that my contribution to the work has been correctly represented. Best regards, James

Appendix B

Copy Right Information

Chenoa Tremblay
PhD Student
Curtin University
Department of Physics and Astronomy
Western Australia

chenoa.tremblay@postgrad.curtin.edu.au

Monday, 26 March 2018

Dear Chenoa Tremblay,

Chenoa D. Tremblay, Andrew J. Walsh, Steven N. Longmore & James S. Urquhart, 'A Search for High-Mass Stars Forming in Isolation using CORNISH and ATLASGAL', *Publications of the Astronomical Society of Australia*, Cambridge University Press, (2015) Vol 32, e047, 9 pages.

C. D. Tremblay, M. Cunningham, P.A. Jones, N. Hurley – Walker, 'Low-Frequency Carbon Recombination Lines in the Orion Molecular Cloud Complex', *Publications of the Astronomical Society of Australia*, Cambridge University Press - yet to be published [2018]

Thank you for notification dated 26/3/2018 in which you requested permission to include the above journal articles in your PhD thesis for Curtin University in WA under the working title 'A Search for Molecules at Low Frequency with the Murchison Widefield Array' for the School of Electrical Engineering, Computing and Mathematical Sciences (2018). You are the first author of the journal articles and your intention is to reuse the content in your PhD. Your PhD will subsequently be placed in Curtin University's repository.

Non-Exclusive Permission is granted subject to the following conditions:

1. The integrity of the material must be assured.
2. That you have checked that the passage(s) in question do(es) not acknowledge any other source(s).

Cambridge gives no warranty or indemnity in respect of any third party copyright material in the article/chapter and the licensee must seek their own permission clearance.

3. Full acknowledgement of the source should be given (author, title, Cambridge University Press, year of publication) together with the appropriate copyright notice, to appear with the article.
4. That you include a link to our online catalogue at:
<https://doi.org/10.1017/pasa.2015.48>

Second link is not available at this time as the article has not been published.




Australia & New Zealand
477 Williamstown Road
Port Melbourne
Victoria 3207
Australia

Correspondence
Private Bag 31
Port Melbourne
Victoria 3207
Australia

www.cambridge.edu.au

Telephone +61 (03) 8671 1400
Fax +61 (03) 9676 9966
Email info@cambridge.edu.au
ABN 28 508 204 178

From: **JOURNALS PERMISSIONS** Journals.Permissions@oup.com 
Subject: RE: Rights to use paper in Thesis
Date: 27 March 2018 at 10:01 PM
To: **Chenoa Tremblay** chenoa.tremblay@postgrad.curtin.edu.au

JP

Self-Archiving Policy P

Dear Chenoa Tremblay,

RE. Chenoa D. Tremblay et al. A first look for molecules between 103 and 133 MHz using the Murchison Widefield Array. *MNRAS* (2017) 471 (4): 4144-4154

Thank you for your email requesting permission to reuse all or part of your article in a thesis/dissertation.

As part of your copyright agreement with Oxford University Press you have retained the right, after publication, to use all or part of the article and abstract, in the preparation of derivative works, extension of the article into a booklength work, in a thesis/dissertation, or in another works collection, provided that a full acknowledgement is made to the original publication in the journal. As a result, you should not require direct permission from Oxford University Press to reuse you article.

Authors may upload a PDF of the accepted manuscript to institutional and/or centrally organized repositories and/or in free public servers, upon acceptance for publication in the journal. Authors may upload the version of record to institutional and/or centrally organized repositories and/or in free public servers, upon publication in the journal.

Please Note: Inclusion under a Creative Commons License or any other Open-Access License allowing onward reuse is prohibited.

For full details of our publication and rights policy, including **credit-lines**, please see the attached link to our website:

https://academic.oup.com/journals/pages/access_purchase/rights_and_permissions/self_archiving_policy_p

If you have any other queries, please feel free to contact us.

Kind regards,
Louise

Miss Louise Eyre | Permissions Executive | Rights Department
Academic and Journals Divisions | Global Business Development
Oxford University Press | Great Clarendon Street | Oxford | OX2 6DP



From: Chenoa Tremblay [mailto:chenoa.tremblay@postgrad.curtin.edu.au]
Sent: 26 March 2018 06:44
To: JOURNALS PERMISSIONS



Confirmation Number: 11719878
Order Date: 05/25/2018

Customer Information

Customer: Chenoa Tremblay
Account Number: 3001290771
Organization: Chenoa Tremblay
Email:
chenoa.tremblay@postgrad.curtin.edu.au
Phone: +61 (4)49081528
Payment Method: Invoice

This is not an invoice

Order Details

Astrophysical Journal

Billing Status:
N/A

Order detail ID: 71212017
CCC System ID: 454881486
Publication Type: Book
Publisher: AIAA

Permission Status: **Granted**
Permission type: Republish or display content
Type of use: Republish in a thesis/dissertation
Order License Id: 4355810486607

Requestor type	Academic institution
Format	Electronic
Portion	chapter/article
Number of pages in chapter/article	4
The requesting person/organization	Chenoa Tremblay
Title or numeric reference of the portion(s)	A Molecular Line Survey around Orion at Low Frequencies with the MWA: Chapter 7 in my Thesis
Title of the article or chapter the portion is from	A Molecular Line Survey around Orion at Low Frequencies with the MWA
Editor of portion(s)	N/A
Author of portion(s)	N/A
Volume of serial or monograph	N/A
Page range of portion	7-10
Publication date of portion	July 2018
Rights for	Main product
Duration of use	Life of current edition
Creation of copies for the disabled	no
With minor editing privileges	no
For distribution to	Worldwide
In the following language(s)	Original language of publication
With incidental promotional use	no
Lifetime unit quantity of new product	Up to 499

Bibliography

- Abel, N. P., C. L. Brogan, G. J. Ferland, et al. (2004, July). Physical Conditions in Orion's Veil. *APJ* 609, 247–260.
- Ahmad, I. A. (1976, October). A Two-Component Model for the Orion a Carbon Radio Recombination Lines. *APJ* 209, 462–465.
- Akeson, R. L., X. Chen, D. Ciardi, M. Crane, J. Good, et al. (2013, August). The NASA Exoplanet Archive: Data and Tools for Exoplanet Research. *PASP* 125, 989.
- Altenhoff, W. J., D. Downes, T. Pauls, and J. Schraml (1979, January). Survey of the galactic plane at 4.875 GHz. *AAPS* 35, 23–54.
- Anantharamaiah, K. R., W. M. Goss, and P. E. Dewdney (1990). Interferometric Observations of HII, CII, and H Regions in Orion B. In M. A. Gordon and R. L. Sorochenko (Eds.), *IAU Colloq. 125: Radio Recombination Lines: 25 Years of Investigation*, Volume 163 of *Astrophysics and Space Science Library*, pp. 123.
- Anantharamaiah, K. R. and N. G. Kantharia (1999). High Rydberg State Carbon Recombination Lines from Interstellar Clouds. In A. R. Taylor, T. L. Landecker, and G. Joncas (Eds.), *New Perspectives on the Interstellar Medium*, Volume 168 of *Astronomical Society of the Pacific Conference Series*, pp. 197.
- Andree-Labsch, S., V. Ossenkopf-Okada, and M. Röllig (2017, February). Modelling clumpy photon-dominated regions in 3D. Understanding the Orion Bar stratification. *AAP* 598, A2.
- Asgekar, A., J. B. R. Oonk, S. Yatawatta, R. J. van Weeren, J. P. McKean, et al. (2013, March). LOFAR detections of low-frequency radio recombination lines towards Cassiopeia A. *AAP* 551, L11.

- Aver, E., K. A. Olive, R. L. Porter, and E. D. Skillman (2013, November). The primordial helium abundance from updated emissivities. *JCAP* 11, 17.
- Baars, J. W. M., R. Genzel, I. I. K. Pauliny-Toth, and A. Witzel (1977, October). Reprint of 1977A&A....61...99B. The absolute spectrum of Cas A; an accurate flux density scale and a set of secondary calibrators. *AAP* 500, 135–142.
- Barker, J. R., L. J. Allamandola, and A. G. G. M. Tielens (1987, April). Anharmonicity and the interstellar polycyclic aromatic hydrocarbon infrared emission spectrum. *APJL* 315, L61–L65.
- Bastian, N., K. R. Covey, and M. R. Meyer (2010, September). A Universal Stellar Initial Mass Function? A Critical Look at Variations. *ARAA* 48, 339–389.
- Baudry, A., N. Brouillet, and D. Despois (2016, November). Star formation and chemical complexity in the Orion nebula: A new view with the IRAM and ALMA interferometers. *Comptes Rendus Physique* 17, 976–984.
- Beck, T. L., J. S. Bary, and P. J. McGregor (2010, October). Spatially Extended Brackett Gamma Emission in the Environments of Young Stars. *APJ* 722, 1360–1372.
- Becker, R. H., R. L. White, D. J. Helfand, and S. Zoonematkermani (1994, March). A 5 GHz VLA survey of the galactic plane. *APJS* 91, 347–387.
- Bell, M. B., P. A. Feldman, M. J. Travers, M. C. McCarthy, C. A. Gottlieb, and P. Thaddeus (1997, July). Detection of HC₁₁N in the Cold Dust Cloud TMC-1. *APJL* 483, L61–L64.
- Bell Burnell, S. J. (1979, January). Little Green Men, White Dwarfs or Pulsars? *Cosmic Search* 1, 16.
- Benjamin, R. A., E. Churchwell, B. L. Babler, T. M. Bania, D. P. Clemens, M. Cohen, and et al (2003, August). GLIMPSE. I. An SIRTf Legacy Project to Map the Inner Galaxy. *PASP* 115, 953–964.
- Bennett, C. J., T. Hama, Y. S. Kim, M. Kawasaki, and R. I. Kaiser (2011, January). Laboratory Studies on the Formation of Formic Acid (HCOOH) in Interstellar and Cometary Ices. *APJ* 727, 27.

- Benson, P. J., I. R. Little-Marenin, T. C. Woods, J. M. Attridge, K. A. Blais, D. B. Rudolph, M. E. Rubiera, and H. L. Keefe (1990, December). A catalog of observations for stellar masers. *SPJS* 74, 911–1074.
- Bisschop, S. E., G. W. Fuchs, A. C. A. Boogert, E. F. van Dishoeck, and H. Linhartz (2007, August). Infrared spectroscopy of HCOOH in interstellar ice analogues. *AAP* 470, 749–759.
- Blake, D. H., R. M. Crutcher, and W. D. Watson (1980, October). Identification of the anomalous 26.131-MHz nitrogen line observed towards CAS A. *Nature* 287, 707.
- Boch, T. and P. Fernique (2014, May). Aladin Lite: Embed your Sky in the Browser. In N. Manset and P. Forshay (Eds.), *Astronomical Data Analysis Software and Systems XXIII*, Volume 485 of *Astronomical Society of the Pacific Conference Series*, pp. 277.
- Bonnarel, F., P. Fernique, O. Bienaymé, D. Egret, F. Genova, et al. (2000, April). The ALADIN interactive sky atlas. A reference tool for identification of astronomical sources. *AAPS* 143, 33–40.
- Bonnell, I. A. and M. R. Bate (2006, July). Star formation through gravitational collapse and competitive accretion. *MNRAS* 370, 488–494.
- Bonnell, I. A., M. R. Bate, C. J. Clarke, and J. E. Pringle (2001, May). Competitive accretion in embedded stellar clusters. *MNRAS* 323, 785–794.
- Bonnell, I. A., M. R. Bate, and H. Zinnecker (1998, July). On the formation of massive stars. *MNRAS* 298, 93–102.
- Bonnell, I. A., S. G. Vine, and M. R. Bate (2004, April). Massive star formation: nurture, not nature. *MNRAS* 349, 735–741.
- Boughton, W. L. (1978, June). Carbon recombination lines and the neutral hydrogen clouds near the Orion Nebula. *APJ* 222, 517–526.
- Bowman, J. D., I. Cairns, D. L. Kaplan, et al. (2013, April). Science with the Murchison Widefield Array. *PASA* 30, e031.
- Brand, J. and L. Blitz (1993, August). The Velocity Field of the Outer Galaxy. *AAP* 275, 67.

- Bressert, E., N. Bastian, C. J. Evans, H. Sana, V. Hénault-Brunet, et al. (2012, June). The VLT-FLAMES Tarantula Survey. IV. Candidates for isolated high-mass star formation in 30 Doradus. *AAP* 542, A49.
- Briggs, D. S. (1995, December). High Fidelity Interferometric Imaging: Robust Weighting and NNLS Deconvolution. In *American Astronomical Society Meeting Abstracts*, Volume 27 of *Bulletin of the American Astronomical Society*, pp. 1444.
- Bruderer, S., A. O. Benz, P. Stäuber, and S. D. Doty (2010, September). Multi-dimensional Chemical Modeling of Young Stellar Objects. III. The Influence of Geometry on the Abundance and Excitation of Diatomic Hydrides. *APJ* 720, 1432–1453.
- Burke, D. J. and W. A. Brown (2010). Ice in space: surface science investigations of the thermal desorption of model interstellar ices on dust grain analogue surfaces. *Physical Chemistry Chemical Physics (Incorporating Faraday Transactions)* 12, 5947.
- Cami, J., J. Bernard-Salas, E. Peeters, and S. E. Malek (2010, September). Detection of C₆₀ and C₇₀ in a Young Planetary Nebula. *Science* 329, 1180.
- Carey, S. J., A. Noriega-Crespo, D. R. Mizuno, S. Shenoy, R. Paladini, et al. (2009, January). MIPS GAL: A Survey of the Inner Galactic Plane at 24 and 70 μm . *PASP* 121, 76.
- Carvajal, M., I. Kleiner, and J. Demaison (2010, October). Global Assignment and Extension of Millimeter- and Submillimeter-wave Spectral Database of ¹³C₁-methyl Formate (H¹³COOCH₃) in the Ground and First Excited States. *APJS* 190, 315–321.
- Casoli, F., F. Combes, C. Dupraz, M. Gerin, and F. Boulanger (1986, November). (C-13)O and (C-12)O observations of cold IRAS unidentified point sources in the Galaxy. *AAP* 169, 281–297.
- Cernicharo, J., M. Guélin, M. Agúndez, J. R. Pardo, S. Massalkhi, J. P. Fonfría, L. Velilla Prieto, G. Quintana-Lacaci, N. Marcelino, C. Marka, S. Navarro, and C. Kramer (2018, October). IRC +10216 as a spectroscopic laboratory: improved rotational constants for SiC₂, its isotopologues, and Si₂C. *AAP* 618, A4.

- Chaisson, E. J. and C. J. Lada (1974, April). Recombination Lines from H i Gas Toward Orion a. *APJ* 189, 227–238.
- Chambers, E. T., F. Yusef-Zadeh, and J. Ott (2014, March). Star formation sites toward the Galactic center region. The correlation of CH₃OH masers, H₂O masers, and near-IR green sources. *AAP* 563, A68.
- Chen, J.-H., P. F. Goldsmith, S. Viti, R. Snell, D. C. Lis, et al. (2014, October). Herschel HIFI Observations of O₂ toward Orion: Special Conditions for Shock Enhanced Emission. *APJ* 793, 111.
- Churchwell, E., B. L. Babler, M. R. Meade, B. A. Whitney, R. Benjamin, R. Indebetouw, C. Cyganowski, T. P. Robitaille, M. Povich, C. Watson, and S. Bracker (2009, March). The Spitzer/GLIMPSE Surveys: A New View of the Milky Way. *PASP* 121, 213–230.
- Clancy, P. F. (1980, November). Some advantages of wide over narrow band signals in the search for extraterrestrial intelligence (SETI). *Journal of the British Interplanetary Society* 33, 391–395.
- Clark, C. J. R., L. Dunne, H. L. Gomez, et al. (2015, September). Herschel-ATLAS: the surprising diversity of dust-selected galaxies in the local submillimetre Universe. *MNRAS* 452, 397–430.
- Cocconi, G. and P. Morrison (1959, September). Searching for Interstellar Communications. *NAT* 184, 844–846.
- Codella, C., L. Podio, F. Fontani, I. Jimenez-Serra, P. Caselli, et al. (2015, April). Complex organic molecules in protostellar environments in the SKA era. *Advancing Astrophysics with the Square Kilometre Array (AASKA14)*, 123.
- Comito, C., P. Schilke, M. Gerin, T. G. Phillips, J. Zmuidzinas, et al. (2003, May). The line-of-sight distribution of water in the SgrB2 complex. *AAP* 402, 635–645.
- Commerçon, B., P. Hennebelle, and T. Henning (2011, November). Collapse of Massive Magnetized Dense Cores Using Radiation Magnetohydrodynamics: Early Fragmentation Inhibition. *APJL* 742, L9.
- Condon, J. J. and S. M. Ransom (2016). *Essential Radio Astronomy*.

- Contreras, Y., F. Schuller, J. S. Urquhart, T. Csengeri, F. Wyrowski, et al. (2013, January). ATLASGAL - compact source catalogue: 330deg–21deg. *AAP* 549, A45.
- Cornwell, T. J., K. Golap, and S. Bhatnagar (2005, March). Wide field imaging problems in radio astronomy. *Astrophysics and Space Science Proceedings* 5.
- Cornwell, T. J., J. M. Uson, and N. Haddad (1992, May). Radio-interferometric imaging of spectral lines - The problem of continuum subtraction. *AAP* 258, 583–590.
- Cosmovici, C. B. (1979). Extraterrestrial molecules - Present and future observations from space. In M. F. McCarthy, A. G. D. Philip, and G. V. Coyne (Eds.), *IAU Colloq. 47: Spectral Classification of the Future*, Volume 9 of *Ricerche Astronomiche*, pp. 439–456.
- Crockett, N. R., E. A. Bergin, J. L. Neill, C. Favre, P. Schilke, et al. (2014, June). Herschel Observations of Extraordinary Sources: Analysis of the HIFI 1.2 THz Wide Spectral Survey toward Orion KL. I. Methods. *APJ* 787, 112.
- Cunningham, M. R., P. A. Jones, P. D. Godfrey, D. M. Cragg, I. Bains, et al. (2007, April). A search for propylene oxide and glycine in Sagittarius B2 (LMH) and Orion. *MNRAS* 376, 1201–1210.
- Cyburt, R. H., B. D. Fields, K. A. Olive, and T.-H. Yeh (2016, January). Big bang nucleosynthesis: Present status. *Reviews of Modern Physics* 88(1), 015004.
- Dalgarno, A. (2008, September). A Serendipitous Journey. *ARAA* 46, 1–20.
- Dame, T. M., D. Hartmann, and P. Thaddeus (2001, February). The Milky Way in Molecular Clouds: A New Complete CO Survey. *APJ* 547, 792–813.
- Dame, T. M., H. Ungerechts, R. S. Cohen, E. J. de Geus, I. A. Grenier, J. May, D. C. Murphy, L.-A. Nyman, and P. Thaddeus (1987, November). A composite CO survey of the entire Milky Way. *APJ* 322, 706–720.
- Danilovich, T., E. De Beck, J. H. Black, H. Olofsson, and K. Justtanont (2016, April). Sulphur molecules in the circumstellar envelopes of M-type AGB stars. *AAP* 588, A119.
- Das, A., L. Majumdar, S. K. Chakrabarti, and D. Sahu (2015, February). Deuterium enrichment of the interstellar medium. *NA* 35, 53–70.

- Davies, B., M. G. Hoare, S. L. Lumsden, T. Hosokawa, R. D. Oudmaijer, J. S. Urquhart, J. C. Mottram, and J. Stead (2011, September). The Red MSX Source survey: critical tests of accretion models for the formation of massive stars. *MNRAS* *416*, 972–990.
- Dawson, J. R., A. J. Walsh, P. A. Jones, et al. (2014, April). SPLASH: the Southern Parkes Large-Area Survey in Hydroxyl - first science from the pilot region. *MNRAS* *439*, 1596–1614.
- de Wit, W. J., L. Testi, F. Palla, and H. Zinnecker (2005, July). The origin of massive O-type field stars: II. Field O stars as runaways. *AAP* *437*, 247–255.
- Decin, L., E. De Beck, S. Brünken, et al. (2010, June). Circumstellar molecular composition of the oxygen-rich AGB star IK Tauri. II. In-depth non-LTE chemical abundance analysis. *AAP* *516*, A69.
- Defrees, D. J. and A. D. McLean (1986). A priori predictions of the rotational constants for protonated formaldehyde and protonated methanol. *Chemical Physics Letters* *131*, 403–408.
- Dempsey, J. T., H. S. Thomas, and M. J. Currie (2013, November). CO (3 - 2) High-resolution Survey of the Galactic Plane: R1. *APJS* *209*, 8.
- Dobbs, C. L., M. R. Krumholz, J. Ballesteros-Paredes, A. D. Bolatto, Y. Fukui, et al. (2014). Formation of Molecular Clouds and Global Conditions for Star Formation. *Protostars and Planets VI*, 3–26.
- Du, Z. M., J. J. Zhou, J. Esimbek, X. H. Han, and C. P. Zhang (2011, August). A H₂CO and H110 α survey of H ii regions with the 25-m radio telescope of Nanshan Station. *AAP* *532*, A127.
- Egan, M. P., S. D. Price, and K. E. Kraemer (2003, December). The Midcourse Space Experiment Point Source Catalog Version 2.3. In *American Astronomical Society Meeting Abstracts*, Volume 35 of *Bulletin of the American Astronomical Society*, pp. 1301.
- Enriquez, J. E. and Breakthrough Listen Team (2018, January). The Breakthrough Listen Search for Intelligent Life: the first SETI results and other future science. In *American Astronomical Society Meeting Abstracts No. 231*, Volume 231 of *American Astronomical Society Meeting Abstracts*, pp. 401.02.

- Fedoseev, G., S. Ioppolo, T. Lamberts, J. F. Zhen, H. M. Cuppen, and H. Linnartz (2012, August). Efficient surface formation route of interstellar hydroxylamine through NO hydrogenation. II. The multilayer regime in interstellar relevant ices. *JCP* 137(5), 054714–054714.
- Feelisch, M. and J. Martin (1995). The early role of nitric oxide in evolution. *Evolutionary Ecology* 9(3), iii–iii.
- Feldt, M., B. Stecklum, T. Henning, T. L. Hayward, T. Lehmann, and R. Klein (1998, November). The ultracompact H II region G45.45+0.06. A pearl necklace in the sky. *AAP* 339, 759–772.
- Ferrière, K. M. (2001, October). The interstellar environment of our galaxy. *Reviews of Modern Physics* 73, 1031–1066.
- Finkbeiner, D. P. (2003, June). A Full-Sky H α Template for Microwave Foreground Prediction. *APJS* 146, 407–415.
- Fletcher, N. H. (2002, December). Harmonic? Anharmonic? Inharmonic? *AJP* 70, 1205–1207.
- Fonfría, J. P., J. Cernicharo, M. J. Richter, and J. H. Lacy (2011, February). The Abundances of Polyacetylenes Toward CRL618. *ApJ* 728, 43.
- Garrett, M., A. Siemion, and W. van Cappellen (2017, September). All-sky Radio SETI. *ArXiv e-prints*.
- Garwood, R. W., R. A. Perley, J. M. Dickey, and M. A. Murray (1988, November). A VLA snapshot continuum survey of the first quadrant of the Galactic plane at 1.5 GHz. *AJ* 96, 1655–1670.
- Gerin, M., Y. Viala, F. Pauzat, and Y. Ellinger (1992, December). The abundance of nitric oxide in molecular clouds. *AAP* 266, 463–478.
- Girardi, L., A. Bressan, C. Chiosi, G. Bertelli, and E. Nasi (1996, May). Evolutionary sequences of stellar models with new radiative opacities. VI. Z=0.0001. *AAPs* 117, 113–125.
- Godard, B., E. Falgarone, M. Gerin, et al. (2012, April). Comparative study of CH⁺ and SH⁺ absorption lines observed towards distant star-forming regions. *AAP* 540, A87.

- Goldberg, L. (1966, June). Stimulated Emission of Radio-Frequency Lines of Hydrogen. *ApJ* 144, 1225–1231.
- Goldsmith, P. F., R. Liseau, T. A. Bell, J. H. Black, J.-H. Chen, et al. (2011, August). Herschel Measurements of Molecular Oxygen in Orion. *APJ* 737, 96.
- Gooch, R. (1996). Karma: a Visualization Test-Bed. In G. H. Jacoby and J. Barnes (Eds.), *Astronomical Data Analysis Software and Systems V*, Volume 101 of *Astronomical Society of the Pacific Conference Series*, pp. 80.
- Gorai, P., A. Das, A. Das, B. Sivaraman, E. E. Etim, and S. K. Chakrabarti (2017, February). A Search for Interstellar Monohydric Thiols. *APJ* 836, 70.
- Gordon, M. A. and R. L. Sorochenko (Eds.) (2009). *Radio Recombination Lines*, Volume 282 of *Astrophysics and Space Science Library*.
- GRAVITY Collaboration, R. Abuter, A. Amorim, M. Bauböck, J. P. Berger, H. Bonnet, et al. (2018, October). Detection of orbital motions near the last stable circular orbit of the massive black hole SgrA*. *ArXiv e-prints*, arXiv:1810.12641.
- Gray, R. H. and K. Mooley (2017, March). A VLA Search for Radio Signals from M31 and M33. *AJ* 153, 110.
- Greene, T. (2001, August). Protostars. *American Scientist* 89, 316.
- Gupta, Y. (2014). The GMRT: current status and upgrade plans. In *Astronomical Society of India Conference Series*, Volume 13 of *Astronomical Society of India Conference Series*, pp. 441–447.
- Hancock, P. J., T. Murphy, B. M. Gaensler, A. Hopkins, and J. R. Curran (2012, May). Compact continuum source finding for next generation radio surveys. *MNRAS* 422, 1812–1824.
- Hancock, P. J., C. M. Trott, and N. Hurley-Walker (2018, March). Source Finding in the Era of the SKA (Precursors): Aegean 2.0. *PASA* 35, e011.
- Handa, T., Y. Sofue, N. Nakai, H. Hirabayashi, and M. Inoue (1987). A radio continuum survey of the Galactic plane at 10 GHz. *PASJ* 39, 709–753.
- Hennebelle, P., B. Commerçon, M. Joos, R. S. Klessen, M. Krumholz, et al. (2011, April). Collapse, outflows and fragmentation of massive, turbulent and magnetized prestellar barotropic cores. *AAP* 528, A72.

- Herbst, E. and E. F. van Dishoeck (2009, September). Complex Organic Interstellar Molecules. *ARAA* 47, 427–480.
- Hildebrand, R. H. (1983, September). The Determination of Cloud Masses and Dust Characteristics from Submillimetre Thermal Emission. *QJRAS* 24, 267.
- Hillenbrand, L. A. and L. W. Hartmann (1998, January). A Preliminary Study of the Orion Nebula Cluster Structure and Dynamics. *APJ* 492, 540–553.
- Hily-Blant, P., M. Walmsley, G. Pineau des Fore‘ts, and D. Flower (2010, April). Nitrogen chemistry and depletion in starless cores. *A&A* 513, A41.
- Himmele, W., W. Bremser, and H. Siege (1979). Selective Deuteration of Enamines with Deuterated Formic Acids. *Angew. Chem. Int. Ed.* 4(18), 320–321.
- Hindson, L., M. Johnston-Hollitt, N. Hurley-Walker, J. R. Callingham, H. Su, et al. (2016, May). A Large-Scale, Low-Frequency Murchison Widefield Array Survey of Galactic H ii Regions between 260 l 340. *PASA* 33, e020.
- Hippke, M. and D. H. Forgan (2017, November). Interstellar communication. III. Optimal frequency to maximize data rate. *ArXiv e-prints*.
- Höfner, S. and A. C. Andersen (2007, April). Winds of M- and S-type AGB stars: an unorthodox suggestion for the driving mechanism. *AAP* 465, L39–L42.
- Hogbom, J. A. and W. N. Brouw (1974, July). The Synthesis Radio Telescope at Westerbork. Principles of Operation, Performance and Data Reduction. *AAP* 33, 289.
- Howe, J. E., D. T. Jaffe, E. N. Grossman, W. F. Wall, J. G. Mangum, and G. J. Stacey (1993, June). Extended CO(7-6) emission from warm gas in Orion. *APJ* 410, 179–187.
- Huettemeister, S. (1998, March). Surveys of molecular gas in the Galactic center region: On the usefulness of tedious projects with moderate-sized telescopes. *Galactic Center Newsletter* 7, 3–6.
- Hurley-Walker, N., J. R. Callingham, P. J. Hancock, T. M. O. Franzen, L. Hindson, et al. (2017, January). GaLactic and Extragalactic All-sky Murchison Widefield Array (GLEAM) survey - I. A low-frequency extragalactic catalogue. *MNRAS* 464, 1146–1167.

- Hurley-Walker, N. and P. J. Hancock (2018, October). De-distorting ionospheric effects in the image plane. *Astronomy and Computing* 25, 94–102.
- Hurley-Walker, N., J. Morgan, R. B. Wayth, et al. (2014, November). The Murchison Widefield Array Commissioning Survey: A Low-Frequency Catalogue of 14 110 Compact Radio Sources over 6 100 Square Degrees. *PASA* 31, e045.
- Ioppolo, S., Y. van Boheemen, H. M. Cuppen, E. F. van Dishoeck, and H. Linnartz (2011, May). Surface formation of CO₂ ice at low temperatures. *MNRAS* 413, 2281–2287.
- Isaacson, H., A. P. V. Siemion, G. W. Marcy, M. Lebofsky, D. C. Price, et al. (2017, August). VizieR Online Data Catalog: Search for extraterrestrial intelligence (Isaacson+, 2017). *VizieR Online Data Catalog* 613.
- Isaacson, H. T. and A. P. V. Siemion (2017, November). Breakthrough Listen: Searching for Signatures of Technology. *LPI Contributions* 2042, 4144.
- Isella, A., C. L. H. Hull, A. Moullet, R. Galván-Madrid, D. Johnstone, et al. (2015, October). Next Generation Very Large Array Memo No. 6, Science Working Group 1: The Cradle of Life. *ArXiv e-prints*.
- Izumi, N., N. Kobayashi, C. Yasui, A. Tokunaga, M. Saito, and S. Hamano (2014, November). Discovery of Star Formation in the Extreme Outer Galaxy Possibly Induced by a High-velocity Cloud Impact. *APJ* 795, 66.
- Jackson, J. M., T. M. Bania, R. Simon, M. Kolpak, D. P. Clemens, and M. Heyer (2002, February). H I Self-Absorption and the Kinematic Distance Ambiguity: The Case of the Molecular Cloud GRSMC 45.6+0.3. *APJL* 566, L81–L84.
- Jackson, J. M., J. M. Rathborne, J. B. Foster, J. S. Whitaker, P. Sanhueza, et al. (2013, November). MALT90: The Millimetre Astronomy Legacy Team 90 GHz Survey. *PASA* 30, e057.
- Jones, P. A., M. G. Burton, M. R. Cunningham, M. A. Requena-Torres, K. M. Menten, et al. (2012, February). Spectral imaging of the Central Molecular Zone in multiple 3-mm molecular lines. *MNRAS* 419, 2961–2986.
- Jones, P. A., M. G. Burton, M. R. Cunningham, N. F. H. Tothill, and A. J. Walsh (2013, July). Spectral imaging of the central molecular zone in multiple 7-mm molecular lines. *MNRAS* 433, 221–234.

- Jordan, C. H., A. J. Walsh, V. Lowe, et al. (2015, April). MALT-45: a 7 mm survey of the southern Galaxy - I. Techniques and spectral line data. *MNRAS* *448*, 2344–2361.
- Karovicova, I., M. Wittkowski, K. Ohnaka, D. A. Boboltz, E. Fossat, and M. Scholz (2013, December). New insights into the dust formation of oxygen-rich AGB stars. *AAP* *560*, A75.
- Kennicutt, R. C. and N. J. Evans (2012, September). Star Formation in the Milky Way and Nearby Galaxies. *ARAAS* *50*, 531–608.
- Kolpak, M. A., J. M. Jackson, T. M. Bania, D. P. Clemens, and J. M. Dickey (2003, January). Resolving the Kinematic Distance Ambiguity toward Galactic H II Regions. *APJ* *582*, 756–769.
- Kong, S., J. C. Tan, P. Caselli, and F. Fontani (2015, May). The Deuteration Clock for Massive Starless Cores. In *EAS Publications Series*, Volume 75 of *EAS Publications Series*, pp. 337–341.
- Konovalenko, A. A. and L. G. Sodin (1980, January). Neutral N-14 in the interstellar medium. *Nature* *283*, 360.
- Koribalski, B. S. (2012a, August). Overview on Spectral Line Source Finding and Visualisation. *PASA* *29*, 359–370.
- Koribalski, B. S. (2012b, September). Source Finding and Visualisation. *PASA* *29*, 213–213.
- Kroupa, P., C. A. Tout, and G. Gilmore (1993, June). The distribution of low-mass stars in the Galactic disc. *MNRAS* *262*, 545–587.
- Kruijssen, J. M. D., J. E. Dale, and S. N. Longmore (2015, February). The dynamical evolution of molecular clouds near the Galactic Centre - I. Orbital structure and evolutionary timeline. *MNRAS* *447*, 1059–1079.
- Krumholz, M. R., R. I. Klein, and C. F. McKee (2007, February). Radiation-Hydrodynamic Simulations of Collapse and Fragmentation in Massive Protostellar Cores. *ApJ* *656*, 959–979.
- Krumholz, M. R., R. I. Klein, C. F. McKee, S. S. R. Offner, and A. J. Cunningham (2009, February). The Formation of Massive Star Systems by Accretion. *Science* *323*, 754.

- Krumholz, M. R. and T. A. Thompson (2012, December). Direct Numerical Simulation of Radiation Pressure-driven Turbulence and Winds in Star Clusters and Galactic Disks. *ApJ* 760, 155.
- Kuiper, R., H. Klahr, H. Beuther, and T. Henning (2010, October). Circumventing the Radiation Pressure Barrier in the Formation of Massive Stars via Disk Accretion. *APJ* 722, 1556–1576.
- Kurtz, S., E. Churchwell, and D. O. S. Wood (1994, April). Ultracompact H II regions. 2: New high-resolution radio images. *APJS* 91, 659–712.
- Lacour, S., M. K. André, P. Sonnentrucker, F. Le Petit, D. E. Welty, J.-M. Desert, R. Ferlet, E. Roueff, and D. G. York (2005, February). Deuterated molecular hydrogen in the Galactic ISM. New observations along seven translucent sightlines. *AAP* 430, 967–977.
- Lada, C. J. (1997, January). Twenty-five years of CO astronomy: revealing the cold universe. In W. B. Latter, S. J. E. Radford, P. R. Jewell, J. G. Mangum, and J. Bally (Eds.), *IAU Symposium*, Volume 170, pp. 387–396.
- Large, M. I., B. Y. Mills, A. G. Little, D. F. Crawford, and J. M. Sutton (1981, February). The Molonglo Reference Catalogue of Radio Sources. *MNRAS* 194, 693.
- Lawrence, A., S. J. Warren, O. Almaini, A. C. Edge, N. C. Hambly, et al. (2007, August). The UKIRT Infrared Deep Sky Survey (UKIDSS). *MNRAS* 379, 1599–1617.
- Leger, A. and J. L. Puget (1984, August). Identification of the ‘unidentified’ IR emission features of interstellar dust? *AAP* 137, L5–L8.
- Lejeune, T. and D. Schaerer (2001, February). Database of Geneva stellar evolution tracks and isochrones for (UBV)_J(RI)_C JHKLL’M, HST-WFPC2, Geneva and Washington photometric systems. *AAP* 366, 538–546.
- Lenc, E., C. S. Anderson, N. Barry, J. D. Bowman, et al. (2017, September). The Challenges of Low-Frequency Radio Polarimetry: Lessons from the Murchison Widefield Array. *PASA* 34, e040.
- Lequeux, J. and E. Roueff (1991, February). Interstellar molecules. *PHYS-REP* 200, 241–299.

- Linnartz, H., S. Ioppolo, and G. Fedoseev (2015, July). Atom addition reactions in interstellar ice analogues. *ArXiv e-prints*.
- Lique, F., M. Jorfi, P. Honvault, P. Halvick, S. Y. Lin, et al. (2009, December). O+OH–O₂+H: A key reaction for interstellar chemistry. New theoretical results and comparison with experiment. *JCP* 131(22), 221104–221104.
- Liszt, H. S. and B. E. Turner (1978, September). Microwave detection of interstellar NO. *APJL* 224, L73–L76.
- Liszt, H. S., R. W. Wilson, A. A. Penzias, K. B. Jefferts, P. G. Wannier, and P. M. Solomon (1974, June). CO and CS in the Orion Nebula. *APJ* 190, 557–564.
- Lockhart, I. A. and W. M. Goss (1978, July). High-resolution mapping of the H I absorption lines in the direction of NGC 2024, Orion A, M17 and W49. *AAP* 67, 355–372.
- Lockman, F. J. (1989, November). A survey of radio H II regions in the northern sky. *APJS* 71, 469–479.
- Lonsdale, C. J., R. J. Cappallo, M. F. Morales, et al. (2009, August). The Murchison Widefield Array: Design Overview. *IEEE Proceedings* 97, 1497–1506.
- Lovas, F. J., J. Coursey, S. Kotochigova, J. Chang, K. Olsen, and R. Dragoset (2003). Triatomic spectral database (version 2.0).
- Mangum, J. G. and Y. L. Shirley (2015, March). How to Calculate Molecular Column Density. *PASP* 127, 266–298.
- Margot, J.-L., A. H. Greenberg, P. Pinchuk, A. Shinde, Y. Alladi, et al. (2018, February). A search for technosignatures from 14 planetary systems in the Kepler field with the Green Bank Telescope at 1.15-1.73 GHz. *ArXiv e-prints*.
- Martín, S., M. A. Requena-Torres, J. Martín-Pintado, and R. Mauersberger (2008, January). The Galactic Center as nearby extragalactic chemical laboratory. *APSS* 313, 303–306.
- Masunaga, H. and S.-i. Inutsuka (2000, June). Infall Signatures in Spectral Line Profiles of Protostellar Envelopes. *APJ* 536, 406–415.

- Maxted, N. I., P. de Wilt, G. P. Rowell, B. P. Nicholas, M. G. Burton, A. Walsh, Y. Fukui, and A. Kawamura (2016, October). Ammonia excitation imaging of shocked gas towards the W28 gamma-ray source HESS J1801-233. *MNRAS* 462, 532–546.
- McGuire, B. A., P. B. Carroll, R. A. Loomis, I. A. Finneran, P. R. Jewell, A. J. Remijan, and G. A. Blake (2016, June). Discovery of the interstellar chiral molecule propylene oxide ($\text{CH}_3\text{CHCH}_2\text{O}$). *Science* 352, 1449–1452.
- McKee, C. F. and E. C. Ostriker (2007, September). Theory of Star Formation. *ARAA* 45, 565–687.
- McKee, C. F. and J. C. Tan (2003, March). The Formation of Massive Stars from Turbulent Cores. *APJ* 585, 850–871.
- McMullin, J. P., B. Waters, D. Schiebel, W. Young, and K. Golap (2007, October). CASA Architecture and Applications. In R. A. Shaw, F. Hill, and D. J. Bell (Eds.), *Astronomical Data Analysis Software and Systems XVI*, Volume 376 of *Astronomical Society of the Pacific Conference Series*, pp. 127.
- Menten, K. M. (2004). Perspective from a Younger Generation - The Astrometry of Gisbert Winnewisser. In S. Pfalzner, C. Kramer, C. Staubmeier, and A. Heithausen (Eds.), *The Dense Interstellar Medium in Galaxies*, pp. 69.
- Menten, K. M., M. J. Reid, J. Forbrich, and A. Brunthaler (2007, November). The distance to the Orion Nebula. *AAP* 474, 515–520.
- Meurer, G. R., T. M. Heckman, and D. Calzetti (1999, August). Dust Absorption and the Ultraviolet Luminosity Density at $z \sim 3$ as Calibrated by Local Starburst Galaxies. *APJ* 521, 64–80.
- Mevius, M., S. van der Tol, V. N. Pandey, H. K. Vedantham, M. A. Brentjens, et al. (2016, July). Probing ionospheric structures using the LOFAR radio telescope. *Radio Science* 51, 927–941.
- Mezger, P. G. and A. P. Henderson (1967, February). Galactic H II Regions. I. Observations of Their Continuum Radiation at the Frequency 5 GHz. *ApJ* 147, 471.
- Miettinen, O. (2012, June). LABOCA 870 μm dust continuum mapping of selected infrared-dark cloud regions in the Galactic plane. *AAP* 542, A101.

- Millar, T. J. and E. Herbst (1990, May). Organo-sulphur chemistry in dense interstellar clouds. *AAP 231*, 466–472.
- Molinari, S., B. Swinyard, J. Bally, M. Barlow, J.-P. Bernard, et al. (2010, March). Hi-GAL: The Herschel Infrared Galactic Plane Survey. *PASP 122*, 314.
- Morabito, L. K., J. B. R. Oonk, F. Salgado, M. C. Toribio, H. J. A. Röttgering, et al. (2014, November). Discovery of Carbon Radio Recombination Lines in M82. *APJL 795*, L33.
- Morales, R. G. E. (2012). Cyanopolynes as Organic Molecular Wires in the Interstellar Medium. *IJA&A 2*, 230–235.
- Morris, M. and E. Serabyn (1996). The Galactic Center Environment. *ARAA 34*, 645–702.
- Morton, D. C. (1975, July). Observations of the interstellar gas with the Copernicus satellite. *Royal Society of London Philosophical Transactions Series A 279*, 299–302.
- Muench, A., K. Getman, L. Hillenbrand, and T. Preibisch (2008, December). *Star Formation in the Orion Nebula I: Stellar Content*, pp. 483.
- Müller, H. S. P., S. Thorwirth, D. A. Roth, and G. Winnewisser (2001, April). The Cologne Database for Molecular Spectroscopy, CDMS. *AAP 370*, L49–L52.
- Myers, A. T., C. F. McKee, A. J. Cunningham, R. I. Klein, and M. R. Krumholz (2013, April). The Fragmentation of Magnetized, Massive Star-forming Cores with Radiative Feedback. *APJ 766*, 97.
- Neben, A. R., J. N. Hewitt, R. F. Bradley, J. S. Dillon, G. Bernardi, et al. (2016, March). Beam-forming Errors in Murchison Widefield Array Phased Array Antennas and their Effects on Epoch of Reionization Science. *APJ 820*, 44.
- Neill, J. L., E. A. Bergin, D. C. Lis, P. Schilke, N. R. Crockett, and et al (2014, July). Herschel Observations of Extraordinary Sources: Analysis of the Full Herschel/HIFI Molecular Line Survey of Sagittarius B2(N). *APJ 789*, 8.

- Neill, J. L., N. R. Crockett, E. A. Bergin, J. C. Pearson, and L.-H. Xu (2013, November). Deuterated Molecules in Orion KL from Herschel/HIFI. *APJ* 777, 85.
- Neufeld, D. A., E. Falgarone, M. Gerin, et al. (2012, June). Discovery of interstellar mercapto radicals (SH) with the GREAT instrument on SOFIA. *AAP* 542, L6.
- Neugebauer, G., B. T. Soifer, G. Miley, H. J. Habing, E. Young, et al. (1984, March). IRAS observations of radio-quiet and radio-loud quasars. *APJL* 278, L83–L85.
- Nishiyama, S., M. Tamura, H. Hatano, D. Kato, T. Tanabé, et al. (2009, May). Interstellar Extinction Law Toward the Galactic Center III: J, H, K_S Bands in the 2MASS and the MKO Systems, and 3.6, 4.5, 5.8, 8.0 μm in the Spitzer/IRAC System. *APJ* 696, 1407–1417.
- O’Dell, C. R., G. J. Ferland, W. J. Henney, M. Peimbert, M. T. García-Díaz, and R. H. Rubin (2015, October). The Nature and Frequency of Outflows from Stars in the Central Orion Nebula Cluster. *AJ* 150, 108.
- Odell, C. R. and Ferland, G. J., R. L. Porter, and P. A. M. V. Hoof (2011). Physical conditions in barnard’s loop, components of the orion–eridanus bubble, and implications for the warm ionized medium component of the interstellar medium. *APJ* 733, 9.
- Offringa, A. R., A. G. de Bruyn, M. Biehl, et al. (2010, June). Post-correlation radio frequency interference classification methods. *MNRAS* 405, 155–167.
- Offringa, A. R., B. McKinley, N. Hurley-Walker, et al. (2014, October). WSCLEAN: an implementation of a fast, generic wide-field imager for radio astronomy. *MNRAS* 444, 606–619.
- Offringa, A. R., C. M. Trott, N. Hurley-Walker, et al. (2016, May). Parametrizing Epoch of Reionization foregrounds: a deep survey of low-frequency point-source spectra with the Murchison Widefield Array. *MNRAS* 458, 1057–1070.
- Offringa, A. R., J. J. van de Gronde, and J. B. T. M. Roerdink (2012, March). A morphological algorithm for improving radio-frequency interference detection. *AAP* 539, A95.

- Offringa, A. R., R. B. Wayth, N. Hurley-Walker, D. L. Kaplan, N. Barry, et al. (2015, March). The Low-Frequency Environment of the Murchison Widefield Array: Radio-Frequency Interference Analysis and Mitigation. *PASA* 32, e008.
- Oh, S. and P. Kroupa (2018, November). Very massive stars in not so massive clusters. *MNRAS* 481, 153–163.
- Oliver, B. M. and J. Billingham (Eds.) (1971). *Project Cyclops: A Design Study of a System for Detecting Extraterrestrial Intelligent Life*.
- Olmi, L., E. D. Araya, P. Hofner, S. Molinari, et al. (2014, June). Discovery of weak 6.7 GHz CH₃OH masers in a sample of high-mass Hi-GAL sources. *AAP* 566, A18.
- Olmi, L., C. M. Persson, and C. Codella (2015, November). Herschel-HIFI observations of H₂O, NH₃, and N₂H⁺ toward high-mass starless and protostellar clumps identified by the Hi-GAL survey. *AAP* 583, A125.
- Olofsson, H., L. E. B. Johansson, A. Hjalmarson, and Nguyen-Quang-Rieu (1982, March). High sensitivity molecular line observations of IRC + 10216. *AAP* 107, 128–144.
- Oonk, J. B. R. et al. (2014, February). Discovery of carbon radio recombination lines in absorption towards Cygnus A. *MNRAS* 437, 3506–3515.
- Ord, S. M., B. Crosse, D. Emrich, D. Pallot, R. B. Wayth, et al. (2015, March). The Murchison Widefield Array Correlator. *PASA* 32, e006.
- Ossenkopf, V. and T. Henning (1994, November). Dust opacities for protostellar cores. *AAP* 291, 943–959.
- Osterbrock, D. and E. Flather (1959, January). Electron Densities in the Orion Nebula. II. *APJ* 129, 26.
- Pagani, L., W. D. Langer, and A. Castets (1993, July). First Tentative Detection of the Molecular Oxygen Isotopomer 16/O/18/O in Interstellar Clouds. *AAP* 274, L13.
- Parker, R. J. and S. P. Goodwin (2007, September). Do O-stars form in isolation? *MNRAS* 380, 1271–1275.

- Payne, H. E., K. R. Anantharamaiah, and W. C. Erickson (1989, June). Stimulated emission of carbon recombination lines from cold clouds in the direction of Cassiopeia A. *ApJ* *341*, 890–900.
- Payne, H. E., K. R. Anantharamaiah, and W. C. Erickson (1994, August). High Rydberg state carbon recombination lines toward Cassiopeia A: Physical conditions and a new class of models. *APJ* *430*, 690–705.
- Perley, R. A., J. Callingham, and B. J. Butler (2016, January). An Accurate, All-Sky, Absolute, Low-Frequency Flux Density Scale. In *American Astronomical Society Meeting Abstracts*, Volume 227 of *American Astronomical Society Meeting Abstracts*, pp. 113.05.
- Perley, R. A., C. J. Chandler, B. J. Butler, and J. M. Wrobel (2011, September). The Expanded Very Large Array: A New Telescope for New Science. *APJL* *739*, L1.
- Peters, T., R. Banerjee, R. S. Klessen, M.-M. Mac Low, R. Galván-Madrid, and E. R. Keto (2010, March). H II Regions: Witnesses to Massive Star Formation. *APJ* *711*, 1017–1028.
- Peters, W. M., T. Clarke, J. Lazio, and N. Kassim (2010, January). Radio Recombination Lines at Decameter Wavelengths: Prospects for the Future. In *American Astronomical Society Meeting Abstracts No. 215*, Volume 42 of *Bulletin of the American Astronomical Society*, pp. 262.
- Pickett, H. M., R. L. Poynter, E. A. Cohen, M. L. Delitsky, J. C. Pearson, and H. S. P. Müller (1998, November). Submillimeter, millimeter and microwave spectral line catalog. *JQSRT* *60*, 883–890.
- Pilbratt, G. L., J. R. Riedinger, T. Passvogel, G. Crone, D. Doyle, U. Gageur, A. M. Heras, C. Jewell, L. Metcalfe, S. Ott, and M. Schmidt (2010, July). Herschel Space Observatory. An ESA facility for far-infrared and submillimetre astronomy. *AAP* *518*.
- Pon, A., D. Johnstone, J. Bally, and C. Heiles (2014, June). The origin of ionized filaments within the Orion-Eridanus superbubble. *MNRAS* *441*, 1095–1104.
- Pon, A., B. B. Ochsendorf, J. Alves, J. Bally, S. Basu, and A. G. G. M. Tielens (2016, August). Kompaneets Model Fitting of the Orion-Eridanus Superbubble. II. Thinking Outside of Barnard’s Loop. *APJ* *827*, 42.

- Price, S. D., M. P. Egan, S. J. Carey, D. R. Mizuno, and T. A. Kuchar (2001, May). Midcourse Space Experiment Survey of the Galactic Plane. *AJ* *121*, 2819–2842.
- Purcell, C. R., M. G. Hoare, W. D. Cotton, S. L. Lumsden, J. S. Urquhart, et al. (2013, March). The Coordinated Radio and Infrared Survey for High-mass Star Formation. II. Source Catalog. *APJS* *205*, 1.
- Purcell, C. R., M. G. Hoare, W. D. Cotton, S. L. Lumsden, J. S. Urquhart, and et al (2013, May). VizieR Online Data Catalog: CORNISH project. II. Source catalog (Purcell+, 2013). *VizieR Online Data Catalog* *220*, 50001.
- Qiao, H.-H., A. J. Walsh, J. A. Green, S. L. Breen, J. R. Dawson, et al. (2016, December). Accurate OH Maser Positions from the SPLASH Pilot Region. *APJS* *227*, 26.
- Quintana-Lacaci, G., M. Agúndez, J. Cernicharo, et al. (2013, December). Detection of circumstellar nitric oxide. Enhanced nitrogen abundance in IRC +10420. *AAP* *560*, L2.
- Remazeilles, M., C. Dickinson, A. J. Banday, M.-A. Bigot-Sazy, and T. Ghosh (2015, August). An improved source-subtracted and destriped 408-MHz all-sky map. *MNRAS* *451*, 4311–4327.
- Remijan, A. J., A. Markwick-Kemper, and ALMA Working Group on Spectral Line Frequencies (2007, December). Splatalogue: Database for Astronomical Spectroscopy. In *American Astronomical Society Meeting Abstracts*, Volume 39 of *Bulletin of the American Astronomical Society*, pp. 963.
- Rice, T. S., B. Reipurth, S. J. Wolk, L. P. Vaz, and N. J. G. Cross (2015, October). Near-infrared Variability in the Orion Nebula Cluster. *AJ* *150*, 132.
- Roshi, D. A., W. M. Goss, and S. Jeyakumar (2014, October). Very Large Array and Green Bank Telescope Observations of Orion B (NGC 2024, W12): Photodissociation Region Properties and Magnetic Field. *ApJ* *793*, 83.
- Rudnitskij, G. M. (2002). Molecular Masers in Variable Stars. *PASA* *19*, 499–504.
- Salas, P., J. B. R. Oonk, R. J. van Weeren, F. Salgado, L. K. Morabito, et al. (2017, May). LOFAR observations of decameter carbon radio recombination lines towards Cassiopeia A. *MNRAS* *467*, 2274–2287.

- Salgado, F., L. K. Morabito, J. B. R. Oonk, P. Salas, M. C. Toribio, et al. (2017a, March). Low-frequency Carbon Radio Recombination Lines. I. Calculations of Departure Coefficients. *APJ* 837, 141.
- Salgado, F., L. K. Morabito, J. B. R. Oonk, P. Salas, M. C. Toribio, et al. (2017b, March). Low-frequency Carbon Radio Recombination Lines. II. The Diffuse Interstellar Medium. *APJ* 837, 142.
- Santana, M. M., J. M. Gonzalez, and C. Cruz (2017, Oct). Nitric oxide accumulation: The evolutionary trigger for phytopathogenesis. *Frontiers in Microbiology* 8.
- Sault, R. J. (1994, October). An analysis of visibility-based continuum subtraction. *AAPS* 107.
- Sault, R. J., P. J. Teuben, and M. C. H. Wright (1995). A Retrospective View of MIRIAD. In R. A. Shaw, H. E. Payne, and J. J. E. Hayes (Eds.), *Astronomical Data Analysis Software and Systems IV*, Volume 77 of *Astronomical Society of the Pacific Conference Series*, pp. 433.
- Scaife, A. M. M. and G. H. Heald (2012, June). A broad-band flux scale for low-frequency radio telescopes. *MNRAS* 423, L30–L34.
- Schilbach, E. and S. Röser (2008, October). On the origin of field O-type stars. *AAP* 489, 105–114.
- Schlegel, D. J., D. P. Finkbeiner, and M. Davis (1998, June). Maps of Dust Infrared Emission for Use in Estimation of Reddening and Cosmic Microwave Background Radiation Foregrounds. *APJ* 500, 525–553.
- Schlingman, W. M., Y. L. Shirley, D. E. Schenk, E. Rosolowsky, J. Bally, et al. (2011, August). The Bolocam Galactic Plane Survey. V. HCO⁺ and N₂H⁺ Spectroscopy of 1.1 mm Dust Continuum Sources. *APJS* 195, 14.
- Schmid-Burgk, J., R. Densing, E. Krugel, H. Nett, H. P. Roser, F. Schafer, G. Schwaab, P. van der Wal, and R. Wattenbach (1989, May). Extended CO (J = 7-6) emission from Orion molecular cloud 1 - Hot ambient gas, two hot-outflow sources. *AAP* 215, 150–164.
- Schuller, F., K. M. Menten, Y. Contreras, F. Wyrowski, P. Schilke, et al. (2009, September). ATLASGAL - The APEX telescope large area survey of the galaxy at 870 μ m. *AAP* 504, 415–427.

- Seon, K.-I., A. Witt, I.-J. Kim, J.-H. Shinn, J. Edelstein, K.-W. Min, and W. Han (2011, December). Comparison of the Diffuse H α and FUV Continuum Backgrounds: On the Origins of the Diffuse H α Background. *APJ* 743, 188.
- Sevenster, M. N., H. J. van Langevelde, R. A. Moody, et al. (2001, February). The ATCA/VLA OH 1612 MHz survey. III. Observations of the Northern Galactic Plane. *AAP* 366, 481–489.
- Shaver, P. A. (1975, October). Characteristics of the interstellar medium as deduced from low-frequency recombination line observations. *AAP* 43, 465–468.
- Shaw, R. A., F. Hill, and D. J. Bell (Eds.) (2007, October). *Astronomical Data Analysis Software and Systems XVI*, Volume 376 of *Astronomical Society of the Pacific Conference Series*.
- Shivaei, I., N. A. Reddy, C. C. Steidel, and A. E. Shapley (2015, May). Investigating H α , UV, and IR Star-formation Rate Diagnostics for a Large Sample of $z \sim 2$ Galaxies. *APJ* 804, 149.
- Shuch, H. P. (2011). *Searching for Extraterrestrial Intelligence*.
- Skouteris, D., F. Vazart, C. Ceccarelli, N. Balucani, C. Puzzarini, and V. Barone (2017, June). New quantum chemical computations of formamide deuteration support gas-phase formation of this prebiotic molecule. *MNRAS* 468, L1–L5.
- Skrutskie, M. F., R. M. Cutri, R. Stiening, M. D. Weinberg, S. Schneider, et al. (2006, February). The Two Micron All Sky Survey (2MASS). *AJ* 131, 1163–1183.
- Smith, M. D. (2014, February). Evolutionary tracks of massive stars during formation. *MNRAS* 438, 1051–1066.
- Sokolowski, M., T. Colegate, A. T. Sutinjo, D. Ung, R. Wayth, et al. (2017, November). Calibration and Stokes Imaging with Full Embedded Element Primary Beam Model for the Murchison Widefield Array. *PASA* 34, e062.
- Sokolowski, M., R. B. Wayth, and T. Ellement (2017, January). The statistics of radio frequency interference propagating from long distances to the Murchison radio-astronomy observatory. In *Radio Frequency Interference (RFI)*, article id. 7833541, pp. 7833541.

- Sorochenko, R. L. and A. P. Tsivilev (2010, August). Detection and application of carbon recombination lines in millimeter range. *Kinematics and Physics of Celestial Bodies* 26, 162–168.
- Soszyński, I., A. Udalski, M. K. Szymański, M. Kubiak, G. Pietrzyński, et al. (2013, March). The Optical Gravitational Lensing Experiment. The OGLE-III Catalog of Variable Stars. XV. Long-Period Variables in the Galactic Bulge. *ACTAA* 63, 21–36.
- Spitzer, L. (1998, May). *Physical Processes in the Interstellar Medium*.
- Stepkin, S. V., A. A. Konovalenko, N. G. Kantharia, and N. Udaya Shankar (2007, January). Radio recombination lines from the largest bound atoms in space. *MNRAS* 374, 852–856.
- Stewart, A. and P. Lubin (2017, September). The trillion planet survey: an optical search for directed intelligence in M31. In *Society of Photo-Optical Instrumentation Engineers (SPIE) Conference Series*, Volume 10401 of *Society of Photo-Optical Instrumentation Engineers (SPIE) Conference Series*, pp. 104010C.
- Stutzki, J., U. U. Graf, R. Genzel, A. I. Harris, R. E. Hills, and A. P. G. Russell (1991). First detection of ^{13}CO J = 6 to 5: large amounts of warm molecular gas. In R. A. James and T. J. Millar (Eds.), *Molecular Clouds*, pp. 17.
- Tan, J. C., M. T. Beltrán, P. Caselli, F. Fontani, A. Fuente, M. R. Krumholz, C. F. McKee, and A. Stolte (2014). Massive Star Formation. *Protostars and Planets VI*, 149–172.
- Taylor, G. B., S. W. Ellingson, N. E. Kassim, J. Craig, J. Dowell, C. N. Wolfe, J. Hartman, G. Bernardi, T. Clarke, A. Cohen, and et al (2012, December). First Light for the First Station of the Long Wavelength Array. *JAI* 1, 50004.
- Taylor, M. B. (2005, December). TOPCAT & STIL: Starlink Table/VOTable Processing Software. In P. Shopbell, M. Britton, and R. Ebert (Eds.), *Astronomical Data Analysis Software and Systems XIV*, Volume 347 of *Astronomical Society of the Pacific Conference Series*, pp. 29.
- Taylor, M. B. (2006, July). STILTS - A Package for Command-Line Processing of Tabular Data. In C. Gabriel, C. Arviset, D. Ponz, and S. Enrique (Eds.), *Astro-*

nomical Data Analysis Software and Systems XV, Volume 351 of *Astronomical Society of the Pacific Conference Series*, pp. 666.

Tercero, B., J. Cernicharo, A. López, et al. (2015, October). Searching for trans ethyl methyl ether in Orion KL. *AAP* 582, L1.

Thiagaraj, P., K. S. Srivani, D. A. Roshi, et al. (2015, March). A digital-receiver for the MurchisonWidefield Array. *EA* 39, 73–93.

Thompson, A. R., J. M. Moran, and J. Swenson, George W. (2017). *Interferometry and Synthesis in Radio Astronomy, 3rd Edition*.

Thompson, R. I. (1984, August). Lyman and Balmer continuum ionization in zero-age main-sequence stars - Applications to the line excess phenomenon. *APJ* 283, 165–168.

Tingay, S. J., R. Goeke, J. D. Bowman, et al. (2013, January). The Murchison Widefield Array: The Square Kilometre Array Precursor at Low Radio Frequencies. *PASA* 30, 7.

Tingay, S. J., C. Tremblay, A. Walsh, and R. Urquhart (2016, August). An Opportunistic Search for Extraterrestrial Intelligence (SETI) with the Murchison Widefield Array. *APJL* 827, L22.

Tingay, S. J., C. D. Tremblay, and S. Croft (2018, March). A Search for Extraterrestrial Intelligence (SETI) toward the Galactic Anticenter with the Murchison Widefield Array. *APJ* 856, 31.

Tout, C. A., S. J. Aarseth, O. R. Pols, and P. P. Eggleton (1997, November). Rapid binary star evolution for N-body simulations and population synthesis. *MNRAS* 291, 732.

Townes, C. H. and A. L. Schawlow (1975). *Microwave spectroscopy*. Dover Publications.

Travers, M. J., M. C. McCarthy, P. Kalmus, C. A. Gottlieb, and P. Thaddeus (1996, November). Laboratory Detection of the Cyanopolyne HC 13N. *APJL* 472, L61.

Tremblay, C. D., N. Hurley-Walker, M. Cunningham, P. A. Jones, P. J. Hancock, R. Wayth, and C. H. Jordan (2017, November). A first look for molecules

- between 103 and 133 MHz using the Murchison Widefield Array. *MNRAS* *471*, 4144–4154.
- Tremblay, C. D., P. A. Jones, M. Cunningham, N. Hurley-Walker, C. H. Jordan, and S. J. Tingay (2018, June). A Molecular Line Survey around Orion at Low Frequencies with the MWA. *APJ* *860*, 145.
- Tremblay, C. D., C. H. Jordan, M. Cunningham, P. A. Jones, and N. Hurley-Walker (2018, May). Low-Frequency Carbon Recombination Lines in the Orion Molecular Cloud Complex. *PASA* *35*, e018.
- Tremblay, C. D., A. J. Walsh, S. N. Longmore, J. S. Urquhart, and C. König (2015, December). A Search for High-Mass Stars Forming in Isolation using CORNISH and ATLASGAL. *PASA* *32*, e047.
- Tremblay, S. E., S. M. Ord, N. D. R. Bhat, et al. (2015, February). The High Time and Frequency Resolution Capabilities of the Murchison Widefield Array. *PASA* *32*, 5.
- Trott, C. M., C. H. Jordan, S. G. Murray, B. Pindor, D. A. Mitchell, et al. (2018, November). Assessment of Ionospheric Activity Tolerances for Epoch of Reionization Science with the Murchison Widefield Array. *APJ* *867*, 15.
- Urquhart, J. S., M. G. Hoare, S. L. Lumsden, R. D. Oudmaijer, T. J. T. Moore, et al. (2012, February). The RMS survey: resolving kinematic distance ambiguities towards a sample of compact H ii regions using H i absorption*. *MNRAS* *420*, 1656–1672.
- Urquhart, J. S., M. A. Thompson, T. J. T. Moore, C. R. Purcell, M. G. Hoare, et al. (2013, October). ATLASGAL - properties of compact H II regions and their natal clumps. *MNRAS* *435*, 400–428.
- van der Werf, P. P., W. M. Goss, and C. R. O’Dell (2013, January). Tearing the Veil: Interaction of the Orion Nebula with its Neutral Environment. *APJ* *762*, 101.
- van Dishoeck, E. F. (2014). Astrochemistry of dust, ice and gas: introduction and overview. *Faraday Discussions* *168*, 9.
- van Haarlem, M. P., M. W. Wise, A. W. Gunst, G. Heald, J. P. McKean, J. W. T. Hessels, A. G. de Bruyn, R. Nijboer, J. Swinbank, and et al (2013, August). LOFAR: The LOW-Frequency ARray. *AAP* *556*, A2.

- Velilla Prieto, L., C. Sánchez Contreras, J. Cernicharo, M. Agúndez, G. Quintana-Lacaci, J. Alcolea, V. Bujarrabal, F. Herpin, K. M. Menten, and F. Wyrowski (2015, March). New N-bearing species towards OH 231.8+4.2. HNCO, HNCS, HC₃N, and NO. *AAP* 575, A84.
- Walsh, A. J., S. L. Breen, T. Britton, K. J. Brooks, M. G. Burton, M. R. Cunningham, and et al (2011, September). The H₂O Southern Galactic Plane Survey (HOPS) - I. Techniques and H₂O maser data. *MNRAS* 416, 1764–1821.
- Walsh, A. J., A. R. Hyland, G. Robinson, and M. G. Burton (1997, October). Studies of ultracompact HII regions - I. Methanol maser survey of IRAS-selected sources. *MNRAS* 291, 261–278.
- Walsh, A. J., C. Purcell, S. Longmore, C. H. Jordan, and V. Lowe (2012, December). Maser Source-Finding Methods in HOPS. *PASA* 29, 262–268.
- Wayth, R. B., S. J. Tingay, C. M. Trott, D. Emrich, M. Johnston-Hollitt, et al. (2018, September). The Phase II Murchison Widefield Array: Design Overview. *ArXiv e-prints*, arXiv:1809.06466.
- Weaver, R., R. McCray, and J. Castor (1977, dec). Interstellar bubbles ii. structure and evolution. *ApJ* 218, 377–395.
- Weidner, C. and P. Kroupa (2005, June). The Variation of Integrated Star Initial Mass Functions among Galaxies. *APJ* 625, 754–762.
- Weidner, C., P. Kroupa, and T. Maschberger (2009, February). The influence of multiple stars on the high-mass stellar initial mass function and age dating of young massive star clusters. *MNRAS* 393, 663–680.
- Wenger, M., F. Ochsenbein, D. Egret, P. Dubois, F. Bonnarel, S. Borde, F. Genova, G. Jasniewicz, S. Laloë, S. Lesteven, and R. Monier (2000, April). The SIMBAD astronomical database. The CDS reference database for astronomical objects. *AAPS* 143, 9–22.
- Whiting, M. T. (2012, April). DUCHAMP: a 3D source finder for spectral-line data. *MNRAS* 421, 3242–3256.
- Wilson, B. A., T. M. Dame, M. R. W. Mashedier, and P. Thaddeus (2005, February). A uniform CO survey of the molecular clouds in Orion and Monoceros. *AAP* 430, 523–539.

- Wilson, R. (2015, January). The Discovery of Interstellar CO. *IEEE Transactions on Terahertz Science and Technology* 5, 14–15.
- Wilson, T. L. and R. Rood (1994). Abundances in the Interstellar Medium. *ARAA* 32, 191–226.
- Woods, P. M., T. J. Millar, E. Herbst, and A. A. Zijlstra (2003, April). The chemistry of protoplanetary nebulae. *AAP* 402, 189–199.
- Wright, J. T. (2018, January). SETI is Part of Astrobiology. *ArXiv e-prints*.
- Wu, C., A. Wicenec, D. Pallot, and A. Checcucci (2013, December). Optimising NGAS for the MWA Archive. *Experimental Astronomy* 36, 679–694.
- Wyrowski, F., P. Schilke, P. Hofner, and C. M. Walmsley (1997, October). Carbon Radio Recombination Lines in the Orion Bar. *APJL* 487, L171–L174.
- Yamamura, I., K. Kawaguchi, and S. T. Ridgway (2000, January). Identification of SH $\Delta v=1$ Ro-vibrational Lines in R Andromedae. *APJL* 528, L33–L36.
- Zheng, H., M. Tegmark, J. S. Dillon, D. A. Kim, A. Liu, et al. (2017, January). An improved model of diffuse galactic radio emission from 10 MHz to 5 THz. *MNRAS* 464, 3486–3497.
- Zinnecker, H. and H. W. Yorke (2007, September). Toward Understanding Massive Star Formation. *ARAA* 45, 481–563.
- Zoonematkermani, S., D. J. Helfand, R. H. Becker, R. L. White, and R. A. Perley (1990, September). A catalog of small-diameter radio sources in the Galactic plane. *APJS* 74, 181–224.

Every reasonable effort has been made to acknowledge the owners of copyright material. I would be pleased to hear from any copyright owner who has been omitted or incorrectly acknowledged.